CORA Cork Open Research Archive
Cartlann Taighde Oscailte Chorcaí

Title	Development of low-cost spectroscopic techniques for measuring Nitrogen Dioxide in urban environments
Authors	Halpin, Eibhlín Francis
Publication date	2024
Original Citation	Halpin, E. F. 2024. Development of low-cost spectroscopic techniques for measuring Nitrogen Dioxide in urban environments. PhD Thesis, University College Cork.
Type of publication	Doctoral thesis
Rights	© 2024, Eibhlín Halpin. - https://creativecommons.org/publicdomain/zero/1.0/
Download date	2026-11-05 20:27:44
Item downloaded from	https://hdl.handle.net/10468/17495



UCC
University College Cork, Ireland
Coláiste na hOllscoile Corcaigh

Development of Low-Cost Spectroscopic Techniques for Measuring Nitrogen Dioxide in Urban Environments

A thesis submitted to

Ollscoil na hÉireann, Corcaigh

National University of Ireland, Cork



UCC

Coláiste na hOllscoile Corcaigh

University College Cork, Ireland

for the degree of

Doctor of Philosophy

by

Eibhlín Francis Halpin

based on research carried out at

School of Chemistry & Environmental Research Institute

Supervisors: *Dr. Dean Venables*

Head of School: *Professor Anita Maguire*

2024

Declaration

This is to certify that the work I am submitting is my own and has not been submitted for another degree, either at University College Cork or elsewhere. All external references and sources are clearly acknowledged and identified within the contents. I have read and understood the regulations of University College Cork concerning plagiarism and intellectual property.



Eibhlín Halpin

Acknowledgements

I would firstly like to sincerely thank my supervisor, Dr Dean Venables, for his unwavering guidance, support, and encouragement throughout my PhD journey. Beyond academic guidance, I am especially grateful for your kindness and sense of humour that really made this an enjoyable and rewarding four years.

Thank you to all members of the CRAC group, including Prof John Wenger, Prof Andy Ruth, and Dr Stig Hellebust for their sound advice and good company. I am grateful to the group's talented researchers, Niall, Meng, Mixtli and Satheesh, for their insightful advice and for sharing their expertise. To everyone who worked with me out in the ERI, Rósín, Hayley, Clara, Conor, Rohit and Chaitra, thank you for the fun distractions and long lunch breaks when needed. The CRAC group was a great environment to carry out my PhD with lovely people and a great sense of community.

I wouldn't have gotten to this point without the support of my parents, Tricia and Jimmy, who made me believe I could accomplish anything I set my mind to, and my siblings, Sadhbh and Tom, who always brought me back down to earth. To my closest friends, Jane, Eoin, Huan, and Hannah, who listened to me complain and cheered me up in difficult times, and Sandi who was there for me at home and away, thank you. Finally, I can't forget to mention Cosmo the cat whose persistence and determination turned out to be very distracting and hugely unhelpful.

This thesis began during the first lockdowns in 2020, based out of my bedroom. Four years later, I completed a field campaign in the living room. It's fair to say the trip downstairs taught me a lot.

Thanks for the craic.

Dedication

For Jimmy - Stay cool.

Abstract

Nitrogen dioxide (NO_2), a priority air pollutant in Ireland, is a toxic gas released during combustion processes, making traffic and transport major sources in urban environments. Commercial NO_2 monitors used by official monitoring bodies have low spatial resolution and do not capture the complex distribution of NO_2, particularly in the presence of mobile sources, like vehicles, and low-cost electrochemical NO_2 sensing is not accurate or reliable enough for consistent air pollutant monitoring.

In this thesis, spectroscopic techniques were explored for achieving selective and sensitive NO_2 measurements at a reasonably low cost using LED light sources and non-dispersive detectors for *in situ* or remote applications. Two-channel spectroscopic methods were simulated, and a narrowband two-channel system was tested in an atmospheric simulation chamber to confirm a response to NO_2, however, this system was not sensitive to ambient NO_2 levels without appropriate signal amplification.

A single-channel wideband instrument was therefore built with improved sensitivity but reduced selectivity to NO_2. The single-channel instrument was used to measure ambient NO_2 near a primary school in Cork City to assess the feasibility of capturing NO_2 concentrations with high temporal resolution at a relatively low cost. The effect of school traffic on local NO_2 emissions was explored in the context of a street canyon microenvironment.

This work aims to bridge the gap between expensive NO_2 monitoring systems and unreliable low-cost sensors and discusses the future development of a lower cost two-channel NO_2 detector with a recommended instrument design and approximate cost analysis.

Table of Contents

Declaration i

Acknowledgements ii

Dedication iii

Abstract iv

Chapter 1 Introduction 7

1.1 Air pollution 7

1.2 Sources, chemistry, and impacts of nitrogen dioxide 21

1.3. Measurement of nitrogen dioxide 29

1.4 Signal enhancement in spectroscopic measurements 46

1.5 Thesis objectives and outline 54

Chapter 2 Theory and Simulations of Two-channel Absorption Spectroscopy . 56

2.1 Theoretical development of two-channel ratiometric spectroscopy 56

2.2 Application of two narrow channels for NO_2 detection 60

2.3 Simulated responses 66

Chapter 3 Characterisation of system components 96

3.1 Introduction 96

3.2 Characterisation of instrument components 97

3.3 Spectral considerations in using nondispersive detectors with optical cavities 108

3.4 Wide bandpass CEAS system 123

3.5 Discussion 125

Chapter 4 Instrument validation in atmospheric simulation chambers 128

4.1 Atmospheric simulation chamber experiments 128

4.2 Ratiometric two-narrowband channel method 132

4.3 Signal amplification using lock-in detection 145

4.4 Single-channel CEAS system 149

4.5 Comparison of instruments and measurement strategies 163

Chapter 5 Field measurements in an urban traffic environment 168

5.1 Introduction 168

5.2 Description of the measurement site 170
5.3 Instrument description 176
5.4 Results 180
5.4 Discussion 206
Chapter 6 Conclusions 211
6.1 Future prospects 215
References 218

Chapter 1 Introduction

1.1 Air pollution

Major air pollutants in the troposphere

Air pollution causes major health and environmental problems across the globe. In 2016, the World Health Organisation (WHO) reported that 92% of the earth's population was exposed to harmful levels of ambient air pollution (World Health Organisation, 2016). Monitoring ambient air pollutants allows official bodies to identify areas where air quality is a concern. Strategies to improve air quality are developed by assessing the local chemical regime and air pollutants (Yang et al., 2022). Mitigation actions to improve air quality can reduce trace gas and greenhouse gas emissions, benefitting human health and the environment in many ways. Air quality is influenced by the trace gases and particulate matter present in the atmosphere, particularly the troposphere.

The atmosphere is separated into several layers based on its temperature-altitude profile, with the troposphere occurring from the surface up to about 10 km. Within the troposphere, pressure decreases as altitude increases toward the tropopause (the upper bound of the troposphere). The 'boundary layer' describes the lowest region of the troposphere near the surface where the air is turbulent, mixing heat, moisture, and pollutants. Above the troposphere is the stratosphere, which extends from 10 - 50 km in altitude and contains most of the atmosphere's ozone. This ozone layer absorbs high energy ultraviolet (UV) solar radiation, preventing it from reaching the surface and damaging living organisms. Absorption of UV radiation heats the stratosphere, resulting in increasing temperatures with altitude. Beyond the stratosphere, the mesosphere (50 – 80 km), thermosphere (80 – 500 km), and exosphere (> 500 km) contain compounds and ions which absorb or scatter light. The following discussion focuses on sources, sinks, and chemical processes in the troposphere, where human exposure occurs.

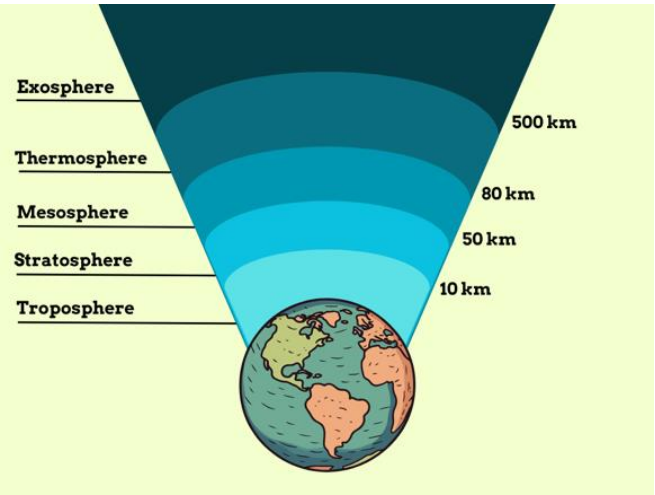


Figure 1.1. Structure of the atmosphere showing the troposphere (<10km), stratosphere (10-50km), mesosphere (50-80km), thermosphere (80-500km), and exosphere (>500km).

Several components of the troposphere are major air pollutants. These include harmful gases like nitrogen oxides (NO_x), ground-level ozone (O_3), sulfur oxides (SO_x), ammonia (NH_3), and some volatile organic compounds (VOCs). Particulate matter, a stable suspension of solid or liquid particles in air, is also a key pollutant. The sources and reactions of these components are introduced below.

NO_x, consisting of nitric oxide (NO) and nitrogen dioxide (NO_2), is produced naturally by lightning and wildfire events and human sources such as combustion processes in industrial settings and internal combustion in vehicle engines. These processes also produce particulate matter. Particulate matter (PM) suspended in a gas is referred to as an 'aerosol' (Wayne, 2000). Primary aerosols are produced from a variety of anthropogenic sources, including traffic, road dust, domestic and industrial burning, as well as natural sources such as sea spray, sand, dust, and pollen. Secondary aerosols are formed from the oxidation of precursor gases to form low volatility products which condense on existing particles or nucleation of new particles in the atmosphere (Myhre et al., 2013). While O_3 plays a vital role in the stratosphere by filtering out harmful UV radiation, tropospheric or ground-level ozone is a toxic pollutant and contributes to smog formation. Tropospheric O_3 is generally a secondary pollutant formed after the photolysis and reactions of VOCs or NO_x, which are emitted from industrial and traffic-related activities.

SO_x, primarily sulfur dioxide (SO_2), is a major contributor to shipping, industrial and power plant emissions. SO_2 is also naturally produced by volcanic activity and can be converted into sulfuric acid (H_2SO_4) and sulfate particles in the atmosphere. Ammonia is strongly associated with agricultural practices. It is released after application of nitrogen-based fertilizers and from manure and reacts readily with H_2SO_4 and HNO_3 to form secondary particulate matter.

Atmospheric chemistry processes are largely driven by radical species. The hydroxyl radical (OH) governs daytime chemistry by oxidizing carbon monoxide (CO) and hydrocarbons (HCs). At night, the nitrate radical, NO_3, is the dominant oxidant but is rapidly photolyzed during the day. O_3 is also a major atmospheric oxidant. NO_x and SO_x compounds also take part in these oxidation processes, with products like nitrous oxide (N_2O), methane (CH_4), and methyl chloride (CH_3Cl) eventually being transported to the stratosphere. These species contribute to the formation of radicals such as NO_x, HO_x, and ClO_x, which destroy stratospheric ozone and led to the formation of an "ozone hole" (Wayne, 2000):

$$H + O_3 \rightarrow OH + O_2 \quad \text{(R. 1.1)}$$

$$OH + O \rightarrow H + O_2 \quad \text{(R. 1.2)}$$

Net: $\mathbf{O + O_3 \rightarrow O_2 + O_2}$ (R. 1.3)

$$OH + O_3 \rightarrow HO_2 + O_2 \quad \text{(R. 1.4)}$$

$$HO_2 + O \rightarrow OH + O_2 \quad \text{(R. 1.5)}$$

Net: $\mathbf{O + O_3 \rightarrow O_2 + O_2}$ (R. 1.6)

$$NO + O_3 \rightarrow NO_2 + O_2 \quad \text{(R. 1.7)}$$

$$NO_2 + O \rightarrow NO + O_2 \quad \text{(R. 1.8)}$$

Net: $\mathbf{O + O_3 \rightarrow O_2 + O_2}$ (R. 1.9)

$$Cl + O_3 \rightarrow ClO + O_2 \quad \text{(R. 1.10)}$$

$$ClO + O \rightarrow Cl + O_2 \quad \text{(R. 1.11)}$$

Net: $\mathbf{O + O_3 \rightarrow O_2 + O_2}$ (R. 1.12)

VOCs are emitted from a range of solids and liquids, such as paints, solvents, domestic and industrial cleaning supplies, and petroleum-based fuels as well as natural sources such as plant and animal emissions. VOCs can contribute to the formation of ground-level O_3, aerosols, and groundwater contamination. HCs include terpenes ($C_{10}H_{16}$) such as isoprene and α- and β-pinene which are emitted from trees and plants. Methane and other light alkanes are also produced naturally by digestion processes in cattle and wild animals and are emitted from natural wetlands like swamps and boglands. Increased livestock numbers have resulted in rising methane emissions (Johnson & Johnson, 1995; Maze et al., 2024).

Natural sources, like wildfires or volcanic activity contribute to air pollution. Wildfires may be ignited by lightning, as in July 2002 in Quebec, Canada, when over 250 fires were started by lightning strikes, burning over one million hectares of forest. Wildfires are also driven by warm and dry conditions caused by climate change, and human ignition (e.g., agricultural burning (Xu & You, 2023), land use changes, vandalism, arson). In the USA, anthropogenic wildfires accounted for 84% of wildfires between 1992 – 2012 and 44% of the area burned (Balch et al., 2017).

Traffic-related air pollutants (TRAPs), often featuring in slow-moving traffic with vehicles idling at intersections, are a serious contributor to air pollution in cities and large towns. Additionally, tall buildings in cities can disrupt natural ventilation and hinder pollutant dispersion (Chew & Norford, 2018). Topography plays a crucial role as well, with cities situated in valleys experiencing heightened air pollution levels. For instance, in the Po Valley, Italy, high urban and industrial emissions are amplified by tropospheric temperature inversions caused by the Western Alps (Rendón et al., 2014). Field observations in this thesis were carried out in Cork City, Ireland, which is situated in a valley with predominantly narrow city streets.

Health and environmental impacts of air pollution

Air pollutants can have complex and often harmful effects on the environment in which we live. There is strong evidence that air pollution has a serious effect on public health (Liu et al., 2024). According to the World Health Organisation (2021) ambient air pollution causes up to 3 million premature deaths globally every year. The

Environmental Protection Agency (2021) reported over 1,300 premature deaths due to air pollution in Ireland. Urban areas with high population densities see high concentrations of traffic-related air pollutants (TRAPs) which include NO_2, CO, PAHs, VOCs and particulate matter (PM_{10} and $PM_{2.5}$), among other emission sources (Boogaard et al., 2022). Humans are vulnerable to airborne pollutants because the olfactory system draws pollutants into the lungs which can cause a wide range of complicated health effects (Kang et al., 2024; S. Wei et al., 2021). Some pollutants may exacerbate these health effects by reacting together within the lungs, as O_3 has been found to worsen the effects of $PM_{2.5}$ exposure (Jiang et al., 2024).

In December 2020, air pollution was recognised as the cause of death of 9-year-old Ella Adoo-Kissi-Debrah, who suffered an acute asthma attack brought on by exposure to high levels of air pollution in London, 2013 (*The Ella Roberta Foundation*, 2024). This was the first time poor air quality was identified in a coroner's report as a cause of death and highlighted the dangers of exposure to air pollutants, particularly for vulnerable groups (Vilcins et al., 2024).

Although Adoo-Kissi-Debra's death was the first to list air pollution as an official cause of death, air pollution has long been associated with cardiovascular mortality and sudden cardiac arrest (SCA). Zhao et al. (2020) investigated the link between incidences of sudden cardiac arrest with PM, CO, NO_2, O_x and SO_2 concentrations up to 3 days prior to onset in Japan. Pollutant concentrations were measured by a monitoring station in the same region as the hospital. Daily incidences of SCA increased with a 10 $\mu g/m^3$ increase in PM concentrations, with a similar effect noted for other pollutants, highlighting that local pollutant monitoring is required to quantify their effects on public health. As discussed by Luo et al. (2024), previous studies into the onset of cardiac arrest triggered by acute air pollutant exposures only consider already vulnerable patients. Long-term exposure to PM and NO_x was found to increase the risk of sudden cardiac arrest and intermediate cardiovascular diseases more than was previously reported and Luo and coworkers recommended examining a link to the development of chronic cardiovascular diseases, such as COPD. Local air pollutant concentrations can heavily impact cardiovascular health.

$PM_{2.5}$ was shown to have a negative effect on cognitive function in school children in China by Xu et al. (2023). Students were tested academically in a room with air

purifiers turned on and tested again with the purifiers turned off. Test scores were significantly higher when air purifiers were used, showing the effects of air quality on mental health in addition to physical health.

Smog events have an acute and long-lasting effect on public health. Photochemical smog occurs when NO_2 is photolyzed in the atmosphere, leading to the formation of secondary particles and tropospheric ozone causing an orange or brown haze. Ozone is a strong oxidant and is harmful to humans and vegetation (Wong et al., 2024). O_3-related respiratory deaths increased by 46 % globally from 2000 – 2019 (Dong et al., 2024) due to increased ground-level concentrations of O_3. The non-linear relationship between NO_x, VOCs and O_3 is discussed further in Section 1.2. Increased deaths due to O_3 exposure were mostly seen during warm seasons because of increased photochemical activity.

The Great London Smog of 1952 is a well-documented extreme air pollution episode that directly caused 4,000 deaths and has been estimated to cause up to 12,000 deaths including the months following the pollution event (Bell et al., 2004). The great smog served as a natural experiment to observe the long-term effects of exposure to extreme air pollution at a young age. Bharadwaj et al. (2016) found that exposure to the Great Smog as an infant increased the likelihood of childhood asthma by 20 % and exposure in early life increased the likelihood of developing asthma as an adult by 10 %. The Great Smog had concentrations of SO_2 and PM up to 4,000 $\mu g/m^3$ (Mills et al., 2022; Wilkins, 1954). Emission regulations, new technologies and fuel have led to great improvements in air quality in London and across wealthy countries over the last several decades. However, adverse health effects persist as anthropogenic sources, like fuel combustion, shipping, industry, and agricultural activities, still contribute to air pollution.

Air pollutants also affect climate and the environment. Trace gases in the atmosphere significantly impact the rate of production of stratospheric O_3. Trace gases such as CH_4, N_2O and fluorinated compounds (HFC, CFCs) contribute to the warming of the atmosphere by absorbing low energy radiation. This causes a greenhouse gas effect and raises the temperature of the Earth, contributing to global warming and climate change. Atmospheric aerosols strongly affect the radiative forcing of incoming solar radiation. Black carbon absorbs light and adds to atmospheric warming. Other

aerosols such as nitrates and sulphates mostly scatter light, which increases the albedo of the atmosphere and has a cooling effect. Particles also reduce radiative forcing by acting as cloud condensation nuclei (CCN) and enhancing cloud cover (de Jonge et al., 2024).

Wildfires emit greenhouse gases (CO_2, CH_4 and N_2O), $PM_{2.5}$ and ground-level O_3 precursors (CO, VOCs, NO_x), as reported by the National Air Pollution Surveillance (Schneider et al., 2021). Following wildfires in California in 2020, formaldehyde (HCHO) and NO_2 emissions increased by 16 % and 9 % respectively (Jin et al., 2023). NO_2 emissions were highly concentrated near active burning regions, whereas HCHO emissions reached beyond their sources to urban areas. A larger increase in NO_2 emissions was observed in NO_x-limited regions with larger HCHO emissions observed in VOC-limited regions. Both regimes result in enhanced ground-level O_3 production. NO_x emissions are also converted to peroxyacyl nitrates (PANs), particulate HNO_3 and organic nitrogen-containing species (Peng et al., 2021). Wildfires are a major source of air pollutants that leave surrounding urban areas detrimentally impacted in terms of environment and public health (Cedeño Laurent et al., 2024; Maji et al., 2024).

The impacts of these pollutants are not limited to the air alone — soil and water quality are also affected. NO_x and NH_3 compounds react with water vapour in the atmosphere to produce nitric acid, which forms acid rain. Nitrates are then deposited into soils, increasing soil pH and degrading plant health. Nitrate compounds run off soils or directly enter water systems, where excess nitrate causes eutrophication within water bodies, degrading water quality and loss of biodiversity (European Commission, 2021; Yang et al., 2008).

Guidelines & mitigation

The World Health Organization (WHO) compiles global air pollutant measurement data as an indicator for the progress towards the Sustainable Development Goals and air quality assurance in cities. The WHO introduced air quality guidelines that are expert scientific recommendations based on established evidence of harms caused by different air pollutants over different exposure times. The previous Air Quality

Guidelines (AQGs) from 2005 were revised in 2021. These recent AQGs reduced the recommended annual and daily limits of air pollutants across the globe for $PM_{2.5}$, PM_{10}, O_3, NO_2, SO_2 and CO (Table 1). These classical air pollutants are known for their significant negative effects on public health globally. At the regulatory level, the European Union (EU) set legal air pollutant limits based broadly on the WHO 2005 guidelines. Table 1.1 compares the WHO and EU limits. The most recent WHO guidelines are considerably lower than the EU regulations, particularly for PM, NO_2, SO_2 and CO. The EU limits are expected to be reduced in-line with the WHO guidelines within the Ambient Air Quality Directive which will be in place by 2030. This directive will drive EU member states towards a zero-pollution framework by 2050 (European Commission, 2021).

Table 1.1. WHO 2005 and 2021 Air Quality Guideline values along with the EU regulatory limits for these pollutants. Long-term limits denote annual mean values, apart from O_3 which shows the peak season limit (average of daily 8-hour mean concentrations during 6 months of peak ozone concentrations). Short-term limits are based on 24 hour mean values, except for the 2008 NO_2 EU limit (*) which is 1-hourly.

Pollutant		WHO 2005 Guideline limit ($\mu g/m^3$)	WHO 2021 Guideline limit ($\mu g/m^3$)	EU legal limits 2008 ($\mu g/m^3$)	EU Ambient Air Quality Directive 2024 ($\mu g/m^3$)
$PM_{2.5}$	Long-term	10	5	25	10
	Short-term	25	15	-	25
PM_{10}	Long-term	20	15	40	20
	Short-term	50	45	50	45
O_3	Long-term	-	60	-	-
	Short-term	100	100	120	100
NO_2	Long-term	40	10	40	20
	Short-term	-	25	200 *	50
SO_2		20	40	125	20
CO		-	4000	10000	4000

TRAPs are major contributors to air pollution in EU countries. Recognising this, the EU has been setting increasingly strict vehicle emission standards since the

introduction of EURO I vehicle emission standards in 1992. These standards limit emissions of key exhaust pollutants for petrol and diesel cars for CO, PM, hydrocarbons (HCs, THC) and non-methane hydrocarbons (NMHC) (Table 1.2 and Table 1.3). Updated testing procedures were introduced with Euro III to better represent real-world driving emissions and included limits for NO_x emissions, with a stricter limit set for petrol cars than for diesel. These NO_x limits have been progressively lowered in Euro IV (2005), V (2009) and VI (2014). Euro VII standards are projected to be published in 2025 and will include limits for ammonia (NH_3) emissions for the first time. NH_3 is formed from the decomposition of urea in the selective catalytic reduction (SCR) and may be emitted as exhaust. As NO_x emission limits become more stringent, transport may become a major source of NH_3 in urban areas (Hopke & Querol, 2022). To ensure that these standards are adhered to, widespread monitoring is required with fast time resolution so that emissions from individual vehicles can be measured. This approach will deter the use of emission control defeat devices, such as Volkswagen used in their 2009-2015 2.0-litre diesel engine vehicles which emitted 10 to 40 times more NO_x pollution than the EPA standard in real world driving (Barrett et al., 2015).

Table 1.2. Petrol EURO emission standards. Note that the HC+NO_x limit was replaced by separate HC and NO_x limits from EURO III. EURO V introduced PM and NMHC limits.

Petrol emission standards (g/km)						
Standard	**CO**	**PM**	**HC+NO_x**	**NO_x**	**THC**	**NMHC**
EURO I (1992)	2.72	-	0.97	-	-	-
EURO II (1996)	2.2	-	0.5	-	-	-
EURO III (2000)	2.3	-	-	0.15	0.2	-
EURO IV (2005)	1.0	-	-	0.08	0.1	-
EURO V (2009)	1.0	0.005	-	0.06	0.1	0.068
EURO VI (2014)	1.0	0.0045	-	0.06	0.1	0.068

Table 1.3. Diesel EURO emissions standards for passenger cars (g/km).. Note the addition of individual NO_x standards from EURO III.

Diesel emission standards (g/km)				
Standard	**CO**	**PM**	**HC+NO_x**	**NO_x**
EURO I (1992)	2.72	0.14	0.97	-
EURO II (1996)	1.0	0.008	0.7	-
EURO III (2000)	0.66	0.05	0.56	0.5
EURO IV (2005)	0.5	0.025	0.30	0.25
EURO V (2009)	0.5	0.005	0.23	0.18
EURO VI (2014)	0.5	0.0045	0.17	0.008

The introduction of pollutant limits has improved air quality. Wong et al. (2024) observed a 73% reduction in cancer risk from inhalation associated with limits on diesel particulates, solvent and gasoline-related VOCs, and PAHs emitted during coal and biomass burning. Between 2000-2004 there were 1707 cases of cancer per million in Hong Kong, China and only 451 per million between 2016-2020. The reduction was attributed to the correct classification of toxic air pollutants and mitigation strategies based on data from a regional air quality monitoring network.

However, reducing air pollutant concentrations is not straight-forward. Complex trends and reactions in the atmosphere were seen in China following the Clean Air Actions in 2013 - 2017. For example, since O_3 is a secondary pollutant and has a non-linear relationship to NO_x and VOCs, lower NO_x emissions resulted in an increase in ground-level O_3 concentrations (Liu et al., 2023). A decrease in NO_x emissions results in a decrease in O_3 in a NO_x-limited chemical regime, but in a VOC-limited regime, a decrease in VOC concentrations reduces O_3 production while lower NO_x emissions increase O_3 concentrations (Qian et al., 2019). During the first phase of China's Clean Air Actions, NO_x, SO_2, and $PM_{2.5}$ emissions were reduced, but not VOC emissions. As a result, O_3 concentrations increased despite a general improvement in air quality. The second phase of the Clean Air Actions included VOC emission reductions after

recognising the need for coordinated NO_x-VOC control to accurately reduce ground-level O_3 formation. Both NO_x and VOCs have high spatial and temporal variability and must be monitored closely to identify appropriate mitigation strategies. Dong et al. (2024) demonstrated that reducing NO_x emissions in the late-spring and early-summer and controlling VOCs during spring and autumn resulted in a 10% reduction in O_3-related mortality.

The effect of air pollutant mitigation policies was reported by (Huang et al., 2024) following the relaxation of fireworks restrictions in China during the Chinese Spring Festival in 2023. By comparing restricted and unrestricted festivals, it was found that unrestricted firework use accounted for 70 % of ambient $PM_{2.5}$ concentrations (188 $\mu g/m^3$). This study highlights the importance of implementing clean air policies to reduce emissions and of regularly monitoring these sites to understand the local chemical trends and sources.

Some cities have introduced low-emission zones (LEZ), ultra-low emission zones (ULEZ) or clean air zones (CAZ) to tackle air pollution from vehicles. CAZ are areas with a restriction on the standards of vehicles permitted to drive in the designated zone. Holman et al. (2015) reviewed the effects of CAZ on European cities in five countries: Denmark, Germany, the Netherlands, Italy and the UK. Zones that restricted both light-duty passenger vehicles and heavy-duty vehicles (HDVs) saw a reduction in the long-term average of NO_2 of up to 8%, and far greater reductions in PM concentrations. Smaller decreases in emissions were observed in cities which only restricted HDV use (Liu et al., 2023). The small observed effect of CAZ on NO_2 concentrations could be due to the high spatial and temporal distribution of NO_2, meaning that sources near the monitoring site could be masking changes in on-road concentrations.

The composition of the vehicle fleet is also an important factor. Vehicles of Euro V standard and beyond should emit relatively little NO_x, so removing these vehicles from CAZ would not have a substantial effect. Electric cars are also gaining in popularity and release no NO_2 emissions. The Greater London Authority reported roadside NO_2 reductions up to 53% in central London since the introduction of ULEZ which restricted the use of cars and vans that did not meet EURO IV (petrol) or EURO VI (diesel) standards (Greater London Authority, 2024). NO_2 concentrations even

reduced by 9% in areas outside of London, highlighting the spatial distribution of pollutants. Robust monitoring networks with good spatial-temporal resolution will be required to measure the efficacy of CAZ to reduce urban air pollution.

Monitoring

There have been many advances in pollution measurement technologies in the last 20 years, giving a fuller understanding of tropospheric air pollutant concentrations and trends. Most cities in high-income countries benefit from partial monitoring networks. On the other hand, cities in low-income countries, as well as smaller cities, towns and rural areas in most countries have little-to-no monitoring infrastructure due to high costs and maintenance demands of instrumentation.

Regulatory monitoring is conducted by official designated agencies in expensive monitoring stations. Instrumentation in these monitoring stations has excellent sensitivity for detecting trace gases but is sometimes vulnerable to interferences, particularly ozone. Such fixed location measurements therefore cannot provide the spatial and temporal resolution required to properly assess exposures to NO_2. Typically, air quality instrumentation measure concentrations over a minute or more and often only hourly or daily averages are reported to the public. While this information is valuable to the public and governing bodies, the lack of spatial resolution means that certain sources (such as passing vehicles in the traffic environment) and locations are not captured by the existing monitoring infrastructure. As a result, this infrastructure cannot be used to accurately assess on-road compliance with car emission standards or personal exposure to TRAP and other pollutants, such as NO_2. Many different factors can affect one's exposure to poor air quality, including proximity and mobility around pollution sources (Liu et al., 2023).

Pollutant concentrations vary from region to region which means that localised air quality monitoring is important for citizens to make informed decisions. In Ireland, the Environmental Protection Agency (EPA) has identified particulate matter (PM) and nitrogen dioxide (NO_2) as priority air pollutants. Traffic and transport are a major source of nitrogen oxides (NO_x), comprising nitric oxide (NO) and NO_2, and PM emissions largely come from solid fuel burning (Environmental Protection Agency,

2023). Before these emissions can be reduced to healthy levels, local sources must be identified and the pollutants' chemistry in the atmosphere must be understood. Continued monitoring of airborne pollutants is essential for developing air quality forecasting. Forecasting disseminates information to the public about the local air quality and has potential to reduce personal exposure to pollutants, especially among vulnerable groups such as children, elderly, and those suffering from pre-existing illnesses such as asthma. Services like air quality forecasting also raises public awareness around air pollution and can encourage changes to less polluting behaviours.

There has been much interest in the development of low-cost, portable sensors to fill the gap created by standard monitoring stations. Low-cost sensors can complement expensive regulatory monitoring infrastructure and lead to deeper insight into the spatial and temporal characteristics of ambient air pollution and the sources and transport of urban air pollutants (Byrne et al., 2023; Wei et al., 2024, Manchanda et al., 2024; Okure et al., 2022). Portable low-cost sensors add a further dimension in that they allow mobile measurements on board light vehicles and unmanned aerial vehicles or on bicycles or in backpacks. Low-cost sensors require calibration which can be carried out by colocation with stationary monitoring stations (Spinelle et al., 2015). Low-cost sensors are simple to operate and well-suited to citizen science projects.

Low-cost sensing has been used in multiple citizen science projects in Ireland in recent years, including Clean Air Together (CAT) and the GLOBE programme (Global Learning and Observations for the Benefit of the Environment) in schools. CAT has engaged citizens living in Irish cities (Dublin, Cork, Galway, Limerick) to monitor local NO_2 concentrations over a 4-week period using diffusion tubes. Passive monitoring techniques like diffusion tubes sample air for several weeks at a time, resulting in a long time-averaged measurement. Their time resolution is therefore minimal but large numbers of tubes can give insight into the spatial distribution of pollutants (Rowell et al., 2021). The CAT project created a snapshot map of NO_2 levels across Cork City (Environmental Protection Agency, 2023) (Figure 1.2). The spatial distribution of NO_2 indicated that the sources are strongly linked to traffic. Highest concentrations were recorded in the city centre or on major national roads, with concentrations above 20 $\mu g/m^3$, more than double the 2021 WHO annual mean limit.

This citizen science study indicated that NO_2 pollution in Cork City is largely caused by internal combustion engine vehicles (ICEV).

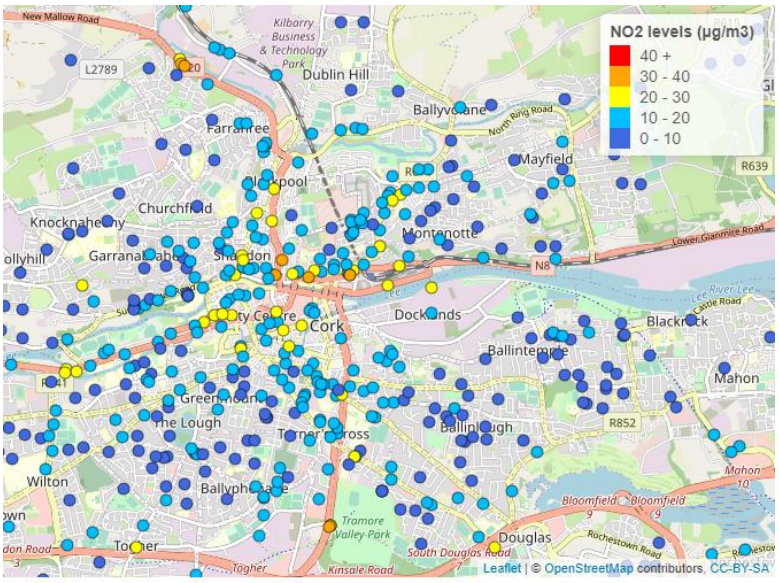


Figure 1.2 . Spatial distribution of NO_2 across Cork city in Oct 2022 as reported by Clean Air Together citizen science project (Environmental Protection Agency, 2023b).

These citizen science projects highlight the growing interest in monitoring TRAPs with high spatial resolution while engaging with the public on questions of local air quality (Diez et al., 2024). Although these low-cost measurements provide high spatial resolution, they only provide a one-month average concentration and do not capture periods where emissions rapidly increase or decrease. The sensitivity, selectivity and time resolution of low-cost sensing must be improved to identify and quantify emission sources and encourage changes in public behaviours.

The remainder of this chapter focuses on NO_2, an urban air pollutant strongly associated with ICEV emissions. The anthropogenic and natural sources of NO_2 and its tropospheric chemistry, as well as the WHO and EU air quality limits and guidelines, will be discussed. Established measurement techniques and their advantages and disadvantages will be reviewed in the context of urban air pollutant monitoring.

1.2 Sources, chemistry, and impacts of nitrogen dioxide

Sources of NO_2

NO_2 is a brown gas emitted during combustion in industry, power and transport sectors. In urban areas, it is primarily produced by petrol and diesel vehicles, with heavy-duty diesel vehicles having the biggest impact. It is produced naturally by lightning strikes, soil emissions and biomass burning (Griffin et al., 2021; L. Huang et al., 2024; Huber et al., 2020). NO_2 is a major product of combustion when nitrogen-containing fuel is burned, but NO_x can also be formed from the nitrogen (N_2) and oxygen (O_2) present in air under high temperature conditions. NO formed under these conditions can be further oxidised to produce NO_2 (Bratrakov, 2016). This is known as the Zel'dovich mechanism and is shown below (Zel'dovich, 1946).

$$N_2 + O \xrightarrow{\Delta\Delta\Delta} NO + N \qquad \text{(R. 1.13)}$$

$$N + O_2 \xrightarrow{\Delta\Delta\Delta} NO + O \qquad \text{(R. 1.14)}$$

$$NO + HO_2 \rightarrow NO_2 + OH \qquad \text{(R. 1.15)}$$

NO_2 produced from lightning (LNO_2) follows the same mechanism where lightning is the heat source. LNO_2 has a longer atmospheric lifetime than NO_2 as it is formed in the upper troposphere where temperatures and thus reaction rates are slower (Zhang et al., 2023). LNO_2 does not generally impact air quality due to its altitude.

The burning of fuel in vehicle engines is a major source of urban NO_2 pollution. Although tailpipe emissions typically have more NO than NO_2 (Bishop et al., 2022), NO is readily oxidised to form secondary NO_2. Selective catalytic reduction (SCR) aftertreatment systems in diesel vehicles have helped to reduce on-road NO_x emissions since their introduction in 2011 (Jung et al., 2019). SCR aftertreatment techniques were introduced when European car standards were tightened to reduce vehicle emissions. SCR systems first inject a urea solution into the exhaust gas which thermally decomposes to NH_3 and adsorbs onto the catalyst-coated SCR substrate.

Gaseous NO_x can then be reduced by the adsorbed NH_3, to nitrogen and water (Yuan et al., 2015). The overall SCR reaction can be expressed as:

$$4NH_{3\,(ads)}^{\downarrow} + 2NO + 2NO_2 \longrightarrow 4N_2 + 6H_2O \qquad \text{(R. 1.16)}$$

Since this conversion relies on thermal decomposition, SCR convertors are less effective at removing NO_x emissions at lower temperatures, such as short or low speed journeys after a cold start (Gao et al., 2021; Fu et al., 2013). A 2021 study reported that heavy-duty diesel vehicles (HDDVs) accounted for 30% of total NO_x emissions from the transport sector in London, where over 96% of the bus fleet comprised diesel and diesel-hybrid buses (Phantawesak et al., 2022). The study found that retrofitting buses to improve SCR systems lowered NO_x emissions by a factor of 1.7, but this figure varied with driving conditions. If SCR converter temperatures were low, NO_x was not converted efficiently to N_2 and H_2O. The time of year was also found to have a large impact on SCR efficiency as lower winter temperatures reduced NO_x conversion efficiency.

Atmospheric chemistry of NO_2

NO_2 is a key part in major chemical processes in the atmosphere. It is reactive and has an atmospheric lifetime of several hours. The reactivity of NO_2 and the distribution of its sources results in high spatial and temporal variability in urban centres. (Pommier, 2022) Concentrations of NO_2 in cities usually peak in the morning and evening with rush-hour traffic (Edwards et al., 2024) and are suppressed in the afternoon largely through photolysis.

NO_2 is photolyzed by sunlight below 400 nm. Photolysis produces NO and a free oxygen radical (O•) which is highly reactive in the atmosphere and a precursor to the formation of ozone (O_3). The NO formed can also be oxidized to regenerate NO_2.

$$NO_2 \xrightarrow{\lambda<400nm} NO + O \qquad \text{(R. 1.17)}$$

$$O\cdot + O_2 \rightarrow O_3 \qquad \text{(R. 1.18)}$$

$$O\cdot + NO \rightarrow NO_2 \qquad \text{(R. 1.19)}$$

NO_2 acts as a precursor to ozone formation, but its photolysis product also acts as an O_3 sink to reform NO_2:

$$NO + O_3 \rightarrow NO_2 + O_2 \quad \text{(R. 1.20)}$$

Tropospheric O_3 concentrations are generally increased by NO_2. Ground-level ozone poses health risks, adds to secondary PM formation and is a major contributor to smog events (Z. Dong et al., 2024; Ryffel et al., 2019). Limiting NO_x can reduce or increase tropospheric ozone concentrations depending on whether the active chemical regime in the area is NO_x- or VOC-limited, as shown during China's Clean Air Strategy 2013 - 2017. A negative correlation between O_3 and NO_2 concentrations in European cities was also reported by Wolf et al. (2022). This anti-correlation is most distinct in VOC-limited regions where high NO_2 concentrations can also lead to the formation of secondary aerosols such as ammonium salts that contribute to haze events in the wintertime (U.S. Environmental Protection Agency, 2008; Wang et al., 2023; Yombo Phaka et al., 2023).

NO_2 and NO_3, the nitrate radical and an important nocturnal oxidant, are in a temperature-dependent equilibrium with N_2O_5. NO_3 can be formed from NO_2 and O_3. N_2O_5 concentrations are driven largely by O_3, relative humidity and NO_2 (Chen et al., 2024).

$$N_2O_5 \leftrightarrow NO_2 + NO_3 \quad \text{(R. 1.21)}$$

$$NO_2 + O_3 \rightarrow NO_3 + O_2 \quad \text{(R. 1.22)}$$

N_2O_5 and NO_3 contribute to O_3 production and removal. N_2O_5 also plays an important role in heterogeneous chemistry, where it reacts with chloride ions to form $ClNO_2$, a photolytic precursor of daytime chlorine radicals (Mielke et al., 2013) which consumes stratospheric ozone.

NO_2 also reacts with the hydroxyl radical, OH•, to form nitric acid, HNO_3, impacting water, soil and plant health (Lobell et al., 2022). This reaction is particularly relevant for LNO_2 where there are usually high water vapour concentrations (Wayne, 2000). HONO is also produced in this reaction, which is an important precursor to the OH radical (Ermel et al., 2018).

$$2NO_2 + H_2O \rightarrow HONO + HNO_3 \quad \text{(R. 1.23)}$$

Monitoring reactive nitrogen chemistry requires high spatial and temporal resolution to account for the short atmospheric lifetime, mobile sources, and geographical distribution of NO_2. NO_x emissions contribute significantly to the chemistry of the atmosphere and accurate measurements can lead to improved chemical transport models (Peng et al., 2021) and pollution forecasting.

Health impacts of NO_2

Exposure to NO_2 is associated with increased cardiovascular and respiratory mortality. A study of the short-term effects of ambient air pollutants on public health in 29 European cities (Katsouyanni et al., 2001) showed that an increase in 10 μg/m^3 of PM with diameter < 10 μm (PM_{10}) was associated with a 0.19% rise in daily mortality in cities with low NO_2 levels, but 0.80% in cities with high NO_2 levels (although the results may have been skewed by the health of the sample and differences in climate). Air quality data was averaged over 24-hours in each city, giving poor time resolution. Meng et al. (2021) investigated the effect of short-term exposure (1-3 days) to NO_2 across 398 cities worldwide. They found a strong linear correlation between NO_2 concentrations and non-accidental deaths; the correlation increased when accounting for other TRAP, such as CO, SO_2 and O_3, but decreased by 19% when accounting for PM, indicating that PM and NO_2 emissions are linked. By increasing the sample size and area of study, Meng et al. (2021) overcame some of the limitations of the earlier European study, finding that a 10 μg/m^3 rise in NO_2 concentration increased cardiovascular and respiratory mortality by 0.37% and 0.47% the following day. An increased risk of cardiovascular and respiratory mortality was also shown to be associated with long-term exposure to low levels of NO_2 (< 53 ppb annual mean) (Shi et al., 2022), highlighting the importance of monitoring even low levels of NO_2 to improve public health. The efficacy of EURO standards in the city of Milan was investigated by Crosignani et al (2021). The measured emissions were compared to a model which assumed the vehicle fleet complied with relevant diesel EURO standards. A breach of 6.6 μg/m^3 in vehicle emission standards led to 547 additional

cardiovascular and respiratory deaths. NO_2 has a clear negative impact on public health and requires robust monitoring to identify areas of concern

Long-term exposure to NO_2 has been found to increase cases of allergic rhinitis, causing eye irritation and sneezing (Luo et al., 2023). NO_2 also causes inflammation of the lungs, and exposure is particularly dangerous for those already suffering from respiratory illnesses such as asthma. Patients are vulnerable to asthma attacks in the presence of allergens or air pollutants (Cheng et al., 2022). NO_2 has a strong correlation with asthma onset and diagnosis. Cheng et al. found that for each incremental increase of 5 $\mu g/m^3$ of NO_2, the risk of asthma onset increased. A similar correlation was found by Liu et al. (2023) who observed an increase in hospitalisations for respiratory illnesses when NO_2 concentrations increased.

Air pollutants, including NO_2 and PM, pose a threat to pregnant women. Goin et al. (2021) found a linear correlation between exposure to NO_2 and risk of preeclampsia and other hypertensive disorders, a result of increased blood pressure resulting from the oxidative stress caused by NO_2. They therefore recommended that pregnant women be included in "at-risk" categories in air quality reporting.

A link has been found between prenatal exposure to NO_2 and anxiety and depression in male offspring (Li et al., 2022). Increased exposures can disturb the natural metabolism of placental neurotransmitters and lead to neurodevelopmental disorders and high-risk diseases. Air pollutants have been shown to increase the risk of anxiety and depression and impair cognition in adults (Li et al., 2021). Crooijmans et al. (2024) suggested that exposure to NO_2 under the age of 2 can affect attention span and working memory since the prefrontal cortex develops slowly throughout pregnancy and childhood. For males, the negative cognitive effects of NO_2 may last longer because their brains take longer to mature than females'. Improvements in air quality and reduced exposure to NO_2 were associated with a lower risk of dementia in older women (Wang et al., 2021). The correlation held after accounting for sociodemographic, lifestyle and clinical factors, establishing that exposure to NO_2 in later years contributes to pathological brain aging and risk of dementia.

NO_2 emissions clearly have a large impact on public health, leading to increased deaths as well as medical costs borne by society. Changes in air quality guidelines and

policies must be informed by relevant local measurements and monitored to ensure compliance with updated standards.

Air Quality Guidelines for NO_2

The World Health Organization (WHO) has laid out air quality guidelines and limits to aid authorities in reducing the negative health impact of air pollutants such as NO_2. A review of current NO_2 concentrations and their correlation to health effects was carried out to choose a guideline limit value. Huangfu & Atkinson (2020) found a positive linear relationship between NO_2 exposure levels per 10 $\mu g/m^3$ and COPD and acute respiratory mortality. The lowest 5^{th} percentile concentrations were considered and the average lowest reported NO_2 concentration was 8.8 $\mu g/m^3$ (Carey et al., 2013; Tonne & Wilkinson, 2013; Turner et al., 2016), which still saw significant health effects. This was used as a starting point and a long-term NO_2 limit of 10 $\mu g/m^3$ was recommended. Interim guidelines of 30 and 20 $\mu g/m^3$ were also released to help authorities reduce NO_2 levels incrementally from the previous limit of 40 $\mu g/m^3$. Short-term limits were also assigned to NO_2, given the health effects discussed Section 1.2. It was found that daily concentrations are approximately a factor of 2.5 higher than annual mean concentrations (Liu et al., 2019). This led to the introduction of a 24-hour mean limit of 25 $\mu g/m^3$ in 2021.

The legal EU limit is currently based on the 2005 WHO limit of 40 $\mu g/m^3$ and is expected to be reduced in line with the interim targets laid out by WHO. The EU is currently working towards lowering NO_2 limits in all member states by 2030 (The European Parliament, 2024). To quantify the efficacy of the new lower limits, NO_2 monitoring must be sensitive to concentrations below 10 $\mu g/m^3$, selective to NO_2 and give fast, real-time measurements. Many European cities have breached the previous limits of 40 $\mu g/m^3$ (European Commission, 2017) so infractions of the new, lower limits are expected, emphasising the need for improved monitoring frameworks and the ability to identify the greatest sources of pollution.

Transport of NO_2

NO_2 has spatially heterogeneous sources and is chemically active in the atmosphere (Section 1.2 Sources, chemistry, and impacts of nitrogen dioxide) which leads to large variations in NO_2 concentrations across space and time. Emissions follow a diurnal trend with a morning and evening peak that align with peak traffic times (Voiculescu et al., 2020). Concentrations are high in the morning due to surface emissions with a low mixing height and therefore less dilution. In the afternoon, NO_2 concentrations reduce due to photolysis. NO_2 emissions are also lower over the weekend compared to weekdays, and during the summer compared to the winter (Anderson et al., 2021). The lifetime of NO_x emissions has been shown to be non-linearly dependent on concentration and is controlled by the active chemistry in a given air mass. In a VOC-limited regime, the lifetime increases with increasing NO_x concentrations. The inverse is true for NO_x-limited regimes (Laughner & Cohen, 2019).

Surface winds also affect the mixing rate of NO_2 and other transport emissions away from the source site. Lower wind speeds result in increased NO_2 concentrations close to sources, giving characteristic NO_2 decay gradients that depend on the region's active ambient chemistry and physical parameters such as wind speed and direction (Ahmad et al., 2024). Dressel et al. (2022) reported that inhabitants of residential properties near busy roads had a high attendance at doctor visits for asthma and respiratory issues as well as hypertensive disorders during pregnancy, showing that residents near NO_2 sources are exposed to higher concentrations and related health risks.

NO_2 emissions can be transported over state boundaries and can lead to an imbalance between emission contribution and exposure. Trans-boundary emissions must therefore be considered in air quality guidelines. Remote sensing techniques are typically used to measure NO_2 vertical column densities to analyse the large-scale spatial distribution of the gas.

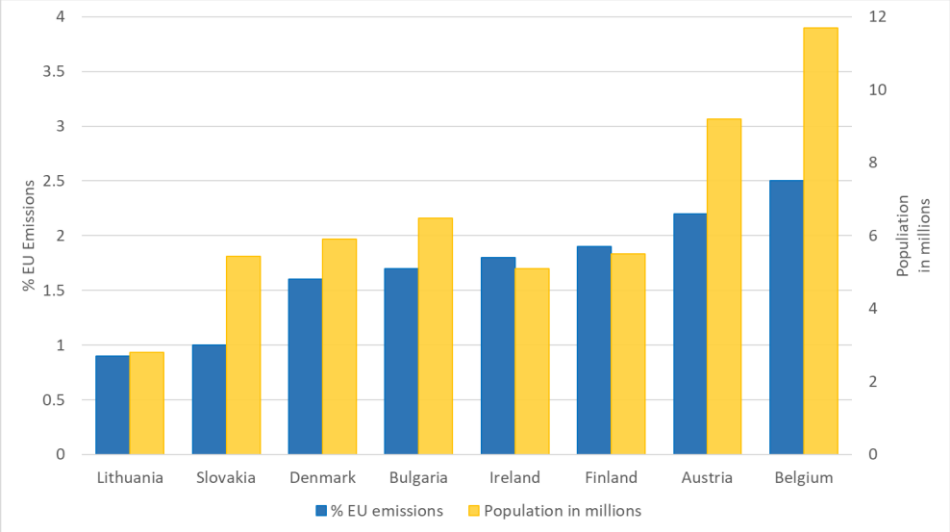


Figure 1.3. Country fractional contributions to total EU NO_x emissions in 2021 for countries with populations between 3 and 12 million. Data based on European Union Emission Inventory Report 1990-2021 (European Environment Agency, 2023).

The EU has laid out restrictions and limits for ambient pollutant concentrations which all member states must meet. Figure 1.3 shows the contributions of smaller EU countries to the total EU NO_2 emissions in 2021 (European Environment Agency, 2023). Emission contributions increase with population as expected. In Ireland, emissions are predominantly caused by urban sprawl and dependence on car travel. Emissions vary from country to country and can be transported across borders, skewing emission source data. Region-specific monitoring is required to attribute emissions to the correct state and measure the efficacy of air quality policies.

Disparities in NO_2 exposure have been linked to socio-demographics such as race, ethnicity and income. In New York City, increased NO_2 concentrations were observed in non-white areas (28-30%) and areas that fell under the poverty line (25%) (Dressel et al., 2022). The COVID-19 pandemic and resulting lockdown measures also revealed significant inequalities in NO_2 distribution. Before 2020, predominantly white areas had 3 times less NO_2 than non-white areas. During the pandemic, the greatest reductions in emissions were seen in non-white and Hispanic areas, probably driven by reduced vehicle numbers on major roads and highways near these areas (Hunter Kerr et al., 2021). The same holds when accounting for income and educational background. Proximity to sources is the major cause of these inequalities, as poorer,

non-white areas are usually built up around busy roads and industrial activity. Localised monitoring is needed to ensure legislations to improve air pollution inequalities are being enforced and new NO_2 sources are not introduced to over-burdened areas.

In many areas, school children are exposed to increased NO_2 concentrations at drop-off and pick-up times due to high levels of localised traffic. Children are especially vulnerable to negative health effects from pollution because their bodies are still developing. Because they have a higher breathing rate, they inhale high levels of emissions compared to their body size. Social and economic demographics also influence school children's exposures. Children who are part of minority groups are less likely than white children to live and attend school in an area below the WHO air quality guidelines (Bechle et al., 2023).

1.3. Measurement of nitrogen dioxide

Modelling the chemical transport of pollutants shows that traffic is a major source of emissions, but NO_2 monitoring frameworks lack the spatial and temporal resolution to confirm that these exposures are from the transport sector. Hyper-localised data was obtained using a Google streetcar with mobile monitoring equipment to assess subjects' personal exposures in the US (Qi et al., 2022). Pollution levels in the area of study were below the required guidelines at that time (World Health Organization Regional Office for Europe, 2006), underlining the need for more stringent air quality regulations and monitoring systems that can accurately measure the impact of updated regulations.

The development of novel NO_2 monitoring techniques that overcome the limitations of existing approaches is a topic of continuing research. Many research groups are aiming to create NO_2 sensors that are more compact, lower cost and sensitive to ambient NO_2 mixing ratios (Bailey et al., 2024; Kuhn et al., 2022; Womack et al., 2022; Yang et al., 2023; Zheng et al., 2024a; Zhou et al., 2022). This section reviews commercial monitoring systems and the limitations of these approaches.

Chemiluminescence

The standard approach to monitoring NOx for regulatory purposes is based on the chemiluminescence produced when NO in the sample reacts with excess O_3 to form NO_2. The newly formed NO_2 product has excess energy which is released as infrared radiation and detected by photomultiplier tubes. This measurement is therefore fundamentally a measurement of NO. To measure NO_x (NO + NO_2), the analyser draws sample air over heated molybdenum to reduce NO_2 to NO. By successively switching between measurements of NO and NO_x, an inferred NO_2 concentration is obtained (Teledyne, 2010). Chemiluminescence measurements are sensitive but are susceptible to interferences from ambient ozone, humidity (which enhances chemiluminescent quenching), alkyl and peroxy nitrates (Alam et al., 2020; Kebabian et al., 2008; Suzuki et al., 2011) and may be better suited to measuring total nitrogen oxides. These monitors are not readily portable and take single point measurements, typically averaged over 1 – 15 minutes.

Low-cost sensors

Conventional air quality monitoring requires a big financial investment, special expertise for running and maintaining equipment and is therefore limited in terms of spatial coverage. Low-cost sensors based on metal oxides, electrochemical reactions, gas diffusion or particle scattering have been used to create large sensor networks that can capture the spatial distribution of air pollutants (Byrne et al., 2024; Dallo et al., 2021; Giordano et al., 2021; Okure et al., 2022). Low-cost sensors require careful calibration (for example, through co-location with regulatory air quality monitoring stations) and can complement regulatory monitoring stations by providing greater information on the spatial distribution of pollutants (Manchanda et al., 2024).

Most commercially-available NO_2 sensors (e.g., AlphaSense, Cairclip, Urban AirQ) are based on electrochemical reactions where NO_2 diffuses through a membrane and is chemically reduced at a working electrode to generate a current. A counter electrode produces an opposing current to balance the working electrode (Mijling et al., 2018). These sensors are normally equipped with temperature and relative humidity monitors because the response to NO_2 is highly dependent on these parameters. Extracting

useful data from low-cost sensor networks requires complex modelling such as multilinear regression, machine learning and deep learning to increase sensor accuracy (Jain et al., 2021; Kim et al., 2024).

Electrochemical NO_2 sensors are also vulnerable to interference from O_3 which causes an underestimation of NO_2 concentrations, an effect that is amplified in rural measurements where NO_2 concentrations are low and O_3 concentrations are high (Spinelle et al., 2015). Spinelle and coworkers tested the accuracy of O_3 and NO_2 low-cost sensors in a semi-rural environment and found that the hourly Data Quality Objectives were not met for electrochemical NO_2 sensors, likely due to low concentrations, making these sensors unsuitable for official pollutant monitoring.

Electrochemical sensors cannot function correctly above 30 °C and can be irreversibly damaged by hot summer conditions, making them unsuitable for applications in hot climates or near combustion sources (Papaconstantinou et al., 2023). Chemiresistive sensors are thermally stable and withstand high temperatures. They can be used in exhaust or smokestack emission monitoring at mixing ratios in the range from 0.25 to 2 ppm (Yang et al., 2023). Chemiresistive sensors work by attracting NO_2 to a polymer where it can easily abduct electrons, thus creating more mobile holes and decreasing resistivity.

Diffusion tubes are small, capped plastic tubes with a mesh under the cap that is coated in triethanolamine (TEA), a chemical that absorbs NO_2 (Kirby et al., 2000). Analysing the changes to the TEA gives an indicative average for NO_2 concentrations over several weeks. Diffusion tubes are inexpensive and widely used in citizen monitoring campaigns and can provide information on the spatial distribution of NO_2 (Department for Environment Food & Rural Affairs, 2022; Environmental Protection Agency, 2023; Okure et al., 2022). However, they are not suited for monitoring temporal variability of pollutants.

Citizen science projects benefit from low-cost sensing as large spatial distributions of pollutants can be measured. Low-cost sensor networks are ideal for use in urban regions where there are areas and times with high exposure risks that may not be captured by regulatory instruments. Wearable sensors have even been developed that can give information on personal exposures to pollutants (Tryner et al., 2023).Low-to-middle income countries with minimal monitoring may benefit the most from low-

cost sensing networks, making air quality information available where previously none existed.

While there have been many advancements in low-cost sensing, NO_2 sensors are still not accurate enough to impact change in policy or behaviour. In Europe, NO_2 is the most popular gas-phase pollutant to be measured in low-cost monitoring campaigns, highlighting the need for novel low-cost methods for detecting this toxic pollutant (Okorn & Iraci, 2024). Low-cost, light-based detection of NO_2 may bridge the gap in selectivity, reliability and accuracy of regulatory and low-cost monitoring (Giordano et al., 2021).

Spectroscopic Measurement of NO_2

Spectroscopic techniques based on the absorption or fluorescence of the target species can be used to measure atmospheric trace gases. NO_2 has a highly structured and unique absorption spectrum. Spectral methods with good sensitivity to NO_2 include cavity-enhanced absorption spectroscopy, cavity-attenuated phase-shift spectroscopy, cavity ringdown spectroscopy, differential absorption LIDAR (light detection and ranging), differential optical absorption spectroscopy, gas correlation spectroscopy, photometry, interferometry, photoacoustic spectroscopy and laser-induced fluorescence. These techniques will be discussed in this section.

Optical Cavity Techniques

Cavity ring-down spectroscopy (CRDS)

Cavity ring-down spectroscopy, first reported by O'Keefe & Deacon (1988) uses high finesse optical cavities which reflect light pulses many times through the sample, transmitting a small fraction of light after each round trip. The intensity of light decreases exponentially over time (Wheeler et al., 1998). Light decays within the cavity due to mirror losses, Mie and Rayleigh scattering, and absorption and scattering in the sample. The decay rate, or 'ring-down time', of the light pulse is determined by the cavity mirror reflectivity, spacing between the mirrors and the concentration of an absorbing gas in the cavity (Zalicki & Zare, 1995). When there is no absorbing gas in

the cavity, the ring-down time, τ_0, only depends on the mirror reflectivities, R, and mirror separation, l:

$$\tau_0 = \frac{l}{c(1-R)} \quad 1.1$$

where c is the speed of light in m/s. The sensitivity of the absorption measurement improves with increasing cavity mirror reflectivity, which increases the light pathlength through the sample. The ring-down time decreases with sample absorption. Wada & Orr-Ewing (2005) detected between 0.2 – 80 ppb of NO_2 with a limit of detection of 0.1 ppb in 50 seconds using a continuous wave laser and a photomultiplier tube (PMT) and Mazurenka et al. (2005) found an upper limit of 150 ppt also using a laser and PMT. CRDS has been used for exhaust NO_2 and NO measurements with an upper limit of 29 ppm by increasing the integration time to 7 minutes (Evertsen et al., 2002). CRDS systems typically have a good temporal resolution on the order of minutes (Evertsen et al., 2002; Fuchs et al., 2008; Wada & Orr-Ewing, 2005). Fast-Fourier Transforms (FFT) can be applied to the CRDS fitting algorithm to give real-time ring-down decay fitting (Mazurenka et al., 2005), improving the temporal resolution but reducing the upper concentration limit.

CRDS typically uses lasers rather than broadband sources, such as LEDs, because the decay becomes multiexponential if the spectral width of the light source is wider than the molecular absorption feature. Quantitative measurements of gas absorption can be made when the spectral distribution of the broadband light source is known. DOAS analysis can also be performed on broadband sources to analyse interfering species that absorb in the same spectral region (Ball & Jones, 2003).

CRDS is suitable for field measurements of NO_2, provided that a particle filter is used to reduce scattering from particles and that other absorbers such as ozone in the spectral region are corrected for. Osthoff et al. (2006) constructed an instrument consisting of three optical cavities that used CRDS to measure NO_2, NO_3 and N_2O_5 simultaneously for airborne measurements. NO_2 was measured up to 200 ppb with a detection limit of 40 ppt in 1 second, giving an attractive measurement range and time resolution for ambient air quality monitoring. Taking regular zero-air measurements in which NO_2 was scrubbed from the inlet line also improved sensitivity and system stability (Castellanos et al., 2009).

Monochromatic CRDS measurements are vulnerable to interferences from gases that absorb in the same wavelength region as NO_2. Information on concentrations of other gases is therefore required to correct NO_2 concentrations (Osthoff et al., 2006). CRDS instrument sensitivity may also degrade with field use since it depends on the high reflectivity of the cavity mirrors, which can become dirty over time and so require regular cleaning and maintenance (Wheeler et al., 1998).

Cavity-enhanced absorption spectroscopy (CEAS)

Cavity enhanced absorption spectroscopy (CEAS) has been widely used for trace gas detection in the atmosphere (Liu et al., 2016; Wang et al., 2017). The Beer-Lambert relation (Equation 1.2.) implies that increasing the pathlength through the sample results in a larger decrease in intensity for a given sample.

$$\log\left[\frac{I_0}{I}\right] = N\sigma L \qquad 1.2$$

Like CRDS, CEAS systems use optical cavities comprising two planar-curved mirrors with a high reflectivity coating (R > 99%) causing light to be reflected back and forth between the mirrors many times, thereby creating a long effective path length through the sample. Optical cavities increase the absorption sensitivity by a factor of $\frac{1}{1-R}$. The minimum detectable concentration of the system decreases as the reflectivity increases and thereby lengthens the effective path length. The characteristics of optical cavities will be discussed further in Section 1.4.

While initial CEAS systems used lasers as light sources, Fiedler et al. reported the first use of incoherent broadband light sources in 2003 (Fiedler et al., 2003). Their initial demonstration of incoherent broadband cavity-enhanced absorption spectroscopy (IBBCEAS) used a xenon arc lamp, grating monochromator and photodiode array to determine the light absorbed within an optical cavity to measure the absorption of molecular oxygen and gaseous azulene. IBBCEAS instruments do not require sophisticated electronics such as feedback loops and have a relatively simple optical set-up. However, they require substantial post-processing algorithms to analyse the absorption spectra. Broadband light sources do not require mode matching when coupling light into the optical cavity, as is the case with lasers. The relatively wide spectral coverage of broadband light sources allows multiple absorbing gases to be

measured simultaneously (Nam et al., 2022; Wang et al., 2023; Washenfelder et al., 2008; Yi et al., 2021). Aerosols scatter light and may interfere with absorption measurements, so a PTFE filter is often used to remove particulates from the sample (Zheng et al., 2018; Zheng et al., 2024).

The reflectivity of the cavity mirrors must be calibrated in CEAS and IBBCEAS for quantitative absorption measurements. Several calibrations methods have been used. The difference in Rayleigh scattering between two gases (often He and N_2) is commonly used but requires external gas supplies. The response to a known gas concentration may also be used to calibrate the mirror reflectivity, or the relationship between the phase shift in the cavity and the modulated signal frequency, as in CAPS measurements. Purging cavity mirrors with an external air supply protects the mirrors and maintains their high reflectivity.

Light emitting diodes (LEDs) are appealing light sources for IBBCEAS systems because they have a broad spectral output, low power consumption and a long lifetime (Zheng et al., 2018). They typically have a lower optical power output than lasers or arc lamps, are safer to use, and much less expensive. IBBCEAS systems with LEDs have been used to quantify NO_2 concentrations with sub-ppb limits of detection in a compact instrument (Langridge et al., 2008; Wang et al., 2017; Wu et al., 2014; Zheng et al., 2024). Typically, high power LEDs that require active temperature control are used with collimating optics to increase light throughput in the system (Womack et al., 2022). LED emitters are vulnerable to spectral shifts from fluctuations in supply current or voltage and ambient temperature. Therefore, it is important to consider active temperature control and voltage regulation for LED light sources.

Sensitive photodetectors are required to monitor the LED cavity output, such as grating spectrometers equipped with charge-coupled device (CCD) detectors, or non-dispersive detectors like photomultiplier tubes or silicon photomultipliers (Bailey et al., 2024). Zheng et al. (2024) reported a mini-IBBCEAS system that could be mounted on an unmanned aerial vehicle (UAV) for measuring vertical column densities of NO_2. This system used a short optical cavity (<11cm) with a grating spectrometer and charge-coupled device (CCD) to measure <0.1 ppb of NO_2 with a time resolution of 2 seconds. Precise wavelength calibration and absorption cross-sections are required to analyse the spectral data. UAVs are attractive for low altitude

airborne monitoring as they are cheap compared to manned aircraft. However, UAVs have low payloads and require that devices are small, light and run automatically, making IBBCEAS a desirable option.

The sensitivity of CEAS systems can be improved by modulating the light source and using phase-sensitive detectors (PSD). Phase-sensitive detection mixes a signal and reference waveform that are modulated at the same frequency. The output signal is then low pass filtered to observe the selected frequency. PSD and lock-in amplification will be discussed further in Section 1.4.3. Zhou et al. (2022) used amplitude-modulated CEAS (AM-CEAS) to measure ambient NO_2 with a detection limit of 8 ppt in 30 seconds. It is important to note that AM-CEAS does not require the modulation frequency to be matched to the induced phase shift in the optical cavity, as is the case in cavity-attenuated phase-shift spectroscopy (CAPS). The optical cavity produced an effective path length of 3.26 km. The reflectivity was preserved by employing a PM filter, rather than using an external purge gas supply. This instrument used a multimode diode laser with an emission at 405 nm and output power of ~150 mW and photomultiplier tube (PMT) detector. The laser required active temperature and current control, an optical isolator to reduce laser feedback, and a bandpass filter to reduce stray light. Although the Zhou AM-CEAS achieved excellent sensitivity to ambient NO_2, the system has drawbacks of high-cost and complex control electronics. Laser-driven systems also require precise optical alignment and high mechanical stability. These requirements are relaxed for LED systems as the broadband emission diverges, creating a larger spot size that is less sensitive to small misalignments.

IBBCEAS systems can be improved further by increasing the light throughput using high-power, directional light sources such as superluminescent LEDs (SLEDs) (Denzer et al., 2009). SLEDs combine the broad spectral characteristics of LEDs with the narrow dispersion angle characteristic of a laser and are well-suited for quantifying

gas species with broad spectral features. SLEDs are not yet widely used in trace gas sensing but are a promising emerging light source.

Cavity-attenuated phase-shift spectroscopy (CAPS)

When a modulated light signal is passed through an optical cavity, a characteristic phase-shift is seen as a distortion in the transmitted waveform. The phase-shift is determined by device properties (absorption cell length, cavity mirror separation and reflectivity and light modulation frequency) and the absorption coefficient of the sample. The relationship between these variables is (Kebabian et al., 2008):

$$cot\vartheta = cot\vartheta_0 + \frac{c}{2\pi f}\alpha_{NO_2}(T,P)\chi \qquad 1.3$$

where ϑ_0 and ϑ are the phase-shift in NO_2-free air and the sample air, respectively. α represents the absorption coefficient of NO_2 at a fixed temperature (T) and pressure (P), c is the speed of light, f is the modulation frequency and χ is the mixing ratio of the target gas.

Kebabian et al. (2008) reported a CAPS instrument that used a blue LED centred at 440 nm with a 20 nm bandpass. The LED was modulated at 16 kHz. This instrument achieved a limit of detection of < 0.06 ppb with a 10 s response time using a vacuum photodiode. A Nafion dryer was also used to reduce humidity, but it had a negligible effect on NO_2 measurements because water vapour absorbs weakly at 440 ± 20 nm. The instrument was susceptible to other spectral interferences, such as glyoxal (CHOCHO) and methylglyoxal (CH_3COCHO) which absorb in this region. However, NO_2 absorbs more strongly here by a factor of approximately 5 and urban concentrations of glyoxal and methylglyoxal are typically an order of magnitude lower than NO_2 (Thalman & Volkamer, 2010). The CAPS method therefore offers attractive sensitivity for NO_2 detection; however, it is vulnerable to spectral interferences and requires active temperature control to reduce drifts in the signal baseline.

Other long-path measurements

Photometry

Photometry measures the absorption of a species based on the wavelength-dependent absorption cross-section. A compact folded tubular photometer was developed by Birks et al. that made direct measurements of gas phase NO_2 absorption using a blue LED centred at 405 nm and a photodiode (Birks et al., 2018). The compact system consisted of a 2.1 m folded tube with mirror modules to fold the light path several times across a moderate spatial footprint. Although laser light sources provide more output power and directionality, the system used LED as the more stable light source. An LED with a low output power was used to reduce photodissociation of NO_2 (< 420 nm) during the measurement (Burkholder et al., 2015; Wilkinson et al., 2010). These practical limits will be considered for the systems discussed in Chapter 2 onwards.

Long path absorption photometry (LOPAP) is used to detect trace gases including NO_2, HONO and NO after reaction in a solution. LOPAP NO_2 measurements can be vulnerable to interferences. Villena et al. removed O_3 and HONO from the sample flow and reacted NO_2 with a Griess-Saltzman reagent to produce a brightly coloured dye solution whose absorbance was measured using a tunable white light diode and a spectrometer (Saltzman, 1954; Villena et al., 2011). The effect of system fluctuations such as temperature, pressure and relative humidity was reduced by taking regular zero-air measurements where NO_2 was scrubbed from the sample. In addition, the log ratio of the light intensity at two distinct wavelengths was measured to suppress variations in the light source intensity. High sensitivity was achieved by using a long Teflon tube, resulting in a limit of detection of 2 ppt in 3 minutes. The time resolution and light throughput of the system degrade as the light path increases so path lengths of a few metres are used in LOPAP systems (Kleffmann et al., 2006; Kleffmann & Wiesen, 2008). These path lengths set upper concentration limits (e.g., > 300 ppb (Villena et al., 2011)) which might be unsuited for monitoring environments that have periods of high pollution levels. Choosing wavelengths with lower absorption cross-sections causes the absorption to saturate at a higher concentration, increasing the upper bound. While LOPAP systems offer exceptional sensitivity to gases like HONO and NO_2, their time resolution is only moderate, interferences can be a major problem,

and the handling and changing of liquid solutions makes them unsuited to many applications.

Differential absorption LIDAR (DIAL)

Light detection and ranging (LIDAR) is a common remote sensing technique. In atmospheric applications, LIDAR uses pulsed lasers to measure the range-resolved composition of the atmosphere based on the inverse relationship between the transmitted light and the light path length. Differential absorption LIDAR (DIAL) uses the LIDAR principle at two or more closely separated wavelengths, λ_{on} and λ_{off}, at which the target species has a large difference in absorption cross section (Volten et al., 2009). The resulting difference in backscattered light at each wavelength can be used to calculate the number density of the target. Choosing nearby wavelengths minimises broadband interference from aerosol backscattering and other spectral interferences as the Rayleigh and Mie scattering effects are approximately constant over small differences in wavelength. Monitoring $\log\left(\frac{I(\lambda_{on})}{I(\lambda_{off})}\right)$ reduces the effect of system drift on measured NO_2 concentrations (Su et al., 2021). The selection of these wavelengths can be achieved using tunable lasers or LEDs with narrow bandpass filters. Su et al. (2021) found that high concentrations of ambient aerosols were problematic in DIAL measurements using two wavelengths. They used a modified 3-wavelength approach, where wavelengths with low, medium, and high absorption cross-sections ($\sigma_1(\lambda_1) < \sigma_2(\lambda_2) > \sigma_3(\lambda_3)$) across an absorption peak were used.

LEDs can replace lasers as light sources in DIAL measurements, reducing power demand and vulnerability to electrical fluctuations. Shiina et al. (2019), developed a mini-LIDAR instrument for atmospheric detection. LEDs with sufficient output power were found to be an effective light source for LIDAR measurements. LEDs were found to have a relatively stable output over long periods so active temperature control was not required. Since LED beams diverge far more than laser beams, collimating optics must be used to efficiently transmit light through the atmosphere. A photomultiplier tube was also used as a detector in this instrument as DIAL measurements require high amplification for weak signals and a fast time response.

DIAL measurements can be applied to gases other than NO_2 that have structured absorption features. SO_2 vertical profiles were measured by Fujii et al. (2001) using a 3-wavelegnth DIAL approach with a measurement error < 1.1 ppb. Liu et al. have developed a compact CO_2 LIDAR system that could be applied in the space industry for Mars missions (Liu et al., 2024), measuring CO_2 column densities and surface pressures and temperatures to deduce atmospheric pressure profiles. DIAL is a robust and powerful method for measuring gas absorptions in the atmosphere using long path lengths, provided suitable operating wavelengths, light sources and detectors are chosen.

Differential optical absorption spectroscopy (DOAS)

Differential optical absorption spectroscopy (DOAS) techniques analyse atmospheric absorption spectra that are typically recorded using grating spectrometers and charge-coupled devices (CCD) by comparing with known absorption cross-sections of the target species. Overlying spectral structures can be removed through separating the narrow and broadband absorption features to resolve changes in the signal of interest. Long path measurements can have high variability in light sources and light path due to fluctuations in the atmosphere, so absolute intensity measurements are not viable for this type of measurement. A differential approach effectively eliminates these variations. Interferences such as aerosol scattering are usually present as broadband structures in absorption spectra (Platt & Stutz, 2008). Overlying structures are removed based on reference absorption cross-sections convolved with the instrument resolution, and filtering should be applied to all reference and measured spectra equally. Optical detection systems can observe reductions in the optical density of Fraunhofer emission lines, known as the Ring effect (Grainger & Ring, 1962). Some trace gas absorptions can be an order of magnitude smaller than the apparent Ring effect which led Solomon et al. (1987) to propose a ‘Ring spectrum’ in 1987 so that this spectrum could be removed from measured spectra. This correction was applied to simultaneous NO_2 and O_3 measurements at McMurdo station in Antarctica, 1987, which supported evidence of the ‘ozone hole’, where reactive chlorine radicals consumed O_3 products, leading to reduced formation rates and a ‘hole’ in stratospheric ozone coverage (Mount et al., 1987).

The detection limit, D_{limit}, of a DOAS instrument can be expressed in terms of the noise level, σ, and a given number of pixels, *n*.

$$D_{limit} \approx \sigma \times \frac{6}{\sqrt{n-1}} \quad 1.4$$

Stutz and Platt validated this expression using DOAS with least squares fitting. Sub-ppb detection limits were reported for O_3, NO_2, SO_2 and HCHO when overlapping spectra were separated by fitting to literature cross-sections (Stutz & Platt, 1996). Residual spectral structures of random noise or stray ambient light interfered with these measurements, particularly in passive DOAS systems which use scattered sunlight as a light source.

Active DOAS systems use artificial broadband light sources such as Xe arc lamps or LEDs. Arc lamps offer a spectrally wide (~1000 nm) and high-power emission profile which allows simultaneous monitoring of many different absorbing species. Xe arc lamps have been used with DOAS systems to measure over long path lengths (<1 km) with good sensitivity. Telescopes are used to collimate and project light across large distances, as well as to collect and focus light into fibres connected to spectrometers (Lee et al., 2008). However, arc lamps require large power supplies and high voltage sources to ignite. Other disadvantages include the risk of explosion of the high pressure lamps, relatively short lamp lifetimes (< 2000 hours), and formation of O_3 in the vicinity of the lamp (Kern et al., 2006). These disadvantages have contributed to a decline in arc lamp use as light sources.

LEDs are an attractive alternative to arc lamps because they are low cost, safer to operate, have long lifetimes, and have comparable spectral power density to arc lamps at their peak emission wavelength. LED emission spectra can also be approximated to a Gaussian curve, simplifying fitting regimes (Ab-Rahman et al., 2012; Bauer, 2021; Jin et al., 2013). However, Fabry-Pérot étalon-induced structures in the LED emission spectrum can interfere with DOAS measurements when LEDs are not kept at a stable temperature (Kern et al., 2006). This effect was investigated by Sihler et al. (2009) who found that tilting the LED emitter removed étalon effects and increased the radiant flux transmitted through the system. If the active emission area is sufficiently large, then the light intensity is independent of the tilt angle of the emitter.

Implementing these techniques improved the limit of detection over a long (~ 6 km) path length by a factor of 2.

A low-cost compact DOAS system was demonstrated by Bacaoco et al. (2020) that used an LED emitting 430-450 nm, fibre optics, CCD spectrometer and emitter and receiver telescopes. NO_2 and aerosols were simultaneously measured across a 547 m path length in the Philippines. NO_2 concentrations ranged between 100 and 600 ppb. The aerosol optical thickness was derived from measured spectra by subtracting the NO_2 absorption contribution. Capturing the full spectral response makes DOAS a powerful tool for simultaneous trace gas and aerosol measurements.

Laser driven light sources (LDLS) have more recently been used with DOAS systems. They have a wide spectral output like an arc lamp but have superior stability, spectral radiance, and lamp life. They produce high-power emission and improve the signal-to-noise ratio (SNR) (Li et al., 2017). LDLS used with fibre optics to collect transmitted light give higher light throughput, better optical coupling and reduced stray light within the system. Nasse et al. (2019) used a LDLS DOAS system to measure trace gas concentrations in Antarctica, including NO_2, ClO and BrO. Measurements were averaged over 2-40 minutes with an NO_2 detection limit of 180 ppt in 2 minutes and 138 ppt in 40 minutes. Their system used a simplified optical design with a single telescope to send and receive light. LDLS systems require precise optical alignment and are vulnerable to misalignment and atmospheric variability.

Optimisation of spectrographs in DOAS systems has been discussed by (Platt et al., 2021). Most spectrograph resolutions are limited by the product of the free entrance area and the solid angle of acceptance of the optics, known as the étendue. To increase the spectral resolution, the entrance area is increased together with the acceptance angle (F number). Parallel identical instruments can also be used to increase the spatial averaging and thereby the instrument resolution without affecting the physical dimensions.

DOAS techniques are widely used to validate satellite measurements from instruments such as the Geostationary Environmental Monitoring Spectrometer (GEMS), and TROPOspheric Monitoring Instrument (TROPOMI). PANDONIA Global Network comprises a network of ground-based DOAS instruments (PANDORA) measuring UV-vis absorption (Edwards et al., 2024; Rawat et al., 2024). GEMS measures

scattered sunlight to record NO_2 column densities with a spatial resolution up to 7×7.7 km^2 every hour (< 10 readings a day depending on season). These measurements often overestimate ground-level NO_2 because the tropospheric and stratospheric contributions cannot be clearly separated (Lange et al., 2024) and higher surface level NO_2 concentrations in urban areas cannot be resolved (Ha et al., 2024).

Gas correlation Spectroscopy (GCS)

While spectroscopic methods can be highly selective to trace gases in the atmosphere, they are less suited to real-time imaging measurements of NO_2 as they have poor spatiotemporal resolution and require longer acquisition times to improve spatial and spectral resolution. Kuhn et al. demonstrated a novel NO_2 imaging sensor based on gas correlation spectroscopy (GCS) (Kuhn et al., 2022). This system used a reference "absorbing" gas cell with a high concentration of the target gas and an "empty" cell containing air to be sampled. Light transmitted through each cell is recorded by a camera. The absorbing cell acts as a spectral filter across the full absorption of NO_2. GCS measures the logarithmic ratio of channel 1 and channel 2, minimising the effect of other spectral interferences and instrument drift.

This method requires active temperature control, especially within the absorbing cell where fluctuations in temperature may affect the stability of the gas concentration due to the temperature-dependent equilibrium of NO_2 with N_2O_4 (Platt & Stutz, 2008). Employing two cameras for detection means that the detector signals are vulnerable to variations in the optical path induced by differences in path length or NO_2 concentrations in the path.

Interferometry

Fabry-Pérot interferometers (FPI) have been widely used for atmospheric measurements (Bonilla-Manrique et al., 2019a; Kuhn et al., 2021; F. Liu et al., 2021; Wang et al., 2011a). FPI have also been applied in real-time space monitoring for capturing events such as fast radio bursts, pulsars and rotating radio transients (Murphy et al., 2021) and have high time and spectral resolution.

FPIs consists of two parallel planar mirrors with reflective coatings which allow incident light to be reflected between these surfaces a number of times depending on the mirror separation, d, and the refractive index of the medium between the parallel mirrors, n. Interference between the reflected and transmitted beams leads to transmission of high order interference patterns (Jacquinot, 1960). A detector array captures the intensity of different spectral channels. The spectrum shifts due to small changes in the incidence angle, α. This angle dependence is used to separate the spectrum into different channels for spectral analysis.

FPI allow greater light throughput than commercial grating spectrometers and can increase the spectral resolution of spectroscopic systems while maintaining portability and fast response times (Jacquinot, 1954; Zhong et al., 2024). Different interferometry methods, such as Sagnac interferometry and Mach-Zehnder interferometry are common techniques for sensing and communications and have been used for trace gas and VOC detection (Khan et al., 2020). These methods use optical fibres to split and recombine light beams and monitor the induced interference between beams. FPI have been integrated into photoacoustic spectroscopy systems to replace traditional piezoelectric detectors (Köhring et al., 2011a). When a gas absorbs radiation, the internal energy increases which allows a modulated laser that is resonant with species' absorption features to create pressure waves which can be monitored by a microphone, piezoelectric detectors or FPI (Wheeler et al., 1998).

Although interferometers greatly improve spectral resolution, grating spectrometers typically have suitable resolution for measuring ambient or trace gases in the atmosphere. Interferometers require additional optics for order sorting and are not widely available, unlike grating spectrometers. Interferometers are also susceptible to external vibrations and changes in temperature or relative humidity.

Photoacoustic spectroscopy (PAS)

Photoacoustic spectroscopy is a well-researched detection method that can be applied to solid, liquid and gas samples (Li et al., 2011). PAS will be discussed here in the context of trace gas detection. PAS works by passing a modulated light beam through a photoacoustic resonant cell containing the target absorber. The absorbing gas is

heated periodically at the modulation frequency, creating a periodic pressure change, or 'pressure wave' (Wang et al., 2011). The amplitude of the pressure wave depends on the light intensity, absorber concentration and its absorption cross-section.

The periodic pressure wave was conventionally detected using condenser or piezo-electric microphones. However, these electronic microphones are not appropriate for use at high temperatures or relative humidities and are vulnerable to electromagnetic interference. A cantilever-based approach was reported by Laurila et al. (2006) which used an interferometer to detect the periodic deflection of a cantilever in response to an induced pressure wave. Laurila and coworkers could detect CO_2 with a limit of detection of 0.23 ppm using this technique. A similar approach was taken by Wang & Yu (2010) who placed a diaphragm near the end of a fiber optic so that the periodic movement of diaphragm could be detected by a Fabry-Pérot interferometer. They found that the system sensitivity was limited by the diaphragm size and thickness. Tuning forks have also been widely applied to PAS systems, but they are vulnerable to thermal noise and require stable temperature conditions (Köhring et al., 2011).

Liu et al. (2009) and Rück et al. (2018) used an off-beam configuration for straightforward alignment that did not have to be aligned through the tuning fork. This technique provided high quality resonance amplification that increased the system sensitivity. PAS benefits from sensitive and selective detection of trace gasses as well as a linear response to increasing concentrations (Wang et al., 2011). PAS systems can be configured into a compact instrument (Bonilla-Manrique et al., 2019) provided that appropriate amplifiers can be built into small circuitry. PAS has been widely used for the detection of gasses such as CO_2 (Laurila et al., 2006), O_2 (Köhring et al., 2011), NH_3 (Bonilla-Manrique et al., 2019), H_2O (Liu et al., 2009) and NO_2 (Kerschhofer et al., 2018; Yi et al., 2011).

Laser-induced fluorescence (LIF)

Laser-induced fluorescence, first reported by Zare and Dagdigian (1974), uses a laser to excite a molecule from its ground-state to an excited state. The excited molecule spontaneously relaxes to its ground state, emitting photons that can be detected by sensitive photodetectors. Compounds have unique absorption and fluorescence

spectra, giving LIF good specificity to target species. The wavelength selection should consider interfering molecules and the cross product of the maximum fluorescence and the laser intensity at a given wavelength (Thornton et al., 2000).

LIF measures NO_2 directly and so has better specificity than established but indirect techniques like chemiluminescence. Suzuki et al. (2011) compared LIF to CL measurements and found that CL overestimated NO_2 concentrations, particularly in high-O_3 environments. The specificity of LIF was demonstrated by George and O'Brien (1991) by scrubbing sample air of NO_2 every 10 s (50% duty cycle) — no fluorescence signal was seen in NO_2-free air. George and O'Brien achieved good sensitivity to NO_2 with a limit of detection of 450 ppt in a 20 s sampling time.

LIF has been used to measure NO_2 with excellent sensitivity. Fong and Brune (1997) reported a limit of detection of 280 ppt in 2.5 minutes; Thornton et al. (2000) reported a detection limit of 15 ppt in 10 s for the measurement of tropospheric NO_2. LIF is also appropriate for monitoring urban NO_2. Using a laser wavelength of 226 nm, Peng et al. (1995) measured NO_2 with a detection limit of 10 ppb in 3 minutes. There is a large peak in oxygen fluorescence at 225 nm that interfered with the NO_2 measurement and degraded the detection limit. Dari-Salisburgo et al. (2009) measured NO_2 with a limit of detection of 10 ppt in 60 s at 532 nm with a single pass optical configuration. LIF instruments are generally used in research applications.

1.4 Signal enhancement in spectroscopic measurements

Spectroscopic techniques often deal with low levels of light, either from long optical path lengths or substantial optical filtering for the selection of a wavelength region of interest. This section presents several optical and digital techniques for increasing system sensitivity by enhancing signal amplitude and reducing noise.

1.4.1 Optical cavities

The sensitivity of in situ absorption measurements can be increased by employing high-finesse, optical cavities, as is used in CRDS and CEAS approaches (G. Wang et

al., 2023). An optical cavity typically comprises two high reflectivity (HR) mirrors with a curved, reflective inner surface. The HR coating on the mirrors combined with their curved geometry, causes light of a specific wavelength to resonate within the optical cavity and be reflected multiple times. A small amount of light is transmitted through the cavity mirrors. Optical cavities dramatically increase the path length of light through the sample. Consider the Beer-Lambert equation:

$$N = \frac{\ln\left(\frac{\Delta I}{I}\right)}{\sigma L} \tag{1.5}$$

As the pathlength, L, increases, the minimum detectable concentration decreases, improving the sensitivity of the system overall. An optical cavity increases the pathlength by a factor of $\frac{1}{1-R}$, where R is the cavity mirror reflectivity:

$$N = \frac{\ln\left(\frac{\Delta I}{I}\right)(1-R)}{\sigma L} \tag{1.6}$$

Light must be geometrically constrained within the cavity and certain stability criteria must be fulfilled. The so-called g-parameters describe the cavity stability in terms of its geometry, which is defined by mirror separation, d, and radii of curvature, r_1 and r_2, of the two mirrors. If the cavity is unstable, photons will not be retained in the cavity. The g-parameters are defined as:

$$g_{1,2} = 1 - \frac{d}{r_{1,2}} \tag{1.7}$$

The cavity is stable if $0 < g_1 g_2 < 1$ is satisfied. The range of accepted g-parameters is represented graphically in Figure 1.4 (Spuler & Linne, 2002). An optical cavity can be described as a symmetric resonator when both cavity mirrors have the same radius of curvature and therefore $g_1 = g_2$. If the mirror separation equals the radius of curvature, the mirrors have the same focal point and $g_1 = g_2 = 0$. This is the confocal cavity configuration and gives the highest signal throughput (Fiedler et al., 2007). However, confocal cavities are sensitive to alignment and near-confocal arrangements are preferred (Kebabian et al., 2007).

The mirror reflectivity, R, largely dictates the improvement in sensitivity. As $R \to 1$, photons travel an increasingly long path within the cavity, increasing the sensitivity to sample extinction. A drawback of higher mirror reflectivities is that less light is transmitted out of the cavity. There is therefore a trade-off in terms of light throughput and effective pathlength of light in the cavity. Although mirrors of a lower reflectivity have shorter effective pathlengths in the cavity, their greater transmission makes it easier to measure signals with standard detectors (Dasgupta et al., 2014). In addition, less reflective mirrors cost less. In this thesis, where the target species, NO_2, is typically found at moderate concentrations, lower reflectivity systems have been used to achieve suitable sensitivity at moderate system cost.

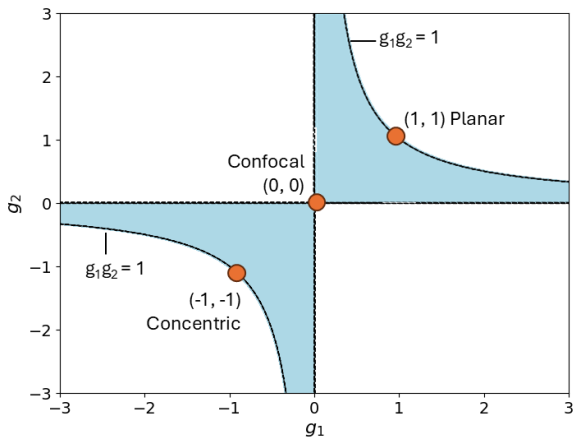


Figure 1.4. Graphical representation of criterion for stable cavities. The cavity is stable if (g_1, g_2) lies within the shaded region.

1.4.2 Balanced detection

Balanced detection is a useful technique for reducing common-mode noise in the system. Common-mode noise (CMN) describes interferences that equally affect the reference and signal paths in a detection system. CMN can be caused by radiofrequency or electromagnetic interference, fluctuations in the power supply or light source, as well as environmental factors, such as cloud cover, and changes in atmospheric transmission. CMN has a large effect on the measurement accuracy and

reduces the signal-to-noise ratio of a system. When both wavelength signals originate from the same light source, fluctuations or drift in the system should be common in both signals. CMN can be reduced by using balanced detection techniques.

The basic principle of balanced detection is that a reference channel and signal channel are measured and compared, either by subtraction or division (normalisation), so that noise that is common to both signals is cancelled out. The resulting balanced signal can then be amplified to further increase the signal-to-noise ratio. Balanced detection removes the need for regular background measurements, which are otherwise needed for small changes in signal (Hobbs, 1997). For balanced detection, both beams must travel an almost identical light path until they reach their respective detectors. This ensures that fluctuations in the light path occur equally in both signals. It is also important that the optical power striking each detector is approximately equal so that small changes in intensity can be observed (Haller & Hobbs, 1991).

Hobbs described ultrasensitive laser measurements with balanced detection with the ability to measure fractional changes in intensity below 10^{-4} (Hobbs, 1997). According to the Beer-Lambert relation (Equation 1.5), the minimum detectable number density decreases when smaller changes in intensity can be measured. While measuring two photocurrents produced by laser absorption, a noise canceller is applied to suppress a large noise floor. This noise canceller works by applying feedback independent of the signal path to adjust the ratio of the photocurrents so that when they are subtracted the resulting DC component is zero. The result is that common-mode noise in the system is suppressed. Hobbs reported that this noise cancelling approach has some pitfalls: the signal is highly dependent on the beam position and polarisation, light detectors must have uniform responses, incidental étalon fringes can be problematic, and electrical components used in the circuit building must be carefully selected.

Balanced detection with two independent light sources has been previously used in spectroscopic measurements. Chen et al. (2020) used two lasers at wavelengths near 405 nm, where NO_2 has strong absorption. The ratio of these laser signals was recorded to measure NO_2 without the collective noise of broad baseline features such as aerosol extinction interference. This instrument was capable of making real-time measurements with high time resolution and good sensitivity.

Soldevila et al. (2016), also used balanced detection techniques to improve single-pixel camera imaging in the presence of ambient or background noise. The frame rate of the camera was increased by a factor of 2 by taking a differential, balanced measurement and dependence on environmental light was removed. This has potential applications in infrared imaging and real-time biological imaging where small changes in signal need to be captured.

1.4.3 Lock-in amplification

Lock-in amplification is a signal processing technique that is used to measure small AC signals that are masked by noise. Absorption measurements often measure low levels of light that vary slowly over time. These signals are difficult to detect in the atmosphere where they are usually obscured by high-level, low frequency optical interference and noise (Dorrington & Künnemeyer, 2002). Amplitude modulating the signal at frequency, ν, moves it away from low frequency noise and allows the use of phase-sensitive detection to pick out the signal at a specific reference frequency and phase. Signal not modulated at the reference frequency is excluded. Modulation also allows discrimination of an active light source from background light.

Phase-sensitive detection (PSD) mixes the reference frequency signal with the detected signal of interest, resulting in sum and difference frequency components. A low-pass filter isolates the difference component, rejecting noise and interference at other frequencies. The resulting signal is then amplified to give a high signal-to-noise ratio (SNR). Lock-in amplification (LIA) takes advantage of PSD but reduces noise further by synchronising the reference and measurement signal.

To understand how the signals are mixed, first consider a periodic signal $V(T)$.

$$V(t) = V_{sig} \sin(\omega T) \tag{1.8}$$

where V_{sig} is the signal amplitude and T is the period. The angular frequency ω can be expressed as $\omega = \frac{2\pi}{T} = 2\pi f$. As stated in Fourier's theorem, functions can be written as a sum of trigonometric or exponential functions of suitable frequency and amplitude (Torzo & Delfitto, 2022). The LIA produces a DC output that is proportional

to the amplitude of the modulated input signal. The LIA used in this research was a Stanford Research Systems SR830 (Stanford Research Systems, 1993). The functional block diagram for the SR830 is shown in Figure 1.5. The amplified input signal is multiplied by the reference signal by a PSD. The output of the PSD, V_{PSD}, can be expressed as two AC signals.

$$V_{PSD} = V_{sig}V_{ref}\sin(\omega_{sig}t + \theta_{sig})\sin(\omega_{ref}t + \theta_{ref}) \quad 1.9$$

where V_{sig} and V_{ref} are the signal and reference voltage, respectively, ω_{sig} and ω_{ref} are the signal and reference angular frequency and θ_{sig} and θ_{ref} are the signal and reference phase, respectively. The PSD output is then passed through a low-pass filter which eliminates both AC signals when $\omega_{sig} \neq \omega_{ref}$. For equal angular frequencies, the difference component of the signal is expressed as a DC signal:

$$V_{PSD} = \frac{1}{2}V_{sig}V_{ref}\cos(\Delta\theta) \quad 1.10$$

where $\Delta\theta = \theta_{sig} - \theta_{ref}$. The phase difference, $\Delta\theta$, of the output signal can be set to zero by adjusting the phase of the reference signal so that V_{PSD} only depends on the amplitude of the input and reference signal. A second PSD multiplies the signal by a reference signal which has been shifted 90°. This results in 'in-phase' (X) and 'quadrature' (Y) components:

$$X = V_{sig}cos\theta \quad 1.11$$

$$Y = V_{sig}sin\theta \quad 1.12$$

$$R = \sqrt{X^2 + Y^2} = V_{sig} \quad 1.13$$

When θ is zero, X measures the signal and Y is zero. The magnitude vector, R, gives the magnitude of the signal independent of phase.

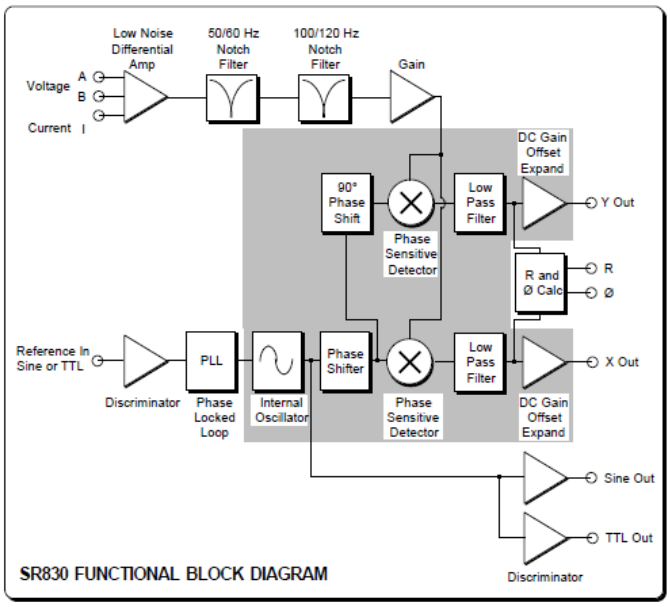


Figure 1.5. SR830 lock-in amplifier functional block diagram, as seen in the SR830 user manual (Stanford Research Systems, 1993)

The sensitivity and stability of the LIA can be optimised by modifying the time constant, reference frequency ω_{ref}, and gain. Optimisation of these parameters is discussed in Chapter 3.

Lock-in amplifiers have many potential applications, including environmental monitoring where gas concentrations are relatively low and masked by large background signals (De Marcellis et al., 2012, 2017; Gong et al., 2020; Maya-Hernández et al., 2014; Zhang et al., 2020). Measurements through the atmosphere are often masked in noise and photodetectors respond to frequencies outside the range of interest. LIAs significantly reduce the effect of these signal interferences and allow small changes in signal to be observed. Spectroscopic systems may have low light levels due to the use of long light paths or optical filtering to select a spectral range, making LIAs appealing for signal processing.

Most commercial LIAs are expensive benchtop instruments and unsuited for portable or mobile measurements. For development of low-cost and compact instruments, low-cost digital LIA systems have recently been developed for optical detection techniques, including optical spectroscopy and imaging (Fonseca et al., 2022; Nadgir et al., 2021; Wang et al., 2017), photoacoustic spectroscopy (Kerschhofer et al., 2018),

and non-linear spectroscopy (Uhl et al., 2021). An open access digital lock-in amplifier (OLIA) using a microcontroller was reported by Harvie and De Mello (2023) for optical detection applications (Harvie et al., 2021). OLIA is suitable for low-cost portable sensor development —it has a build cost of only $35 and is the size of a credit card. An internal 3.3 V reference square wave generated by the microcontroller can be used drive an LED, allowing the reference and measured signals to be inherently synchronised. Methods to control the LED input current and voltage are discussed in Chapter 3. A graphical user interface allows the user to set the time constant, input gain and reference source (internal/external), and to record the output signal amplitude (R), in-phase and quadrature components (X and Y), noise (S) and phase (φ).

1.4.4 Signal filtering

Digital filtering processes may be applied to data and can improve the SNR of a system. Kalman and Savitzky-Golay filtering techniques will be discussed in this section in the context of trace gas detection schemes.

Kalman filtering is an attractive signal processing technique for trace gas monitoring that improves the sensitivity of small, noisy signals while maintaining a similar time response. In contrast, simple arithmetic averaging reduces the system's time resolution and reduces the number of data points (Van Veen & De Loos-Vollebregt, 1990). During a measurement, the Kalman filter monitors the current signal state and its variables. When the next measurement is available the signal state variables are updated using a weighted average favouring variables with greater certainty (Fang et al., 2017), allowing continuous filtering that can be done in real time (Brunner et al., 2011; Xia et al., 2021). The Kalman filter is therefore an adaptive filter and can adjust to changes in the statistics of the signal, although large variations in signal can affect the accuracy (Leleux et al., 2002).

Kalman filtering has been used to improve the sensitivity of the measurements of trace gases such as NO_2, glyoxal (Fang et al., 2017), SO_2 (Tang et al., 2009), NH_3 (Leleux et al., 2002)and methane (Xia et al., 2021). It has also been used on low-cost NO_2 and O_3 sensor data and significantly improves the agreement with reference monitors (Christakis et al., 2023). Zhou et al. could improve sensitivity by a factor of 23 by

using an adaptive Kalman filter that reduced variations in noise even further (Zhou et al., 2019).

Savitsky-Golay (SG) filtering can also be applied to environmental data to improve measurement sensitivity without misrepresenting the signal features by suppressing noise (Ji et al., 2022; Zhang et al., 2018). This is achieved by fitting subsets of neighbouring data points with a low degree polynomial, resulting in convolution coefficients that are then applied to the next subset to give a signal that has been smoothed from the centre of each subset (Liu et al., 2022; Savitzky & Golay, 1964). SG filtering has simple input parameters (window and polynomial order) and accessible software libraries and packages, making it a superior filter for low-cost measurements that require high temporal resolution (Zhang et al., 2018). However, system perturbations may decrease the filter accuracy since the polynomial order and window are empirically set by the user. Adaptive SG filtering that updates these parameters has been shown to enhance sensitivity of measurements by a factor of 5 (Zhang et al., 2021). SG filtering has been applied to the detection of many trace gases to improve the signal-to-noise ratio (Chen et al., 2021; Li, 2011; Liu et al., 2022).

1.5 Thesis objectives and outline

This thesis considers spectroscopic methods for detecting NO_2 with high time resolution in an urban traffic environment. To reduce the cost of the spectroscopic systems, LED light sources and non-dispersive photodetectors are explored as detector components. A narrowband two-channel approach is explored, and a single-channel wideband instrument is tested in the field for its applicability to measuring urban NO_2. This work adds to the active field of developing low-cost NO_2 sensors and monitoring instruments and is an active research space with continuing advancements in the area.

Chapter 2 describes two-channel spectroscopic methods for fast, selective detection of NO_2. The two-channel schemes are achieved using either optical or gas filters. The response of each method to NO_2 and relevant interfering compounds is simulated, and the advantages and disadvantages of the methods is discussed, primarily within the context of urban NO_2 monitoring.

An optical system for a novel two-channel ratiometric approach is characterised in Chapter 3 and optimisation methods are reported. A single-channel wide bandpass CEAS system is described and characterised.

Chapter 4 demonstrates the efficacy of the two-channel ratiometric method and reports the performance of the detection system in an atmospheric simulation chamber by comparison with chemiluminescence monitors or robust spectroscopic techniques, such as DOAS. A wideband CEAS instrument was built and tested in atmospheric simulation chambers to assess its ability to measure ambient NO_2 concentrations in a traffic environment, and its performance is characterised.

Chapter 5 details field measurements carried out in Cork City in close proximity to a primary school. This measurement campaign spanned 2 months and gave insights into the relationship between school pick-up and drop-off times and NO_2 concentrations and tested the wideband CEAS instrument in a traffic environment. This chapter discusses the performance of the instrument and suitability for field measurements, and gives recommendations for reducing local air pollution around schools to improve the health and well-being of schoolchildren.

Chapter 2 Theory and Simulations of Two-channel Absorption Spectroscopy

2.1 Theoretical development of two-channel ratiometric spectroscopy

A principle of operation proposed in this thesis is based on differential absorption spectroscopy in two spectral channels using non-dispersive spectral selection. A wideband single channel method is also discussed and developed further in Chapters 4 and 5. Spectroscopic techniques typically use dispersive detectors such as grating spectrometers to monitor light intensity at different wavelengths. The resulting absorption spectra can be fitted to reference absorption cross-sections. Alternatively, if appropriate optical filtering is employed such that only the wavelengths of interest fall on the photodetector, then non-dispersive detectors such as photodiodes or photomultiplier tubes may be suitable.

Non-dispersive infrared spectroscopy (NDIR) is a common technique for sensing gaseous compounds with strong line absorptions in the IR region such as NO, NO_2, CO, CO_2, H_2O, O_3, NH_3 and CH_4 (Dong et al., 2017; Popa & Udrea, 2019; Xing et al., 2018). NDIR techniques typically require robust signal amplification to achieve an appropriate signal-to-noise ratio for measuring ambient gas concentrations. This chapter develops the theory of a two-spectral channel approach to detect NO_2 in the visible region of the spectrum. The goal of this approach, in combination with LEDs and non-dispersive detectors, is to achieve a fast, selective, and cost-effective spectroscopic sensor in the visible light region for NO_2, with intended use in urban settings and traffic microenvironments where mixing ratios of tens of ppb are common.

Monitoring the relative change in intensity of strong and weak NO_2-absorbing wavelengths is expected to give significant selectivity to NO_2 and mitigate the effect of interferences from other absorbers that do not have the same structured absorption features as NO_2. The approach is similar to that in DIAL measurements where "on" and "off" wavelengths are produced by a tunable laser and beam paths are identical (Su et al., 2021; Volten et al., 2009). Closely spaced operating wavelengths are recommended for DIAL applications so that changes in optical depth from interferences and aerosols are approximately spectrally flat in the on and off channels (Liu et al., 2024).

The two-channel method uses a single broadband light source that is split into two narrow spectral channels after passing through a gas sample. The use of a single, broadband light source and a single optical path through the atmosphere allows common-mode noise to be suppressed. Fluctuations in the intensity of the light source are readily removed in a ratiometric measurement — that is, by taking the ratio of the two wavelength channels. Changes in atmospheric transmission along the light path are minimised as the light path through the sample is the same for both wavelengths. This chapter will use simulations to demonstrate that the two channel approach has good selectivity to NO_2 and could be applied to other absorbing gases with highly structured absorption spectra, such as SO_2 (Kuhn et al., 2019), by choosing a light source, cavity mirrors and bandpass filters to match the corresponding absorbing wavelengths.

Chemical compounds absorb light at different wavelengths depending on electronic transitions within the compound. NO_2 absorbs light across the UV/visible region between 250 and 650 nm with structured spectral absorption; at some wavelengths, a large differential absorption occurs at closely spaced wavelengths. The two channel method is based on the Beer-Lambert law which relates the observed intensity to the sample's extinction at a given wavelength, λ, and time, t:

$$\mathrm{I}(\lambda, t) = I_0(\lambda, t)\exp\left(-\varepsilon(\lambda, t)L\right) \qquad 2.1$$

where $I_0(\lambda, t)$ is the initial light intensity and $I(\lambda, t)$ the light intensity after absorption occurs, $\varepsilon(\lambda, t)$ is the sample extinction coefficient (cm^{-1}), and L is the path length (cm). The Beer-Lambert law allows gas concentrations to be calculated from measured light

intensities in a given experimental system. For two wavelengths λ_1 and λ_2, the corresponding light intensities, $I_1(\lambda_1, t)$ and $I_2(\lambda_2, t)$, can be written as

$$I_1 = I_{10} \exp(-\varepsilon_1 L) \quad 2.2$$

$$I_2 = I_{20} \exp(-\varepsilon_2 L) \quad 2.3$$

where $I_{10}(\lambda)$ and $I_{20}(\lambda)$ are the initial light intensities at wavelengths λ_1 and λ_2. Here, the wavelength and time dependence of I_0, I, and ε have been omitted for brevity (i.e., $I_{10} = I_{10}(\lambda_1, t)$, etc.). The ratio of the two intensities is then:

$$\frac{I_1}{I_2} = \left(\frac{I_{10}}{I_{20}}\right)\left(\frac{\exp(-\varepsilon_1 L)}{\exp(-\varepsilon_2 L)}\right) \quad 2.4$$

or more conveniently expressed as

$$\ln\left(\frac{I_1}{I_2}\right) = \ln\left(\frac{I_{10}}{I_{20}}\right) - L(\varepsilon_1 - \varepsilon_2) \quad 2.5$$

Assuming both wavelength channels are quasi-monochromatic and spectrally stable (i.e., that $\left(\frac{I_{10}}{I_{20}}\right)$ is constant with time), the difference in extinction at the two wavelengths can be determined.

In scenarios such as NO_2 in urban environments, a single (target) absorber can dominate the difference in extinction at two wavelengths:

$$\varepsilon_1 = N\sigma_1 + \varepsilon_c \quad 2.6$$

$$\varepsilon_2 = N\sigma_2 + \varepsilon_c \quad 2.7$$

where N is the number density of the target gas (molecules cm^{-3}), σ_1 and σ_2 are the absorption cross sections of the target at λ_1 and λ_2, and ε_c is the spectrally flat extinction arising from other gases and particles (i.e., $\varepsilon_c(\lambda_1) = \varepsilon_c(\lambda_2)$). In this case,

$$\varepsilon_1 - \varepsilon_2 = N(\sigma_1 - \sigma_2) = N\Delta\sigma \quad 2.8$$

where $\Delta\sigma = (\sigma_1 - \sigma_2)$. Substituting Eq. (5) gives the absorber concentration:

$$N = \frac{\ln\left(\frac{I_{10}}{I_{20}}\right) - \ln\left(\frac{I_1}{I_2}\right)}{L\Delta\sigma} \quad 2.9$$

Thus, if the intensity ratio of the light source, $\left(\frac{I_{10}}{I_{20}}\right)$, in the absence of sample absorption is known, the concentration of the target absorber N can be determined

based on the measured ratio at two intensities where a large difference in cross section occurs and contributions of other absorbers are negligible.

The minimum detectable N of a two-channel system can be reduced by increasing the path length. Conventionally, the pathlength of a compact optical system is increased by using a multipass cell, a long physical pathlength through the atmosphere (such as with long path DOAS), or optical cavities. Using optical cavities produces an effective pathlength, L_{eff}, of

$$L_{eff} = \frac{L}{1-R} \tag{2.10}$$

where R is the cavity mirror reflectivity. For cavity transmission, the concentration is related to the fractional change in the intensity as follows:

$$N = \frac{\ln\left(\frac{I_{10}}{I_{20}}\right) - \ln\left(\frac{I_1}{I_2}\right)(1-R)}{L\Delta\sigma} \tag{2.11}$$

The selectivity of the two-channels is dependent on matching λ_1 and λ_2 to the spectral absorption features of the target species. The bandwidth of each channel must be carefully considered to avoid overlapping spectral features in the two-channels.

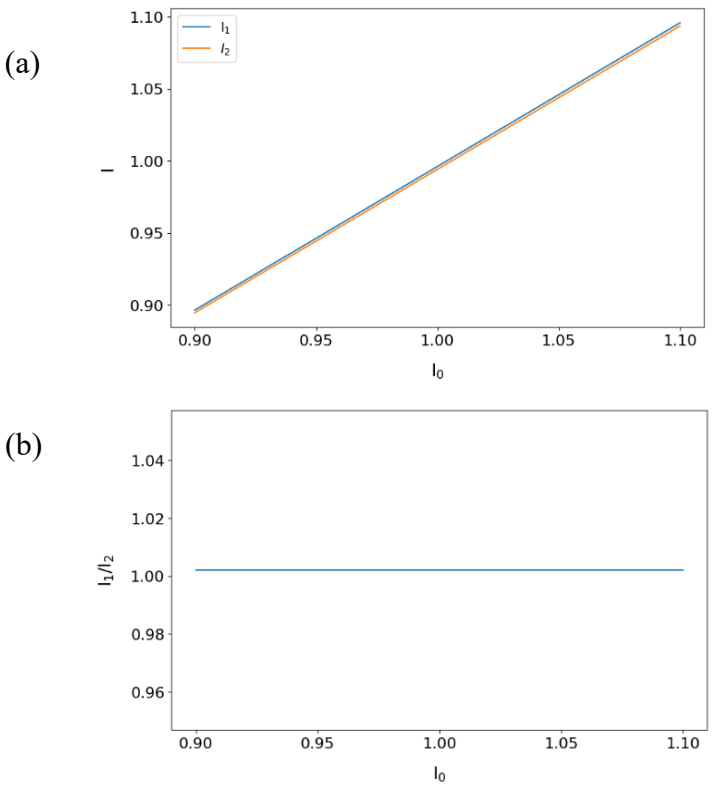


Figure 2.1 (a) Response of I_1 and I_2 for small changes in I_0. (b) Change in ratio of I_1/I_2 for small changes in I_0. The ratio is constant, compared to the single channels which depend linearly on I_0.

2.2 Application of two narrow channels for NO_2 detection

The absorption spectrum of NO_2 must be carefully considered to select the optimum operating wavelengths of the instrument, λ_1 and λ_2. Figure 2.2 shows that NO_2 has highly structured absorption features, with large changes in absorption cross section between nearby wavelengths, especially between 430 – 450 nm. The few atmospheric gases that absorb in this region include glyoxal, methylglyoxal, as well as H_2O, O_3 and the O_2 dimer. These gases have smaller absorption cross-sections and (for the dicarbonyl species) lower concentrations than NO_2. Interfering absorptions from these other gases are less likely in urban measurements where ambient NO_2 concentrations are elevated. (Horowitz et al., 2001; Thalman et al., 2015; Thalman & Volkamer,

2010). The effect of interferences on NO_2 measurements will be explored through Python simulations in Section 2.3.

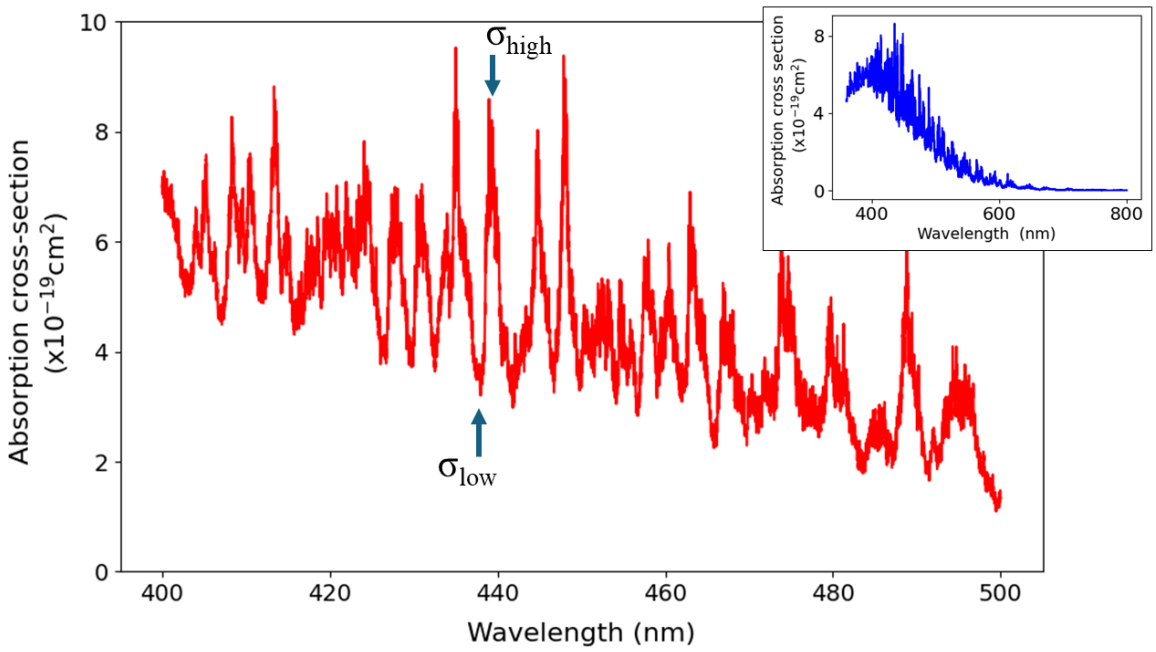


Figure 2.2 Absorption cross-section of NO_2 reported by Coquart et al. (1995) from 400 – 500 nm with 0.01 nm spectral resolution. Inset: Absorption spectrum reported by Voigt et al. (2002) from 360 – 800 nm with 0.004 nm spectral resolution.

An appropriate narrow dielectric filter whose transmission bandwidth matches the width of the chosen absorption features can be used for spectral selection. Such narrow bandpass filters (nBPF) are commercially available (e.g., from Semrock) and have a FWHM of approximately 1.7 nm at blue wavelengths. A narrow bandpass (dielectric) filter isolates specific wavelengths by passing light through two highly reflective surfaces separated by layers, similar to a Fabry-Perot Interferometer (FPI), resulting in efficient transmission of a relatively narrow, well-defined range of wavelengths, while blocking other, unwanted wavelengths.

The central transmission wavelength (λ_0) of the filter can be shifted to shorter wavelengths (λ_θ) by increasing the angle of incidence, θ_i (Hecht, 2002):

$$\lambda_\theta = \lambda_0 \sqrt{1 - \left(\frac{n_0}{n_f}\sin(\theta_i)\right)^2} \qquad 2.12$$

where n_0 and n_f are the refractive indices of air and the dielectric medium, respectively. The wavelength-angle dependence of the nBPF allows the operating wavelengths to be selected by turning the filter, provided the beam has been appropriately collimated.

A two-channel detection scheme can, in principle, select both operating wavelengths using a single nBPF. Both beams must be aligned through the nBPF at precise angles, θ_1 and θ_2, to produce the desired operating wavelengths, λ_1 and λ_2. Figure 2.3 shows an optical configuration with minimal optical components. The optimum optical configuration will be discussed in Section 3.2.

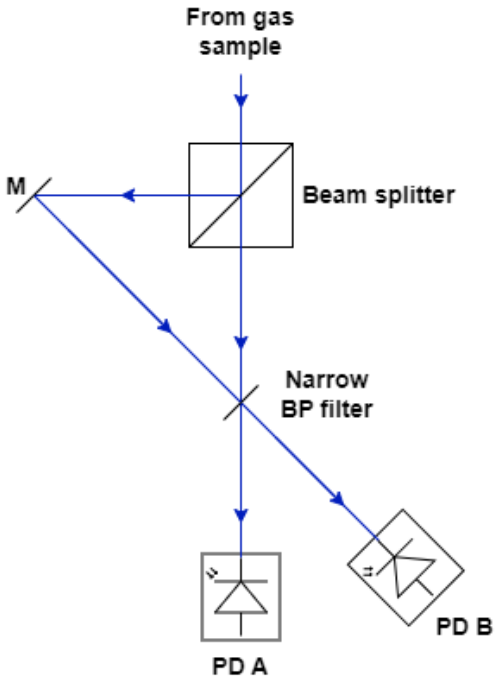


Figure 2.3. Narrow two-channel detection scheme with a single nBPF. M: planar mirror, PD: photodiode.

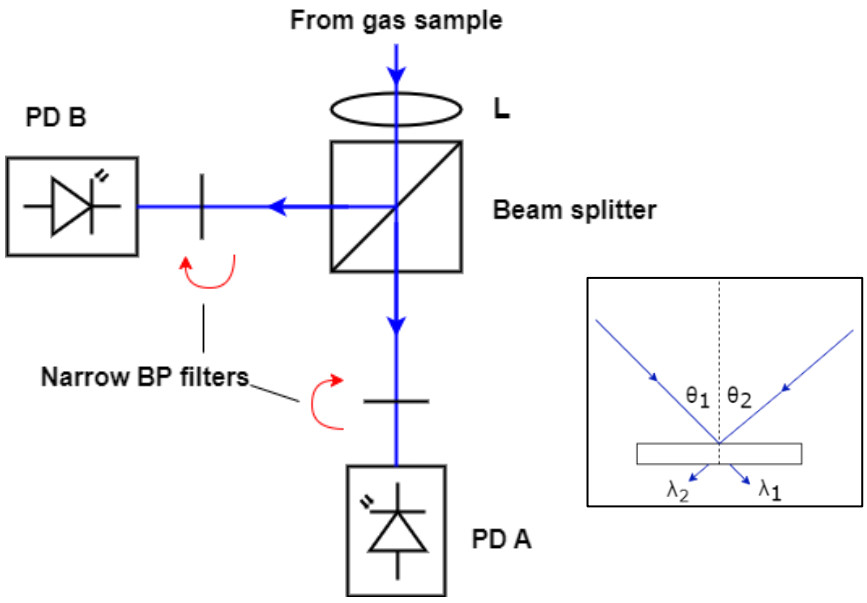


Figure 2.4. Alternative narrow two-channel detection scheme using two nBPF for better alignment. Inset: A narrow bandpass filter showing incident angles and resulting wavelengths.

The two-channel method has some advantages over established spectroscopic measurement techniques. It is less vulnerable to direct spectral interferences, unlike the CAPS method reported by Kebabian et al. (2008), which can be affected by compounds such as glyoxal and methylglyoxal which absorb in the visible (blue) region. A narrowband two-channel method has reduced sensitivity compared with CAPS because the narrow spectral range reduces the signal amplitude. Interference from aerosol extinction can also be reduced using multiple-wavelength detection (Su et al., 2021). Elastic scattering of photons by aerosols and the air is described by Mie and Rayleigh extinction coefficients which vary with wavelength as follows:

$$\varepsilon_M(\lambda) = \varepsilon_{M0}\lambda^{-\alpha} \quad 2.13$$

$$\varepsilon_R(\lambda) = \sigma_{R0}\lambda^{-4}c_{air} \quad 2.14$$

The Mie scattering is dependent on the aerosol loading conditions in the sample of interest. Values of ε_{M0} and α close to zero are found for clean air, whereas coefficient values > 1 indicate air with a high concentration of particulate matter (Ponczek et al., 2022; Sigrist et al., 1994; Xue et al., 2019). The Rayleigh scattering in this wavelength region is relatively weak and the response is largely unchanging since Rayleigh scattering is dominated by scattering of O_2 and N_2 molecules in air, whose

concentrations vary little with changes in ambient pressure and temperature. A more prominent Rayleigh scattering effect may be seen from water vapour since the concentration can vary considerably in the atmosphere. The effects of these scattering processes will be considered for different 2-channel methods simulated in this chapter. If high aerosol concentrations are expected, a PTFE particle filter may be used in *in situ* measurements to remove particles from the gas sample.

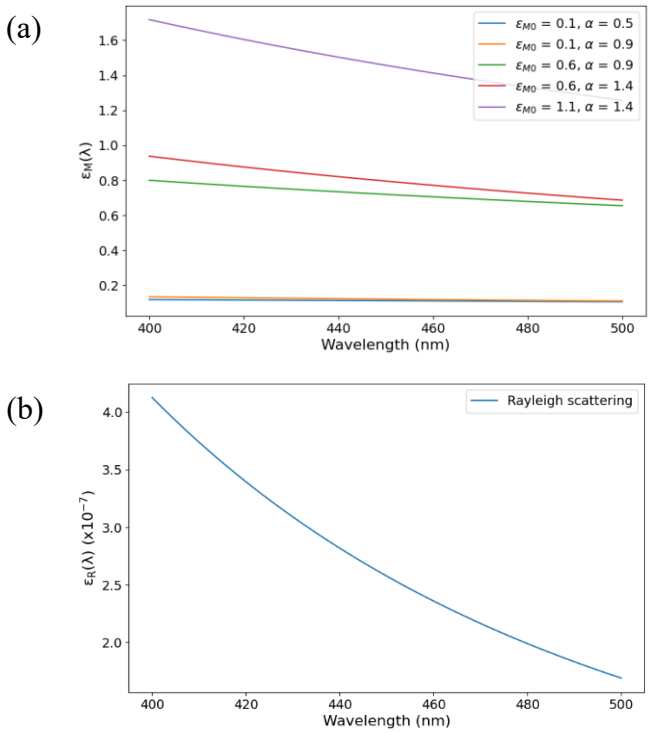


Figure 2.5 (a) Mie scattering over 400-500 nm shown for low aerosol loading (blue and orange lines), medium aerosol loading (red and green lines) and high aerosol loading (purple line) over 1 km pathlength. (b) Rayleigh scattering in air varying with wavelength.

A two-channel measurement is also less susceptible to environmental changes and light source fluctuations. Assuming these changes will be reflected approximately equally in both operating wavelengths, they are largely cancelled out when signals are divided by each other, as demonstrated in Figure 2.1. The ratiometric approach gives the system good common-mode noise rejection (CMNR) and a stable measured signal. This method can be used in both *in situ* and long atmospheric path configurations, making it a potentially powerful environmental monitoring tool. The two-channel

sensor could facilitate fast measurements with a response time on the order of seconds, improving on the temporal resolution of commercial monitors which typically average data over a minute to an hour.

The approach envisaged here also aims to be relatively low-cost compared to conventional air quality monitoring equipment. Both λ_1 and λ_2 are produced from the same light source, and the system does not necessarily require a reference lamp or gas cell as in other spectroscopic methods (Kuhn et al., 2022). The use of a broadband (LED) light source reduces the cost compared to laser-based instruments and lowers safety risks to the user. Reduced risk would make the system more attractive for use in citizen science and engagement projects which could see the public using or even building their own spectroscopic instrument. Modulating the light signal also allows discrimination against ambient background light which is particularly useful for long path measurements during the day. In other spectral fitting methods like DOAS, the solar spectrum must be removed to correct for daylight.

There are also drawbacks to a two-channel approach. The two-channel approach contains inherently less spectral information than a full spectral measurement. The reduced spectral information limits the approach to detecting a single target species. In contrast, approaches like DOAS and IBBCEAS measure much richer spectral information and can quantify multiple absorbing compounds concurrently. Moreover, the spectral resolution of the method is not especially high, partially reducing the selectivity to the target species. Using a nBPF to select the system's operating wavelengths removes most of the spectrum of light resulting in low levels of light incident on the photodetector. This means use of more sensitive detectors (e.g., photomultiplier tubes) or of a less sensitive detector (e.g., a photodiode) with lock-in amplification to discriminate the signal from surrounding noise. To compare λ_1 and λ_2 accurately, their path lengths must match exactly and the initial optical power on each detector must be equal (Haller & Hobbs, 1991).

2.3 Simulated responses

Narrowband two-channel method

To evaluate the potential of the two-channel method to measure ambient NO_2 in the presence of interfering compounds, the theoretical response to these compounds was simulated. The bandwidth of a narrow bandpass filter (Semrock Maxline laser clean-up filter, LL01-442-12.5; centre wavelength 441.6 nm and typical bandwidth of 1.7 nm) was first characterised. Figure 2.6 shows the spectrum of light from a blue LED centred at 435 nm and split into two paths using a beam splitter, each of which was redirected through a narrow bandpass filter at different angles. One of these curves was fitted with a Gaussian curve, which agreed closely with the measured transmission band (Fig. 2.7), as shown by Ab-Rahman et al. (2012) and Bauer (2021). The fitted Gaussian curve represents the instrument response with a full-width at half-maximum (FWHM) of 0.6067 nm, corresponding to a bandwidth of 1.36 nm. This Gaussian function is therefore used in further analysis of the system response.

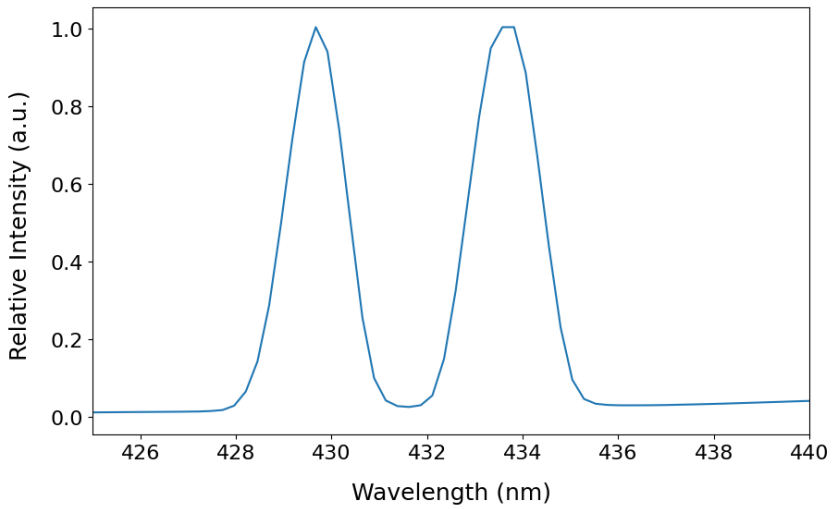


Figure 2.6. Measured transmitted intensity of a collimated beam from an LED, split into two paths and passed through a narrow bandpass filter (Semrock LL01-442-12.5) at different angles of incidence.

Convolving a high resolution NO_2 absorption spectrum (Coquart et al., 1995) with the fitted Gaussian curve for different peak wavelengths shows the spectral features at the

system resolution (Fig. 2.8). As expected, the convolved spectrum has lower spectral resolution than the literature spectrum, but high and low absorption features can still be seen clearly. The reported literature values for the absorption cross-section at 435 and 438 nm are 8.0×10^{-19} and 3.3×10^{-19} cm^2/molecule, respectively. These absorption features are reduced by ~25% in the simulated system output with absorption cross-sections of 6.5×10^{-19} and 4.3×10^{-19} cm^2/molecule at 435 and 438 nm, with a ratio $\frac{\sigma_{435nm}}{\sigma_{438nm}} = 1.5$. Similar absorption cross-sections are found at 437.3 nm and 439.4 nm where the ratio of absorption cross-sections is $\frac{\sigma_{439.4nm}}{\sigma_{437.3nm}} = 1.5$. The suitability of a range of wavelength pairs for the detection of NO_2 will be explored later in this section, with a focus on suppressing interference from other absorbing gases. The two-channel method may be applied to any closely spaced peaks and troughs in the absorption spectrum of the target gas.

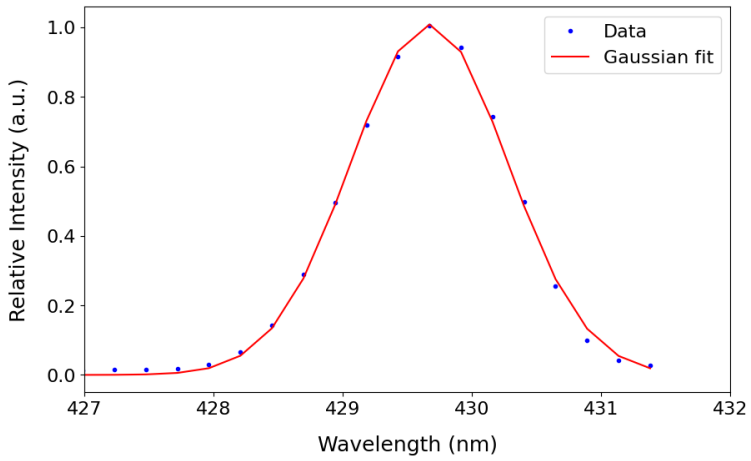


Figure 2.7. Gaussian fit of λ_1 showing a curve at 430 nm with FWHM 0.6067 nm.

The effect of spectral interferences such as glyoxal and methylglyoxal was obtained by convolving the Gaussian filter function with the literature absorption cross sections (Horowitz et al., 2001; Meller et al., 1991). Figure 2.9 shows that glyoxal has considerable differential structure around 450 nm whereas methylglyoxal has much smaller features in its spectrum. Flowerday et al. (2023) used the differential absorption of glyoxal between 450 and 460 nm to measure glyoxal down to 10 ppt.

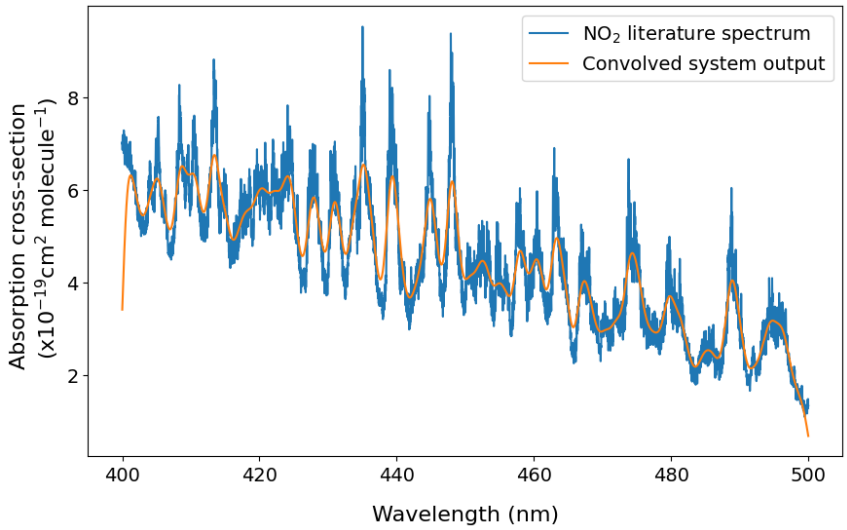


Figure 2.8. NO_2 absorption cross section spectrum with 0.01 nm resolution (from Coquart et al. (1995)) compared to the spectrum convolved with the Gaussian function describing the band pass filter transmission bandwidth. The convolved absorption spectrum allows the absorption cross-section values at the system's resolution to be estimated.

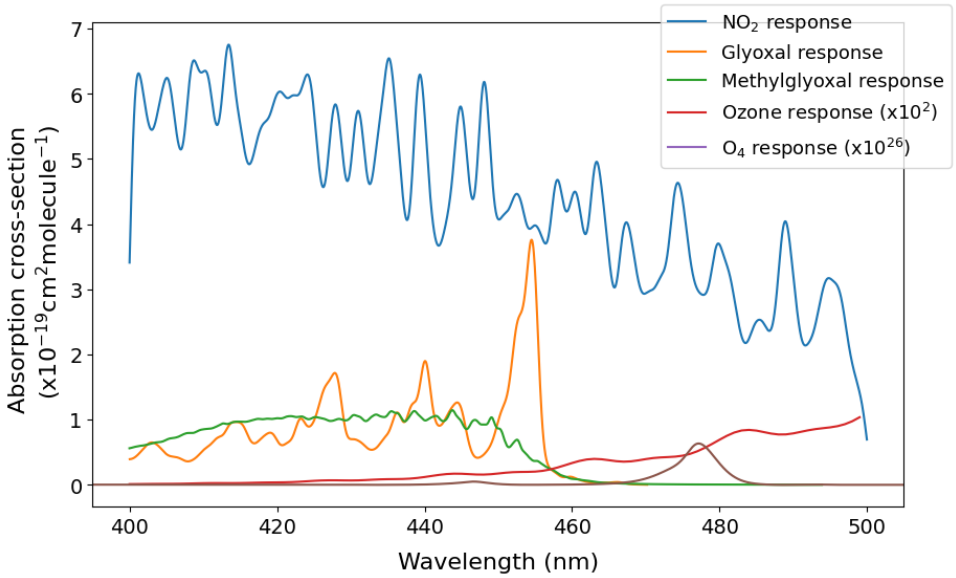


Figure 2.9. Absorption cross section spectra of NO_2, glyoxal, methylglyoxal ozone and the oxygen dimer, O_4, convolved with a gaussian function of the narrow bandpass filter transmission band. NO_2 has the larger absorption cross section and more highly structured absorption features across most of this region compared to glyoxal and methylglyoxal.

In urban air, concentrations of glyoxal and methylglyoxal are typically at the ppt-level, ranging between 0-500 ppt for glyoxal and 0-570 ppt for methylglyoxal (Mitsuishi et

al., 2018; Thalman et al., 2015). Therefore, in an urban traffic environment where NO_2 concentrations are easily an order of magnitude higher, these gases are not expected to strongly influence measured NO_2 concentrations. In environments where glyoxal and methylglyoxal could be appreciable interferences, one strategy would be to use a two wavelength method at above 460 nm, since the absorption of both interfering species reduces substantially above 460 nm, whereas NO_2 still retains significant structure in its spectrum.

Use of a narrow bandpass filter to choose the system operating wavelengths allows selection of operating wavelengths that are less affected by these interfering compounds. Given the values discussed for NO_2 absorption cross-sections at 435 and 438 nm, the differential cross-section, $\Delta\sigma$, is 2.2×10^{-19} cm^2/molecule. The convolved glyoxal response has absorption cross-sections of 7.9×10^{-20} and 1.2×10^{-19} cm^2/molecule at 435 and 438 nm, respectively, resulting in a differential absorption cross-section of 0.4×10^{-19} cm^2/molecule, almost three times smaller than the effect of NO_2 for the same concentration. The convolved methylglyoxal response has absorption cross-sections of 1.074×10^{-19} and 1.056×10^{-19} cm^2/molecule at 435 and 438 nm, with a resulting differential absorption cross-section of 0.018×10^{-19} cm^2/molecule, two orders of magnitudes smaller than the NO_2 response. Interference from methylgloxal absorption is therefore expected to be negligible in most settings where NO_2 concentrations are much higher than methylglyoxal. From this analysis, 435 and 438 nm are appropriate operating wavelengths for this system.

Beyond 460 nm the spectral interference from glyoxal and methylglyoxal is negligible, however, these wavelengths are beyond the band pass of this system (420-460 nm). The magnitude of the NO_2 absorption cross-section also decreases. There may also be greater interference from O_3 and O_4 which absorb more strongly above 460 nm. Considering different values for λ_1 and λ_2, 437.3 nm and 439.4 nm for example, the differential absorption cross-sections for NO_2 remain over an order of magnitude higher than those of glyoxal and methylglyoxal.

Possible interference from Mie scattering by aerosols and Raleigh scattering in air must be considered. To simulate different aerosol environments, different loading parameters were explored. The extinction coefficient, α, increases with aerosol concentration and is dependent on the particle size and composition. Lv et al. (2017)

reported that $\alpha \approx 0$ represents a clean environment with $C_{PM} \approx 10\ \mu g/m^3$ and that $\alpha > 1$ represents an extremely polluted environment ($C_{PM} > 150\ \mu g/m^3$) when relative humidity is less than 90%. In clean conditions, the aerosol optical depth varies slowly with wavelength, with a small effect on the narrowband retrieval for a ratiometric two-channel system. As aerosol loading increases, the slope of the optical depth function increases, creating more interference in ratiometric two-channel measurements as the difference between nearby wavelengths is increased. Choosing operating wavelengths that are sufficiently close will reduce the effect of aerosols on the measured NO_2 signal.

The simulated change in ratio of two channels with increasing gas mixing ratios over a 100 m pathlength is shown in Figure 2.10. The spectral interference from methylglyoxal (MGLY) is negligible at these mixing ratios, especially considering MGLY is typically at sub-ppb levels in urban environments. The response to glyoxal (GLY) is larger, resulting in a positive interference and over-estimation of NO_2. Nevertheless, GLY occurs at sub-ppb mixing ratios in urban environments; at these concentrations the effect on NO_2 measurements will also be minor (García-Alonso et al., 2006; Li et al., 2022; Washenfelder et al., 2008). Low and medium aerosol loading conditions also yield a small interference signal, whereas high concentrations of particulate matter would affect the system selectivity to NO_2. If the particulate matter concentrations are known, then the contribution of aerosols can be estimated to correct the NO_2 concentration measurement.

Two channel measurements depend on the ability to discern small changes in the ratio of channels against background noise. Increasing the path length of the measured signal increases the sensitivity to a given sample absorption and larger changes in the ratio of beam intensities (Equation 2.8). The effect of pathlength is shown in Figure 2.11 for 100 ppb of NO_2. A long path length can be achieved using a long open path, as in remote sensing applications, or an optical cavity for *in situ* measurements. For air quality monitoring systems, a limit of detection (3σ) of less than 5 ppb is desirable, based on the 2021 WHO Air Quality Guidelines as discussed in Section 1.2.

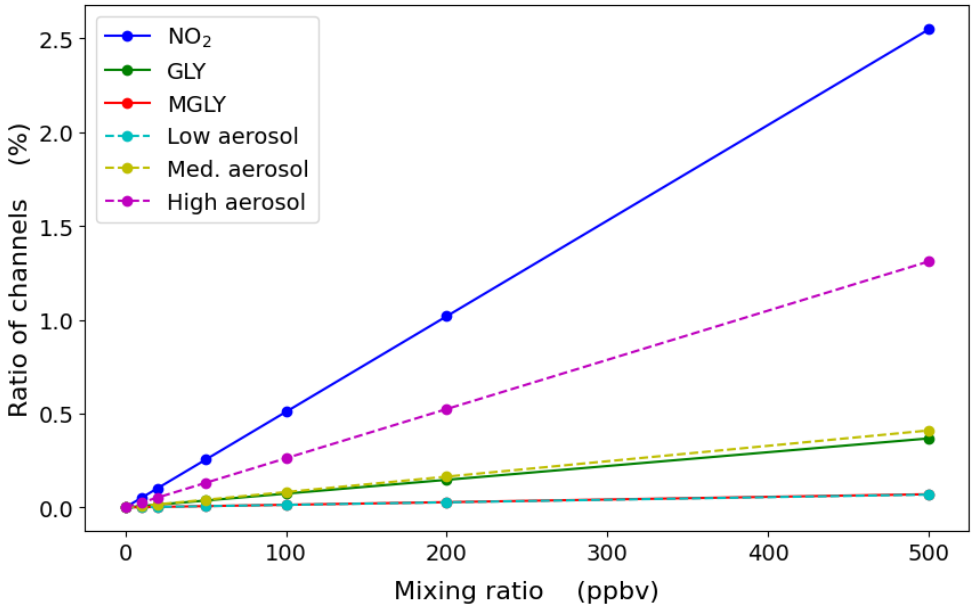


Figure 2.10. Simulated change in ratio of 437.3 and 439.4 nm channels (%) at a range of mixing ratios for a pathlength of 100 m. Note that glyoxal (GLY) and methylglyoxal (MGLY) are typically found at sub-ppb mixing ratios in urban areas.

At low ambient concentrations the change in ratio is below 0.1%, therefore signal amplification to improve the SNR, such as lock-in amplification (Section 1.4.3), a highly sensitive detector, such as a photomultiplier tube or grating spectrometer, is required to discriminate small signals from large background noise levels. For applications with much higher NO_2 concentrations such as continuous emissions monitoring (Carslaw & Beevers, 2005; Wang et al., 2023) (where mixing ratios are above 100 ppb), the two-channel approach will have a stronger response. In the traffic microenvironment, spikes of high NO_2 concentrations are expected due to passing vehicles and these emissions will have a wider effect on urban air quality (Anderson et al., 2021; Bishop et al., 2022; Schreier et al., 2019). A detection system with high time resolution and good sensitivity to NO_2 with a high upper concentration limit is required to study fast-moving mobile emission sources.

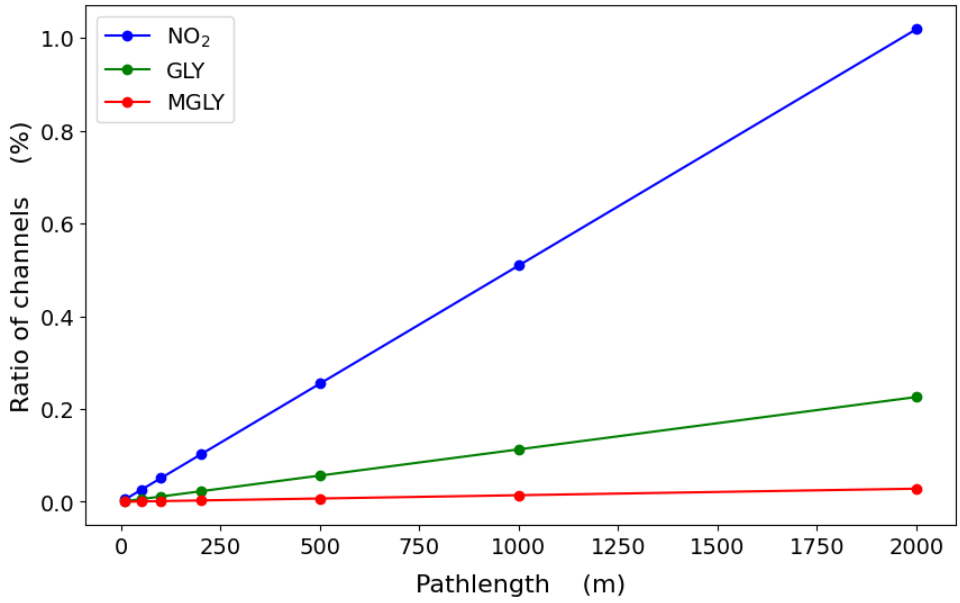


Figure 2.11. Simulated change in ratio of 437.3 and 439.4 nm channels (%) at a range of pathlengths for a 100 ppb mixing ratio. Note that GLY and MGLY are typically at sub-ppb levels in urban areas.

Operating Wavelength Selection

When choosing a sensor system's operating wavelengths, the full NO_2 absorption spectrum and the differential absorption spectrum must be considered. The NO_2 absorption spectrum has an underlying broadband baseline with narrowband structured features superimposed. To analyse the differential absorption cross-section ($\Delta\sigma = \sigma_{NO2} - \sigma_{BG}$) of NO_2, its absorption cross section spectrum (σ_{NO2}) was smoothed to identify the broadband absorption (σ_{BG}) and calculate $\Delta\sigma$. Although the highest absolute absorption cross-sections are found around 400 nm, the differential absorption is not especially large with $\Delta\sigma \approx 1.4\times10^{-19}$ cm^2/molecule. Below 400 nm, the absorption features are less structured and interferences from aerosol scattering and absorption by a wider range of gases would be greater than at longer, visible wavelengths.

Wavelengths greater than 490 nm have a moderate differential absorption up to $\Delta\sigma \approx 2.0\times10^{-19}$ cm^2/molecule, even though the absolute values of the absorption cross-sections are 2-3 times smaller than the peak absorption. Interference from O_3 differential absorption may also become an issue at these wavelengths, as seen in

Figure 2.9. Therefore, the optimal operating wavelengths for maximum sensitivity to NO_2 is between 430 – 450 nm where the differential absorption is sufficiently large (> 2.0×10^{-19} cm^2/molecule). The responses of a selection of strong and weak absorbing wavelengths to NO_2 and interferences (GLY, MGLY, aerosols, O_3 and water vapour (H_2O)) were simulated to determine the most favourable pair.

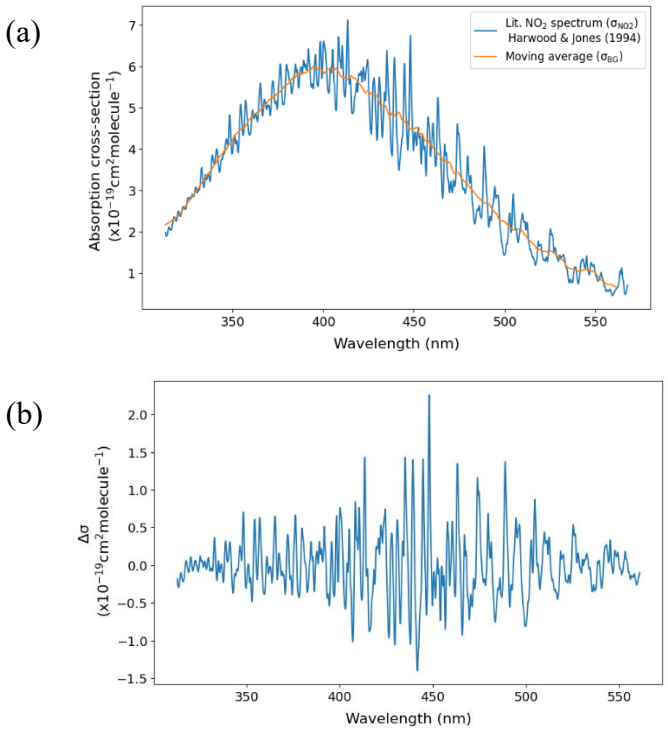


Figure 2.12. (a) NO_2 absorption cross section spectrum as reported by Harwood and Jones (1994) (0.15 nm resolution). The moving average (orange line) captures the underlying broadband absorption of NO_2. (b) The differential NO_2 cross section spectrum showing narrowband absorption features.

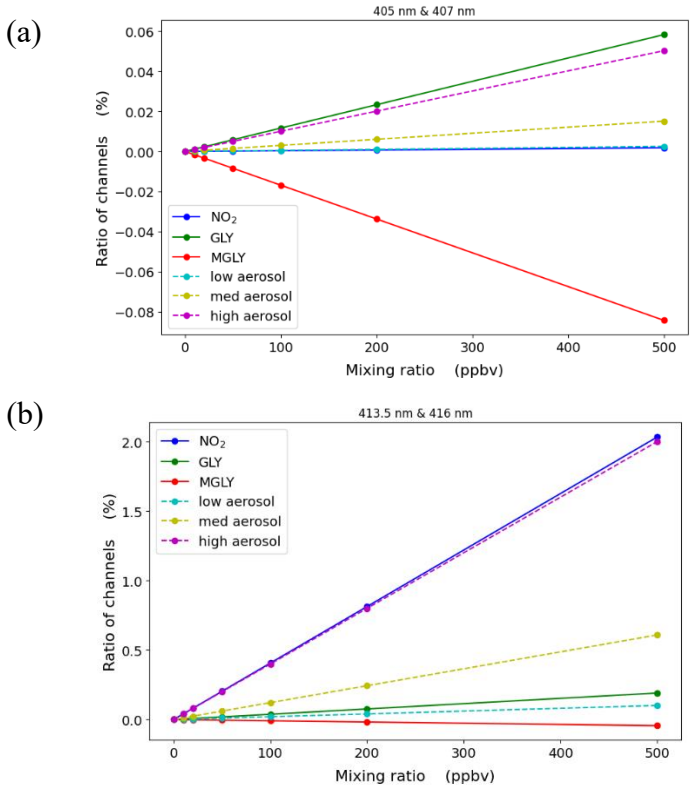


Figure 2.13. Simulated two-channel response for selected wavelength pairs to increasing mixing ratios of NO_2, GLY, MGLY, O_3, H2O and aerosols under different loading conditions at (a) 405.0 and 407.0 nm, and (b) 413.5 and 416 nm

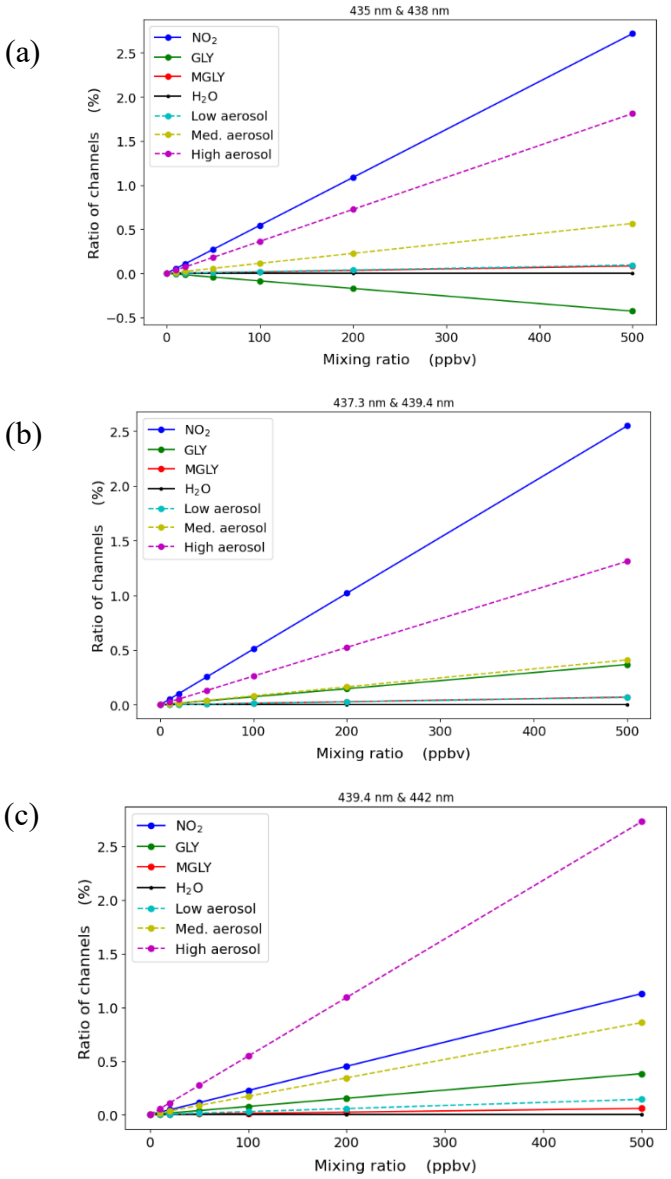


Figure 2.14. Simulated two-channel response for selected wavelength pairs to increasing mixing ratios of NO2, GLY, MGLY, O3, H2O and aerosols under different loading conditions at (a) 435.0 and 438.0 nm, (b) 437.3 and 439.4 nm, and (c) 439.4 and 442.0 nm.

(a)

(b)

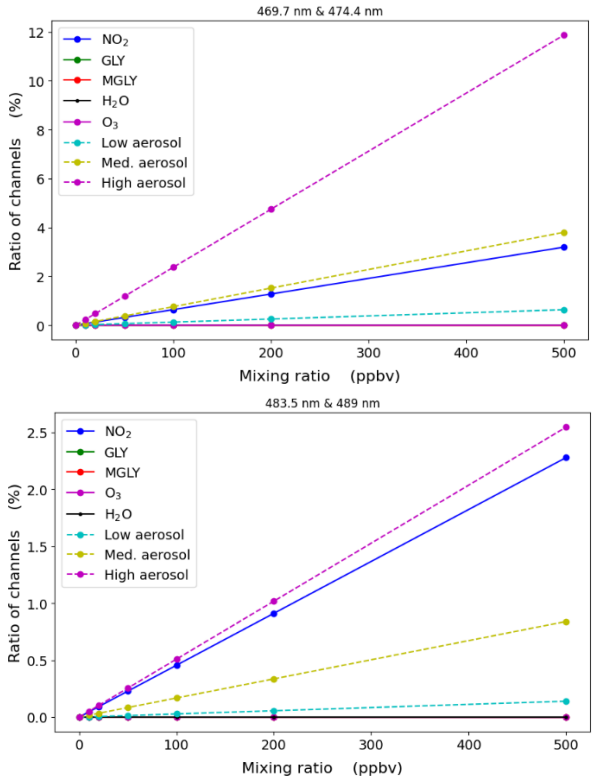


Figure 2.15. Simulated two-channel response for selected wavelength pairs to increasing mixing ratios of NO_2, GLY, MGLY, O_3, H_2O and aerosols under different loading conditions at (a) 469.7 and 474.4 nm and (b) 483.5 and 489.0 nm.

The percent change in ratio of 405.0 and 407.0 nm for increasing gas concentrations is shown in Figure 2.13(a). The response to NO_2 is weak due to the small differential absorption cross-section, $\Delta\sigma = 2 \times 10^{-22}$ cm^2/molecule. Absorption by interfering species has both a positive and negative effect and would lead to over- and underestimations of NO_2, depending on the composition of the sample. Figure 2.13 (b) shows the strong NO_2 response of 413.5 and 416 nm with a small effect from glyoxal and methylglyoxal. However, there is a large positive impact from high concentrations of aerosols that would lead to overestimation of NO_2 concentrations by a factor of 2. The influence of scattering is larger because these wavelengths are separated by almost 3 nm, making the system response more vulnerable to interference from aerosol scattering (Liu et al., 2024).

The response of wavelength pairs between 430 – 450 nm with the largest differential absorption are shown in Figure 2.14. Wavelength pairs of 439.4 and 442.0 nm (Figure 2.14 (c)) have a weaker response to NO_2 than 435.0 and 438.0 nm (Figure 2.14 (a)),

and 437.3 and 439.4 nm (Figure 2.14 (b)) due to a lower differential absorption. The wavelength pairs 437.3 and 439.4 nm (Figure 2.14 (b)) have better selectivity, particularly to aerosols, owing to the closer spacing of wavelengths. In highly polluted areas and without particle filtering, aerosol scattering could lead to overestimation of NO_2 concentrations. There may be a small effect from water vapour present in the air, as was observed by Bailey et al. (2024).

Longer wavelength pairs above 460 nm were also considered as this region has excellent selectivity to NO_2 compared to other absorbing gases. However, wavelengths of peaks and troughs in the NO_2 absorption spectrum are further apart at longer wavelengths, making the system more susceptible to interference from aerosols. Interference from glyoxal and methylglyoxal is negligible at these wavelengths. Ozone also absorbs at these wavelengths, but the absolute and differential absorption cross-sections are small compared with NO_2, as shown in Figure 2.15.

Based on these simulations, 437.3 and 439.4 nm were chosen as suitable operating wavelengths for the two wavelength channels owing to their considerable differential absorption cross-sections and the moderate influence from interfering absorption by other species. This spectral region also benefits from readily available LEDs with high output power and directionality, and standard commercially-available narrow bandpass filters. LEDs give better spectral stability than lasers as their broadband structure varies more slowly with wavelength (Birks et al., 2018). A further practical consideration is that the laboratory had existing optical cavity mirrors with high reflectivity around 440 nm, saving the cost of purchasing custom cavity mirrors. On the detector side, silicon photodiode responsivity extends into this region, although it is relatively low ($\Re > 0.10$) compared to the responsivity maximum around 760 nm. Careful amplification of such photodiode signals, or use of an alternative detector with better responsivity to blue light, must be considered.

Influence of filter bandwidth

When using bandpass filters, the sensitivity and selectivity of the two-channel approach depends on the FWHM of the narrow bandpass filter used for wavelength selection. The spectral response of a Semrock filter (LL01-442-12.5, measured

bandwidth = 1.36 nm) was compared to one wider case, 2.0 nm (Figure 2.16), and two narrower bandwidth cases, 0.4 and 0.8 nm (Figure 2.17). The spectral resolution of the system improves as the bandwidth decreases, making the differential structure of the NO_2 absorption spectrum more prominent, giving rise to larger values for $\Delta\sigma$ and thus reducing the minimum detectable number density, N. In general, narrower bandwidth should also improve selectivity to the target species compared to other absorbing gases.

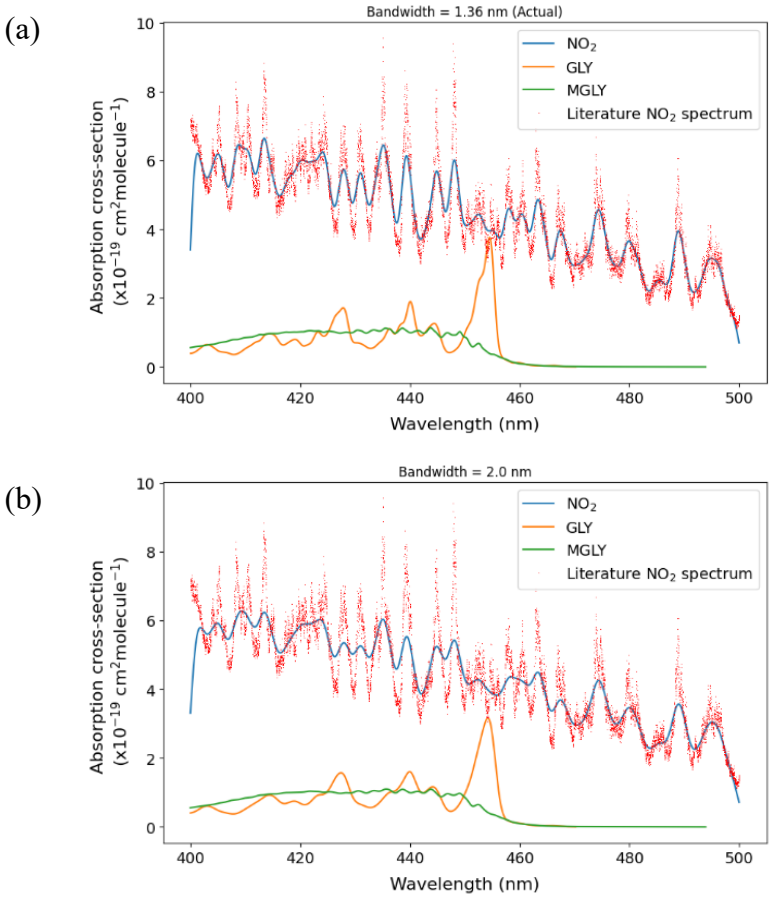


Figure 2.16. Convolved system response for bandwidths: (a) 1.36 nm, the actual bandwidth of the Semrock filter, and (b) 2.0 nm.

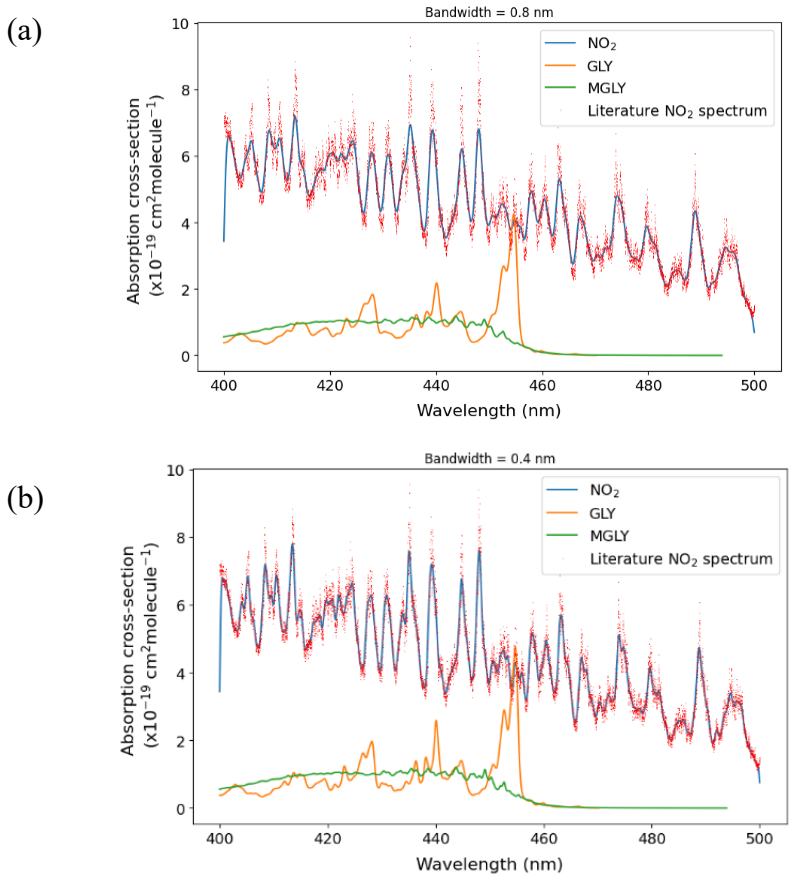


Figure 2.17. Convolved system response for bandwidths: (a) 0.8 nm and (b) 0.4 nm. The resolution improves as the bandwidth narrows.

A narrower filter allows high and low absorbing wavelengths to be chosen more precisely and minimises spectral overlap of the channels. In contrast, the resolution deteriorates as the bandwidth increases to 2.0 nm, reducing the differential response to NO_2 (Figure 2.18). Greater resolution can make the system more vulnerable to instabilities in the spectral selection of the two channels because σ_{abs} varies more quickly with wavelength. Such uncertainty in the wavelength selection would contribute to the uncertainty in $\Delta\sigma$ and hence in the retrieved calculation. The narrow bandwidths considered are not based on commercially available filters but show the potential resolution of the system with appropriate optics that could, in principle, be custom fabricated.

There is a strong negative linear correlation between $\Delta\sigma_{NO2}$ and bandwidth with a slope of -1.5 cm^2 molecule nm^{-1}. The absorption cross-section values for NO_2 and interfering absorbers are summarised in Table 2.1. Changes in the filter bandwidth

have a smaller effect on the differential glyoxal and methylglyoxal responses due to their broader absorption features in this region. Other considerations notwithstanding, the high frequency variability in the NO_2 absorption spectrum makes narrower channels desirable for sensitivity and selectivity.

Table 2.1. Convolved absorption cross-sections (in units of 10^{-19} cm^2/molecule) for different bandwidths (0.4, 0.8, 2.0 nm) compared to the Semrock filter bandwidth, 1.36 nm.

Band-width		**σ_{NO2}**	**$\sigma_{Glyoxal}$**	**$\sigma_{Methylglyoxal}$**	**$\alpha_{low_aerosol}$**	**$\alpha_{high_aerosol}$**
1.36nm (actual)	437.3 nm	4.18	1.04	1.00	7.37	49.63
	439.4 nm	6.13	1.57	1.05	7.34	49.30
	$\Delta\varsigma$	**1.95**	**0.53**	**0.05**	**0.03**	**0.33**
0.4 nm	437.3 nm	3.55	0.87	1.00	2.46	16.54
	439.4 nm	6.95	1.33	1.05	2.45	16.43
	$\Delta\varsigma$	**3.40**	**0.46**	**0.05**	**0.01**	**0.11**
0.8 nm	437.3 nm	3.76	0.97	0.99	4.92	33.09
	439.4 nm	6.67	1.47	1.05	4.90	32.86
	$\Delta\varsigma$	**2.91**	**0.50**	**0.06**	**0.02**	**0.22**
2.0 nm	437.3 nm	4.59	1.08	0.99	12.29	82.71
	439.4 nm	5.53	1.53	1.05	12.24	82.16
	$\Delta\sigma$	**1.07**	**0.45**	**0.06**	**0.05**	**0.55**

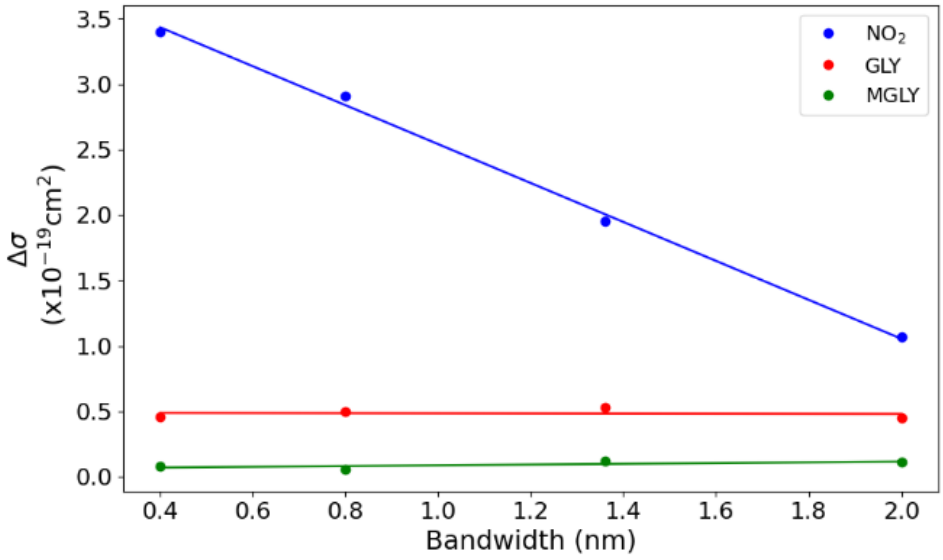


Figure 2.18. Convolved differential absorption cross-sections for a range of bandwidths with λ_1 = 437.3 nm and λ_2 = 439.4nm.

Single-channel method

The two-channel method described above gives good selectivity to NO_2 but greatly reduces light levels at the photodetector, thereby reducing the signal-to-noise ratio and the instrument's overall sensitivity. As an alternative, a single-channel system was considered with a wide bandpass filter (Semrock FF01-440-40) with a transmission band between 420 and 460 nm (Figure 2.19). This single-channel approach is in a region in which NO_2 has a large absorption cross-section. The filter transmission was convolved with an LED with centre wavelength at 440 nm to give the LED-weighted filter transmission. The transmitted signal is highest at the peak LED emission wavelength and will vary for different LED choices.

The filter transmission curve was convolved with a literature NO_2 absorption spectrum. The full integrated signal will be used to monitor NO_2 concentrations so high-resolution spectral features are not necessary here. Using a wider bandwidth filter greatly increases the light throughput compared with the use of narrow bandpass filters, thereby improving the SNR and sensitivity of the system. The convolved absorption cross-sections were then integrated between 420 – 460 nm to plot the

expected change in intensity for a range of NO_2 concentrations (Figure 2.20). The signal is 6.5 times stronger in the single-channel wideband system when compared to the ratiometric two-channel approach discussed previously. There is a stronger contribution from GLY and MGLY in the single-channel than the two-channel method, although it should be noted that mixing ratios in Figure 2.20 greatly exceed those reported in the atmosphere.

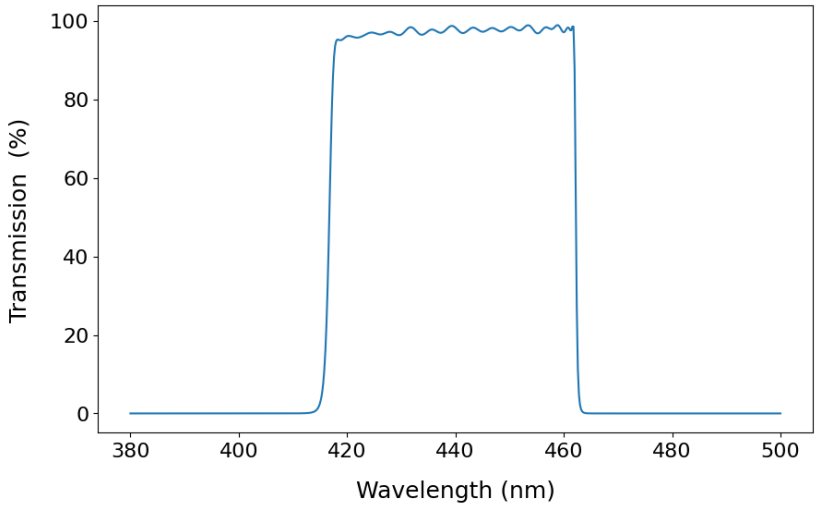


Figure 2.19. Transmission spectrum of the Semrock FF01-440-40 wide bandpass filter.

Between 420 and 460 nm, the integrated absorption cross-section of glyoxal is 8.24×10^{-16} cm^2 nm/molecule, while methylglyoxal has an integrated absorption cross-section of 6.60×10^{-16} cm^2 nm/molecule. Both are an order of magnitude less than the integrated absorption cross-section of NO_2, which is 3.89×10^{-15} cm^2 nm/molecule, offering good specificity against other absorbing gases, owing to the strong absorption of NO_2 in this region. Because urban and traffic environments are dominated by NO_2, and glyoxal and methylglyoxal concentrations are low, interference from these compounds should be small.

Aerosols are expected to interfere strongly with the single-channel response since the system bandpass is far wider than typical fine particle diameters. Even under low aerosol loading conditions the response may be affected. To minimise interferences from aerosols, a particle filter can be used to remove particulate matter from the sample.

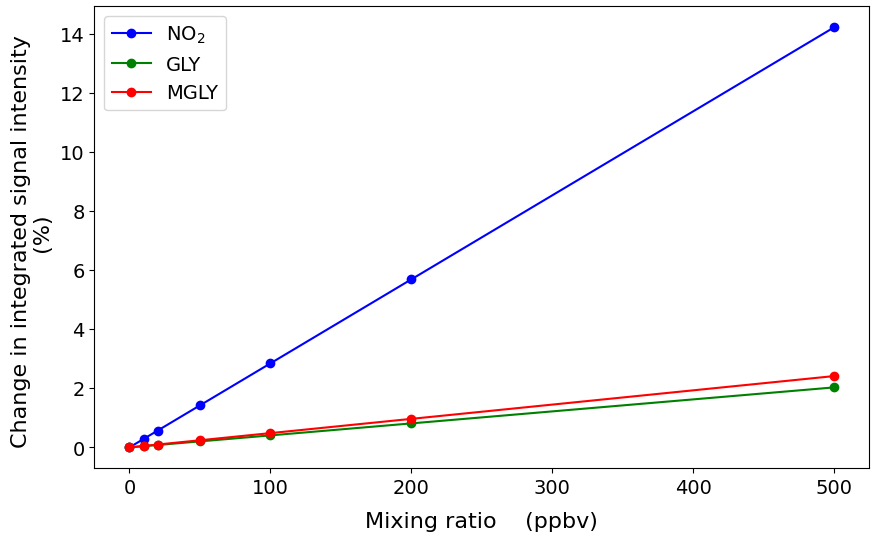


Figure 2.20. Convolved system response to different mixing ratios of NO_2, glyoxal (GLY) and methylglyoxal (MGLY).

2-channels with dielectric filter

The use of two narrow spectral channels to measure a differential signal, as considered in the preceding section, results in low levels of light as most of the LED emission spectrum is removed by the narrow bandpass filters. Here we consider an alternative strategy using a much wider two channel approach in which a larger proportion of the LED spectrum was measured. In this approach, two broad spectral channels are considered — a long wavelength channel and a short wavelength channel — with a large difference in absorption cross-section in each channel. A schematic of a potential optical detection scheme is shown in Figure 2.21.

Figure 2.22 shows the NO_2 absorption spectrum for an extended wavelength region, 415 – 570 nm. The absorption cross-section above 500 nm (orange line) is much smaller than that below 500 nm (blue line). On the basis of these short and long wavelength channels, a differential high-absorbing and low-absorbing signal could be extracted. These channels may be defined using one LED light source and a dielectric cut-off filter.

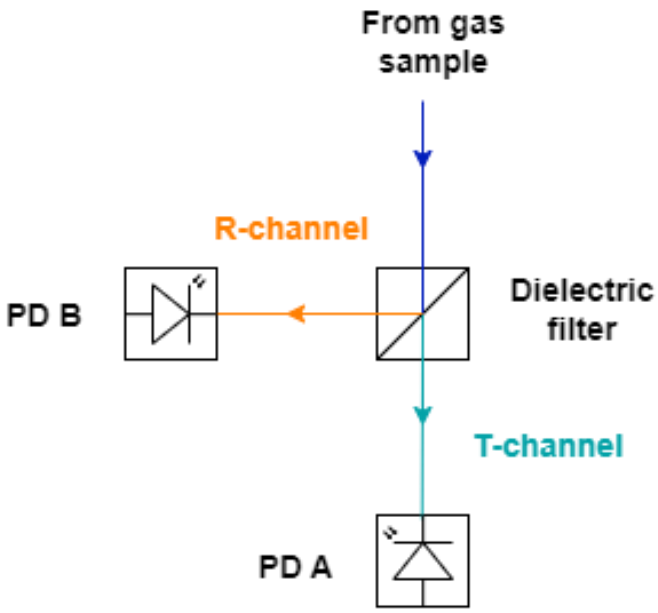


Figure 2.21. Detection schematic for two broad spectral channels instrument. A dielectric filter is used to split the incoming beam into transmitted and reflected channels.

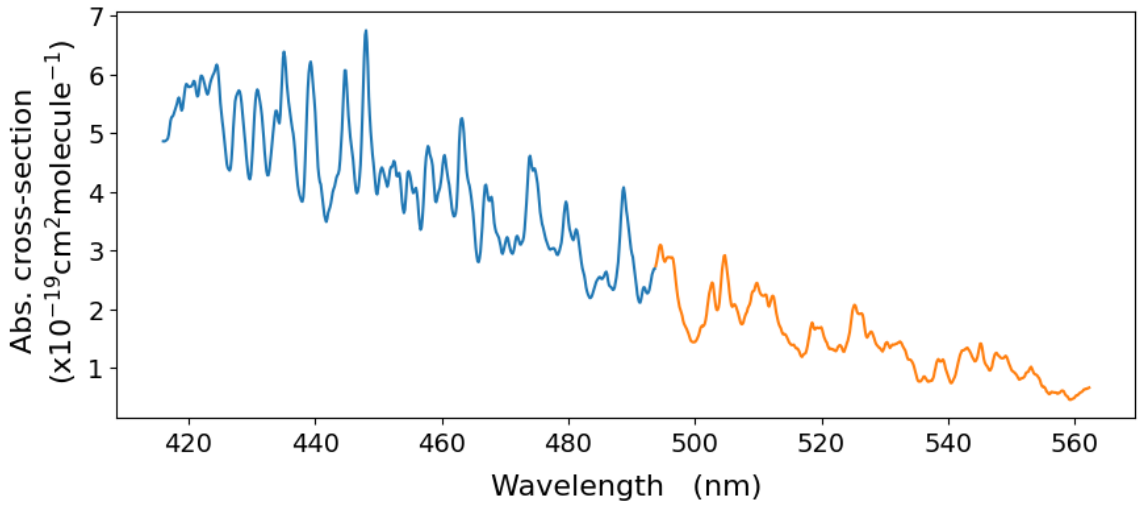


Figure 2.22. NO_2 absorption cross sections for an extended wavelength region 415 - 570 nm, from Harwood Jones et al (1995).

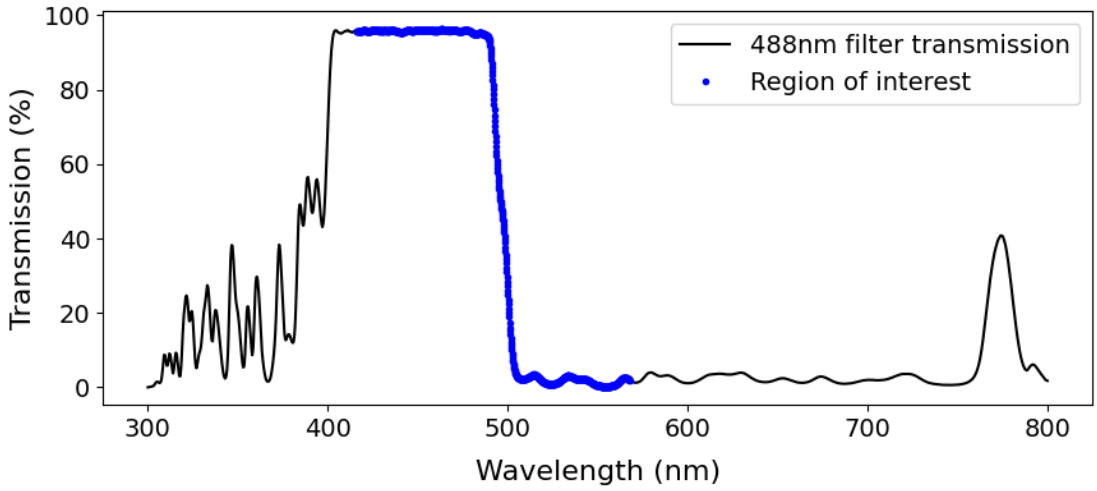


Figure 2.23. Transmission spectrum of Semrock Di01-T488 dielectric filter which cuts-off at 488 nm. Where transmission is near 0%, reflection is almost 100%. The reflected beam will be used as the second channel in this two-channel system.

The transmission of a real 488 nm dielectric filter (Semrock Di01-T488, Figure 2.23) was convolved against a simulated LED emission spectrum in the form of a Gaussian curve with centre wavelength 490 nm and FWHM of 15 nm (Figure 2.24). The result was then convolved against a high resolution NO_2 absorption spectrum to give the system's expected response to NO_2, as shown in Figure 2.24. The transmitted channel (T-channel) is larger than the reflected channel (R-channel) giving a differential signal. Figure 2.25 (b) shows the change in ratio of channels with changing NO_2 mixing ratio (0 - 500 ppb) over 1 km pathlength.

The ratio signal is almost twice as high as the two narrowband system simulated previously, showing that this broadband two channel system has improved sensitivity to NO_2. Recording a broader spectrum of light also increases the total light throughput in the system, improving the SNR. These operating wavelengths also extend further to longer wavelengths where silicon photodiodes have greater responsivity, increasing the signal magnitude and lessening the need for more sensitive and expensive detectors, such as photomultiplier tubes.

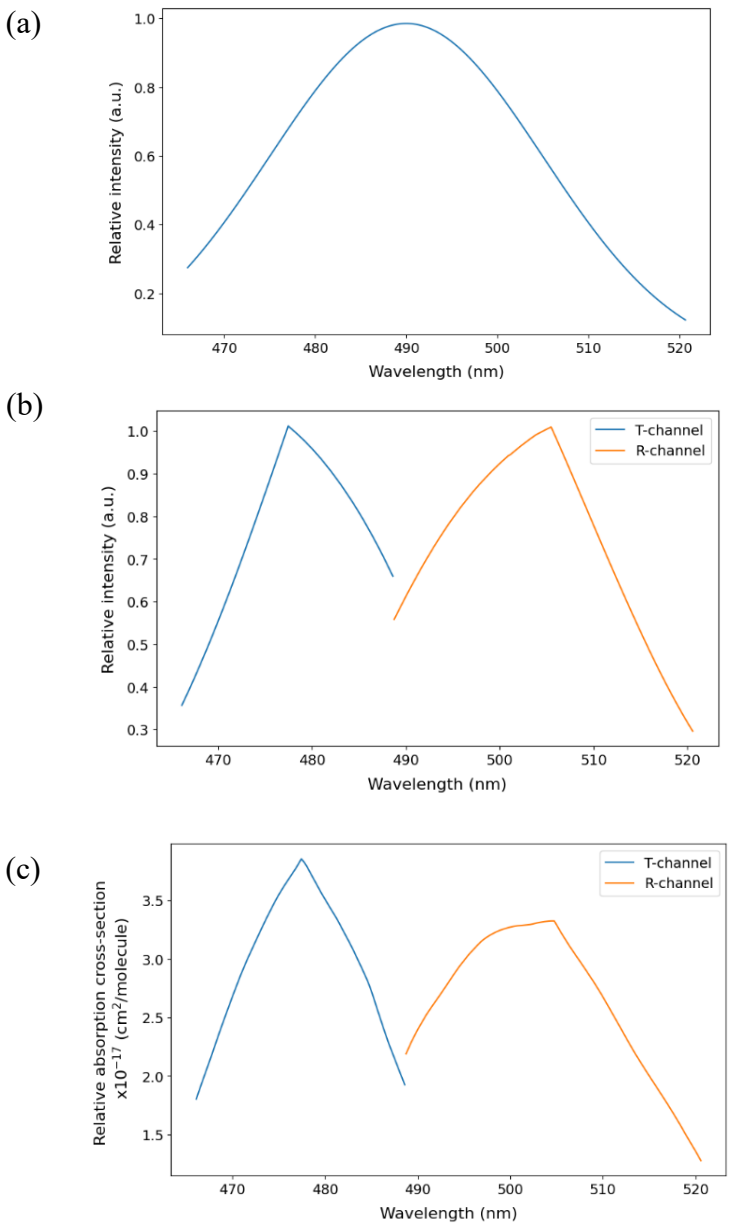


Figure 2.24 (a) Simulated LED emission outputs based on a Gaussian profile with centre wavelength 490 nm and FWHM of 15 nm. (b) Convolved filter transmission using a simulated LED centred at 490nm. The reflected (R-channel) and transmitted (T-channel) channels are shown, yielding regions of high- and low- absorption cross-sections. (c) Convolved NO_2 response using simulated LED and a cut-off filter. There is an appreciable difference in integrated cross-sections in the R- and T-channels.

Nevertheless, the proposed T-R two-channel system is vulnerable to interference from ozone absorption which has stronger absorption features in this wavelength region and is present in the troposphere in similar concentrations to NO_2. Particles would also

need to be removed from the sample as scattering effects would lead to overestimation of NO_2 concentrations due to the broad bandpass of this system.

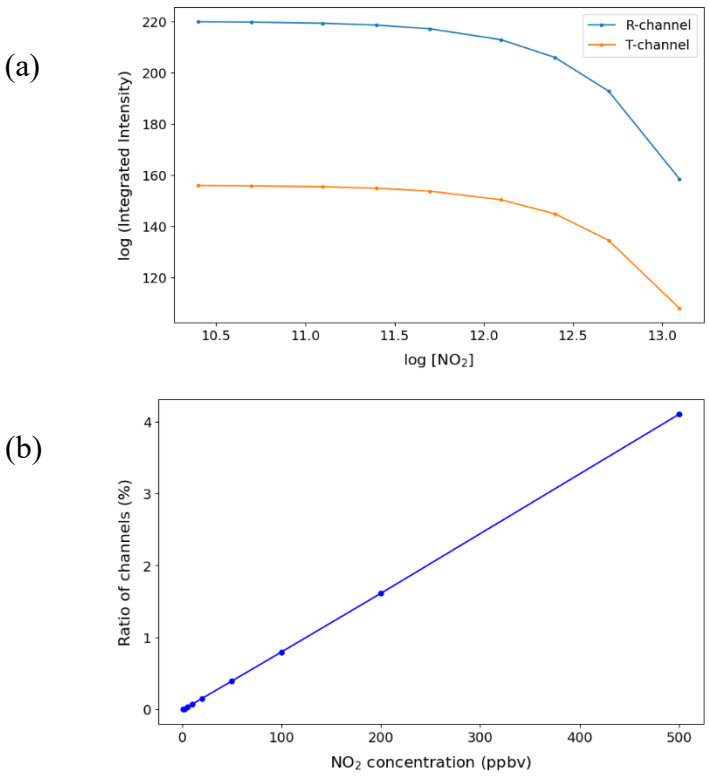


Figure 2.25. (a) Integrated intensities of R- and T-channels over a range of NO_2 mixing ratios (0 - 500 ppb) over a 1 km path length. (b) Simulated change in ratio of channels (%) for a range of NO_2 mixing ratios over 1 km path length.

Gas correlation cell

The previously discussed methods rely on optical filters to select the operating wavelengths in a two-channel system. An alternative approach is gas correlation spectroscopy in which light in one channel passes through a gas cell filled with a known amount of the target molecule, and then compared to light in a second, reference channel. A schematic of the gas correlation cell is shown in Figure 2.26. Gas correlation techniques are long-established in the infrared spectral region where they are used to quantify target species based on their rotational-vibrational spectra (Dakin et al., 1995; Davies, 1970; Noda, 2014). This approach can also be coupled with long

path remote sensing techniques like LIDAR (Thomas et al., 2012), and have been applied to the visible region for imaging high concentrations of pollutants such as NO_2 which have a strong absorption at these wavelengths (Kebabian et al., 2000; Kuhn et al., 2022).

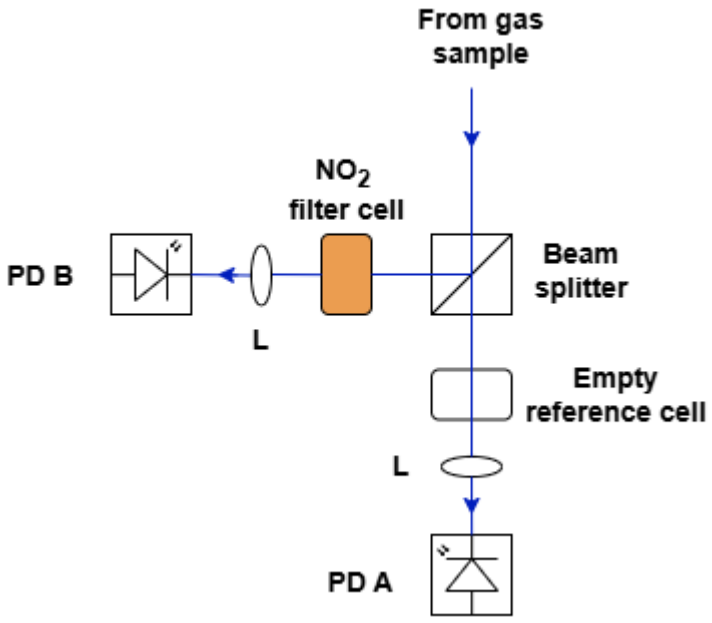


Figure 2.26. GCS detection scheme. The incoming light is split into two channels with one channel filtered by an NO_2 gas cell and the other unfiltered.

The following considers the use of a two-channel system in which a cell with NO_2 is used as a spectral filter for one channel. Figure 2.27 shows the transmission spectrum between 430 and 450 nm through a 1 cm gas cell filled with 1 ppm of NO_2 at a partial pressure of 0.5 Pa. To maximise the difference in the intensity ratio of the channel with the NO_2 gas cell and the reference channel, the optimum vapour pressure of the NO_2 filter cell must be found that gives the largest difference between the channels. Maxima and minima in the absorption spectrum are identified and the transmission at these maxima and minima are plotted over a range of partial pressures (Figure 2.27). As expected, light intensity falls off more rapidly at wavelengths where the absorption is strong compared to those where absorption is weaker.

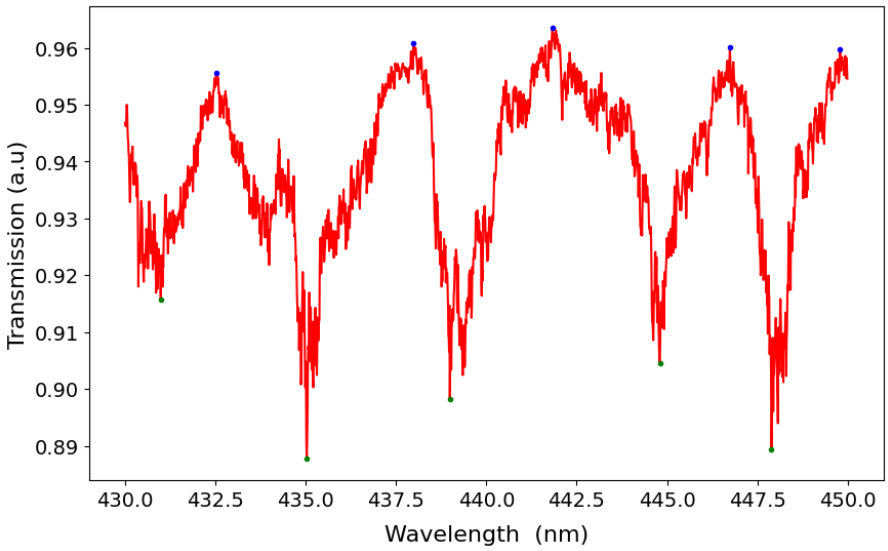


Figure 2.27. NO_2 transmission spectrum showing maximum (blue dots) and minimum (green dots) absorptions. Maximum wavelengths are 432.52, 437.99, 441.83, 446.74 and 449.79 nm and minimum wavelengths are 430.99, 435.03, 438.99, 444.8 and 447.89 nm.

There is a strong differential signal between the maximum peaks and nearby minimum peaks' transmissions, shown in Figure 2.27**Figure 2.29**, where the maximum transmission wavelengths are 432.52, 437.99, 441.83, 446.74 and 449.79 nm and the minimum transmission wavelengths are 430.99, 435.03, 438.99, 444.8 and 447.89 nm.. The maximum differential transmission varies between 0.1 and 0.4 at nearby absorption maxima and minima. The largest differential signals are observed when the partial pressure of NO_2 is in the range 6.9 – 7.6 Pa, which is the partial pressure needed to maximise the sensitivity to NO_2 in the gas correlation cell. The differential transmission varies slowly in this vapour pressure range, with the result that small fluctuations in partial pressure in the gas filter cell will not have a large effect on the differential signal. This property adds to system robustness. Absorption by NO_2 in the sample will produce a larger effect on the signal in the reference channel compared to the filter channel, since the most strongly absorbing wavelengths of the target species are attenuated in the filtered channel.

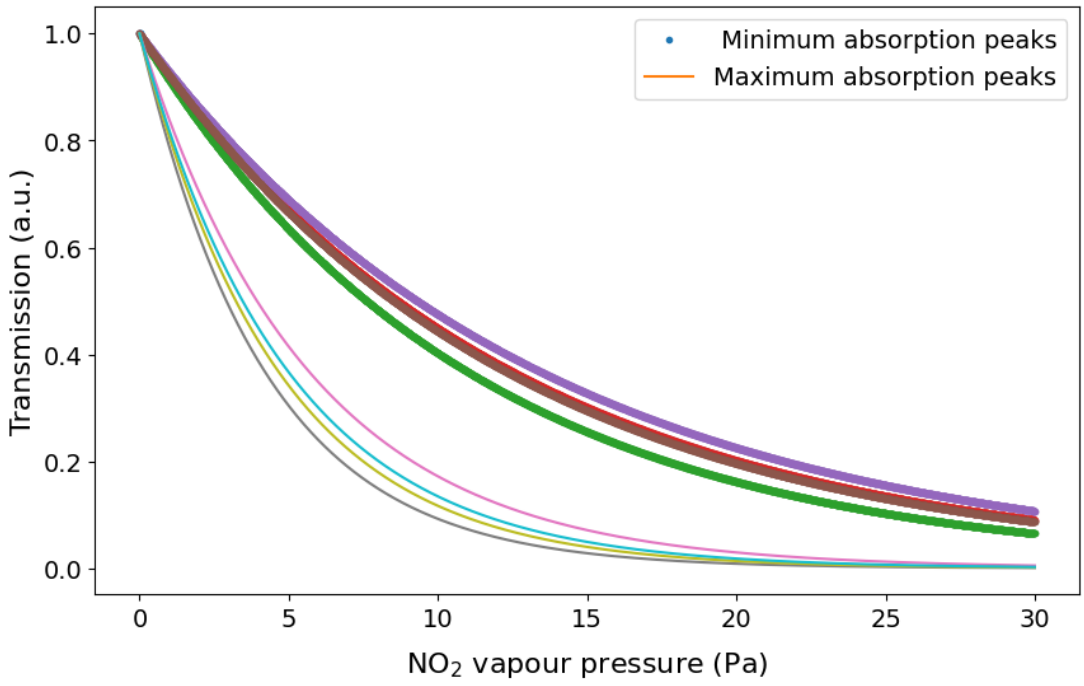


Figure 2.28. Maximum (lines) and minimum (dots/thick line) absorption wavelength transmissions for a range of vapour pressures. Transmission decreases as vapour pressure (and concentration) increases. Maximum wavelengths = 432.5, 438.0, 441.8, 446.7 nm. Minimum wavelengths = 430.99, 435.03, 438.99, 444.8 nm.

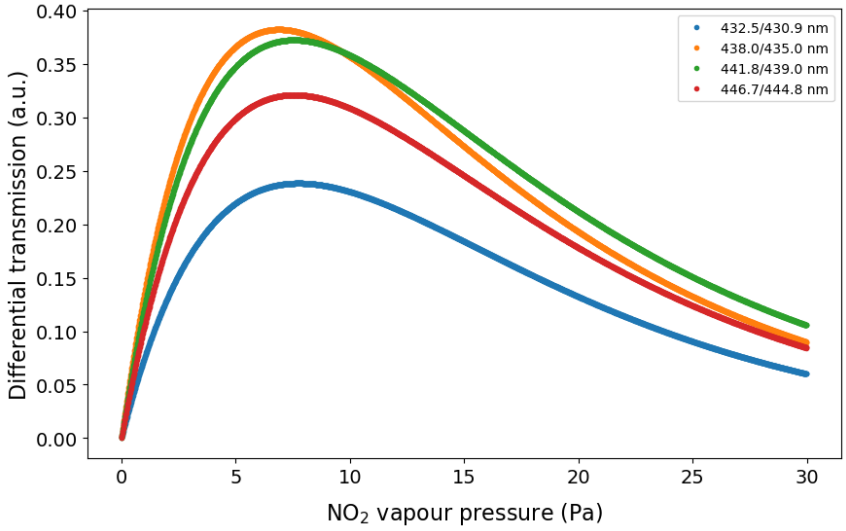


Figure 2.29. Differential transmission at nearby absorption maxima and minima at a range of NO_2 vapour pressures. The transmission maxima are relatively flat and small fluctuations in vapour pressure will not affect the differential transmission. The largest differential signal is found between 6.8 and 7.5 Pa.

The transmission spectrum of 0 – 500 ppb of NO_2 over 1 km path length through the atmosphere, with the filter cell held at 6.9 Pa, is simulated in Figure 2.30 and demonstrates a small but measurable difference in transmission (< 1.0 %) at concentrations below 100 ppb. The transmission in the gas filter channel is calculated using the Beer-Lambert relation $\left(\frac{I}{I_0} = e^{-N\sigma L}\right)$, where the number density N is dependent on the vapour pressure of the NO_2 in the filter cell. The differential signal for 200 ppb of ambient NO_2 across a 1 km pathlength is considered in Figure 2.30. The transmitted intensity through the sample gas (solid blue, Figure 2.30) is multiplied with the transmission through the 1 cm filter cell at v_p = 6.9 Pa (dashed black, Figure 2.30), resulting in the transmitted intensity through the sample gas and filter cell (dotted green, Figure 2.30). The transmission through the sample alone is shown (dashed blue, Figure 2.30), allowing the differential transmission, $\frac{T_f - T_s}{T_f}$ (dashed red, Figure 2.30), measured through the reference channel filter, to be plotted. The differential transmission provides good specificity to NO_2 as the absorption features in the filter cell intrinsically match the target gas.

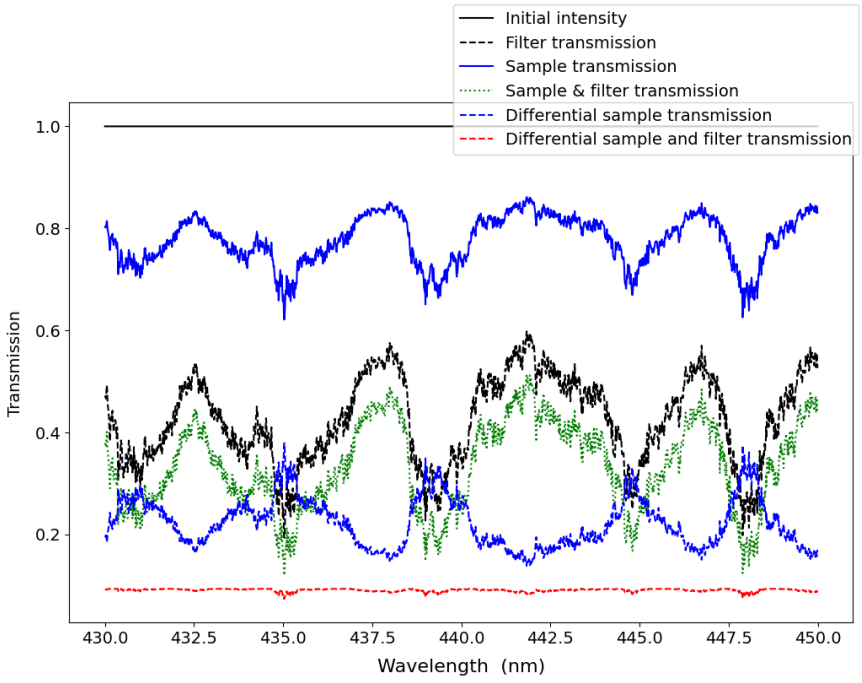


Figure 2.30. Relative transmission intensity as a function of wavelength for a GCS cell. The transmission through a sample gas (200 ppb NO_2 over 1 km, solid blue) in the reference channel is multiplied with the transmission through the filter cell (dashed black) to give the transmission through the sample gas and filter cell (dotted green). The differential signal (dashed red) through the sample and filter has low transmission but good specificity to NO_2.

A gas correlation system such as this has a wider system bandpass than that when using two narrowband filters, giving a larger amplitude signal in each channel and improving the overall system SNR. At the same time, selectivity is good since more target gas absorption features are considered than at two narrow wavelengths.

The integrated intensities of the reference and filter channel may be measured using low-cost photodetectors, such as photodiodes, rather than recording a full spectrum using grating spectrometers. The integrated intensities of the reference and filter channel were convolved with an LED (H2A1-H435) emission spectrum, centred at 435 nm (Figure 2.31) to show the difference in measured intensity in each channel and the ratiometric response.

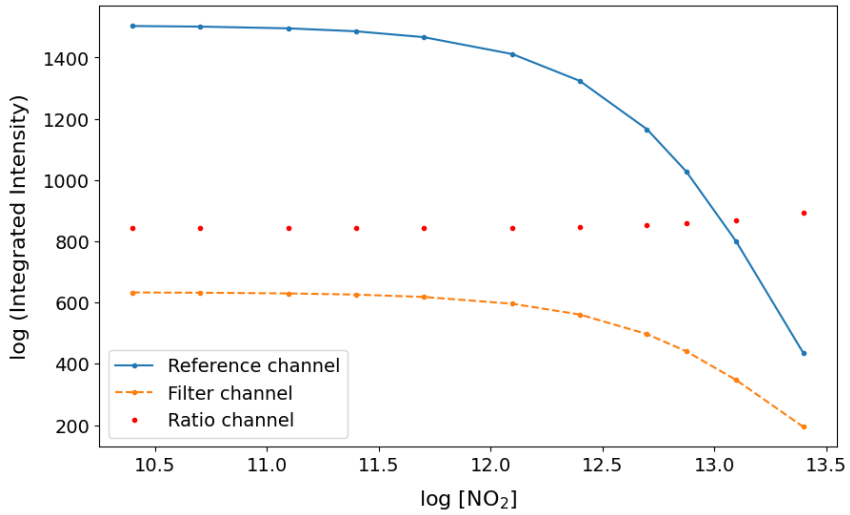


Figure 2.31. The integrated intensity of the reference (blue), filter (orange) and ratio (red) channel when using a blue LED centred at 435 nm (H2A1-H435).

There is a ~ 3.0 % change in the ratio of the reference and filter channel for concentrations up to 500 ppb for a pathlength of 1 km (Figure 2.32). Although the absolute measured signal is larger than with two narrowband filters, the same type of signal processing would be required to extract small differences in absorption. The system shows good selectivity to NO_2 with a small positive effect from glyoxal and a small negative effect from methylglyoxal which would respectively produce a positive or negative interference in measuring NO_2. Using a gas filter cell increases the system

specificity, but the NO_2 concentration within the filter cell must be kept constant and could be susceptible to losses to cell walls and leakage.

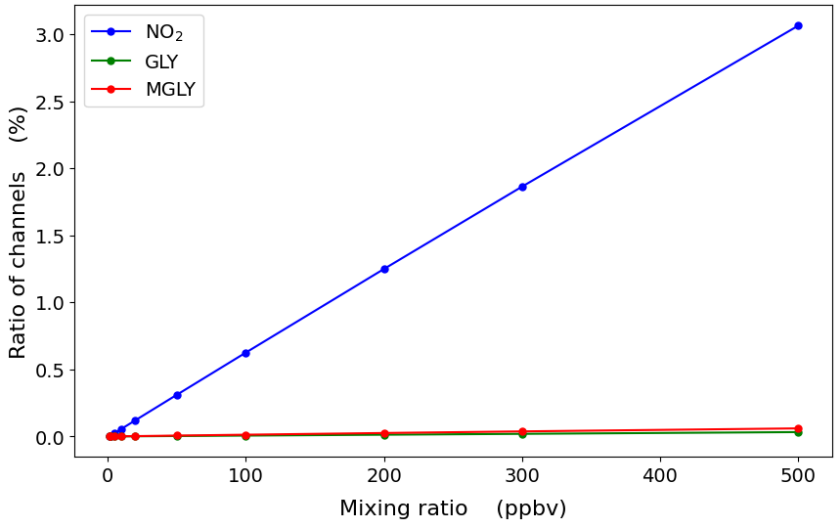


Figure 2.32. The ratiometric response over 1 km of the reference and filter channel for NO_2, glyoxal, (GLY) and methylglyoxal (MGLY).

Although this method offers good selectivity, increased light throughput and improved SNR, requiring a filled gas cell with controlled temperature and pressure adds to the complexity and cost of the system.

Summary of simulated methods

The methods described and simulated in this chapter consider strategies to monitor NO_2 in urban and traffic microenvironments. NO_2 is the dominant gaseous absorber at blue wavelengths under these conditions, which opens the door to simplified and cost-effective absorption measurement strategies using one or two spectral channels. Methods are proposed that use two spectral channels with a single LED light source, providing potential common-mode noise rejection for ambient measurements. A single-channel system was put forward that would increase the signal amplitude, signal-to-noise ratio and therefore system sensitivity.

The simulations shows that two spectrally distinct channels produce different signals and that the ratio of these channels is linearly related to the concentration of NO_2 in the sample. Two narrowband channels targeting strong and weak absorption wavelengths, or a gas cell with an optimised concentration of the target gas, provide the best selectivity to NO_2 in the presence of other absorbing gases. This selectivity is achieved because the measured changes in absorption are matched exactly to narrowband NO_2 absorption features. A T-R method using a dielectric pass filter to separate the light into two larger spectral ranges, with one channel transmitted through the filter and the other reflected, was also considered. The T-R method integrates across a wider wavelength range and still shows good selectivity to NO_2 because the T- and R-channels have a high differential response to NO_2. However, this system is susceptible to interference from O_3 which has stronger absorption in this wavelength region and is present at ground level in similar concentrations as NO_2. Aerosols will interfere strongly with the T-R method due to the broad bandpass of the system and it would be necessary to filter out particles from the sampled air. This system is therefore not suited to open path measurements.

For some measurement situations, such as urban environments, absorption by NO_2 (the product of its absorption cross-sections and number density) is expected to be one to two orders of magnitude greater than the absorption from glyoxal and methylglyoxal. However, this single-channel method does not inherently have good selectivity to spectral features. The aerosol-filtered single channel wideband pass method requires a filter to remove particles from the inlet stream. It may also be necessary to scrub NO_2 from the sampled air periodically in order to get a zero-NO_2 measurement, as was done by Bailey et al. (2024), who used activated charcoal to remove NO_2.

The simulations here do not consider the practical issues of drifts in the outputs of the LED or detection system, or incomplete filtering of particulate matter. In practical applications, a ‘zero-air’ reference line that is scrubbed of NO_2 is often used to compensate for drifts in the system baseline intensity. Active temperature and current control may be needed to stabilise LED outputs, adding to system complexity and cost. Use of two spectrally distinct channels and a single LED has the advantage that a ‘zero-air’ reference should not be needed, assuming that fluctuations in the LED output or atmospheric transmission (apart from absorption by the target species) are

equally reflected in both channels. In these cases, the ratio of the two channels is expected to be highly stable.

The GCS method is attractive due to its intrinsic selectivity and improved light throughput compared to the use of two narrow wavelength channels. However, the concentration of NO_2 in the filter gas cell must be held constant, meaning that a stable temperature and vapour pressure is required. A sealed NO_2 cell could be used if the NO_2 concentration in the cell remained stable for many months.

A drawback of the two-narrowband method is that only a small portion of low light intensities are expected since the narrow bandpass filter removes most of the LED emission spectrum, leaving only two quasi-monochromatic wavelengths. These relatively weak signals must be amplified appropriately. The strategy of the T-R method is to compensate for these low intensities, integrating across many wavelengths and giving a larger measured signal and improved sensitivity. In our simulations with a wavelength split at 490 - 500 nm, the differential absorption cross-section was quite large which yields a larger change in ratio than was seen with the narrow two-channel method. However, this method is not very selective to NO_2 absorption features and is vulnerable to interference from O_3 and aerosols.

As an alternative to the two channel approaches, the single channel wideband pass method covers a wider spectral range and a larger signal is collected by the photodetector, resulting in an increased sensitivity. Here, selectivity relies on a particle filter removing particulate matter from the sample stream (Zhou et al., 2022). Decreasing the path length will increase the upper concentration limit but will reduce the overall sensitivity. This relation is true for all methods simulated here and must be considered when optimising systems for applications in specific environments.

Chapter 3 Characterisation of system components

3.1 Introduction

The optical components, light source and photodetector are essential components of a two-channel ratiometric detector. This chapter focuses on characterising these elements as part of the development of simplified spectrometers for fast, sensitive and selective measurements of NO_2 in an urban traffic environment, where concentrations of this pollutant are expected to dominate the absorption signal of the sample air. Two main spectrometer configurations are considered here: a two channel, narrowband spectrometer and a single channel, wide bandpass system.

In the two channel approach, wavelengths of high and low NO_2 absorption must be selected which have a relatively large difference in absorption cross-section (Volten et al., 2009). This differential absorption is therefore similar to the detection principle used in DIAL. In our approach, operating wavelengths, λ_1 and λ_2, are chosen by rotating narrow bandpass filters to select quasi-monochromatic wavelengths from an LED emission. The stability of the ratio of intensities of the wavelength pair in the presence of simulated fluctuations from the LED power supply or changes in the light path is explored in this chapter. Optical signals propagating through the atmosphere are susceptible to interference from variations in atmospheric optics such as atmospheric transparency, turbidity polarisation (Rozenberg, 2012), scintillation, refractive turbulence and changes in meteorological parameters like wind and temperature which are particularly important over long distances (Averbuch et al., 2022; Shaik, 1988).

The optical configuration of the detection scheme is also considered. To minimise the optical components needed, the two-channel system was first designed using a single narrow bandpass filter to select both operating wavelengths. However, this

configuration was revised to improve light throughput and reduce the complexity of optical alignment by introducing a second narrow bandpass filter.

A drawback of the two-channel ratiometric method is the low levels of light collected by non-dispersive photodetectors following the narrowband filter. Photodiodes and photomultiplier tubes are considered for the detection scheme and appropriate signal amplification techniques are discussed. Recent development of a low cost open-source lock-in amplifier (OLIA) by Harvie and De Mello (2022) and its applicability to a two-channel ratiometric system is discussed.

To increase light throughput in the system and improve the overall system sensitivity, a wideband single-channel CEAS instrument is also characterised. This system has inherently better sensitivity than the ratiometric two-channel method owing to the large, measured signal. However, this instrument has lower spectroscopic selectivity to NO_2 and could be vulnerable to spectral interferences in the operating wavelength region under some circumstances. Applications for the single- and two-channel method presented here will be discussed as well as the advantages and limitations of each.

3.2 Characterisation of instrument components

Optical components and spectral selection

The narrow two-channel system uses a narrow bandpass filter (Semrock, LL01-442-12.5) with a FWHM transmission band of 1.7 nm to select high and low absorbing operating wavelengths, described in Section 2.2. The narrow bandpass filter (nBPF) is mounted on a rotational stand. As the angle of the nBPF increases, the resulting transmitted wavelength of light decreases because of the relationship between angle of incidence and centre wavelength of transmission of a dielectric filter, as discussed in Section 2.1. Figure 3.1 shows the intensity spectrum of the LED along with the light transmitted through the nBPF at specific angles. The general shape of the LED spectrum is seen as the intensity of the signal changes with wavelength. Transmission

at larger angles falls off more rapidly, likely because the edge of the optic holder clipped the beam and the LED emission decreases and tapers off at these wavelengths. The angle dependence of the transmitted light indicates that this nBPF can be used for wavelength selection instead of a dispersive optical element like a grating or prism.

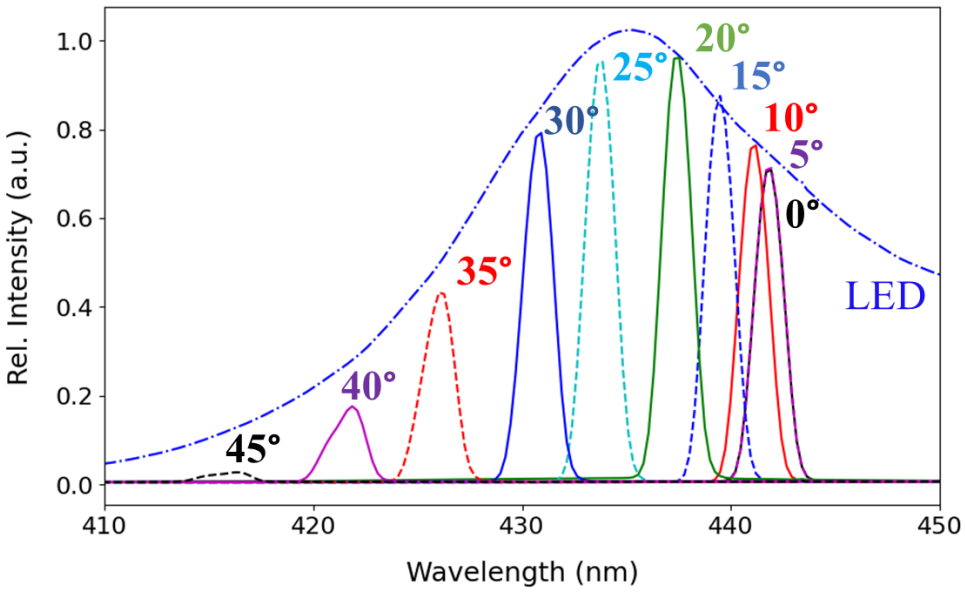


Figure 3.1. Spectral dependence of the narrow bandpass filter transmission bands on incident angle. The LED intensity spectrum (blue dash dot) is overlayed. The transmission at 0° and 5° are overlapped.

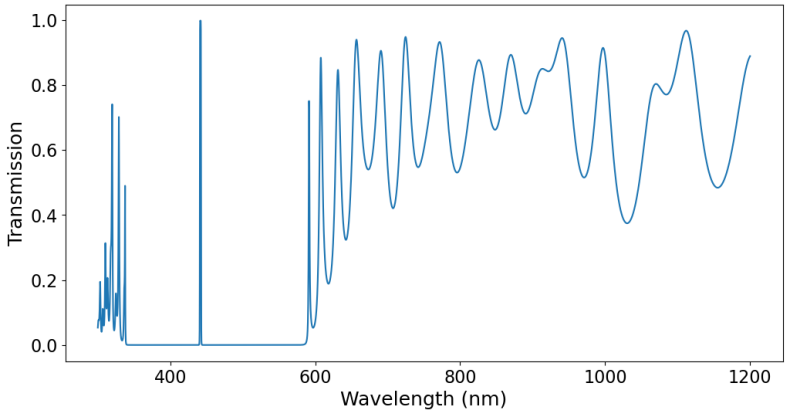


Figure 3.2. Manufacturer's spectrum of the full transmission of the nBPF showing light transmitted <300nm and >600nm.

It is noted from the above figure that the width of the nBPF transmission band varies as θ increases. Each band was fitted to a Gaussian curve and the resulting width (B) and centre of each curve was plotted against θ, the angle of incidence to the filter. These bandwidths were then fitted to a 5th order polynomial in Python to quantify this variation with angle (in units of degrees):

$$B(\theta) = 8.3 \times 10^{-9}\boldsymbol{\theta^5} - 3.9 \times 10^{-7}\boldsymbol{\theta^4} + 5.0 \times 10^{-6}\boldsymbol{\theta^3} + 3.9 \times 10^{-5}\boldsymbol{\theta^2} - 1.0 \times 10^{-3}\boldsymbol{\theta} + 0.68 \quad (3.1)$$

The transmission bandwidth varies relatively slowly for small angles ($\theta < 25°$) with an average bandwidth of 1.35 nm. The bandwidth of the nBPF is approximately constant for small angles of incidence.

The centre wavelength (λ_{cen}) also varies with θ and was fitted to a 3rd order polynomial:

$$\lambda_{cen}(\theta) = 9.40 \times 10^{-5}\boldsymbol{\theta^3} - 1.93 \times 10^{-2}\boldsymbol{\theta^2} + 0.116\boldsymbol{\theta} + 441.8 \quad (3.2)$$

Using this relationship, the required angle of the nBPF for an arbitrary wavelength can be found.

The spectral resolution of the detection system is limited by the bandwidth of the filter. To demonstrate that the nBPF is sufficient to acquire a recognisable absorption spectrum of NO_2, the intensity spectrum of the LED (Roithner, H2A1-H435) was mapped by slowly rotating the nBPF to capture the intensity at each wavelength. A 15 cm gas cell with ½ inch diameter was placed in the beam path. Intensity spectra were recorded using a CCD spectrometer with a cycle time of 1.01s. The area under the peak transmission was integrated to reproduce the response of a non-dispersive photodetector.

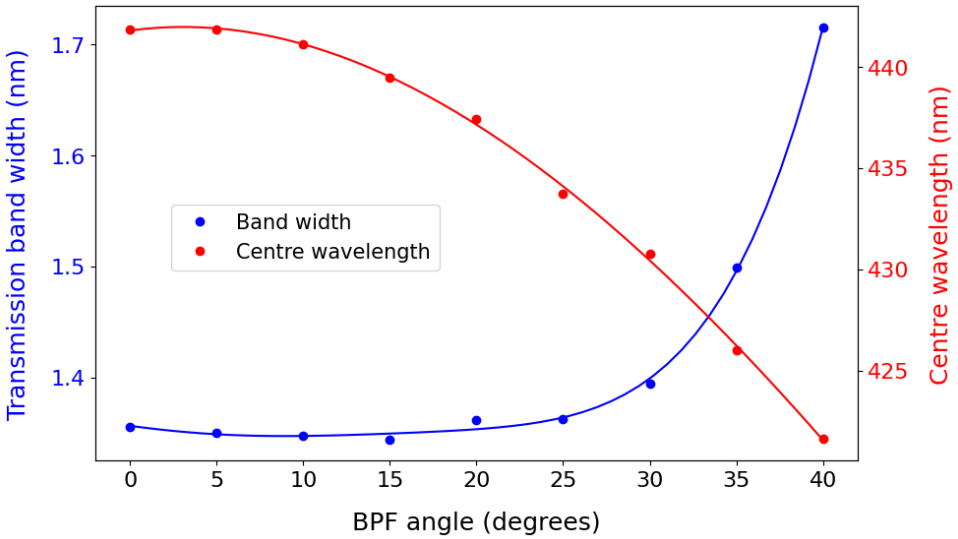


Figure 3.3. Wavelength dependence of the centre wavelength (red dots) and the band width (blue dots) of a Semrock (LL01-442-12.5) narrow bandpass filter. The centre wavelength and width were estimated from Gaussian fits of the measured transmission spectrum at different angles. The solid lines are best fits of a 5th order polynomial function (blue line) and 3rd order polynomial function (red line) to the respective spectral parameters.

This method was then repeated with 1 mL of NO_2 in the sealed gas cell to record a second intensity spectrum. Both intensity spectra are shown in Figure 3.4 as a function of time and in Figure 3.5 as a function of wavelength. The peak LED intensity through the nBPF was observed at 50 s when the angle of incidence produced the centre wavelength of the LED.

The noise to the long wavelength end of the LED spectrum in Figure 3.5 arose because the filter was stationary for several scans at the start of the experiment before the nBPF was rotated. These scans were omitted from the time series to synchronise the timing of both experiments. In the absence of NO_2 absorption, the shape of the LED emission is clearly seen in this mapped spectrum. For the spectrum with NO_2, the strong and weak absorption features of NO_2 are also apparent.

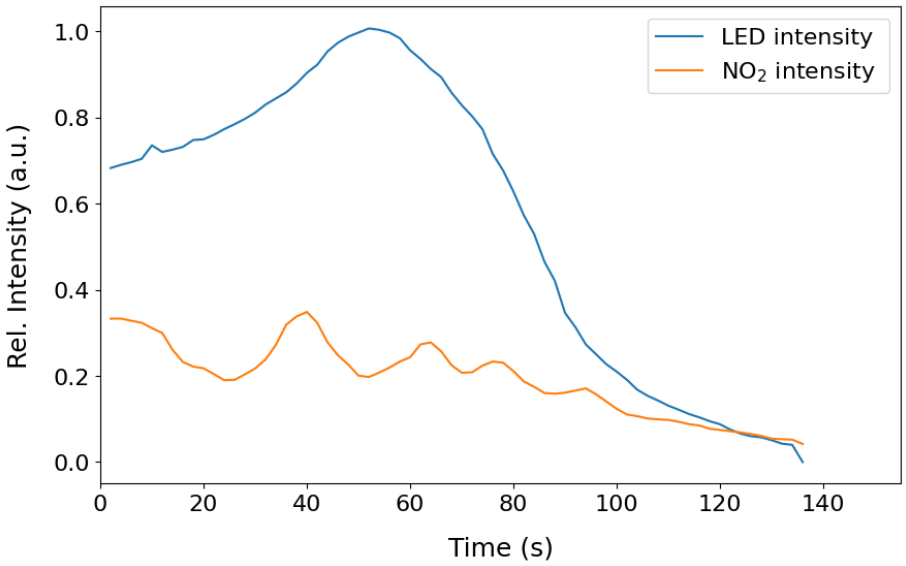


Figure 3.4. Time response of the LED intensity transmitted through the empty gas cell and a gas celled filled with a high concentration of NO_2 while slowly increasing the angle of incidence of light entering the narrow bandpass filter. The peak of the LED intensity was reached at 50 s where the angle of incidence produced the centre wavelength of the LED.

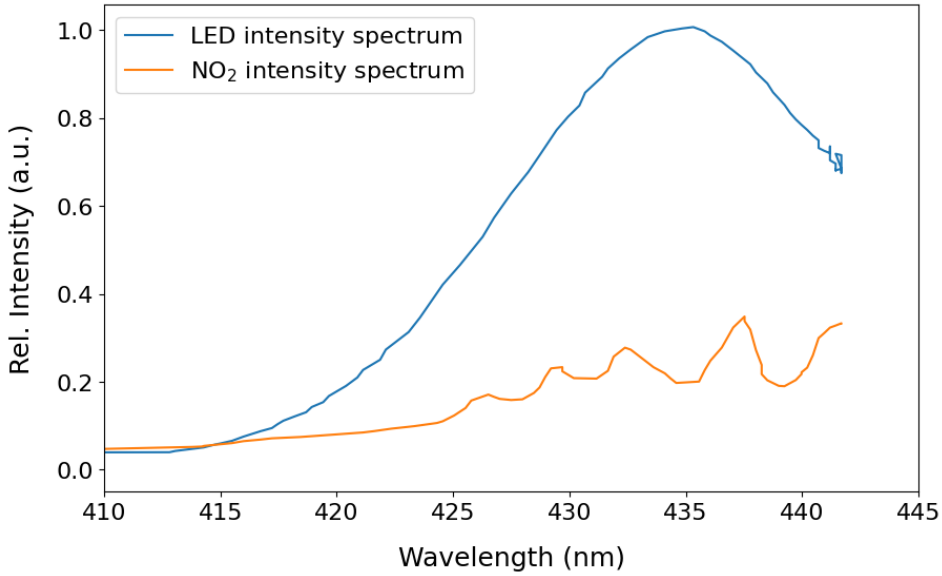


Figure 3.5. Intensity spectra of the LED obtained by slowly rotating the band pass filter with the gas cell filled with air (blue). The orange spectrum is the measurement when the gas cell had been filled with NO_2.

The absorbance, A, of a sample can be found by:

$$A = \log\left(\frac{I_0}{I}\right) \tag{3.3}$$

where I_0 is the intensity without the sample and I is the intensity with the sample NO_2 in the gas cell. The mapped absorption spectrum for NO_2 was compared to the literature absorption spectrum reported by Coquart et al. (1995) which has a spectral resolution of 0.01nm (Figure 3.6). Although the mapped absorption spectrum measured here had a much lower resolution than the Coquart spectrum, the NO_2 absorption structure is clearly seen. Large differences in absorption are most apparent between 430 and 440 nm. The bandwidth of the nBPF is not constant and increases substantially below 430 nm ($\theta_i > 30°$, Figure 3.3), smoothing out much of the structure in the NO_2 absorption spectrum at shorter wavelengths.

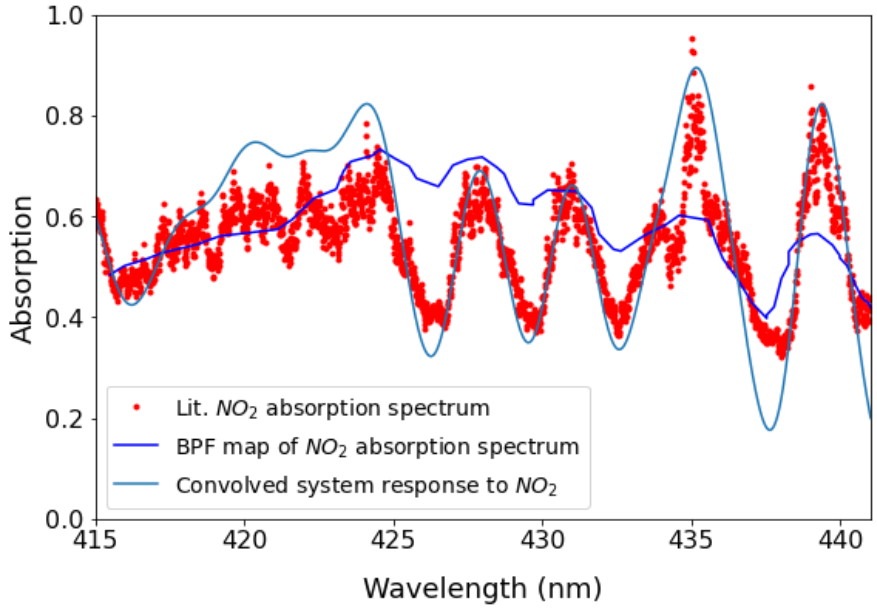


Figure 3.6. NO_2 absorption spectrum based on intensity spectra compared to literature NO_2 absorption spectrum of Coquart et al. (1995).

These results show that the narrow two-channel approach using this particular filter is suited to the region from 430 to 440 nm, where considerable differences in absorption wavelengths occur at nearby wavelengths. A narrow two-channel approach can also

be applied to other wavelength regions, which were considered in Chapter 2, provided that suitable nBPFs are available.

Light source characterisation

Variations in light source stability and atmospheric transmission

This work uses LEDs as light sources for absorption spectroscopy measurements. LEDs are a useful tool for absorption measurements as they have an emission spectrum of tens of nanometres. This bandwidth is wide enough to cover distinct spectral features of the target molecule and is more convenient than extremely broad white light sources like arc lamps, which require extensive filtering, consideration of optical safety, and only use a tiny fraction of the optical power for measurement (Venables et al., 2006). Blue LEDs produce a high spectral radiance (mW mm^{-2} sr^{-1} nm^{-1}) from a small emission area, allowing efficient imaging of optical power through an optical system. The output of LEDs is not as directional as lasers and must be collimated to reduce beam divergence and optical losses. While lasers produce outstandingly high spectral radiance, LEDs are safer to operate than lasers and are available at a fraction of the cost. An important advantage of LEDs for reducing the influence of light source variations and changes in atmospheric transmission is that changes in the emission intensity are expected to vary consistently across the output spectrum. The work below explores the potential of LEDs for effective common mode noise rejection by investigating the correlation between two wavelengths as the light source intensity is strongly diminished.

The optical system comprised a blue LED (Roithner, H2A1-H435, 300 mW, viewing angle = ±75°) with a peak intensity at 435 nm, two polarisers (Thorlabs, Dichroic Film Visible Light Polariser LPVISE2X2), and a CCD spectrograph (Andor iDUS DV-420A-BU camera and SR-163 spectrometer). Light is collimated by a focusing lens (f = 150 mm) and coupled into the spectrometer by a fibre optic. The optical system is shown in Figure 3.7 To study the relationship between two closely spaced wavelengths, the polariser closest to the LED was held in a rotation mount while the following polariser had a fixed orientation and output polarisation. Rotating the first polariser therefore varied the intensity of the transmitted spectrum across a wide

intensity range with small changes in polarisation. The change in ratio of these intensities was monitored to establish the stability of the narrow two-channel method under simulated changes in LED intensity fluctuations, drifts in the alignment of the optical system, and fluctuations in the atmosphere that effect sample transmission. These sorts of changes should have a weak spectral dependence, and two closely spaced wavelengths will therefore be equally affected.

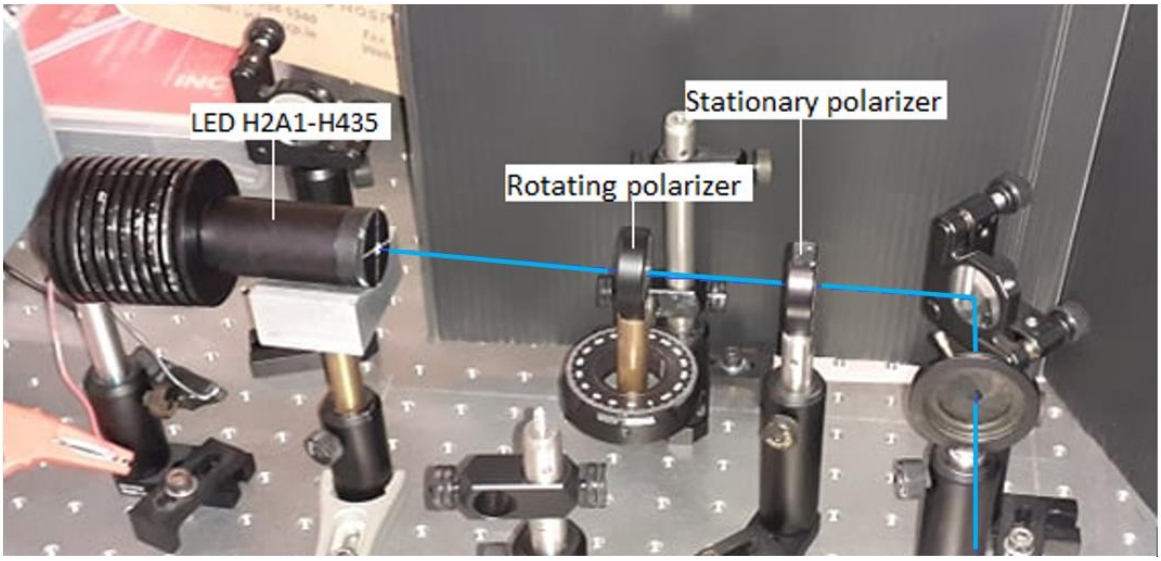


Figure 3.7. Experimental set-up of light source with polarisers to simulate beam path instabilities and light intensity fluctuations. The beam path is shown in blue. The first polariser is on a rotational mount so that its angle and polarisation can be changed relative to the second, static polariser. In this image, the angle of incidence of the first polarizer is rotated around the vertical axis (y); a second configuration is with the polarizer mounted horizontally and rotated around the horizontal axis (x).

The transmitted LED intensity through a nBPF was recorded by a CCD spectrograph such that both operating wavelengths, $\lambda_1 = 435$ nm and $\lambda_2 = 438$ nm, could be observed at once. The first polariser was on a rotational stand to allow the angle of the polariser to be changed continuously over 100 scans. The second polariser was placed just after the first and kept stationary. The rotating polarizer was rotated along the x-direction, parallel to the ground, in the positive and negative direction. The polariser was then repositioned so that it could be rotated along the y-direction, normal with the ground, in the positive and negative direction. This simulated instabilities in the light path by

shifting the beam position, owing to the refractive index of the polariser, as well as small changes in polarisation angle. To investigate the effect of these instabilities on the ratio of the signals, the relative intensity of λ_1 was plotted against that of λ_2.

Figure 3.8 shows the relationship between intensities at 435 nm and 438 nm as the polariser is rotated in different directions, and the correlation statistics are summarised in Table 3.1. The intensities remain highly linear when the polariser is rotated on the x- and y-direction, with $R^2 > 0.997$, a slope of approximately 1, and an intercept near 0 for each of the four different rotations. Small deviations from the 1:1 line likely arose from slight beam path differences as the first polariser was rotated in each direction.

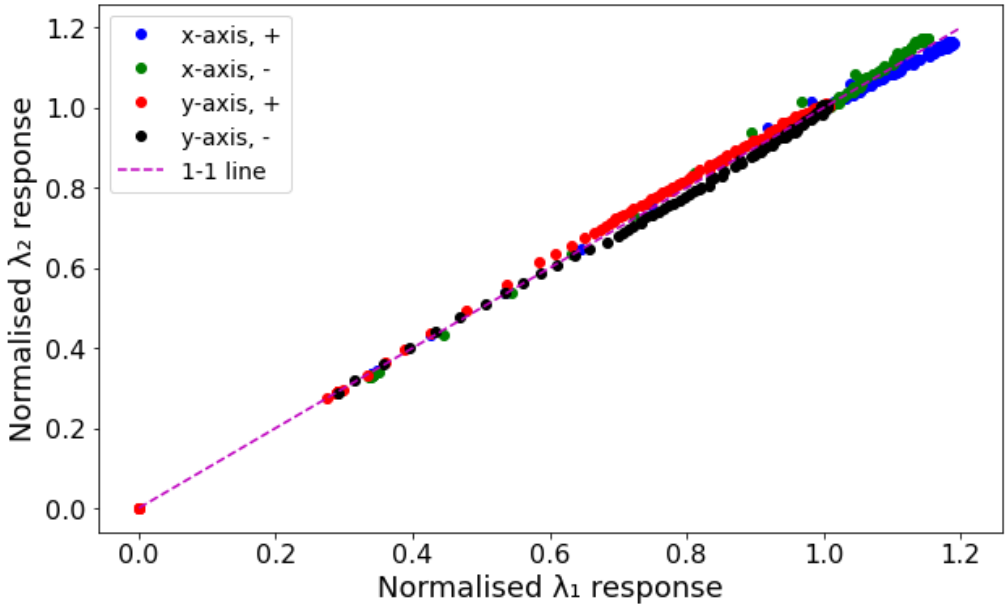


Figure 3.8. Correlation of the normalised intensity at λ_1 = 435 nm against that at λ_2 = 438 nm. The transmitted intensity is altered by rotating the first polarizer around the vertical (y) and horizontal (x) axes while the second polariser remains stationary. Positive and negative signs indicate the two directions of rotation from normal incidence of 0°.

Fluctuations in the light source intensity that are spectrally flat and vary slowly with wavelength will be compensated for by using a ratiometric two-channel method. The stability of the narrow two-channel response when considering intensity fluctuations due to beam path divergence and polarisation in the atmosphere shows the potential to use this method for remote field measurements in the open atmosphere. Optical

variations in the atmosphere such as scintillation and refractive turbulence which distort the phase of the beam will affect both wavelength channels equally as they vary slowly over wavelength. Choosing operating wavelengths that are spectrally close is therefore an important consideration to reduce the effects of optical fluctuations on the measured signal.

Table 3.1. Linear fit characteristics of the relationship between the intensities at 435 nm and 438 nm when the beam path and transmitted intensity is varied by a rotating polariser.

Rotation direction	R^2	Slope	Intercept
x-axis, +	0.9978	0.983	0.0097
x-axis, -	0.9989	1.028	-0.0189
y-axis, +	0.9990	1.016	0.0018
y-axis, -	0.9976	0.998	-0.0068

Power supply stability and spectral output

Variations in the supply voltage affect both the total intensity and the emission spectra of LEDs (Dasgupta et al., 2003; Moe et al., 2005; Ravindran et al., 2020). Such spectral changes would alter the ratio of light at different wavelengths. To assess the effect of small fluctuations in the LED supply voltage on the intensity ratio, the LED emission spectrum was monitored as the supply voltage was changed incrementally. An LED (Roithner H2A1-H435, 300 mW, viewing angle = ±75°) with a passive heat sink was used for the measurements. Active LED temperature control was not used in this experiment.

Figure 3.9 shows the shift in the LED spectrum along the wavelength axis. Between 3.0 V and 3.4 V the emission peak moves to shorter wavelengths. Above 3.4 V, the peak wavelength is relatively stable, although the width of the emission band continues to increase. Figure 3.10 shows the influence of voltage on the intensity ratio, $\frac{I(\lambda_1)}{I(\lambda_2)}$, at the operating wavelengths λ_1 = 437.3 nm and λ_2 = 439.4 nm. The dependence of the

intensity ratio on voltage (V) was well-described by a 2nd order polynomial (Figure 3.10).

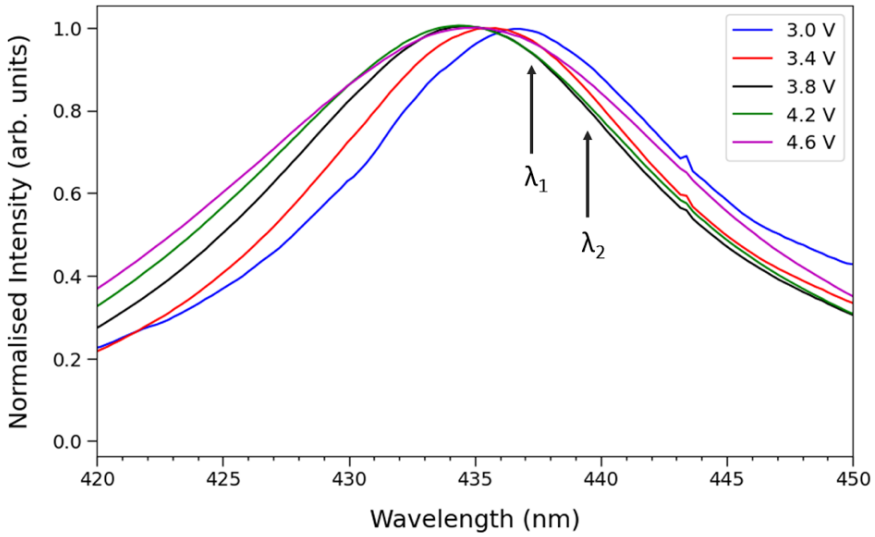


Figure 3.9. Normalised LED emission spectrum at several supply voltages. A spectral shift to shorter wavelengths is seen as the voltage increases along with an increase in the width of the emission band. λ_1 = 437.3 nm and λ_2 = 439.4 nm are the wavelengths of interest in this analysis.

Typical voltage supply stability of ± 2mV is readily achievable according to the manufacturer (AIM-TTi Instruments, 2024). Applying these sort of voltage changes produces a negligible effect on the fractional change in intensities, implying that a high performance voltage source and precise voltage control is not needed for a sensor based on measuring the intensity ratio, reducing both cost and complexity of the system.

Further immunity of the intensity ratio could be secured by driving the LED at the voltage giving the maximum in the intensity ratio where the signal varies slowly. A further strategy to stabilise the intensity ratio across a wider range of supply voltages could be achieved by selecting wavelengths away from the emission maximum; this is examined for wavelengths pairs 430.0 nm and 432.0 nm and 440.0 nm and 442.0 nm on either side of the emission peak (Figure 3.10). The ratio of intensities is most stable when λ_1 = 430 nm and λ_2 = 432 nm, however, the differential NO_2 absorption

cross-section is 40 % smaller here than with wavelength pairs above 435 nm. The longer wavelength side of the LED emission peak broadens at higher voltages so the fractional change in intensities is less stable at 440 nm and 442 nm. When choosing narrow two-channel operating wavelengths, both channels should be positioned on the slope of the peak, near the peak maximum emission, to counteract the effect of spectral drifts in light source.

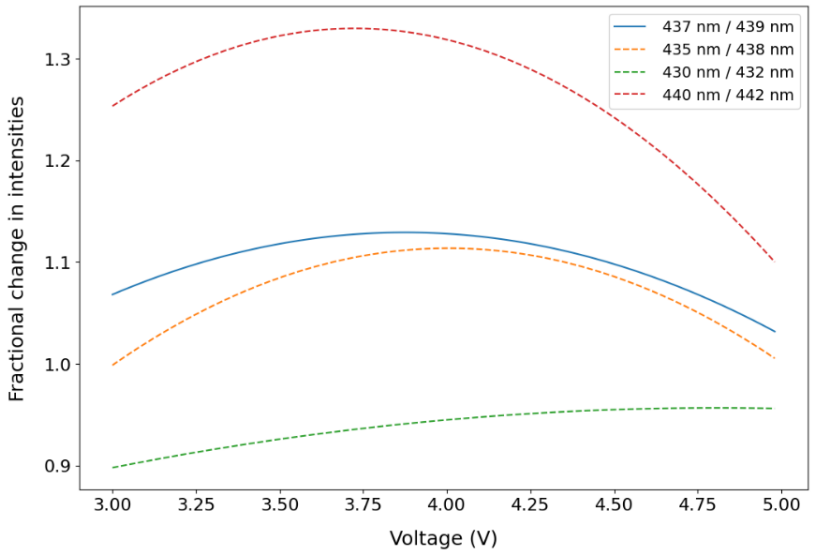


Figure 3.10. Fractional change of the ratio of intensities at four wavelength pairs as a function of voltage; 437 and 439 nm, 435 and 438 nm, 430 and 432nm, and 440 and 442 nm. Experimental data were fitted to a 2nd order polynomial function.

3.3 Spectral considerations in using nondispersive detectors with optical cavities

When using non-dispersive detectors, spectral interferences are an important consideration since all wavelengths incident on the detector contribute to the output signal, weighted by the responsivity curve of the photodetector. Optical cavities act as highly effective band rejection filters since wavelengths within a specific range are effectively rejected and reflected back and forth many times within the cavity, resulting in a small signal output, while wavelengths outside this range are transmitted

highly efficiently and could be a serious interference on a photodetector. To take advantage of the long effective pathlength of an optical cavity, photons of the rejected wavelengths are measured, so optical filtering is required for the out-of-band wavelengths. Similar issues have been encountered in IBBCEAS systems using arc lamps which have extremely broad emission spectra and require careful filtering, as discussed by Venables et al. (2006).

In addition to optical filtering, photodetector selection can also reduce the effect of interference from out-of-band wavelengths. This section considers the spectral responsivity of photodiodes and photomultiplier tubes in the context of NO_2 detection near 440 nm. Lock-in amplification is considered to increase the small optical cavity output signal and discriminate between the modulated signal of interest and background light. A suitable modulation frequency must be chosen that is not near the frequency of stray light that is incident on the photodetector.

Experimental description

A cavity-enhanced system was built with mirrors of high reflectivity (HR = 99.98%) between 400 and 450 nm and two narrowband channels were selected using a single nBPF, shown in Figure 3.11. Two identical photodiodes (Thorlabs, DET10A) were used to collect the signals through the nBPFs. A flip mirror was placed after the nBPF in channel A and directed incoming light to a fibre to analyse the spectral response of the system with a spectrometer (Andor, SR163) and CCD camera (Andor, iDUS DV420A-BV). The purpose of this system was to test the capability of measuring narrowband wavelength intensities through an optical cavity using non-dispersive detectors, with an option to observe the full spectral response to investigate spectral interferences.

The photodiode signals were amplified using a benchtop lock-in amplifier (Stanford Research Systems, SR830), however, both channels could not be amplified simultaneously as the lock-in amplifier only outputs channel A and A-B, without outputting solely the amplified B channel. For the purpose of testing the feasibility of using non-dispersive detection with narrowband wavelength channels, only channel A of the lock-in amplifier was used in the following section. A signal generator (TG2000

series, 20MHz DDS Function Generator) provided a reference modulation frequency of 500 Hz for the lock-in amplifier and modulated the LED at the same frequency.

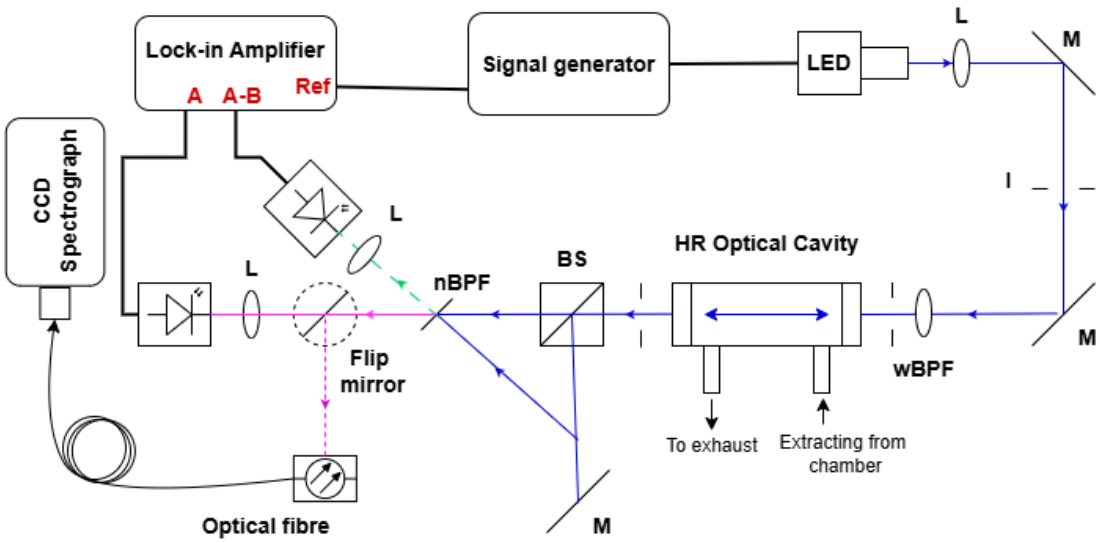


Figure 3.11. Schematic of optical cavity system using non-dispersive detectors (photodiodes) amplified with a lock-in amplifier. A flip mirror was placed after the beam was split so that one channel was directed to a fibre optic to analyse the spectral response and identify spectral interferences. A signal generator provided a reference frequency of 500 Hz for the lock-in amplifier and drove the LED at the same frequency. nBPF = narrow bandpass filter, BS = beam splitter, wBPF = wide bandpass filter, M = turning mirror, L = lens, I = iris.

Influence of lock-in amplification parameters

The lock-in amplifier parameters can be optimised for highly sensitive measurements down to 2 nV. The time constant, τ, dictates the response time of the system as the signal typically takes 3τ to reflect voltage changes. Longer time constants smooth out system noise and improves signal stability and signal-to-noise ratio (Stanford Research Systems, 1993). Varying the modulation frequency can move the system away from low- or high-frequency interferences that are surrounding the optical system.

To optimise the photodiode and lock-in amplifier response, the time constant was varied to observe the effect on response time and signal stability, as seen in Figure 3.12, where $\tau = 3$, 10, 30 s. The LED emission was blocked for 300 s and then opened so that an optical signal of 8 μV was measured by the photodiode and amplified by the lock-in amplifier. As the time constant increased, oscillations seen in the signal smoothed out, improving the signal-to-noise ratio of the measurement. However, the response time of the system is also slower as the time constant increases, reaching up to 90 s when $\tau = 30$ s.

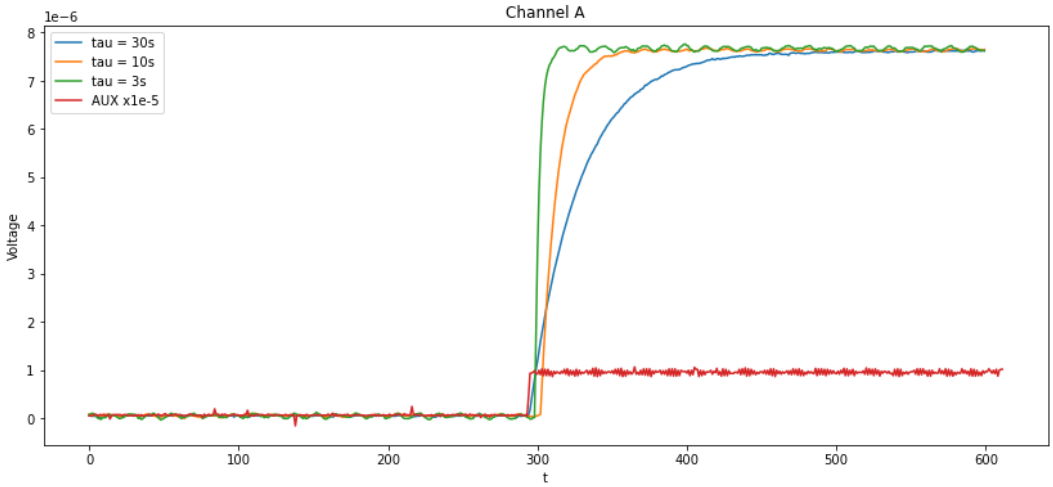


Figure 3.12. Effect of changing the time constant on signal stability. Beat pattern seen in AUX channel due to RC circuit used to demodulate LED signal (R = 15 kΩ, C = 180 + 47 nF).

Depending on whether a fast response or a sensitive response is needed, the value for τ can be changed. A time constant of 3 s suited the purposes of this detection system. An auxiliary (AUX) channel monitored the output intensity of the LED before being filtered through the cavity. Since the LED was modulated, to observe the magnitude of the LED signal, an RC filter was connected to the AUX channel to demodulate the signal, where $R = 15$ kΩ and $C = 227$ nF, causing a beat pattern in the AUX voltage output.

The effect of different modulation frequencies on the photodiode and lock-in amplifier response was also investigated. Depending on the setting of measurements, modulated frequencies from background or stray light may affect the signal, so the

modulation frequency must be chosen from a low-noise region of the system which provides a good signal-to-noise ratio (SNR).

A range of low and high frequencies were selected; 100 Hz, 500 Hz, 1 kHz, 5 kHz, 10 kHz, 100 kHz. After a 5-minute baseline, 0.5 µL of NO_2 was injected into the optical cavity cell and then allowed to diffuse out slowly into exhaust. The magnitude of the signal from this injection is shown in Figure 3.13 and the noise of the signal was evaluated from the baseline measurements by calculating the signal standard deviation during the 5-minute baseline period. The responses at 10 kHz and 100 kHz were excluded from Figure 3.13 as the signals were too noisy and a clear response to NO_2 was not observed. Modulating the LED at either 500 Hz or 1 kHz gave the clearest response with a signal-to-noise ratio of 10 and 12, respectively. It was noted during this experiment that the change in signal intensity was small for a high concentration of NO_2 in the optical cavity cell.

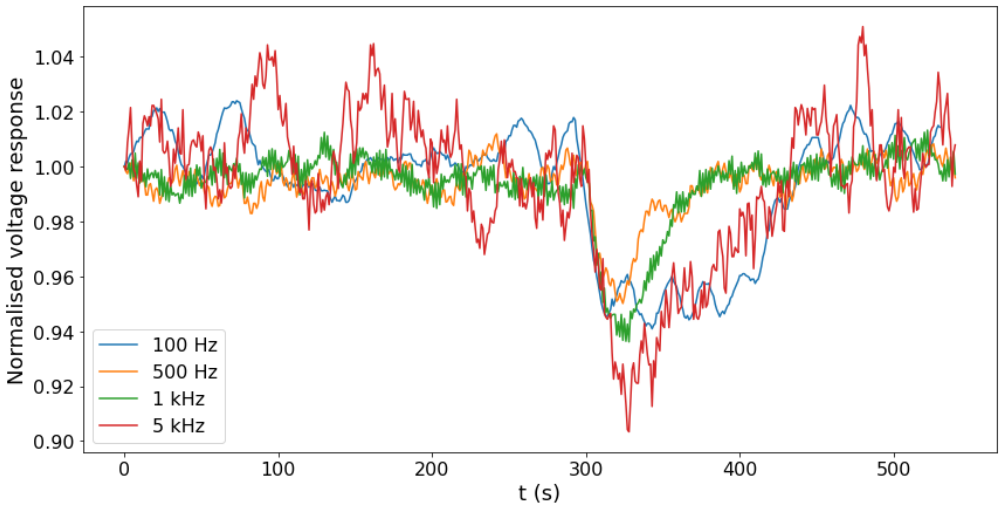


Figure 3.13. Effect of changing modulation frequency on signal-to-noise ratio. LED was modulated at 100 Hz, 500 Hz, 1 kHz and 5 kHz.

Comparison with IBBCEAS measurements

The spectral output of the optical cavity was measured by the spectrometer by putting the flip mirror shown in Figure 3.11 in place. As previously described, 0.5 µL of NO_2 was added into the optical cavity cell after a 5-minute baseline. Spectra were recorded every 10 seconds and the integrated intensity under the peak (439.6 ± 1.9 nm) was

plotted as a time series for comparison to the change in photodiode and lock-in amplifier signal (Figure 3.14). The IBBCEAS measurement saturated when NO_2 was added to the optical cavity cell, whereas the photodiode only measured a small change in intensity. The difference in signal indicated that a large underlying signal, outside of the spectral region of interest, was reaching the photodiode and reducing the sensitivity to absorption by NO_2. Changes in modulation frequency did not affect this large underlying baseline so the interference was most likely coming from the light source through the optical system.

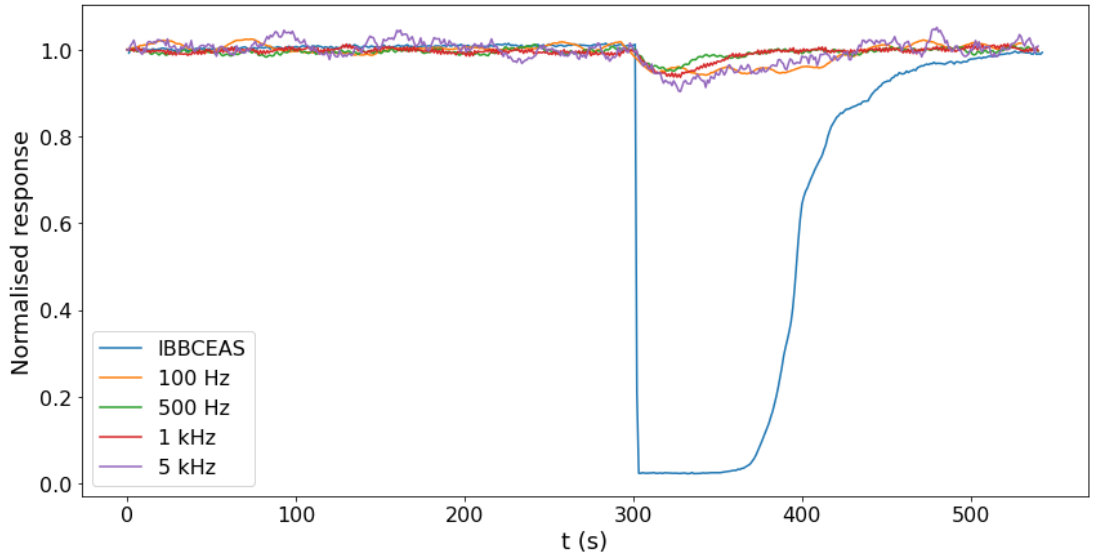


Figure 3.14. Comparing the photodiode and lock-in amplifier response at different frequencies to the full spectral IBBCEAS response from the optical cavity. The normalised response shows a large underlying baseline in the photodiode response.

The underlying baseline was investigated by reducing the light intensity through the optical cavity by placing an aperture between the cavity mirrors. The diameter of the aperture was reduced incrementally every 50 s to reduce the light transmitted through the cavity while the photodiode response and the spectral response for IBBCEAS analysis was recorded every 1 s. The relative change in intensity is shown in Figure 3.15.

It was expected that the intensity would reduce equally, relative to the intensity in the photodiode and IBBCEAS responses. However, when the IBBCEAS system observed large changes in intensity, the photodiode had small signal changes, for example at

150 s where the IBBCEAS intensity had decreased by 60% and the photodiode had only reduced by 15 %. At low light levels, the photodiode sees small changes in intensity that the IBBCEAS system doesn't see. The non-linear relationship is shown in Figure 3.16 and pointed to issues in the photodiode detection; it is evident that the photodiode response has a large underlying baseline outside of the wavelength region of interest.

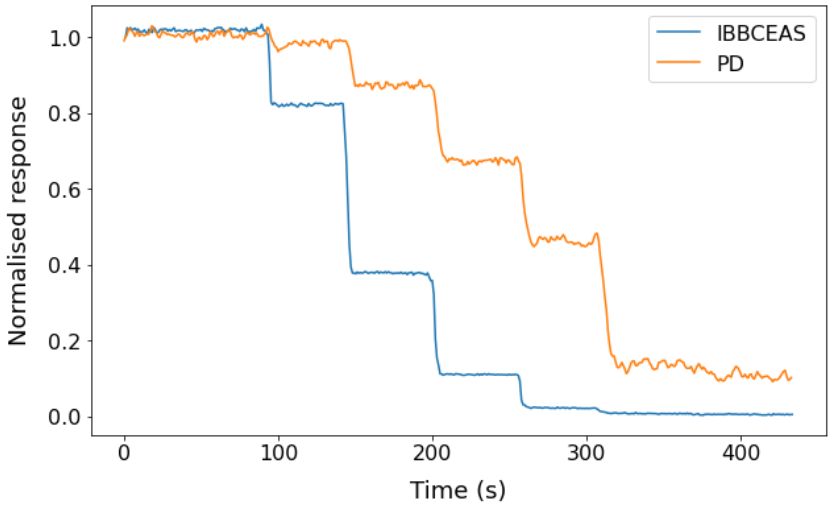


Figure 3.15. Light intensity transmitted through the cavity when light is reduced using an aperture in the centre of the cavity. The photodiode (PD) does not respond as expected to change in light intensity.

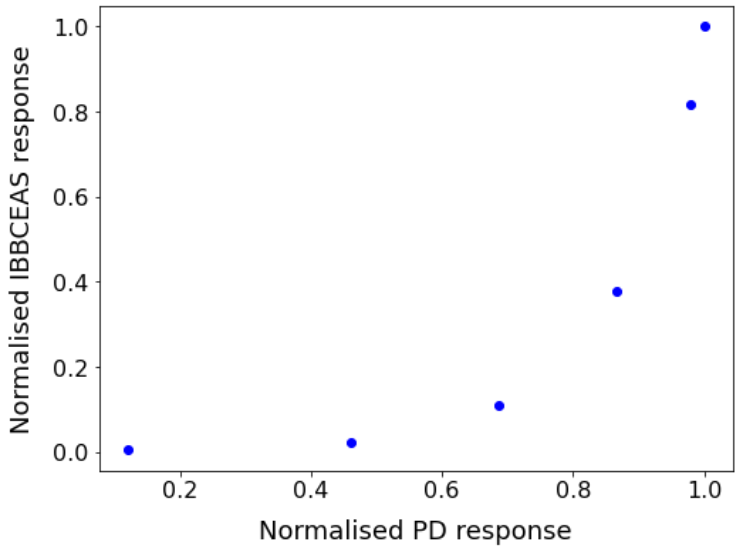


Figure 3.16. Correlation between the photodiode and IBBCEAS response when light in the cavity is reduced incrementally with an aperture. This non-linear relationship points to an issue with photodiode detection.

To investigate whether the apparent raised baseline was a spectral or signal processing issue, a continuously variable neutral density filter (Thorlabs, NDL-10C-2) was introduced at the cavity output to incrementally reduce the intensity for both the IBBCEAS and photodiode response. Neutral density filters reduce the light intensity in a spectrally flat way, i.e., all wavelengths are reduced equally. When the intensity is cut down using a neutral density filter, the relationship between the IBBCEAS and photodiode response is linear with an R^2 value of 0.99 and intercept of 0.06 (Figure 3.17). Therefore, the previously observed non-linearity in signal response was not due to issues with the lock-in amplifier signal processing or the photodiode functionality. Since the neutral density filter reduces all wavelengths of light equally, stray/unwanted wavelengths that come through the cavity are cut down. When NO_2 was added to the cavity cell, interfering wavelengths that do not absorb NO_2 were not reduced, giving a high baseline in the photodiode response. The output of the cavity was visually inspected by looking down the beam path from the cavity. Red light was noted coming through the cavity, clearly showing that interfering wavelengths that the photodiode is sensitive to were coming through the cavity.

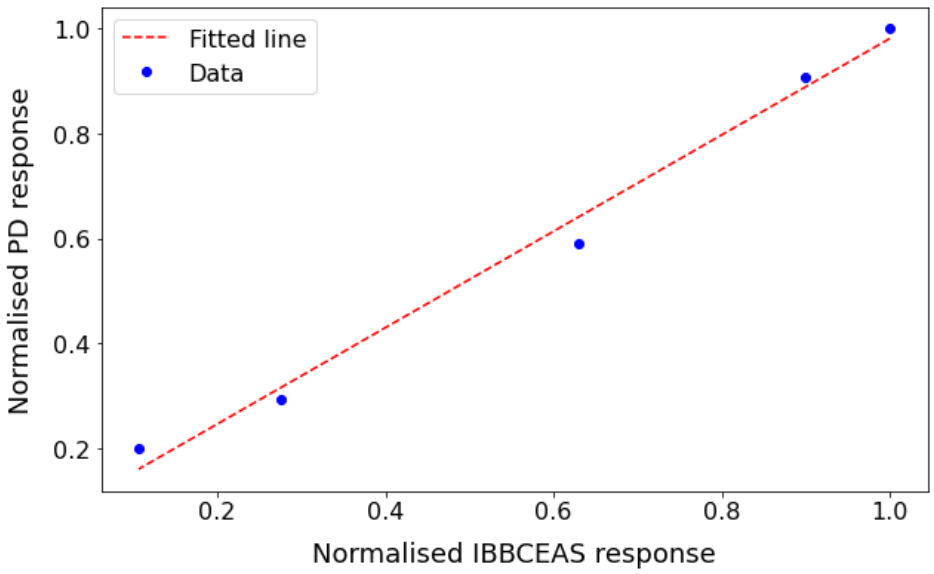


Figure 3.17. Correlation between photodiode and IBBCEAS response when light intensity is reduced incrementally with a neutral density filter (NDF). The linear relationship observed here suggests that previous non-linearity is caused by spectral interference. R^2 = 0.99, slope = 0.92, intercept = 0.06.

Optical filtering

A spectrometer (RedTide USB650, Ocean Optics) was used to capture the full emission spectrum from the cavity shown in Figure 3.18. The cavity emission spectrum showed that even with a wide bandpass filter (Semrock, FF01-440-40, 420 – 460 nm), wavelengths outside of the cavity bandpass were contributing to the signal, particularly longer wavelengths greater than 500 nm. The manufacturer's transmission spectrum of the narrow bandpass filter was shown in Figure 3.2 and it was noted that some wavelength bands were transmitted above 600 nm
The transmission band of a KG3 infrared filter is shown in Figure 3.18. The addition of the KG3 filter lowered the baseline at longer wavelengths and removed spikes in intensity at ~405nm. The IBBCEAS system had significant rejection of out of band light, especially small amounts of long wavelength LED emissions ($\lambda > 600$nm), by using the CCD spectrograph which disperses all wavelengths of incident light so that only the wavelengths of interest can be analysed. However, the non-dispersive photodiode does not benefit from this rejection and even has a higher responsivity to longer wavelengths, with its peak responsivity at 730 nm. Therefore, careful filtering of longer wavelengths is important when using photodiodes to collect low levels of blue light and monitor small changes in intensity cause by absorption.

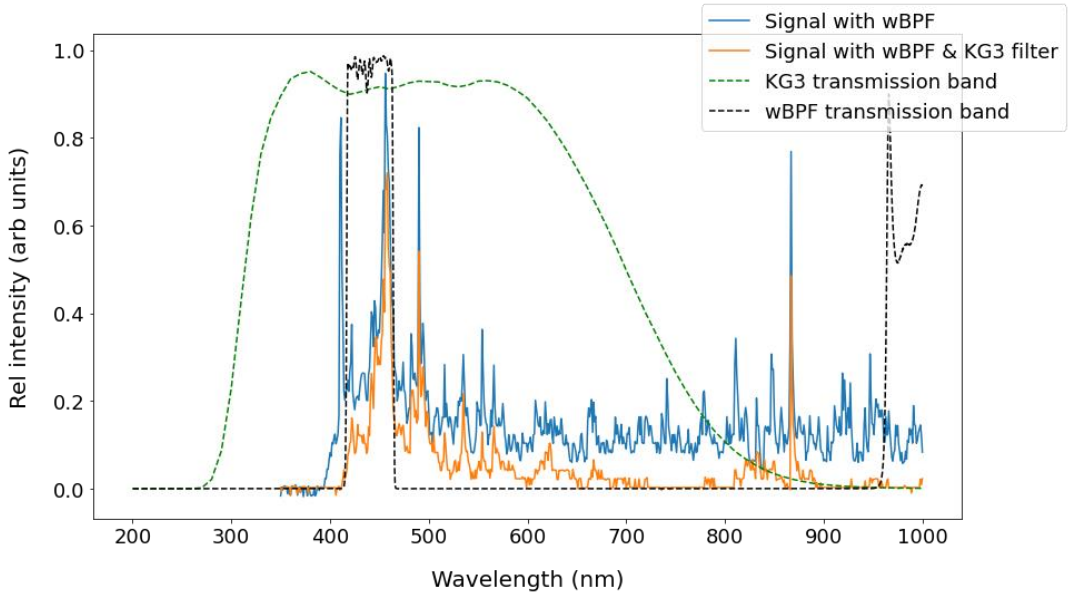


Figure 3.18. Optical cavity emission spectrum from 350 - 1000 nm. The cavity signal is shown with and without filters. Filter transmission bands are shown in dashed lines, as reported by the manufacturer.

After improving the filtering and light-blocking of the system, the previously described experiment was repeated with an aperture placed in the centre of the cavity to reduce the light transmitted through the cavity. The photodiode response is much closer to the IBBCEAS response with optical filters in place, as shown in Figure 3.19, although there still exists a small underlying baseline in the signal. The responses are linear here with R^2 value of 0.97, slope of 0.95 and intercept of 0.10.

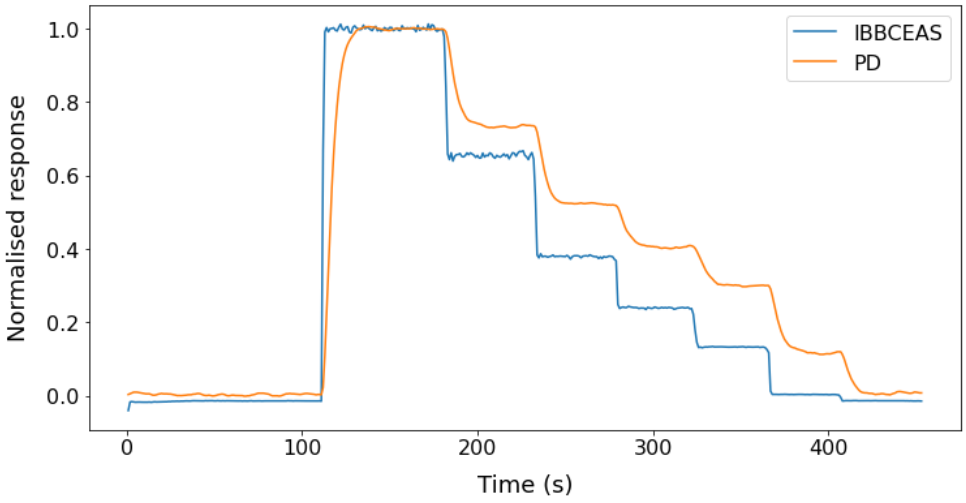


Figure 3.19. Photodiode and IBBCEAS response to reduction in light intensity through the cavity with filtering in place.

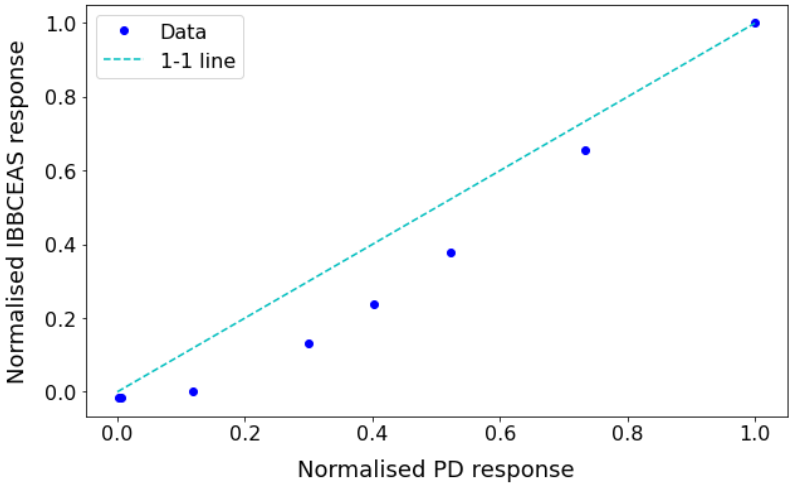


Figure 3.20. Correlation between photodiode and IBBCEAS response. A more linear relationship is seen here compared to previous experiments, suggesting that careful filtering is required for photodiode measurements. R^2 = 0.96, slope = 0.95, intercept = 0.10.

Si photodiodes are responsive to a large range of wavelengths, 200 – 1100 nm, peaking around 730 nm. At the system operating wavelength, near 440 nm, the photodiode responsivity is approximately 0.15 A/W, compared to 0.45 A/W at 730 nm. Hence, unwanted wavelengths that do not absorb NO_2 are transmitted through the optical cavity efficiently and are collected by the photodiode. Most of the background light that the photodiode was sensitive to can be removed by using bandpass or short pass optical filters placed before the cavity. Light source selection is also important here as some LEDs can have longer wavelength emissions that are not necessarily included in the manufacturer's emission spectra and affect the amplified signal since the interfering wavelengths are modulated at the same frequency as the wavelengths of interest. Similar issues were discussed by Venables et al. (2006) when using even broader band arc lamp light sources.

A dilute sample of NO_2 was introduced into the optical cavity cell and the change in intensity was measured for the photodiode and IBBCEAS response, as described in the previous sub-sections, however a very small amount of NO_2 was added in this experiment so that the IBBCEAS absorption signal did not saturate. A wide bandpass filter transmitting wavelengths between 420 and 460 nm, and a KG3 infrared filter were placed before the optical cavity to remove longer wavelengths that the photodiode was sensitive to. Spectra and amplified photodiode voltages were recorded every 1 s and NO_2 was injected after a 100 s baseline (Figure 3.21). Compared with earlier results, the photodiode response is much clearer when looking for a small relative change in the intensity. Although there is still a small baseline intensity at longer wavelengths, this system is now useful for absorption measurement purposes.

A standard deviation of 0.6% for the photodiode and 0.4% for the IBBCEAS response was calculated between 200 – 300 s, when all of the NO_2 had diffused out of the cavity cell and the signals had returned to their initial intensities. The photodiode therefore had a signal-to-noise ratio of 46, a factor of 2 lower than the IBBCEAS which had a signal-to-noise ratio of 87 for the same concentration of NO_2. The signal measured on the photodiode was now useful for measuring small changes in intensity caused by absorption by NO_2 around 440 nm.

The correlation between the photodiode and IBBCEAS response when NO_2 was added and removed from the system was highly linear with an R^2 value of 0.99, an intercept

of 0.18 and slope of 0.82. A photodiode with lock-in amplification was determined to be suitable for measuring two narrowband channels, provided necessary optical filtering is included.

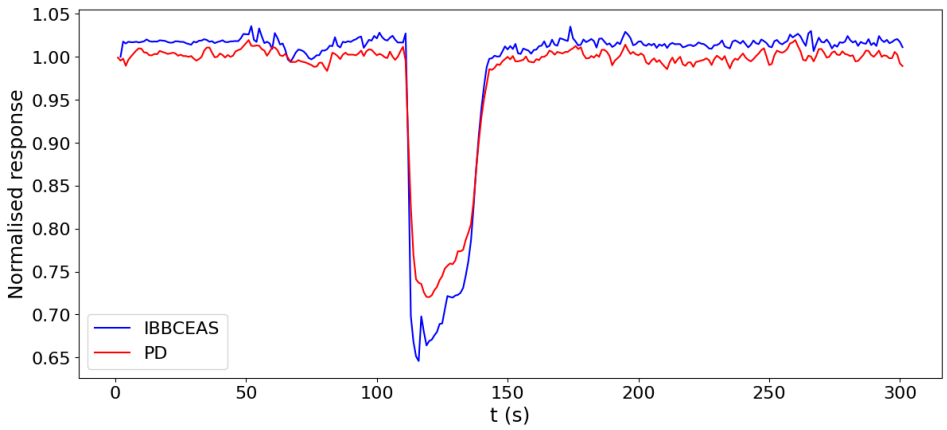


Figure 3.21. Photodiode (PD) response to NO_2 compared with IBBCEAS response with a wide bandpass filter and KG3 infrared filter in place to remove interfering wavelengths that could be transmitted through the system.

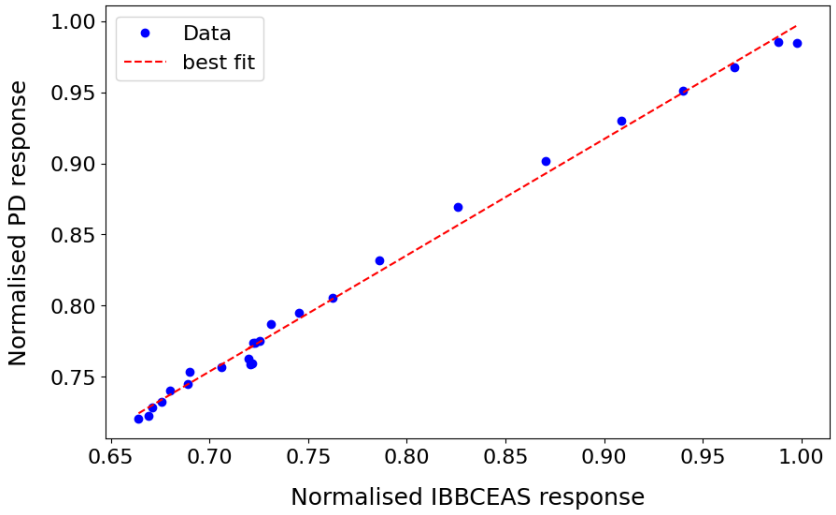


Figure 3.22. Correlation between photodiode (PD) and IBBCEAS response to NO_2. This shows an approx. linear relationship, indicating the system is responding as expected to NO_2.

Considerations for detector selection

Si photodiodes have a higher responsivity to longer wavelengths beyond the system's operating wavelengths near 440nm, and so alternative detectors needed to be considered. Figure 3.23 shows the responsivity curves of a Si photodiode and a photomultiplier tube. The photodiode shows a clear peak in responsivity at 730 nm with relatively low responsivity around 440 nm. The photomultiplier tube (PMT) module shows a peak in responsivity between 330-500 nm (solid red line, Figure 3.23(b)) which is ideal for the operating wavelengths of this system. The PMT also shows good quantum efficiency in this region (dashed red line, Figure 3.23(b))

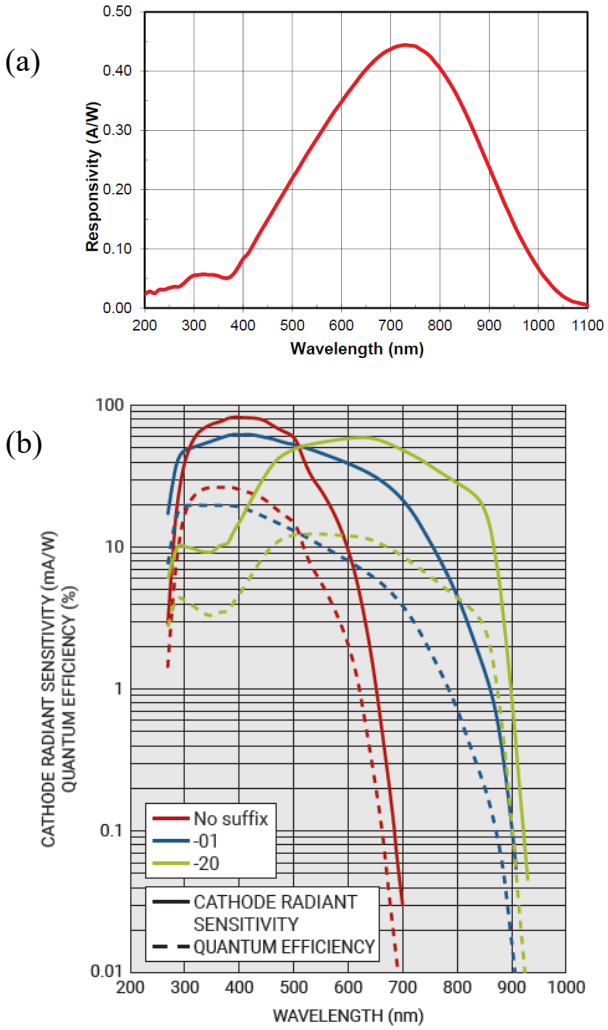


Figure 3.23. Responsivity curves for (a) photodiode (Thorlabs, DET10A) and (b) photomultiplier tube (Hamamatsu, H12405) provided by the manufacturers.

PMTs have their own internal amplification, making them better for detecting small signals. Incident light is converted to photoelectrons by a photocathode. The photoelectrons are then directed to an electron multiplier by an electric field around the photocathode. The electrons accelerate in this electric field and strike a secondary surface to produce secondary electrons. This process is repeated for *n* multiplier stages until the electrons are multiplied roughly one million times and are output as electrical current. The PMT module used in this work has a voltage output which simply converts this output current to voltage. This module also has a built-in high voltage power supply and amplifier, significantly reducing the complexity of the system while increasing the sensitivity.

The use of a PMT as a photodetector for narrow spectral channels was then explored. The optical cavity light throughput was improved by choosing mirrors of a lower reflectivity (R = 99.94%), decreasing the path length but improving the signal-to-noise ratio. The reflectivity of these mirrors extended further, from 400 – 550 nm, meaning that all of the LED emission was reflected within the cavity. The light source was replaced with an LED with a smaller viewing angle (Roithner LED430-06, viewing angle = 8 °). The photodiodes in Figure 3.11 were replaced by PMT modules (Hamamatsu, H12405). The PMT response to a single narrow channel was amplified using a lock-in amplifier and compared with the integrated IBBCEAS response. 8 mL NO_2 was introduced to the ERI atmospheric simulation chamber in 4 steps of 2 mL before the chamber was flushed at a rate of 80 L/min. The CCD had a kinetic cycle time of 1.01 s and a data acquisition unit recorded the lock-in amplifier output, which had a time constant, τ = 300 ms, every 1 s.

The PMT has slightly improved noise characteristics compared to the IBBCEAS measurement, as seen in Figure 3.24. The standard deviation of each detection method was calculated from the first 1000 s of Figure 3.24 when there is no NO_2 in the chamber. The standard deviation of the photodiode was 0.4 % and compared favourably with the IBBCEAS standard deviation of 0.6%. There was a strong linear correlation between both detectors, with an R^2 value of 0.99, slope of 0.67 and intercept of 0.33. The PMT with lock-in amplification is a very sensitive photodetector in this wavelength region, however these components are expensive and PMTs are vulnerable to overexposure from stray light, meaning this detection system may not be suitable in field measurements where a robust instrument is required. The lock-in

amplifier used in this experiment can only measure one input channel at a time and so the two-channel ratiometric method could not be realised using the SR830 lock-in amplifier.

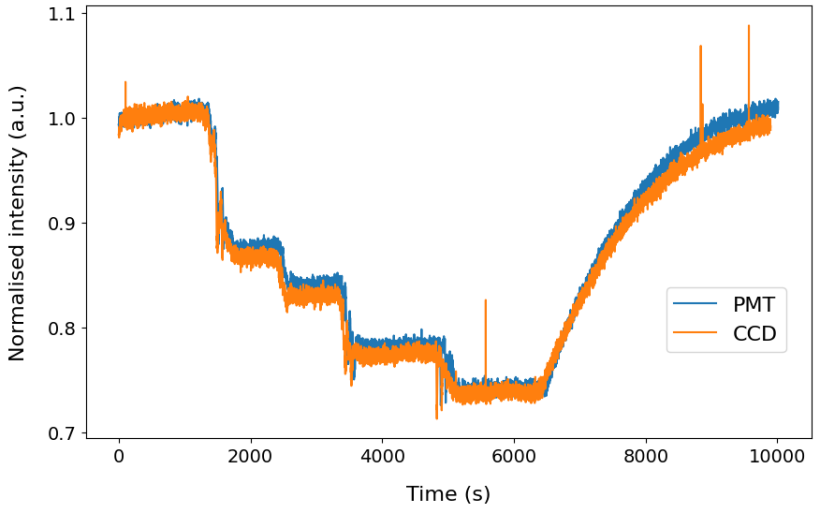


Figure 3.24. Normalised response of PMT and lock-in amplifier compared to the CCD response to one narrow wavelength when NO_2 is added stepwise to the ERI atmospheric simulation chamber.

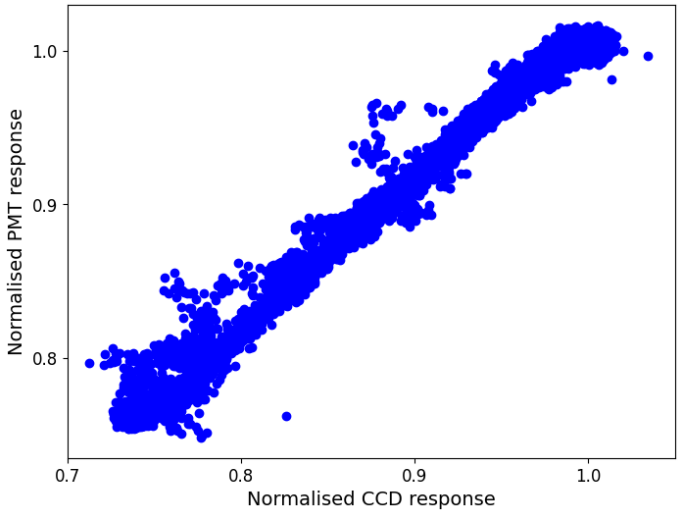


Figure 3.25. Correlation of PMT and CCD responses when NO_2 is introduced. A strong linear relationship is observed with $R^2 = 0.99$, intercept = 0.33, slope = 1.01.

3.4 Wide bandpass CEAS system

A cavity-enhanced system was set-up with a wide bandpass filter (wBPF) to select wavelengths 420 – 460 nm. A photodiode and lock-in amplifier were used to collect the output signal from the cavity to test the limitations of the cavity system with a low-cost detector and complex signal processing. The system schematic can be seen in Figure 3.26, showing that the LED light source was modulated by a signal generator. This modulation signal was also used as the reference channel for the lock-in amplifier, ensuring that the signal and reference were intrinsically matched. A KG3 optical filter was placed in front of the photodiode to remove interference from longer wavelengths that are easily transmitted through the optical cavity. A similar amplitude-modulated CEAS system was reported by Zhou et al. (2022) for making fast measurements of NO_2. Zhou and coworkers used a multimode laser light source with active temperature controls, a PMT as a photodetector, and a long effective optical path length > 3 km to achieve a limit of detection of 8 ppt in 30 s. The modulated single-channel CEAS system described in this section uses an LED light source with significantly lower power. The effective path length through the optical cavity is substantially shorter. For measurements in an urban traffic environment, ppb-level sensitivity is required, therefore the system described here should be suitable for this application.

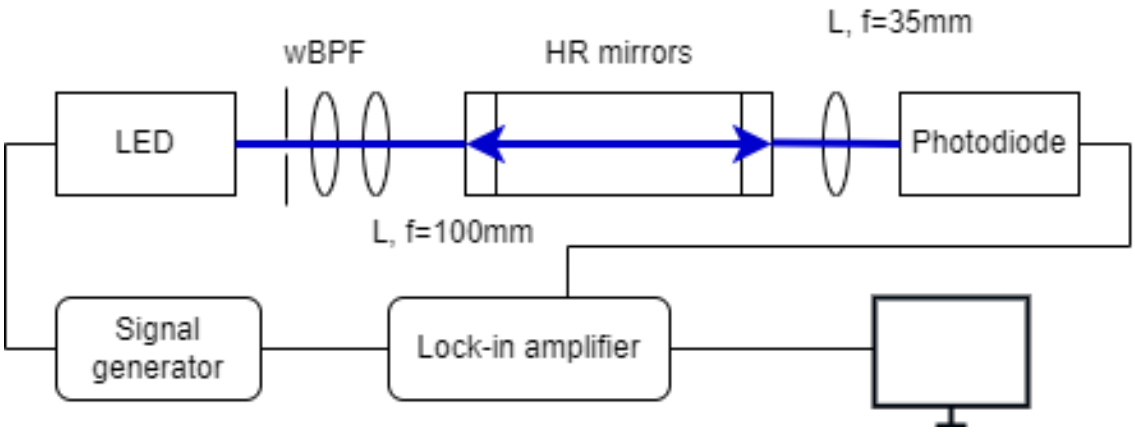


Figure 3.26. Schematic of wBPF cavity-enhanced system. A modulated LED (430 nm peak) is directed through a wBPF, passing wavelengths 420-460 nm. Light transmitted through the cavity is recorded by a photodiode and lock-in amplifier.

The cavity mirrors used in this system have a reflectivity of 99.94% between 400 – 550 nm, radius of curvature of 1000 mm and 1 inch diameter, as stated by the manufacturer. The cavity mirrors were separated by 43 cm, satisfying the stability criterion, $0 < g_1 g_2 < 1$, for optical cavities where $g_{1,2} = 0.57$. Initially, the cavity mirrors were enclosed by a ½ inch diameter tube. However, this narrow tube cut down the light transmitted through the cavity, so a 2 inch diameter tube was used instead. Tubing diameter is less of an issue with laser light sources that have a narrow emission, but it becomes important when using LEDs as light sources as they have a much broader emission beam and larger spot sizes.

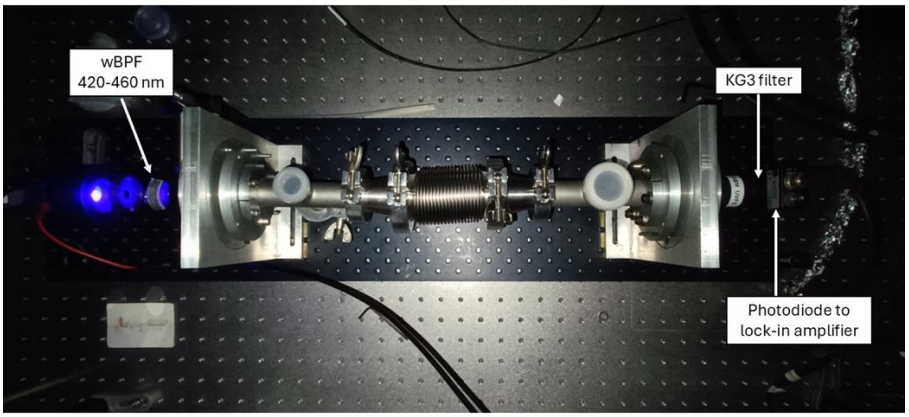


Figure 3.27. Photograph of the wBPF system on an optical bench. The LED (Roithner, LED430-06) was modulated by a signal generator that provided the reference frequency for the lock-in amplifier. A wide bandpass filter (wBPF) and infrared KG3 filter removed longer wavelengths that could interfere with photodiode measurements.

The wideband single-channel system was run for 2 hours with no absorbing gasses present in order to do Allan analysis on the signal. The Allan deviation of a system describes the noise within a signal over time and is a useful tool to identify the minimum detectable system response and the optimised averaging time. From Figure 3.28 it is clearly seen that the noise in the system reduces as the averaging time increases to 100 s, reaching a minimum deviation of 8×10^{-9} V. Beyond 100 s, the noise of the system begins to increase because longer-term drifts begin to be included in the averaged signal. Assuming a time response of 10 s, the Allan deviation of the system

is 10^{-8} V, equating to a minimum detectable number density of 4.3×10^{9} molecules/cm^3 which is equal to a mixing ratio of 0.18 ppb in ambient air. This analysis concludes that the wideband single-channel system is appropriate for measuring ambient NO_2 concentrations in an urban environment in terms of both sensitivity and time response.

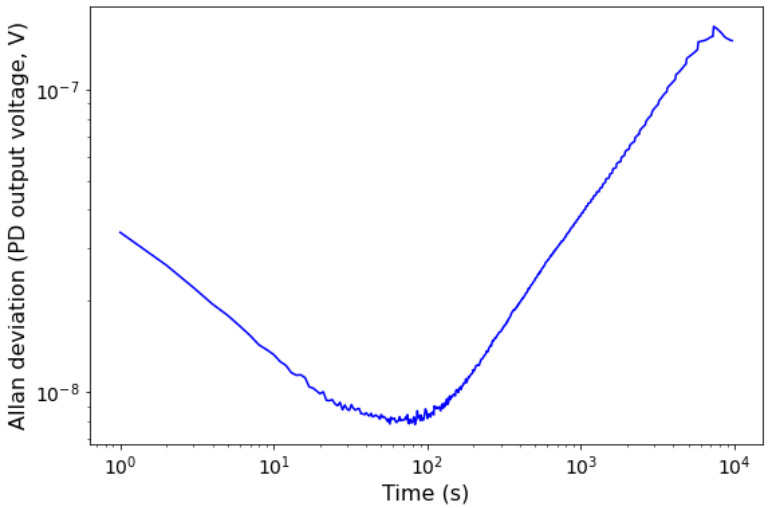


Figure 3.28. Allan deviation of the photodiode (PD) and lock-in amplifier output voltage. The minimum deviation is $8\text{x}10^{-9}$ V in 100 s and 10^{-8} V in 10 s.

3.5 Discussion

This chapter has characterised the optical components of a two-channel ratiometric system. Choosing an LED with an appropriate centre wavelength and viewing angle were discussed and it was concluded that a narrower viewing angle greatly increases the light throughput of a system. The spectral resolution of a two-channel ratiometric system is limited by the bandwidth of the nBPF used, therefore a filter with an appropriate FWHM should be chosen so that a large difference in absorption cross-section can be observed between each spectral channel.

Photodiodes and photomultiplier tubes were considered as photodetectors for this system. When using photodiodes, particularly in the visible region, careful optical filtering is necessary to remove longer wavelengths of light that the photodiode is more

responsive to. PMTs are an attractive alternative to photodiodes for visible light detection as they have their peak responsivity between 400 – 500 nm with a steep cut off around 700 nm. When employing lock-in amplification, the signal response from a photodiode is sufficient for making ambient NO_2 measurements. However, a major hurdle for the two-channel ratiometric system is that typically lock-in amplifiers only measure one channel. There is a growing need for compact, low-cost amplifiers, particularly lock-in amplifiers that can discern a very small signal that is masked in large levels of noise. Harvie & De Mello (2022) published an online open-source digital lock-in amplifier (OLIA) based on a Teensy microcontroller. All user interface programs and PCB designs are available on GitHub (Harvie, 2021).

OLIA can handle signals modulated up to 50 kHz and supports both internal and external referencing. OLIA also features a +5 V rail which can be used to power an LED (V_{ss}) while the internal reference modulates the signal. A schematic for this circuit is shown in Figure 3.29. The current sent through the LED is limited by resistor R2, the value of which should be chosen depending on the LED current and voltage ratings.

The OLIA board was integrated into an optical absorption and fluorescence detector by Harvie and coworkers (2021) for the detection of cholesterol. The OLIA system was preliminarily tested using the low light levels observed in the ratiometric two-channel system. However, the lock-in amplifier was unable to amplify these small signals and must be optimised for the detection of very small absorption measurements. These optimisations were beyond the scope of this thesis and OLIA will not be used in further discussions. Nevertheless, OLIA is a powerful tool that will likely lead to great improvements in the sensitivity of low-cost optical detection systems, while also reducing the cost and size of instruments.

Lock-in amplification is beginning to reduce in cost as demand for compact and low-cost electronics grows, as seen with Harvie's OLIA. Although OLIA also only supports one input channel, two identical boards could be made and driven by the same reference frequency. The development and optimisation of electronic components is beyond the scope of this thesis.

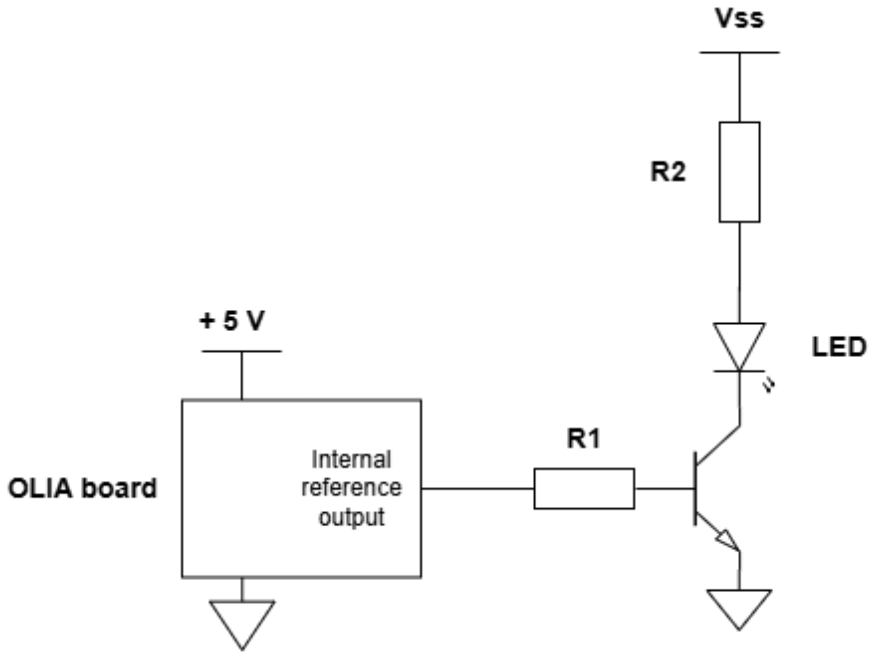


Figure 3.29. Circuit design for electronic switch modulating the LED at the OLIA internal reference frequency. The LED is powered by the 5V rail on the OLIA board and R2 limits the current.

A wide bandpass single-channel cavity instrument was built and the system sensitivity to NO_2 was investigated via Allan analysis. The Allan variance estimates the stability of a signal based on short-term noise processes and system drift. The Allan deviation is the square-root of the Allan variance and describes the fractional error in signal over different averaging times (Marinov et al., 2019). A similar system was shown to be effective in measuring NO_2 by Zhou et al. (2022)using an amplitude modulated wide band CEAS system. The wideband single-channel system described in this chapter had better light throughput than the two-channel ratiometric scheme and used a photodiode and lock-in amplifier to further improve the detection limit of the system. A minimum detectable mixing ratio of 0.18 ppb in 10 s was calculated from the Allan deviation. This detection limit is suitable for measuring ambient NO_2 in a traffic environment and compares well with other optical detection systems with sub-ppb precision (Bailey et al., 2024; Kebabian et al., 2000; Kuhn et al., 2022; Zheng et al., 2024).The wideband single-channel instrument has sufficient sensitivity and time response for making ambient NO_2 measurements in a traffic environment where NO_2 is the dominant absorber.

Chapter 4 Instrument validation in atmospheric simulation chambers

4.1 Atmospheric simulation chamber experiments

The performance of different instruments and measurement strategies developed in this thesis were tested in atmospheric simulation chamber experiments. These chambers consist of chemically inert Teflon enclosures housed in aluminium frames. Gases and particles may be introduced into the chamber in a controlled fashion, allowing chemical processes in the atmosphere, including photolysis and chemical reactions, to be simulated under controlled conditions. Chambers are also useful for testing early-stage instruments because they allow relatively higher concentrations of target analytes and interferences to be tested. Instrument prototypes can be set up in a stable environment and compared with measurements from established methods. Moreover, the effect of potential chemical interferences on the measurement can be investigated in a systematic way.

This chapter describes several instrument configurations that were tested in two atmospheric simulation chambers: a smaller, 2.65 m^3 volume chamber in the Environmental Research Institute, and a larger, 27 m^3 volume chamber, the Irish Atmospheric Simulation Chamber (IASC) housed in the Kane Science Building. A narrowband two-channel system was tested, first using a dispersive CCD spectrograph and a cavity-enhanced signal, and secondly using non-dispersive detectors and a short, folded path of 8 m. Lock-in amplification was explored as a method of increasing the signal magnitude, and therefore the signal-to-noise ratio, to enhance the sensitivity to NO_2 absorption. The drawbacks of the benchtop lock-in amplifier are discussed in the context of a portable 2-channel system. Following these experiments, a wideband single channel CEAS system was built to improve light throughput in the system. Although selectivity to NO_2 is reduced in a wideband system, the sensitivity is greatly

improved. Two non-dispersive detectors are tested with this single channel system; a photodiode with lock-in amplification and a sensitive photomultiplier tube module. All instruments are then discussed in the context of fast urban NO_2 detection, specifically in a traffic environment.

ERI Atmospheric Simulation Chamber

The Environmental Research Institute (ERI) housed an atmospheric simulation chamber with a 2.0 m long cylindrical fluorinated ethylene propylene Teflon bag enclosed in an aluminium frame. The sample volume of the chamber was 2.65 m^3. Large openings with a diameter of 30.7 cm on the front and back end of the chamber were enclosed by perspex windows. These windows were used to create a folded optical path across the chamber in some experiments. Normally, these window openings were covered to prevent ambient light from entering the chamber. Ports on the front and back ends of the chamber were used for sampling from the chamber or for introducing gases and particles into the chamber. Apertures on either end of the chamber allowed CEAS techniques to be used across the 2 m length of the chamber. A small fan circulated the air to ensure a uniform chemical composition within the chamber. Fluorescent UV lamps (Philips, TLK 40W/05, TUV 15W/G15 T8, TLD 18W/08) located beneath the Teflon bag were used to simulate photolysis in the atmosphere but were not used in these experiments.

The chamber operated at atmospheric pressure and room temperature. Temperature and relative humidity were monitored by a Vaisala probe (DMP74A). The chamber was flushed with compressed air that had been dried and cleaned by an air purification system (Zander KA-MT-6) to reduce the relative humidity to below 1%. The relative humidity in the chamber could be increased to approximately 40 % by bubbling compressed air through deionized water and introducing it into the chamber. The ERI atmospheric simulation chamber has been discussed and characterized in detail elsewhere (Ashu-Ayem et al., 2012).



Figure 4.1. Photographs of the 2 m long ERI atmospheric simulation chamber. The Perspex windows, mirror ports and injection ports (top) can be seen as well as the inner Teflon bag and UV lamps for photolysis simulations (bottom).

Irish Atmospheric Simulation Chamber (IASC)

The Irish Atmospheric Simulation Chamber (IASC) is a large, 27 m^3 (4.4 x 3 x 2 m^3) chamber located in the Kane Science Building, UCC. The chamber consisted of a FEP Teflon bag supported on an aluminium frame. The large volume of the chamber allowed more precise control of gas mixing ratios inside the chamber. The chamber had multiple access ports for sampling or introducing gases or aerosols into the chamber. Eight mirror ports on the front and back faces of IASC were used to support optical cavities for detecting NO_2, NO_3, HONO and glyoxal (Kiendler-Scharr et al., 2023; RADICAL, 2024). Concentrations of NO_x and O_3 were measured using

Teledyne instruments (T200, T400). VOCs and other organic compounds were measured using an Aerodyne ToF-CIMS with a Filter Inlet for Gases and AEROsols (FIGAERO) to analyse particulates.

Temperature, relative humidity and pressure probes (Sontay, Flying Lead Temperature Sensor; Vaisala PTU303; Vaisala PDT102) were mounted on either end of the chamber to ensure uniformity. A mixing fan within the chamber ensured that the chemical composition and temperature within the chamber was homogeneous.

The walls of IASC had 14 panels each containing 10 Philips lamps (7 UVA lamps, TL 40W/10 SLV/25; and 3 UVB broadband lamps (TL 40W/12RS SLV/25) to simulate photolysis in the chamber.



Figure 4.2. Photograph of the inside of IASC. Mirror ports, injection ports, UV lamps and mixing fan can be seen.

4.2 Ratiometric two-narrowband channel method

The ratiometric two-narrowband channel method described in Section 2.2 was first demonstrated experimentally using a dispersive spectrograph that can monitor the intensity of both channels simultaneously, with good sensitivity and without the need for additional spectral filtering to remove interfering wavelengths. The sensitivity of this dispersive system was increased further by using an optical cavity to extend the effective pathlength.

Subsequently, the system was modified to simplify the optical alignment, and the spectrograph was swapped for two non-dispersive photomultiplier tubes (PMTs) which are most sensitive to blue light. A relatively short optical pathlength of 8 m was used in the non-dispersive system which reduced the sensitivity to NO_2 absorption but provided a large signal incident on the PMTs. To overcome the limited system sensitivity resulting from the short pathlength, high mixing ratios of NO_2 (> 1 ppm) were introduced into the ERI atmospheric simulation chamber for the purposes of demonstrating the narrowband two-channel method.

Spectrograph demonstration

Optical configuration

An optical system was designed to demonstrate the ratiometric two-channel principle using a high-resolution spectrograph (Andor, Shamrock 163) and CCD detector (Andor iDUS, DV420A-BU) to observe the differential absorption between two nearby wavelengths. Spectrographs allow the intensities of both channels, $I_1(\lambda_1)$ and $I_2(\lambda_2)$, to be measured at the same time. Figure 4.3 shows the optical configuration of the instrument. The emission of an LED (Roithner, H2A1-H435) mounted on a passive heat sink was focused into an optical cavity formed by two high reflectivity mirrors (R_{max} > 99.98% between 390 and 510 nm) separated by 38 cm. The cavity mirrors had a diameter of 25.4 mm and the cavity cell had an inner diameter of 12.7 mm. Light transmitted through the cavity was split into two channels using a 50:50 beam splitter, and both beams were directed at different angles through a single narrow bandpass

filter, to transmit wavelengths λ_1 and λ_2. Both beams were then recombined and focused into the spectrograph for simultaneous detection. The resulting spectrum shows two distinct channels (Figure 4.4). The first channel had a peak intensity at λ_1 = 435 nm, where the convolved absorption cross-section is 6.3×10^{-19} cm^2 molecule^{-1}. The second channel peak was at λ_2 = 438 nm where the convolved absorption cross-section is 4.1×10^{-19} cm^2 molecule^{-1}. The intensities $I_1(\lambda_1)$ and $I_2(\lambda_2)$ were integrated across the peaks' bandwidth of 1.36 nm to simulate the effect of a non-dispersive detector that measured all transmitted wavelengths in each channel's passband. The channels centred at λ_1 and λ_2 were separated to avoid channel overlap, which would reduce the size of the differential signal between the two channels.

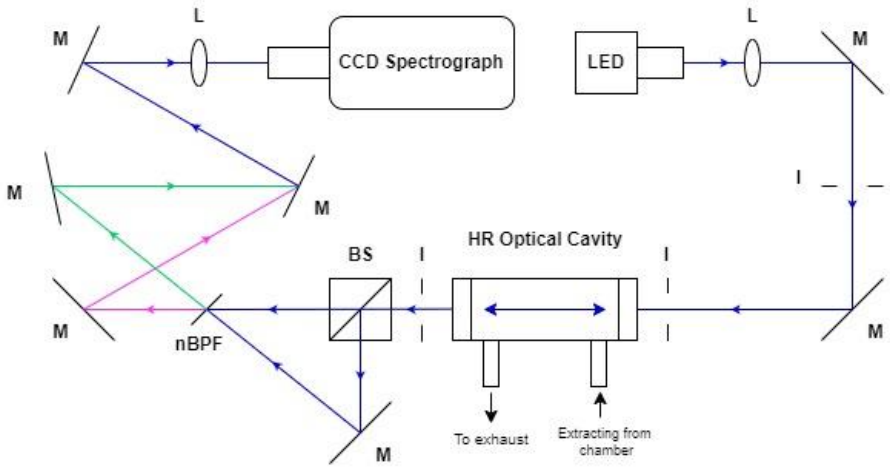


Figure 4.3. Optical configuration of first ratiometric two-channel demonstration; L = lens, M = planar mirror, BS = beam splitter, nBPF = narrow bandpass filter, HR = high reflectivity.

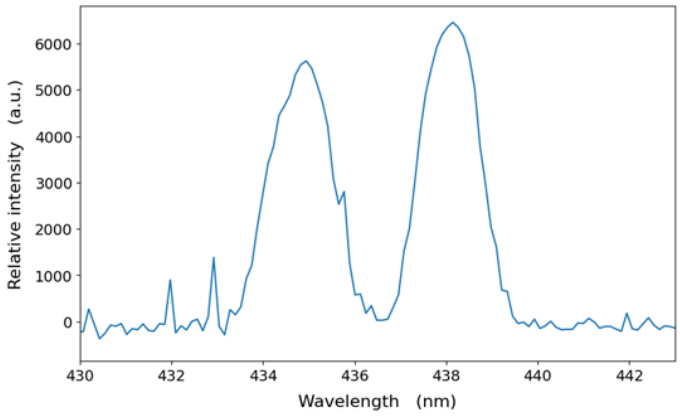


Figure 4.4. Spectrum of the two channels at λ_1 = 435 nm and λ_2 = 438 nm. The peaks are spaced so that overlapping features did not influence measurements.

Ratiometric 2-channel measurement of NO_2

The ratiometric two-channel system sampled air from the ERI atmospheric simulation chamber and was compared with an extractive chemiluminescence NO_x analyser (CL, Teledyne T200) which provided a 1-minute averaged mixing ratio. Both the ratiometric two-channel system and CL instruments sampled air from the opposite side of the chamber to the gas inlet port to avoid localized concentrations of NO_2 when it was added to the chamber.

Figure 4.5 shows the time series of the normalized intensities of λ_1 and λ_2 with spectra recorded every 10 s. NO_2 was sampled from a 98.5% purity NO_2 lecture bottle into a syringe so that a small volume of NO_2 could be added stepwise to the chamber at 1000, 2000, 3000 and 4000 s. After 5000 s, the chamber was flushed at a rate of 80 L min^{-1} and the signals in both channels converge on the intensity at the start of the experiment. Both channels decrease in intensity as the NO_2 concentration in the chamber increases. Since the absorption cross-section at 435 nm is 1.5 times the absorption cross-section at 438 nm, more light is absorbed in the 435 nm channel and a stronger response is observed.

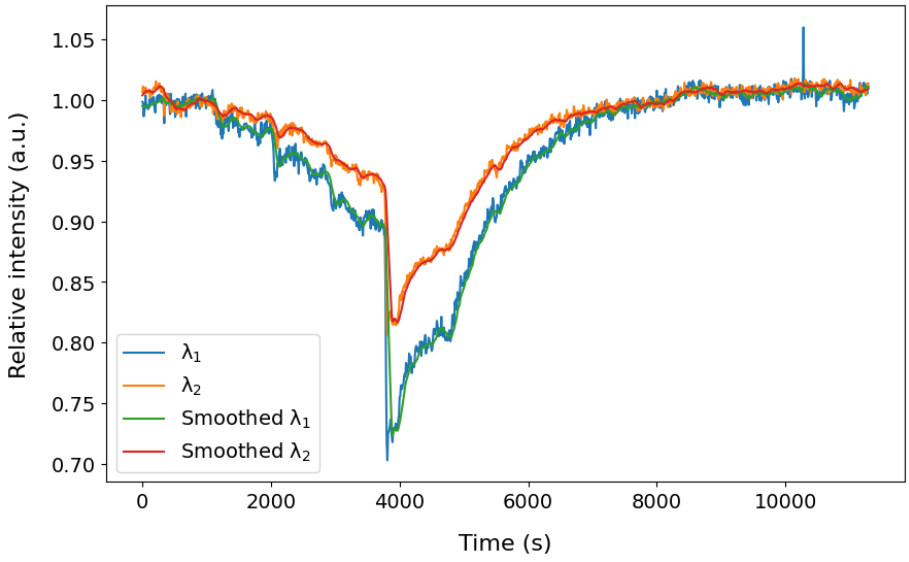


Figure 4.5. Time profile of intensity at λ_1 = 435 nm and λ_2 = 438 nm compared to the signal smoothed over a 15 data point window.

It is evident that fluctuations in intensity occur in both channels at the same time. Apart from intensity fluctuations occurring when NO_2 is added to the chamber, similar noise characteristics are also observed in both channels. These can be attributed to fluctuations in LED current, cavity mirror instability, or background light entering the CCD array. The relative noise in each channel was investigated by smoothing the raw higher time resolution response (10 s) over 15 data points (Figure 4.5) and subtracting the raw measurement from the smoothed response (Figure 4.6). The signal at λ_1 has more high frequency noise than that at λ_2, which may have been caused by differences in optical path and beam clipping at the edge of optics, particularly the nBPF.

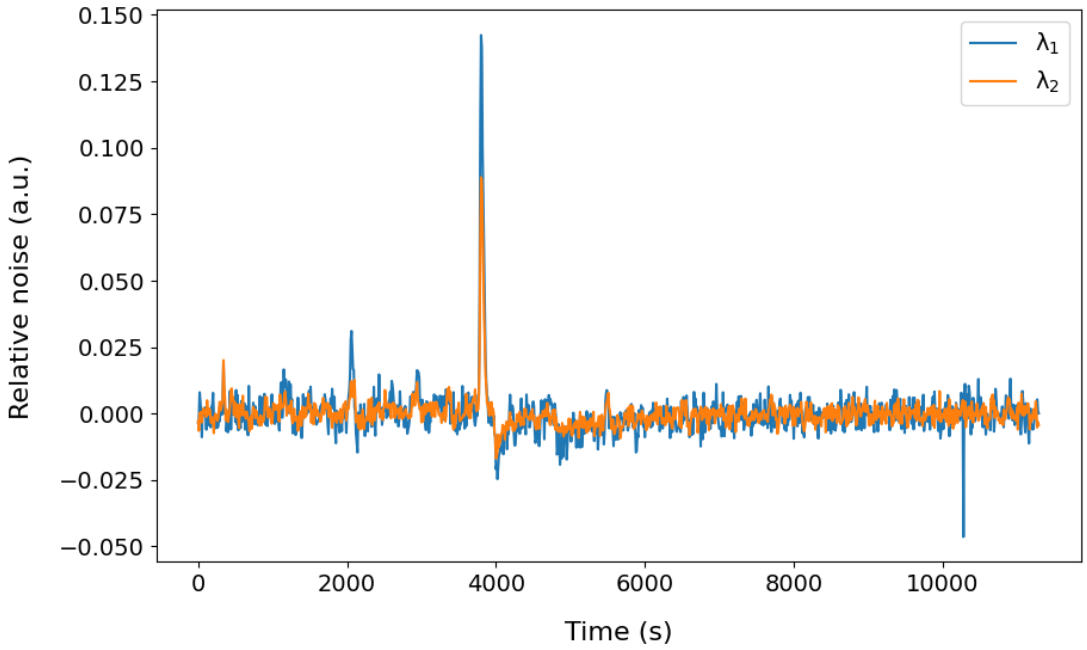


Figure 4.6. The relative noise in each channel (calculated by subtracting the raw signal from the smoothed signal) with λ_1 = 435 nm and λ_2 = 438 nm. Similar fluctuations are observed in each channel and generally occur with the introduction of NO_2 into the chamber and the onset of flushing.

The standard deviation in both channels was calculated from 9000 s to 10000 s when the NO_2 had been flushed from the chamber and both channels had returned to their initial intensities. The two channels do not have identical noise characteristics, with a standard deviation of 0.3 % and 0.2 % in the 435 and 438 nm channel, respectively.

This is evident in the longer-term behaviour of the signal after flushing the chamber, from about 8000 s onwards, which shows smaller fluctuations in the 438 nm channel.

In this experimental system, the intention of splitting of the beam into two channels and later recombining them aimed to demonstrate the principle of the two-channel method. However, the different beam paths and reflection angles in this optical configuration may have contributed to some system noise that was not equal in both channels. The 435 nm channel enters the narrow bandpass filter at a larger angle than the 438 nm channel and is therefore more prone to beam clipping at the edge of the optic. The 435 nm channel also has a longer beam path and an extra turning mirror. Noise with a common source in both channels will be reduced by taking the ratio of the two channels, whereas noise associated with each channel separately will not.

The ratiometric two-channel method (Equation 1.6) was applied to the integrated intensities $I_1(\lambda_1)$ and $I_2(\lambda_2)$ and calibrated against the CL analyser by plotting the CL response against the two-channel response (Figure 4.7). The two-channel response was then scaled to match the CL measured concentrations. The standard deviation (1σ) of the ratiometric two-channel system was calculated from 140 – 160 minutes when NO_2 had been completely flushed from the chamber and was found to be 31 ppb over 1 minute. Kalman filtering (variance in measurement noise, $R = 0.1^2$, and the true concentration variance, $Q = 0.03^2$) was applied to the two-channel response to improve the signal-to-noise ratio (SNR). The standard deviation decreased to 8 ppb after applying the Kalman filter. The effective mirror reflectivity (R_{eff}) was calculated to be 0.9984 giving an effective path length (L_{eff}) of 238 m.

A longer path and higher sensitivity were expected from the optical cavity, and it was later discovered that the cavity mirror purge inlets were inadequately sealed, with the result that the sampled air from the chamber was partially diluted by room air during the experiment. The change in ratio was therefore smaller than expected for a mixing ratio 1 ppm of NO_2. This dilution of the sample led to uncertainty in the calculated effective reflectivity of the cavity mirrors and therefore in the effective pathlength. Potential variability in the dilution ratio inside the optical cavity cell could be responsible for the apparent signal fluctuations in both channels seen in Figure 4.5.

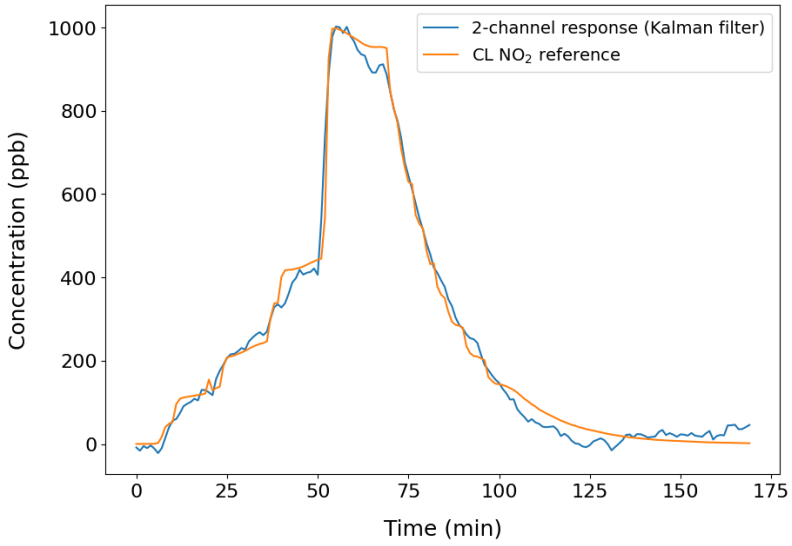


Figure 4.7. Kalman filtered ratiometric two-channel response compared with chemiluminescence reference NO_2 measurement.

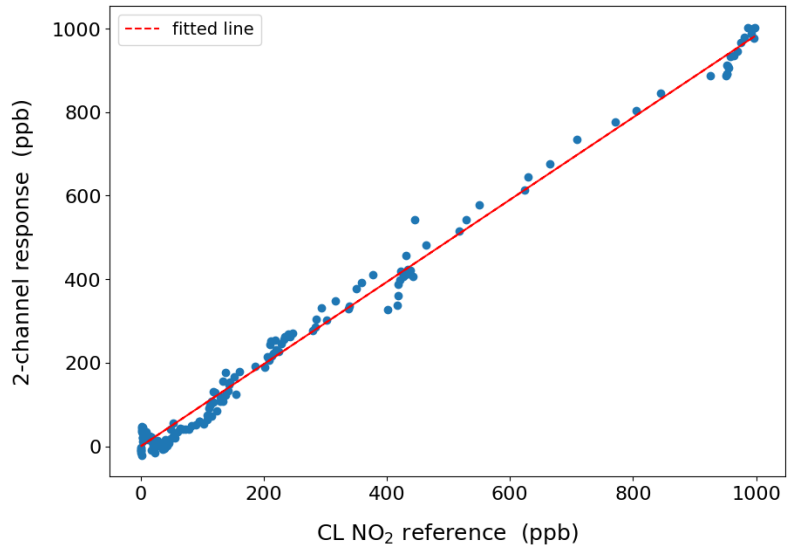


Figure 4.8. Correlation plot of the Kalman filtered ratiometric two-channel response and chemiluminescence (CL) reference response. R^2 = 0.99, slope = 0.98, intercept = -0.51.

Despite the gas leak, a strong linear correlation between the ratiometric two-channel demonstration system and the CL reference was observed with $R^2 > 0.99$ and y-intercept of -0.51 (Figure 4.8). This ratiometric method can achieve fast, in situ measurements of ambient NO_2 with a standard deviation (σ) of 50 ppb in 10 s and 30

ppb over 1 minute. The standard deviation of the CL monitor is 0.3 ppb over 1 minute sampling time, a factor of 100 better than the ratiometric two-channel system.

The sensitivity of the ratiometric instrument could be improved in a number of ways. Firstly, increasing the light throughput in the system is a key consideration. The 12.5 mm diameter of the cavity tube attenuated the light throughput much more than a larger bore tube. The relatively large LED emission angle (± 75°) also resulted in appreciable light losses through the component apertures in the optical system. Overall, however, this optical system demonstrated that it is feasible to use a single narrow bandpass filter to create two spectrally distinct channels. This configuration has the advantage that it reduces the optical component cost of the instrument. Nevertheless, the configuration adds complexity to the system design, is difficult to align, and the channels are prone to clipping, particularly in the shorter wavelength channel where the narrowband filter must be turned to a larger angle.

A CCD spectrograph was used here to confirm that two discrete wavelengths from an LED emission spectrum can be monitored to detect changes in NO_2 concentration at a level of sensitivity suited to ambient levels of NO_2. However, dispersive detectors such as that used in this study are expensive and can be quite sizable. Ultimately the goal of this work is to move towards the use of simpler and cheaper nondispersive detectors like photodiodes in the further development of the ratiometric two-channel approach.

Demonstration using non-dispersive detectors

Since dispersive detectors record the full spectral response of an LED, much of the spectral information gathered (as in the experiment above) is lost by integrating over a small number of pixels. If the selected operating wavelengths, λ_1 and λ_2, are sufficiently narrow they can be treated as quasi-monochromatic, allowing non-dispersive detectors, such as photodiodes or photomultiplier tubes, to be used to monitor the signal in each channel. The advantages of such non-dispersive detectors is that they are more compact, lightweight and cost-effective than spectrographs. Signal analysis is also greatly simplified and does not require user control and oversight of a spectral analysis procedure.

Photodetectors such as photodiodes or V/I output photomultiplier tubes produce a current or voltage proportional to the amount of light received at their active surface area and the device's responsivity ($\Re(\lambda)$). Non-dispersive detection is widely applied to the infrared region (Fu et al., 2023; Popa & Udrea, 2019) and UV/vis (Bailey et al., 2024; Castellanos et al., 2009; Kebabian et al., 2007). The differences between photodiode (PD) and photomultiplier tube (PMT) performance have been discussed in Chapter 3.

Two photomultiplier tube modules (Hamamatsu, MicroPMT H12405) were used to demonstrate the ratiometric two-channel principle with non-dispersive detectors. The chosen PMT modules respond to light between 300 – 650 nm with peak responsivity at 400 nm and output a voltage proportional to the incident light intensity. The PMT modules were driven with ± 5 V from a benchtop power supply (Tenma, 72-2640). For absorption measurements of NO_2 at blue wavelengths, the responsivity spectrum of a PMT is preferable to that of a Si photodiode which has its peak responsivity at ~ 760 nm. The photodiode responsivity to longer wavelengths could be problematic, particularly when using optical cavities which efficiently transmit light outside of its high reflectivity wavelength region (Section 3.3). PMTs are inherently amplified and much more sensitive than photodiodes to light. The PMT gain can be varied from 10^3 to 10^7 by adjusting a control voltage, making these modules suitable for detecting low levels of blue light, as is the case when measuring narrow spectral transmission bands, or when using optical cavities.

The optical configuration of the detection scheme was adapted to use two nBPFs in a more straightforward optical geometry that is easier to align (Figure 2.4). This arrangement is also less prone to losses due to beam clipping, which also reduces instabilities in the relative signals of the channels. The importance of reducing beam clipping in spectroscopic approaches has been discussed by Tuzson et al. (2013), Engel et al. (2001) and Das & Wilson (2011) in order to maximize the signal throughput and reduce instabilities. The new detection scheme was tested using an 8 m folded path across the ERI atmospheric simulation chamber (Figure 4.9).

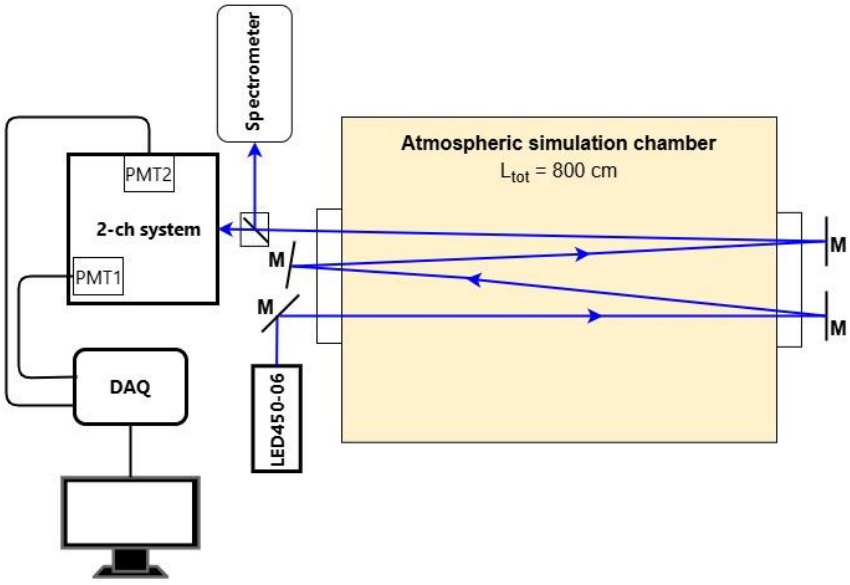


Figure 4.9. Schematic of 8 m folded path across the ERI atmospheric simulation chamber. The beam is split before entering the two-channel detection system and the full spectrum is collected by a spectrometer for DOAS analysis.

The response of both PMTs in the absence of NO_2 in the chamber was recorded with 1 s time resolution to investigate the time-dependence of the system precision. Figure 4.10 shows the Allan deviation of both PMT voltages and of the resulting ratio. The Allan deviation shows that the two PMTs have distinct noise characteristics. The precision of PMT1 is worse than that of PMT2 at short times, but improves with averaging up to 100 s, whereas that of PMT2 only improves up to 20 s. The ratio of the two signals reaches a minimum deviation of 6×10^{-4} over 100 s, equivalent to a mixing ratio of 152 ppb. This is a good sensitivity for such a short pathlength and in an instrument intended to demonstrate the two-channel approach with nondispersive detectors.

The sensitivity of the instrument could be improved by increasing the path length, albeit at the expense of a smaller signal. Moreover, identical photodetectors should be used in balanced detection schemes to ensure that they have similar noise characteristics (Section 1.4). Sihler and coworkers (2009) found that tilting the LED may reduce étalon effects and improve the detection limit, σ, by a factor of 2.

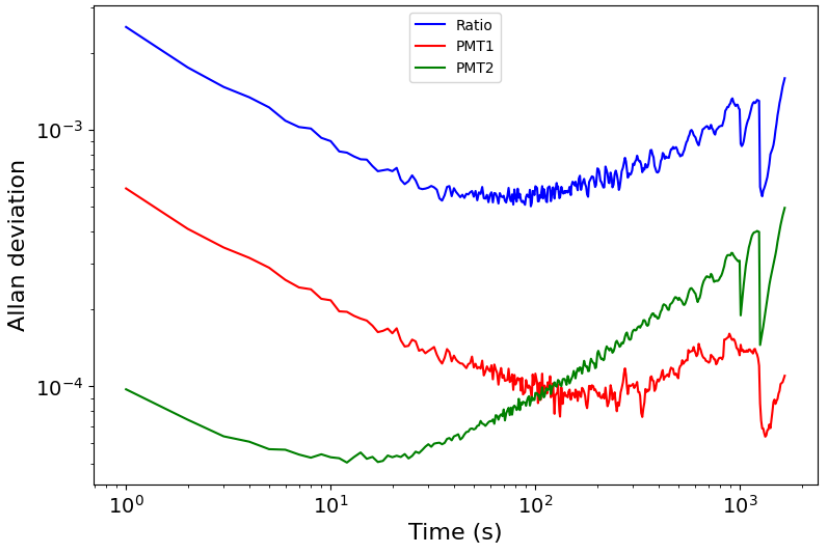


Figure 4.10. Allan deviation of two PMTs and of their ratio. PMT1 and PMT2 have different noise characteristics, with PMT2 being less noisy but subject to greater drift over time.

Incoming light from the chamber was split before the ratiometric two-channel detection scheme so that the full spectrum could be collected and analyzed using the DOASIS spectral analysis program. As the path length through the sample was known precisely, the DOAS measurements were used as a reference method for NO_2 concentrations in the chamber to validate the system being tested. Zheng et al. (2024) used a similar approach to compare a mini-BBCEAS instrument to both CL and CAPS reference methods. DOAS is a robust technique used to validate satellite measurements, for example, in the PANDONIA global network (Edwards et al., 2024; Lange et al., 2024).

Figure 4.11 shows the normalized intensities of the PMTs, $I_1(\lambda_1)$ and $I_2(\lambda_2)$, where λ_1 and λ_2 are the system operating wavelengths at 437.3 and 439.3 nm, respectively, sampling at 1 Sa/s and averaged across 10 s. The absorption cross-sections at the system's resolution (defined by the nBPF bandwidth) are $\sigma_1 = 4.2\times10^{-19}$ cm^{-2} molecule^{-1} and $\sigma_2 = 6.3\times10^{-19}$ cm^{-2} molecule^{-1} yielding a differential absorption cross-section, $\Delta\sigma$, of 2.1×10^{-19} cm^{-2} molecule^{-1}. As expected, there is a larger decrease in signal in the stronger absorbing channel, $I_2(\lambda_2)$, compared to $I_1(\lambda_1)$ of 8.0 % and 4.5 % for 12.5 ppm NO_2. At the baseline intensity before adding NO_2, the standard deviation of the signal from PMT1 is 0.2 % and that of PMT2 is 0.1 %, again indicating

that these photodetectors have different noise characteristics. It is recommended that detectors are purchased at the same time and from the same batch to minimize differences in manufacturing.

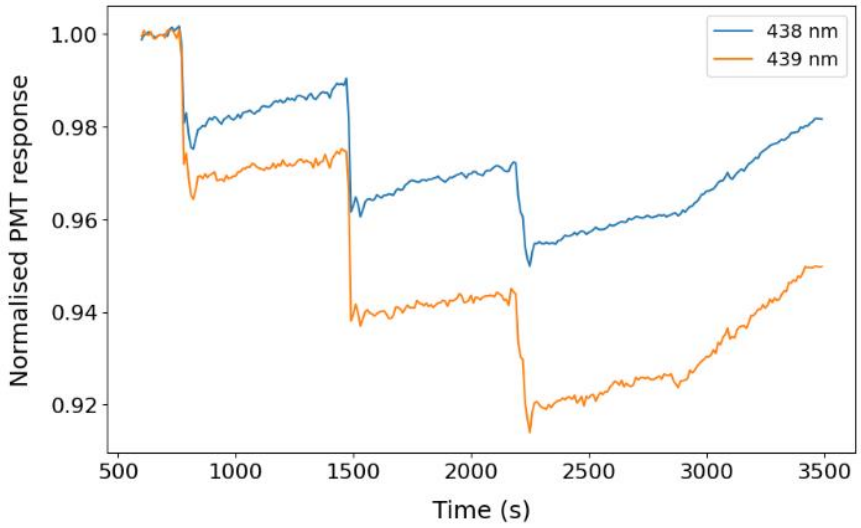


Figure 4.11. Normalised response of PMT1 and PMT2 to NO_2 additions in the atmospheric simulation chamber with an 8 m path length.

Based on the ratio of the measured intensities, the 1σ measurement precision of the two channel system is 136 ppb when averaged across 1 minute, comparing favourably with the DOAS reference which has a limit of 145 ppb for the same averaging time (Figure 4.12). Applying Savitsky-Golay filtering with a window of 50 data points improved the two-channel system limit to 71 ppb. Figure 4.13 shows that the ratiometric two-channel method is well-correlated with the DOAS reference (R^2 > 0.97, y-intercept = 0.99). Assuming other factors do not affect the SNR, we estimate the detection limit would be 2.3 ppb over a 250 m path length. This theoretical improvement agrees well with Chen et al. (2020) who reported a limit of detection of 2 ppb in field measurements using ratiometric open-path dual-beam laser spectroscopy to measure NO_2 across a path length of 1.3 km. Longer path lengths are realized using either long open paths or optical cavities. However, longer paths reduce the signal amplitude so that signal amplification is typically required. Even so, this method is sensitive enough to be applied over short path lengths (for example, industrial exhaust

stacks) for continuous emission monitoring where NO_2 concentrations could be much higher than ambient levels.

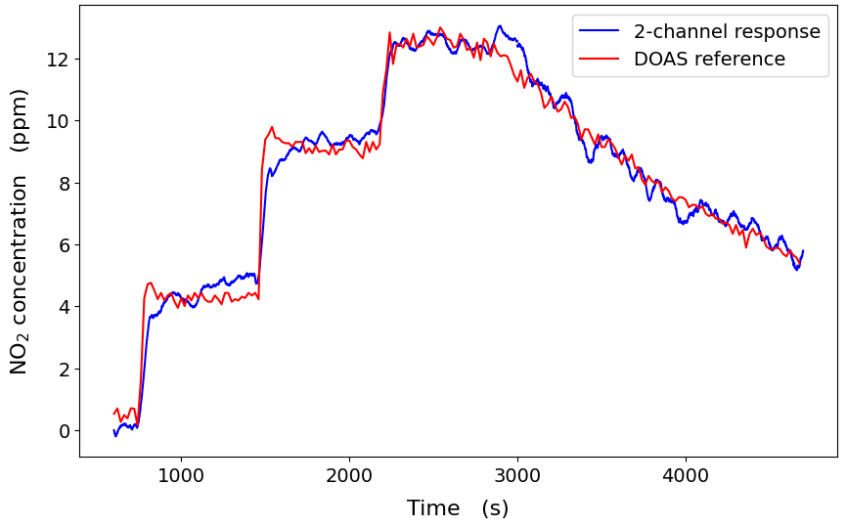


Figure 4.12. Calibrated ratiometric two-channel response (SG filtered) compared with DOAS reference concentrations.

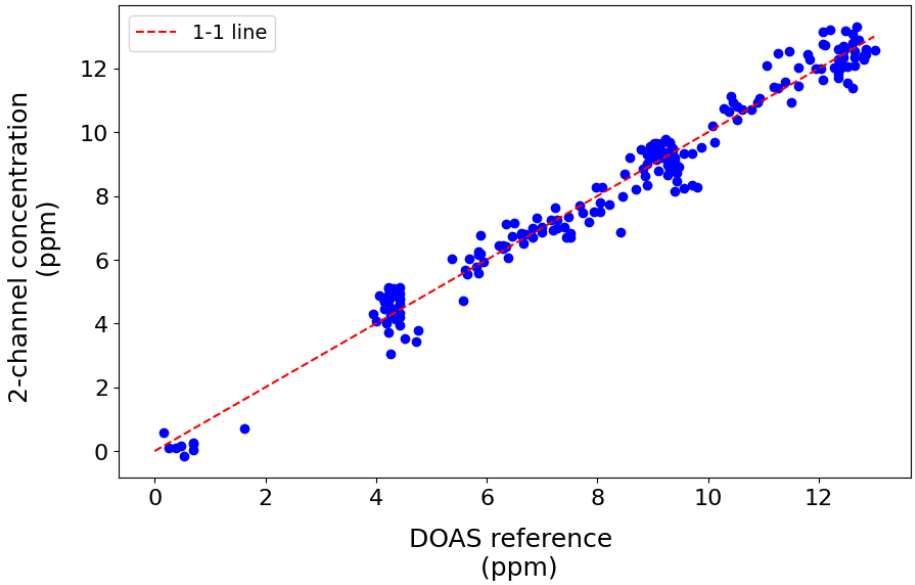


Figure 4.13. Correlation plot of concentrations measured by the ratiometric two-channel and DOAS reference instruments. $R^2 = 0.97$, intercept = 1.

Improving sensitivity to NO_2 over shorter path lengths would advance new applications. In particular, relatively short (e.g., less than 200 m) open path measurements could be made across roads to capture the emissions of passing vehicles. In the field, the signal across a long atmospheric path might fluctuate for several reasons. In addition to changes in the LED output, other common fluctuations include polarisation and other loss processes such as reflection, refraction, and scattering in the atmosphere. To demonstrate that the two channels would strongly suppress noise from a common source, a further experiment was carried out in which the light intensity in both channels was attenuated across a large intensity range.

Two polarisers were mounted on the atmospheric simulation chamber: one polariser was placed immediately after the light source and could be rotated to attenuate the light beam into the detector system and a stationary polariser was placed just before the ratiometric two-channel detection scheme. Figure 4.14 shows the change in normalised intensity in each channel.

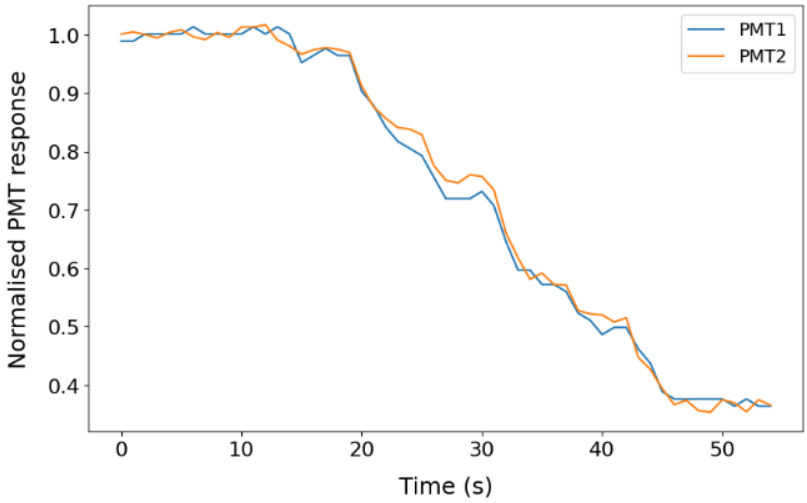


Figure 4.14. Normalised response of PMT1 and PMT2 as the polariser angle is increased continuously over time, changing the beam path and polarisation.

Both PMTs responded similarly as the polarisation angle reduced the light into the detectors, showing that this 2-channel method is relatively insensitive to changes at atmospheric transmission. Figure 4.15 confirms a strong linear relationship between both channels with an R^2 value of 0.995 and y-intercept of 0.0037 when changes in

the signals are not spectrally dependent, as would be the case for changes in NO_2 across the optical path. This experiment highlights the suitability of using the ratiometric two-channel method for long-path field measurements where both channels will decrease or increase simultaneously unless NO_2 is absorbed to change the relative light transmission in each channel.

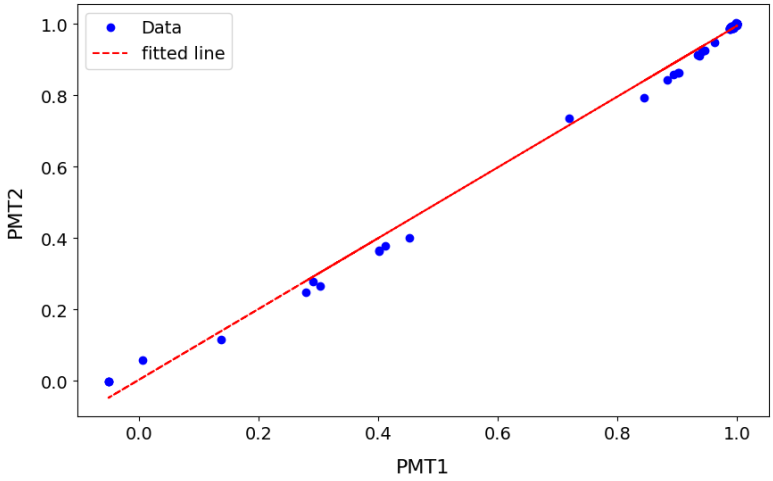


Figure 4.15. Correlation of both PMTs as the polarisation angle is changed. Channels show a linear relationship with $R^2 = 0.99$, slope = 0.99, intercept = 0.0037.

4.3 Signal amplification using lock-in detection

Small optical signals are difficult to process because they can be obscured by noise. Either sensitive detectors or signal amplification (or both) are required to produce a useful response. PMT detectors inherently amplify the signal and are highly sensitive to light. However, they have drawbacks, notably their much higher cost than photodiodes (e.g., €640 for a Hamamatsu H12405 PMT module compared to €14 - €150 for a Thorlabs photodiode). Furthermore, PMTs are vulnerable to damage from overexposure and have a long warm-up period. Photodiodes, on the other hand, do not have internal signal amplification and are much less sensitive than PMTs. Therefore, photodiodes require external signal amplification to measure low levels of light from narrow wavelength channels or light transmitted through an optical cavity. As

discussed in Section 1.4.3, lock-in amplification is a useful strategy for amplifying signals obscured by noise, including for the ratiometric two-channel method. Lock-in amplification is particularly attractive for long-path measurements through the atmosphere because background light is not modulated, and the signal at the reference frequency can be amplified and distinguished from non-modulated background light.

A benchtop lock-in amplifier (Stanford Research Systems, SR830) was used to amplify a biased silicon photodiode (Thorlabs, DET10A) to monitor changes in intensity of the narrow operating wavelengths, $I_1(\lambda_1)$ and $I_2(\lambda_2)$. The signal was modulated at 500 Hz to remove low and high frequency sources of noise. The SR830 lock-in amplifier has one single-ended input channel (A) as well as a differential channel (A-B) which amplifies the difference between channels, but does not output amplified A and B signals, so the ratiometric change in intensities cannot be monitored with this instrument. Since the difference in channels is small for trace levels of NO_2, the differential (A-B) channel was not used in this work. A lock-in amplifier with independent amplification of two single-ended input channels modulated at the same frequency and phase would be desirable for the ratiometric two-channel method. Due to these limitations, this study amplified one narrow wavelength band to test the suitability of lock-in amplification for measuring changes in $I_1(\lambda_1)$ and $I_2(\lambda_2)$ for the ratiometric two-channel method.

As in Figure 4.9, an 8 m folded path was configured across the 2 m long ERI atmospheric simulation chamber by mounting turning mirrors outside the Perspex windows. A schematic of the optical system through the chamber is shown in Figure 4.16. A blue LED (Roithner, LED430-06) mounted in a passive heat sink was driven by 3.6 V and modulated at 1 kHz by a function generator (TTi, TG2000). The lock-in amplifier had a time constant of 300 ms and a data acquisition unit (PicoTech, ADC-20) sampled the output voltage every 1 s.

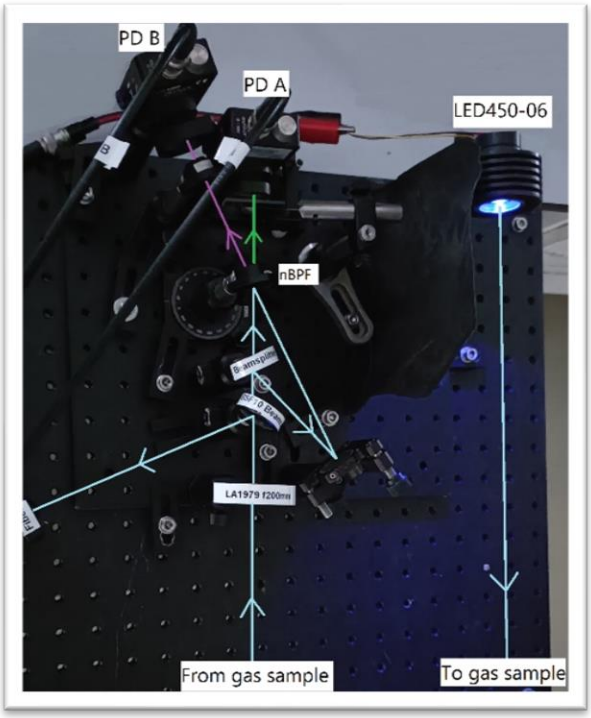


Figure 4.16. Photograph of ratiometric two-channel detector. One narrow bandpass filter is used to select both operating wavelengths. Only the signal from photodiode A is measured as only the lock-in amplifier's single channel input was used.

The path length of 8 m was limited by the dimensions of the simulation chamber and by low light throughout owing to geometric losses. In addition, there were considerable losses to reflections and scattering at the Perspex windows through which the beam passed 8 times. As a result, this configuration was not expected to be highly sensitive, although we note that the sensitivity is readily improved where circumstances permit increasing the light path length, for example, in open path remote sensing applications. An extractive CL NO_x analyser (Teledyne T200 $NO/NO_2/NO_x$ Analyzer) was used as a reference measurement of NO_2 concentrations in the simulation chamber. The CL analyser recorded NO_2 concentrations in 1 minute intervals.

NO_2 was injected in volumes of 5 mL into a stream of air flowing into the chamber. The NO_2 was introduced through a port on the opposite side of the chamber to the CL extraction port to avoid extreme concentrations of NO_2 near the sampling port. The time series of the intensity at λ_1 (439.4 nm; convolved absorption cross-section = 6×10^{-19} cm^2 $molecule^{-1}$) over the experiment is shown in Figure 4.17. The standard

deviation (1σ) was calculated from the first 25 minutes of this experiment when there is no NO_2 present in the chamber and had a value of 58 ppb. Assuming the same signal-to-noise ratio, this precision could be improved to 1.8 ppb over a pathlength of 250 m or 0.46 ppb over 1 km. Such pathlengths are readily realized using optical cavities or long path field measurements.

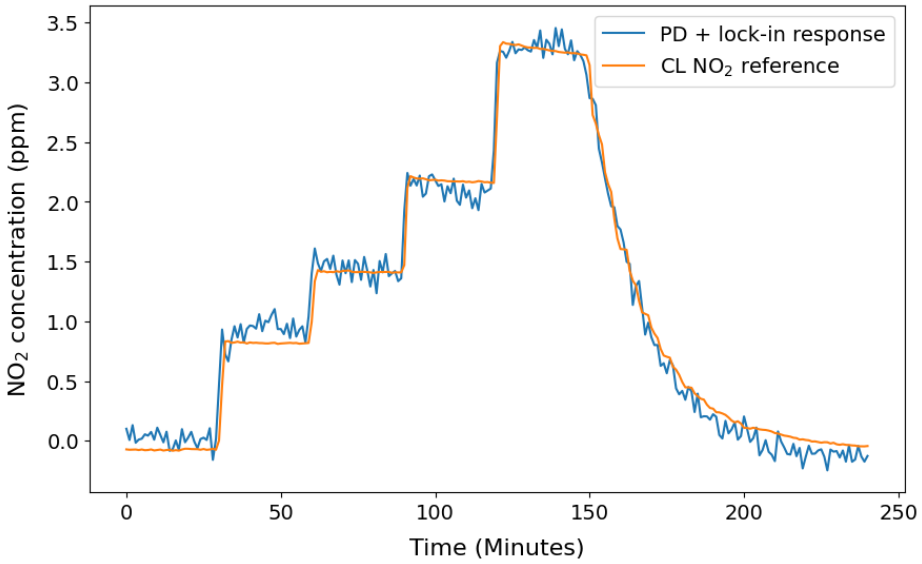


Figure 4.17. Photodiode and lock-in amplifier response to changing NO_2 concentration in the atmospheric simulation chamber compared to chemiluminescence reference NO_x analyser.

Assuming both channels would have comparable and independent noise characteristics in a ratiometric two-channel system, the total system noise limit would be:

$$u = \sqrt{u_1^2 + u_2^2}$$

where u is the total system noise and u_1 and u_2 are the noise levels in each channel. Therefore, the precision of the ratiometric two-channel system over 8 m in 1 minute averaging is 82 ppb, and improves to 2.5 ppb over 250 m, and 0.65 ppb over 1 km. The sensitivity decreases in a ratiometric two-channel method because each channel has its own independent noise. Although common-mode noise is effectively reduced, noise features in each channel are added in quadrature. Nevertheless, the ratiometric

two-channel method gives good selectivity to NO_2 because the ratio of intensities of the operating wavelengths is affected little by scattering or other absorbing species in this wavelength region, especially when considering urban and roadside environments dominated by NO_2. System selectivity is discussed in more detail in Chapter 2.

As with the previous spectroscopic systems, this short, single path configuration of several metres can be applied to continuous emission monitoring in circumstances where high NO_2 concentrations are expected. To monitor ambient levels of NO_2, however, longer path lengths are required to assess compliance with WHO guidelines and EU legal air quality standards. Photodiodes with lock-in amplification are suitable to use in a ratiometric two-channel detection scheme provided the lock-in amplifier can record two input channels such that the ratio of channels can be monitored. Although the lockin amplifier used to demonstrate the measurement principle in this section is an expensive (±€6,000), non-portable benchtop device, there is growing interest in reducing the cost and size of lock-in amplifiers for integration into low-cost systems. One such example is the open-source lock-in amplifier (OLIA) recently published by Harvie and coworkers (2023), which would be potentially useful for this type of measurement. Two identical OLIA modules would be required however, as there is only one input channel. Nevertheless, the low-cost of the OLIA (€35) and similar amplifiers, and their low power consumption and small dimensions, are promising tools for use of modulated spectroscopic instruments, whether in laboratory environments or in field measurements.

4.4 Single-channel CEAS system

The two-channel ratiometric instruments presented above face challenges associated with the low light levels transmitted through the system. The low signal associated with these measurements results in a moderate sensitivity to NO_2. Specialised detectors or amplifiers are also required to measure the small signals from ambient NO_2 concentrations. This section considers an alternative strategy in which a single, wide spectral passband is used in combination with an optical cavity to produce a larger transmitted intensity signal. Selectivity to NO_2 is reduced with less spectral information in this approach; however, this may not be as important in samples where

NO_2 is the dominant absorber and where particulate matter can be removed from the inlet stream, as was done by Bailey et al. (2024), Birks et al. (2018) and Zhou et al. (2022).

43 cm Optical Cavity

An optical cavity was built with a mirror separation, *d*, of 43 cm, with a Semrock FF01-440-40 wide bandpass filter (wBPF) that transmits wavelengths between 420 and 460 nm placed before the optical cavity input to remove longer wavelengths from the cavity input. The system schematic is shown in Figure 4.18. This wavelength region was chosen as other absorbing gases, such as glyoxal and methyglyoxal, have absorption cross-sections an order of magnitude lower than NO_2 over this range and are present in much lower concentrations at ambient level. As a result, interference from other absorbing gases is not expected.

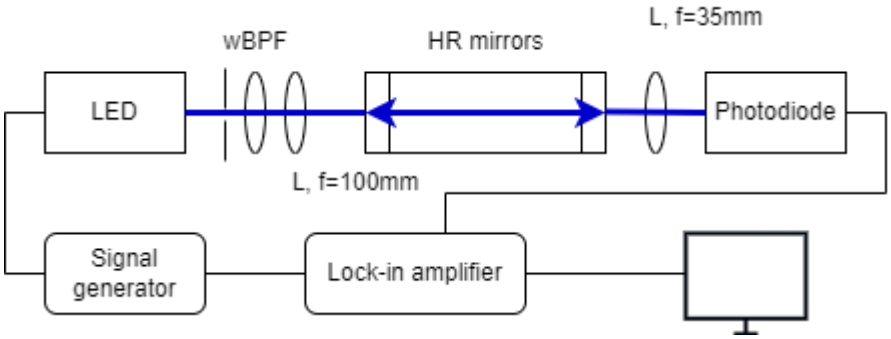


Figure 4.18. Schematic of CEAS wide band pass (wBPF) instrument. The lock-in reference frequency is provided by a signal generator used to drive the LED.

A single-channel wide-bandpass system is susceptible to interference from scattering by particulate matter; to remove interference from aerosol extinction, an inline PTFE filter (Pall 2 µm filter, diameter = 47 mm) was installed in the inlet line. Note that the PTFE filter also served to preserve the cavity mirror reflectivities in this system which had no mirror purge. Similar approaches have been used by other researchers to protect the mirrors and eliminate the need for external gas supplies, such as that as discussed

by Zhou et al. (2022) who used a PTFE filter to remove particles from a diode laser amplitude-modulated CEAS system.

The transmitted light intensity through the cavity was measured with a biased photodiode (Thorlabs, DET10A). The LED (Roithner, LED-430-06, 430 nm maximum output wavelength) was modulated at 1 kHz and the photodiode signal was amplified using a benchtop lock-in amplifier (Standford Research System, SR830). This system was then tested for its potential to make fast NO_2 measurements in an urban traffic environment. The lock-in amplifier had a time constant, τ, of 1 s and the signal from the lock-in amplifier was recorded by a Measurement Computing USB-1208HS-4AO data acquisition unit every 3 s. Air from IASC was sampled at a rate of 4 L/min into the optical cavity cell with volume 844 cm^3, giving a residence time of 13 s inside the cavity.

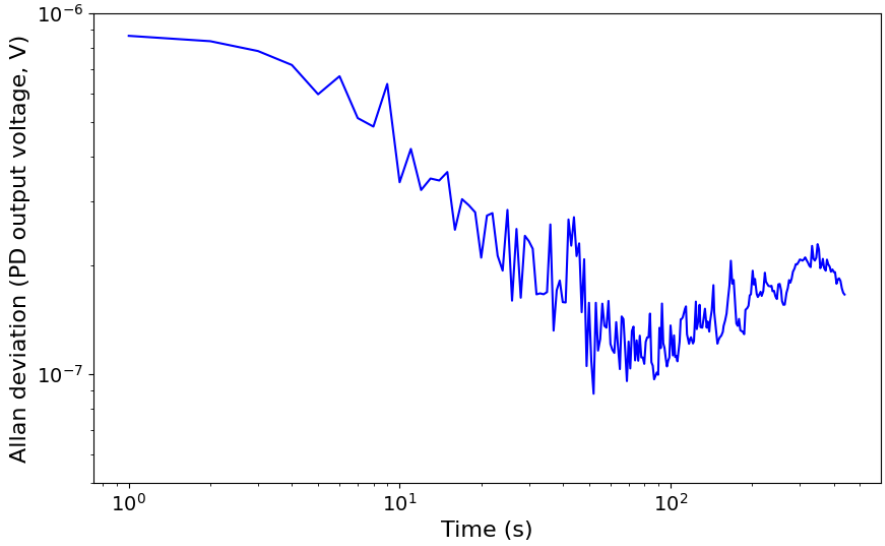


Figure 4.19. Allan deviation of the optical cavity instrument in the absence of absorbers. The sensitivity of the instrument will improve with averaging up to 60 s, after which longer term drifts in the system affect the signal and sensitivity reduces.

Instrument performance was characterised by Allan analysis. The system was run for 1 hour with no absorbing gases present in the simulation chamber. The Allan deviation is shown in Figure 4.19 above. The sensitivity of an instrument improves as averaging time is increased because short term system noise is smoothed, however, if the signal

is averaged for too long, longer term drifts begin to be included in the signal and reduce system sensitivity (Skřínský et al., 2009). The minimum deviation, 10^{-7} V, occurred at 1 minute averaging and was equal to a minimum detectable mixing ratio of 1.5 ppb. After 60 s, the sensitivity of the instrument deteriorates. At 10 s averaging time, the Allan deviation of the system is 2×10^{-7} V resulting in a minimum detectable mixing ratio of 3 ppb. These parameters would be suitable for measuring NO_2 in an urban traffic environment where concentrations are typically well above 3 ppb.

Experiments were carried out in the 28 m^3 IASC atmospheric simulation chamber. A Teledyne NO_x analyser and O_3 monitor (Teledyne T200, T400) recorded 1 min average concentrations; these measurements provided a reference NO_2 concentration for this experiment. NO and O_3 were mixed in a 2:1 ratio (200 ppb NO:100 ppb O_3) to form NO_2. NO was introduced in two steps, at 10 minutes and 40 minutes, followed by addition of O_3 at 55 minutes. The single channel CEAS system response to NO_2 in the chamber is shown in Figure 4.20. Some initial drift in the baseline concentration is seen in this experiment, with the measured value settling near 0 ppb after 30 min. The drift in the CEAS system is presumed to arise from a warm-up period for the system. The standard deviation (1σ) of the original CEAS signal was calculated from 30 min to 50 min in this experiment, where the instrument had warmed up and no NO_2 was present in the chamber. The standard deviation was found to be 6.5 ppb in 3 s, which is not quite low enough for a traffic environment with low baseline concentrations. The CEAS measurements were therefore averaged over 30 s and filtered using both Kalman and Savitsky-Golay filtering to find the optimum method for smoothing data. The standard deviation of the NO_2 mixing ratio for a 30 s running average was 2.2 ppb, improving the signal-to-noise ratio from 14 to 41.

Ideally, a faster time resolution is needed to capture emissions from individual vehicles as they pass a sensor. A Kalman filter ($R = 2^2$, $Q = 0.6^2$) applied to the 3 s measurements reduced the standard deviation of the NO_2 mixing ratio to 1.1 ppb. As can be seen in Figure 4.20, the Kalman filter partially reduced the time response of the instrument. The Savitsky-Golay filter, applied over a 1-minute window with a 3rd order polynomial, reduced the NO_2 standard deviation to 0.95 ppb and maintained a fast time response. It was concluded that Savitsky-Golay filtering is an appropriate choice for reducing system noise while maintaining a fast response time (Chen et al., 2021; Li, 2011).

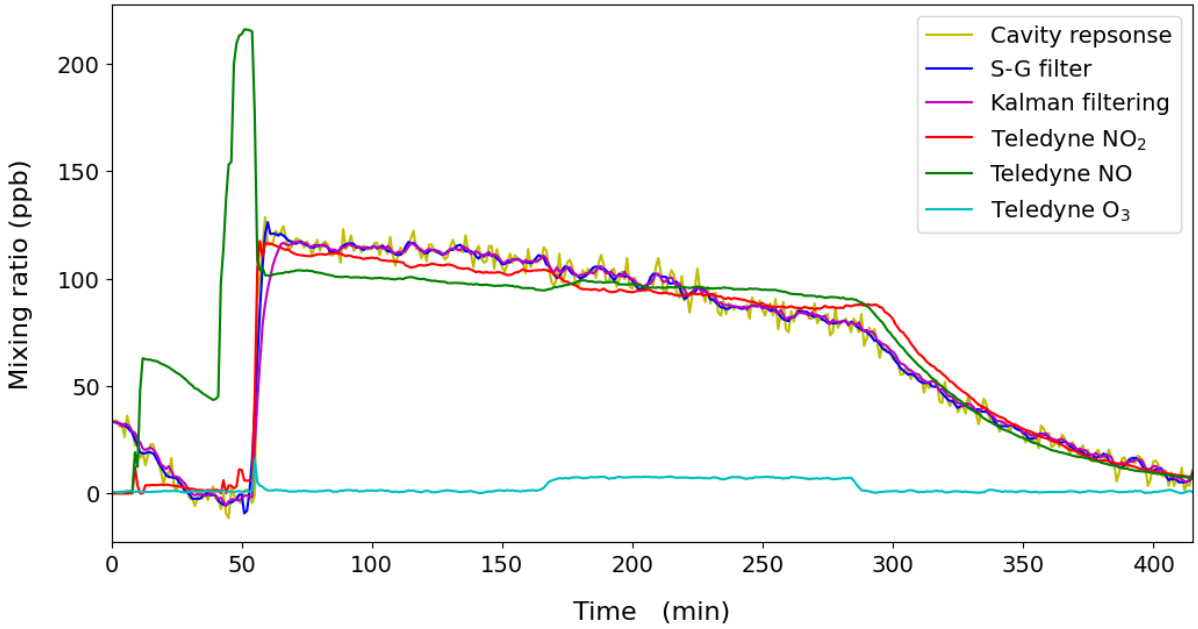


Figure 4.20. Wide-band CEAS instrument response to NO_2 in the IASC chamber. 200 ppb of NO (added in two stages at 20 min and 40 min) and 100 ppb of O_3 (added after 50 min) reacted to form NO_2. The chamber's UV lights were switched on from 160 min to 290 min to photolyse NO_2, and the chamber was flushed after 290 min. Teledyne chemiluminescence analysers were used for reference measurements of NO_2, NO, and O_3 mixing ratios.

The wide-band instrument did not show a distinct drop in signal from NO_2 photolysis after the chamber lights were switched on at 160 minutes. A small time lag is also seen in the Teledyne response to NO_2 when flushing commenced after 290 min, whereas both the Teledyne NO and the CEAS NO_2 mixing ratios began to decrease before the Teledyne NO_2 measurements (red line, Figure 4.20).

Part of the time lag is likely because CL detectors do not measure NO_2 directly but calculate its concentration from a measurement of NO and total NO_x, which are measured sequentially. When NO_2 levels change quickly over time a small delay may be observed in CL measurements. The signal from the wide-band CEAS instrument decreases in line with the other gases, showing the improved time resolution of this instrument. This difference in time response is reflected in the strong linear relationship ($R^2 > 0.97$) shown in Figure 4.21. Deviations from linearity arise around

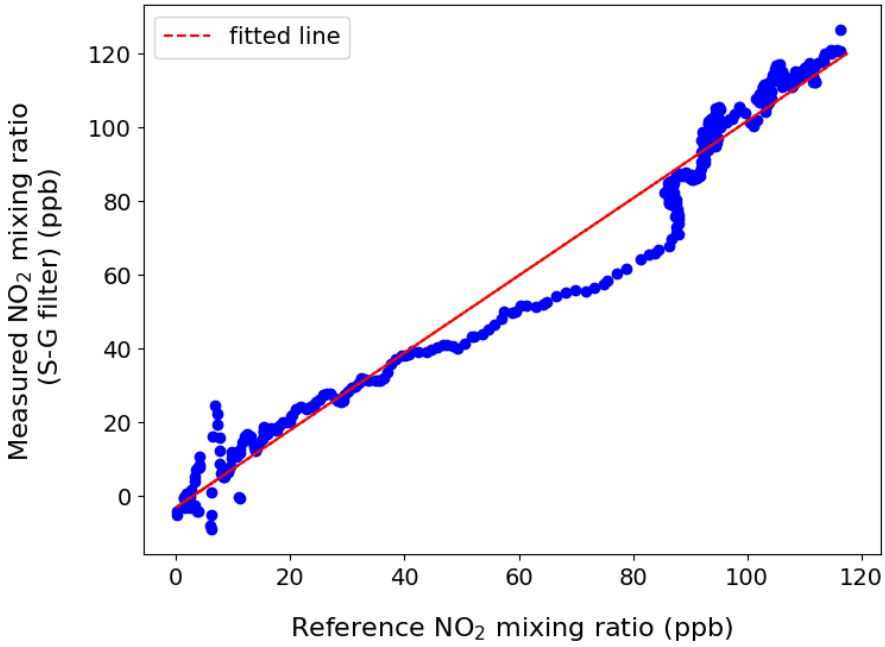


Figure 4.21. Correlation of the reference NO_2 mixing ratios compared with the measured concentrations of the wide-band instrument. Data smoothed by the Savitsky-Golay filter were used here for comparison. The line of best fit is shown with $R^2 = 0.98$, slope = 1.05 and intercept = -3.14.

80 ppb due to the sequential nature of the Teledyne NO_2 measurement during a period in which the concentration changed rapidly. As flushing proceeds and the rate of change of concentration decreases, so the CL measurements re-converge with the wide-band CEAS measurements.

The reflectivity of the cavity mirrors was calibrated based on the reference NO_2 mixing ratio, giving an effective mirror reflectivity, R_{eff}, of 99.21 %. This mirror reflectivity produces an effective path length within the cavity, L_{eff}, of 55 m. This is a short path length for an optical cavity but still demonstrates sensitivity useful for monitoring ambient levels of NO_2 with a good time resolution. It is worth noting that this physical pathlength could be used to measure across a road in an open-path system, which is the focus of other research projects in the research group. The g-parameters of the resonant cavity were $g_{1,2} = 0.57$, satisfying $0 \leq (g_1 g_2) \leq 1$. While this cavity configuration is stable, the cavity length could be further optimised to maximise the output signal, for example, by using a confocal cavity arrangement, as discussed by

Fiedler et al. (2007). Such improvements would further improve the instrument sensitivity and improve its performance for monitoring in the highly dynamic roadside environment and for mobile measurements.

1 m CEAS instrument

A longer optical cavity with 1 m mirror separation was constructed so that the cavity length more closely matched the radius of curvature of the cavity mirrors, giving a near confocal arrangement where $g_{1,2} \sim 0$. A photograph of the instrument is shown in Figure 4.22. This system used the same wide BPF (420 – 460 nm) as the shorter single channel cavity presented above and is termed the 1 m CEAS instrument. To reduce the complexity of the system, the benchtop lock-in amplifier and function generator were removed, and the photodiode was replaced with the same photomultiplier tube module (PMT) that was used in the ratiometric two-channel detection scheme (Section 4.2). Figure 4.23 shows the photodiode and PMT and highlights their similar compact dimensions. The LED (Roithner LED435-03) was driven by a constant voltage and current to increase the duty cycle and reduce the complexity of the system.

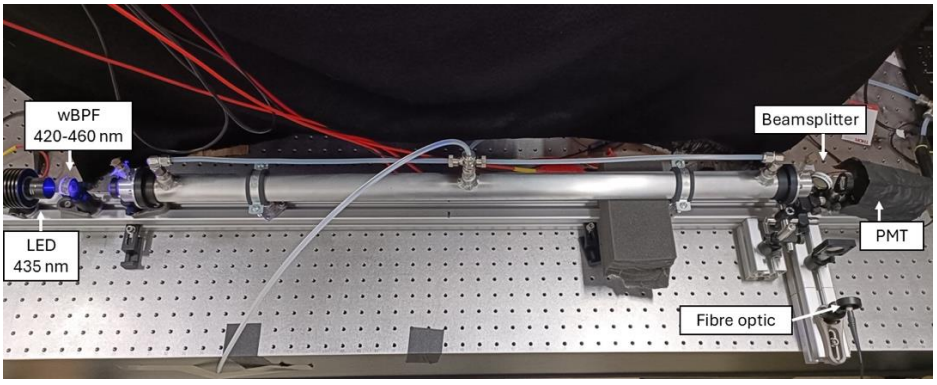


Figure 4.22. Photograph of 1 m CEAS instrument showing a blue LED centred at 435 nm and a wide bandpass filter (wBPF). The cavity output is split by a beamsplitter with one channel focused onto a photomultiplier tube (PMT) and one focused onto a fibre optic to collect the full spectral response.



Figure 4.23. Photograph of the photodiode (Thorlabs, DET10A) and PMT (Hamamatsu, H12405) used in this work.

The 1 m CEAS instrument was tested in the ERI atmospheric simulation chamber where the 8 m folded path DOAS measurement provided reference concentrations. This reference method had some advantages over the chemiluminescence NO_x analyser, which was not available for these experiments. DOAS uses the known wavelength-dependent absorption cross-sections and path length to robustly quantify trace gas species based on the Beer-Lambert law. DOAS is well-established in atmospheric observations and is used to validate data from satellite observations (Lange et al., 2024). For this application, the 8 m DOAS system is therefore considered a reference spectral method that directly detected NO_2 to compare with the 1 m CEAS instrument measurement. As seen previously, however, the short path length (8 m) of the DOAS reference was most suited to measuring high absolute concentrations of NO_2 in the chamber, including for calibrating the mirror reflectivity of the 1 m CEAS instrument.

5 mL of NO_2 was injected into the chamber on the side opposite the extraction port of the 1 m CEAS instrument. DOAS measurements were recorded with a 1 min acquisition time while the 1 m CEAS instrument recorded measurements at 1 s intervals; these measurements were averaged to 1 min resolution for comparison purposes. Figure 4.24 shows the instrument response compared to the DOAS reference measurement. Mixing ratios of up to 660 ppb were observed with a standard deviation of 2.1 ppb in 1 s and 0.6 ppb over 1 min. Applying a Savitsky-Golay filter with a 30 s

window achieved a precision of 0.6 ppb while maintaining the time resolution of the system and matched the instrument response time. The data was well-correlated with the reference measurement with an R^2 value of 0.94 (Figure 4.25). The relatively high level of scatter in the correlation is a result of the large fluctuations in the DOAS reference measurement — a result of the short path. The CEAS instrument saw a 29 % change in signal for 660 ppb, giving a calculated mirror reflectivity of 0.9960, and indicates an effective pathlength of 250 m in the optical cavity.

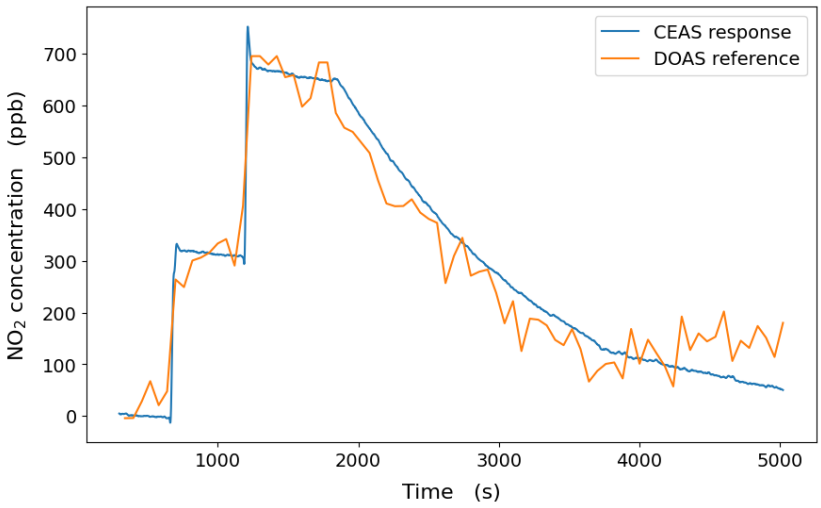


Figure 4.24. Mixing ratios in the ERI chamber experiment to assess the performance of the 1 m CEAS instrument. The CEAS instrument response time was averaged to 1 min and a Savitzky-Golay filter was applied to the measurements and achieved a standard deviation of 0.6 ppb. The DOAS reference measurement signal-to-noise is poor owing to the short, 8 m path.

The light output from the optical cavity was split with a 50:50 beam splitter, coupled via an optical fibre into a spectrometer (Andor, SR163). This reference channel therefore comprises an incoherent broadband cavity-enhanced absorption spectroscopy (IBBCEAS) system. The IBBCEAS spectral measurement was used as a highly selective reference to confirm and quantify NO_2 in the cavity. The IBBCEAS reference spectra were fitted to literature NO_2 absorption cross-sections, verifying the response of the PMT and CEAS instrument to NO_2. The concentration of NO_2 can be determined from these spectra since the effective path length of the cavity is known.

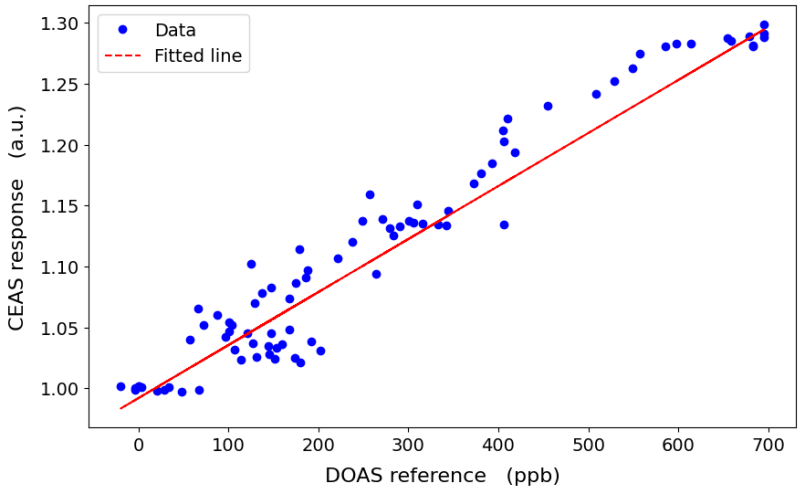


Figure 4.25. Correlation between the 1 m CEAS instrument response $\left(\frac{\Delta I}{I}\right)$ and the DOAS reference mixing ratios. The data are well correlated with an R^2= 0.94 and intercept = 0.99.

The potential of the 1 m CEAS instrument for measuring ambient roadside NO_2 concentrations was tested by sampling outside air. The ERI building is located at the border of a relatively low density residential area and the start of countryside. Air was sampled from the 1st floor laboratory window facing the Lee Road, Cork, on 17 July 2024 from 17:00 until 22:00. This road does not have a high volume of vehicular traffic and, combined with its location at the outskirts of the city, low NO_2 concentrations in air were expected, particularly outside of rush-hour times (5-6 pm). The 1 m CEAS instrument could therefore be tested in terms of measuring real roadside emissions at low mixing ratios.

Since there was no sampling period with zero-NO_2, the lowest PMT response was chosen as the value for I_0, the baseline intensity with no NO_2 present. The 1 m CEAS response compared to the full spectral IBBCEAS response is shown in Figure 4.26. Measurements over this period showed NO_2 mixing ratios were mostly below 10 ppb. Despite these low mixing ratios, the IBBCEAS and CEAS responses are well-correlated, with $R^2 > 0.74$. The IBBCEAS reference signal was small due to the low concentrations of NO_2 sampled. In addition, software problems attenuated the bit resolution of the CCD response, with the spectrometer signal saturating at around 1100 counts rather than around 64000 counts when operating normally. This lower

resolution (12 bits rather than 16 bit resolution) introduced quantisation noise and appreciably degraded the signal-to-noise ratio of the IBBCEAS system.

A UCC-run background air quality monitoring station (AQMS) is situated 2 km to the east of the ERI building. Mixing ratios at the ERI building are up to 10 ppb higher than the AQMS background site during peak driving times and falls off to the same background level at night.

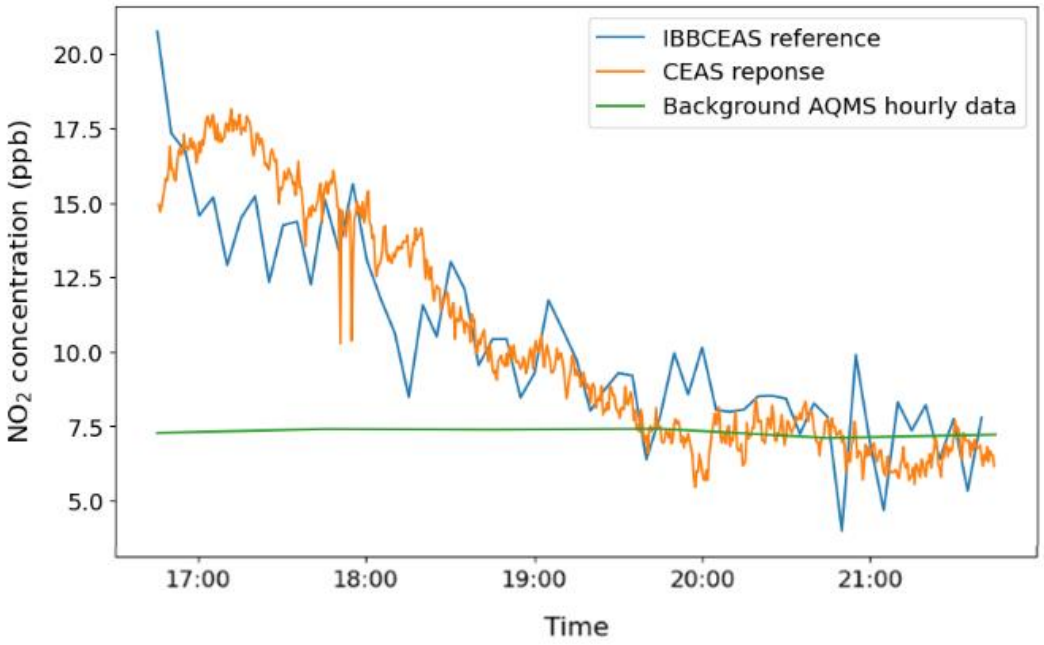


Figure 4.26. PMT CEAS response (orange line) to ambient NO_2 on the Lee Road on 17 July 2024 compared with full spectral response of the IBBCEAS reference (blue line) and measurements from the nearby AQMS (green line).

The measured PMT signal can drift over time, from fluctuations in the LED, changes in ambient temperature, cavity mirror movement, or drifts associated with the PMT itself. To get an accurate baseline reading, the instrument was modified for periodic flushing with NO_2-free air. To do so, the sample inlet was split so that the air could pass through a charcoal filter that scrubbed NO_2 from the air stream (Jeguirim et al., 2018; Yoo et al., 2015; Zhang et al., 2008). However, filtering the sampled air changes the flow rate and the pressure in the system. Figure 4.28 demonstrates that increases

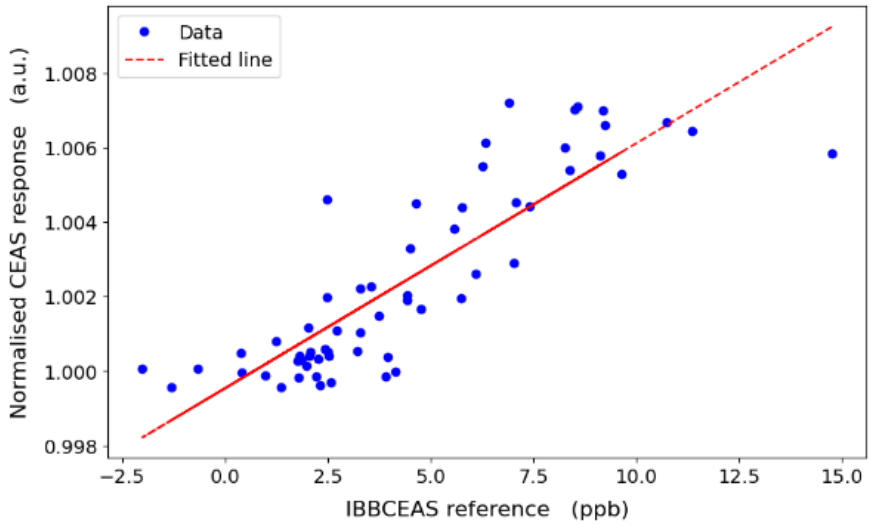


Figure 4.27. Correlation between the IBBCEAS spectral reference and the PMT CEAS response averaged to 1 minute to match IBBCEAS. The line of best fit is shown (dashed red) with $R^2 = 0.74$ and intercept = 0.99.

in flow rate (which is related to pressure changes in the system) resulted in linear changes in the PMT signal. The signal change was small but observable, with an increase in the flow rate from 200 to 600 mL/min giving rise to a 0.6% increase in the PMT signal. To reduce the effects of pressure, a needle valve was added to the unfiltered sample line to match the flow rate of the sample and the scrubbed air streams. A similar approach was taken by Birks et al. (2018) when constructing a folded tubular photometer that measured regular 'zero-air' responses. The instrument sampling scheme is shown in Figure 4.29. A PTFE particulate matter (PM) filter (Pall 2 μm, diameter = 47 mm) was placed after both the sample and reference line. A pump draws air through two inlets at both ends of the cavity so that the gas composition within the cavity is uniform. The system switched between sample or reference air using solenoid valves that were controlled by two relays and an Arduino Uno microcontroller.

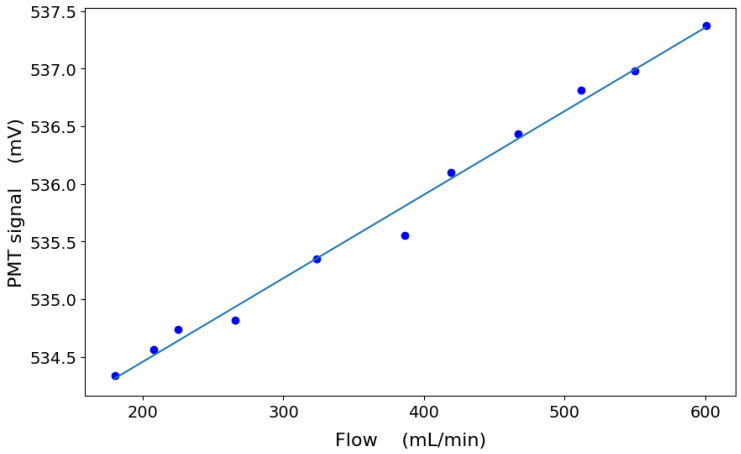


Figure 4.28. Relationship between PMT signal voltage and flow rate, showing a small but observable increase of 0.6% in the PMT signal as the flow rate increased from 200 to 600 mL/min.

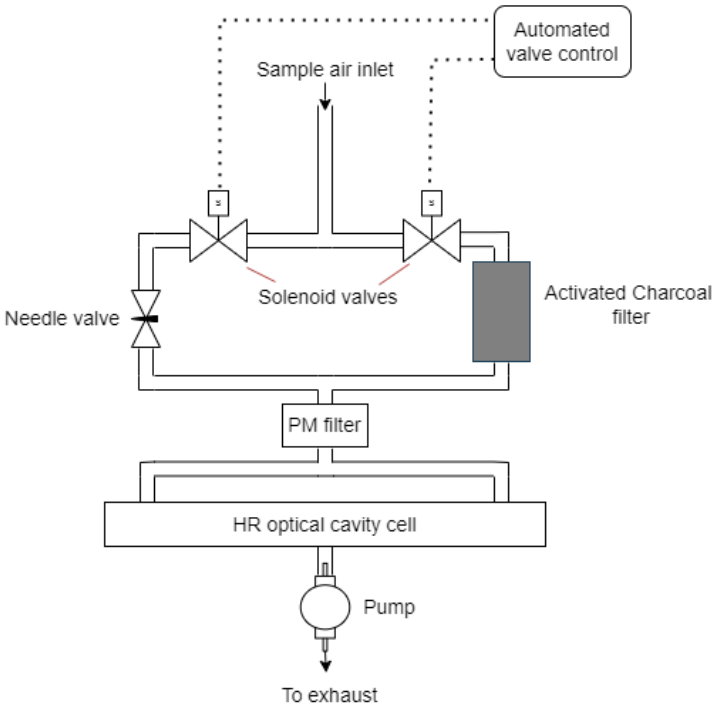


Figure 4.29. Instrument filtering schematic. The air inlet is split into a reference channel with activated charcoal filter to scrub NO_2 and a sample channel with a needle valve to match flow rates between channels. Solenoid valves periodically switch the inlet stream between the sample and the reference channel. A PTFE PM filter is placed just before the cavity inlet to ensure that both channels are filtered of particulate matter.

The PMT response to additions to NO_2 in the atmospheric simulation chamber is shown in Figure 4.30. The raw PMT signal (green dashed line) shows some drift as the experiment progresses, most likely from LED or PMT output drift. This is seen, for example, in the PMT response that is slightly greater than 1.0 at the start of the experiment, while it is below 1.0 towards the end of the experiment, around 5500 s. The response was corrected for drift in the overall system using the reference baseline measurements (red line).

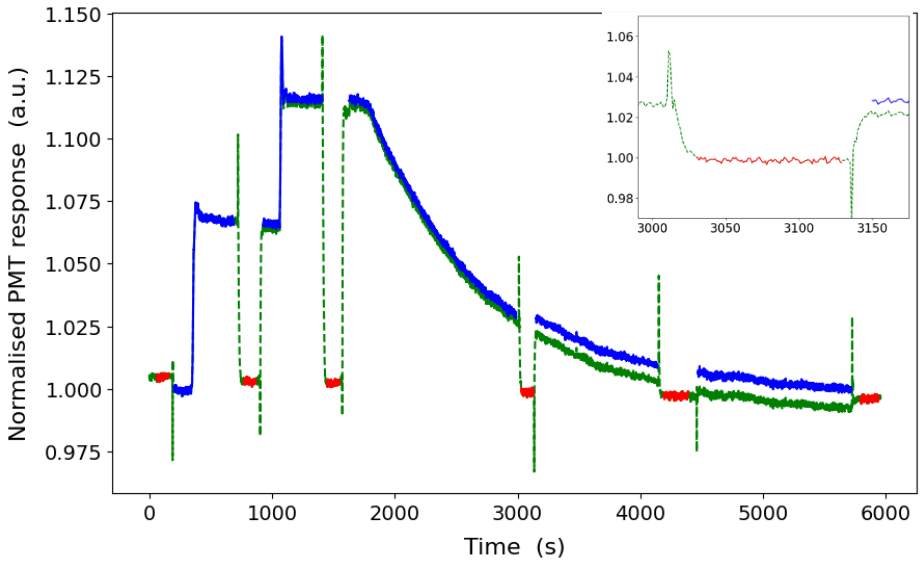


Figure 4.30. The raw PMT response (green dashed) is compared with the corrected PMT response (blue line) based on the reference NO_2-free response (red line). Inset shows a close-up of the system response when switching between sample and NO_2-free air. The instrument response of ~30 s can be seen here.

This experiment also determined the cavity residence time to be 30 seconds, seen here as the time taken for the response to stabilise when switching between sample and NO_2-free air, shown in the inset of Figure 4.30. The residence time determines the overall time resolution of the 1 m CEAS instrument. The instrument's time resolution of 30 s is suited for measurements of ambient concentrations of NO_2 in the dynamic traffic environment. Decreasing the volume of the sample cell (notably, the optical cavity length and the inner diameter of the cavity tube) and shortening the inlet tubing would decrease the cavity residence time, as would increasing the pump flowrate. An

instrument response time of a few seconds is readily achieved with such changes given the relationship between residence time, t_{res}, cell volume and flow rate for a continuous flow through the cell:

$$t_{res} = \frac{cell\ volume}{flow\ rate} \quad 4.1$$

4.5 Comparison of instruments and measurement strategies

Two methods are explored in this chapter, a ratiometric two-channel system and a single-channel wideband system. Both methods have advantages and disadvantages for making urban NO_2 measurements.

The ratiometric two-channel system offers good selectivity to NO_2 by choosing operating wavelengths with a large differential NO_2 absorption cross-section. Ideally, wavelengths should be chosen so that the differential cross-sections of potential interfering compounds are minimised. As shown above (Figure 4.11), the ratio of intensities of these wavelengths, $I_1(\lambda_1)/I_2(\lambda_2)$, provides excellent common-mode noise rejection as fluctuations in the LED emission and variations in light path through the atmosphere are effectively cancelled out. However, the ratiometric two-channel method only uses two narrow-band quasi-monochromatic wavelengths and has the disadvantage that much of the spectral information is discarded. In addition, the narrow bandpass filter results in low light levels that can be obscured by high noise levels. Therefore, the ratiometric two-channel system requires sensitive signal detection and amplification. This work has demonstrated that both lock-in amplification of photodiode signals, or highly sensitive photodetectors like PMTs, can be used for sensitive two channel measurements.

The ratiometric two-channel system, with an 8 m path through the ERI atmospheric simulation chamber, had a measurement standard deviation of 71 ppb for 3 s scans, after applying a 50 point Savitzky-Golay filter. This sensitivity was sufficient for instrument validation, but not ambient measurements. Nevertheless, it should be noted that the 8 m path for the chamber spectrometer is about three orders of magnitude shorter than typical long-path DOAS systems which can have pathlengths of multiple

kilometres and average spectra over 5 to 40 minutes (Bacaoco et al., 2020; Nasse et al., 2019; Platt & Stutz, 2008). The sensitivity of the system can clearly be lowered by increasing the light path length. For a light pathlength of 250 m, the standard deviation would be expected to improve to 2.3 ppb assuming the same signal-to-noise ratio. To optimise the ratiometric two-channel system, appropriate amplifier circuitry must be built and integrated into the signal processing system, a longer light path must be used, and a higher-powered LED may be required to increase the signal amplitude. Signal modulation would be particularly useful in open path applications so that the signal could be discriminated from background light.

The narrow two-channel method could be applied to other absorbing gases, such as glyoxal, which has large differences in absorption cross-section near 460 nm. Flowerday et al. (2023) have recently demonstrated a similar approach to measure glyoxal, for example. In the deep-UV region, a two-channel approach using a gas correlation cell may be applied to measure SO_2 or NH_3. In these cases, the two-channel methods are most effective when the target species is the dominant absorber in the given spectral region and has highly structured absorption.

The 1 m CEAS (single-channel wideband) instrument is better suited than the ratiometric two-channel system for making fast and sensitive NO_2 measurements in an urban traffic environment. The 1 m CEAS instrument is sensitive to ambient levels of NO_2, with an instrument standard deviation of 2.1 ppb in a 1 s measurement, and 0.6 ppb when Savitzky-Golay filtered across a 30 s window with a second order polynomial. The use of a 'zero-air' NO_2 scrubbed inlet allows for regular baseline measurements to account for drifts in the signal, either from the LED emission or PMT output voltage, over long measurement periods. Unlike the ratiometric two-channel system which accounts for drift with two simultaneous measurements, the 1 m CEAS sample and reference measurements are not synchronized. Baseline reference measurements should therefore be taken at regular intervals to account for changes in instrument performance that may vary over time, including in response to environmental variables such as the ambient temperature.

The work presented above demonstrates that the 1 m CEAS instrument has sufficient sensitivity to measure ambient NO_2 in urban environments. This wideband system lacks the selectivity of the ratiometric two-channel method. Nevertheless, interfering

absorptions from compounds such as glyoxal and methylglyoxal are expected to be a minor interference — such compounds have a lower absorption cross section and are expected to be present in much lower mixing ratios than NO_2 in urban settings. In these situations, absorption by NO_2 will strongly dominate the instrument response. Scattering from particulates is removed by filtering particles from the sample air using a PM filter. For the system shown above, the signal is recorded every 1 s and the sample gas has a residence time of 30 s within the cavity. The application of the 1 m CEAS to roadside measurements near a primary school in Cork city will be explored in Chapter 5.

Table 4.1 Summary of instrument performances. Effective reflectivities are shown for cavity-enhanced systems. Note that the ratiometric 2-channel (non-dispersive) system had a folded 8 m path.

Instrument	R_{eff}	L_{eff} (m)	$t_{acquisition}$ (s)	1σ (ppb)	$1\sigma_{filtered}$ (ppb)
Ratiometric 2-channel (dispersive)	0.9984	2	10	31	8
Ratiometric 2-channel (non-dispersive)	-	8	1	136	71
Single channel CEAS (a)	0.9921	55	3	7.2	2.2
Single channel CEAS (b)	0.9960	250	1	2.1	0.6

Instrument cost

A major aim of this thesis was to reduce the cost of a spectroscopic instrument for NO_2 detection. In spectroscopic systems that use dispersive detection, the spectrometer is a large proportion of the total instrument cost (e.g., €25,000 for the Andor spectrometer system) and requires interfacing to a computer. Table 4.2 lists the costs of system components. In this system, expensive system components include specialised optics, especially the high reflectivity cavity mirrors. The cavity mirrors used in the 1 m CEAS instrument described in this work were relatively low cost at only ~€200 per mirror. Non-dispersive photodetectors are typically much lower cost than spectrometers coupled with a CCD. The PMT used in the 1 m CEAS instrument cost €670 from Hamamatsu. The total estimated cost of the 1 m CEAS instrument is €3291.

In the ideal narrow two-channel instrument, the most obvious components that could be swapped for lower cost alternatives are the benchtop power supplies, which could be replaced by battery packs for only ~€30, and the PMT that could be replaced by photodiodes (Thorlabs, €15 - €50 each) and amplified using low-cost open-source digital lock-in amplifiers, estimated to cost only €35 (Harvie & De Mello, 2022). These changes alone would significantly reduce the instrument costs. Data acquisition could be carried out using a programmable Arduino Uno and a lower cost diaphragm positive displacement pump.

Table 4.2. Cost of each component used in the 1 m CEAS instrument. The total cost is €3291.

Component	**Cost (€)**
LED	4
HR cavity mirror (×2)	400
Wide bandpass filter	432
Focussing lenses (×2)	40
KG3 filter	53
Photomultiplier tube module	670
PTFE filter	70
Activated charcoal filter	5
Benchtop power supply (×2)	687
Diaphragm pump	540
Solenoid valves	40
Arduino Uno	30
PicoLog data acquisition unit	320
Total	**€3291**

The components required for the two-channel approach are laid out in Table 4.3, highlighting that in a narrow two-channel system, the main cost will be of the narrow bandpass filters from Semrock, and cavity mirrors for *in situ* measurements, with a total estimated cost of €1526. In an open path configuration, cavity mirrors could be replaced by inexpensive reflector arrays (e.g., €20). There is also no need for pumps, bring the total cost of an open path instrument to €1076, a huge improvement on the current cost of the instrument developed in this work. Costs could be even further

reduced by purchasing greater quantities of components at once for building multiple detectors.

The reduced cost of an NO_2 detection system means that mobile monitoring systems could be expanded to include NO_2 more often, and local communities could monitor the regional levels of this toxic pollutant.

Table 4.3. Cost and components needed for an ideal narrow two-channel system. Components marked * are only applicable in an *in situ* measurement and components marked ** are only suitable in an open path configuration.

Component	**Cost (€)**
LED	4
HR cavity mirror (×2) *	400
KG3 filter	53
Narrow bandpass filter (×2)	834
Focussing lenses (×2)	40
Photodiode (×2)	30
Battery packs	30
OLIA	35
Arduino Uno	30
Diaphragm pump *	70
Reflector array **	20
Total (*in situ*) *	**€1526**
Total (open path) **	**€1076**

Chapter 5 Field measurements in an urban traffic environment

5.1 Introduction

The 1 m CEAS instrument developed in Chapter 4 was tested for its capability of making fast, specific measurements of NO_2 in an urban traffic environment near a primary school in the north of Cork City. The measurement campaign ran for over 2 months and during this time the sensitivity, time response and longevity of instrument components, such as PTFE and charcoal filters or cavity mirror reflectivities, were examined and are reported on in this chapter. Additional findings relating to the complex micro-environment effects on wind flow and ventilation in narrow streets are also discussed here.

Many studies have found increased levels of NO_2 around schools (Alemany et al., 2018; An et al., 2021; Clark et al., 2012). Alvarez-Pedrerol et al. (2017) used estimated local NO_2 concentrations based on land use regression models, and Miller & Vela (2013) interpolated values from nearby monitoring stations to approximate NO_x concentrations around schools. There is a need for studies that directly measure NO_2 levels near schools so that the exposure risk to students and staff can be accurately assessed and effectively reduced. A recent study by Badyda & Rogulski (2024) found that NO_2 concentrations around a school in Warsaw, Poland decreased by 30 % following the introduction of traffic restrictions, greatly improving the local air quality.

Analysis of the surrounding wind field and its effect on measured NO_2 mixing ratios is included and highlights the importance of meteorological data when considering emission sources and transport. The layout of urban areas and the aspect ratio of streets, in terms of height, width and length, contribute to the natural ventilation of

pollutants (Nicholson, 1975; Vardoulakis et al., 2003) and will be discussed in the context of Blarney St.

Traffic conditions vary substantially depending on whether or not schools are in term. A large proportion of students were driven to school by car, and the associated increase in vehicle numbers around the start and end of the school day cause appreciable traffic congestion on the street, as has been observed elsewhere in Ireland (Road Safety Authority, 2021) and Europe (Brown et al., 2024; von Stülpnagel et al., 2024). In addition to cars idling due to congestion, a small number of drivers were observed to leave their vehicles idling while waiting to pick up children from school, further adding to the exhaust emissions in the vicinity.

Blarney St is on a steep hill with the measurement site at an altitude of 40 m. A topographical map of Blarney St and the surrounding area is shown in Figure 5.1. A steep gradient can affect the vertical profile of pollutant distributions and make the street canyon wind field more complex (Limo et al., 2024). The effect of the hill is not explored further in this work; however, it is noted that vehicles driving uphill emit more NO_x than those driving downhill and may lead to variations in the measured ambient mixing ratios (Gidhagen et al., 2004).



Figure 5.1. Topographical map of Blarney St showing the measurement site at 40 m altitude. A steep incline to the west of the measurement site is observed.

There are many contributing factors to ambient NO_2 levels in an urban environment like Blarney St. High spatial and temporal resolution are required to characterise the

sources and dispersion of NO_2. The 1 m CEAS instrument was tested for its application in an urban traffic environment and an analysis on the effect of the proximity to a school and the local wind field is explored in this chapter.

5.2 Description of the measurement site

NO_2 measurements were carried out on Blarney St, a traffic artery on the northside of Cork City. The whole area is characterised by a steep hill and narrow residential streets that are often congested during peak traffic hours. A map and satellite view of Cork City are shown in Figure 5.3 and Figure 5.4. Blarney St is an arterial route serving the north-western residential areas of Cork City and the commuter towns of Kerry Pike, Tower, and Blarney. Parking on the street does not allow free-flowing two-way traffic towards the eastern (lower) end of the street in the vicinity of the measurement site.

The majority of the street has a width (W) between 8 to 10 metres, which is quite narrow compared to the height (H) of the buildings which ranges between 7.5 to 10 metres (largely two and three storey dwellings). The aspect ratio (H/W) of Blarney St therefore varies between 0.75 and 1. A street canyon was first defined as a narrow street with continuous buildings on either side, however, now this term also includes streets that have minor gaps between buildings (Nicholson, 1975; Vardoulakis et al., 2003). Vardoulakis et al. (2003) defines streets with $H/W < 0.5$ as avenue canyons, and streets where $H/W \sim 1$ as regular street canyons, meaning that Blarney St predominantly behaves like a symmetric regular street canyon. The length of a canyon, L, is usually measured as the distance from one major intersection on the road to another. Choosing the two nearest intersections on either side of the measurement site gives a canyon length of 340 m. According to Vardoulakis et al. (2003), this classifies Blarney St as a long street canyon ($L/W > 7$).

The wind field in a street canyon changes depending on the prevailing wind direction at roof-level height. When the wind direction is parallel to the street, channelling effects caused by the Venturi effect, discussed by Sanjaya et al. (2020) and Blocken et al. (2008), lead to higher pollutant concentrations in the street canyon (Hoydysh, 1994). Winds that are perpendicular to the street may follow an isolated roughness

($H/W < 0.3$), wake interference ($H/W \sim 0.5$) or skimming ($H/W \sim 1$) wind flow. Given Blarney St's aspect ratio, a skimming wind flow was assumed here with a small contribution from wake interference, thus, creating a vortex in the canyon that cycles emissions from the downwind (windward) side of the street to the upwind (leeside) side. Small weak vortices are formed on the windward side of the street caused by some wake interference. These assumed wind flow conditions on Blarney St when the wind direction is perpendicular to the direction of the street are illustrated in Figure 5.2.

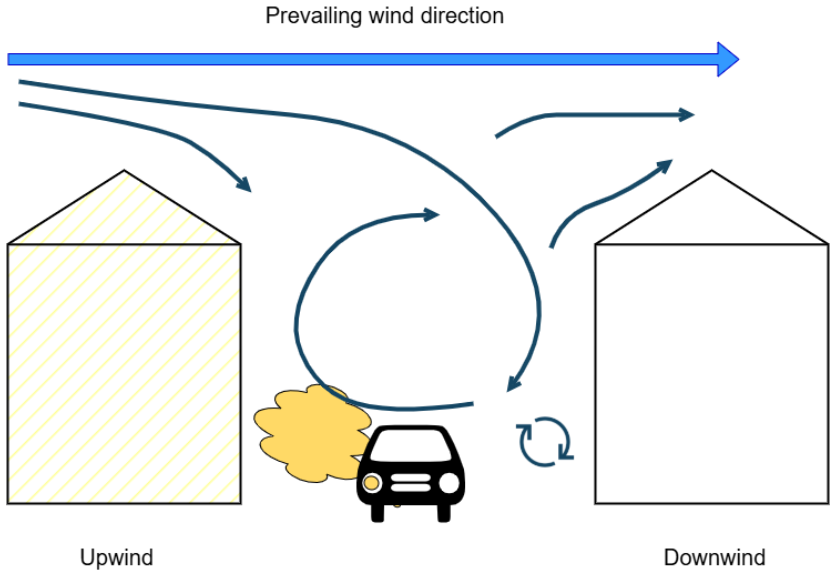


Figure 5.2. A sketch of the expected wind flow over Blarney St when the wind is perpendicular to the street. Air from the windward side of the street is circulated over to the leeside, moving emissions from the road to the leeside as well. Smaller vortices can form on the windward side of the street due to wake interference caused by the street's aspect ratio.

Measurements were carried out near a primary school, Blarney St CBS, from 15 August 2024 to 1 November 2024, an extensive measurement period that included a background week before the start of the school term (BG), an eight week in-term period (SCH), and one week of mid-term break (MT). The primary school began its school term on 29 August, and students were off school for a mid-term break from 28 October until 1 November. The school began at 08:20 each morning. The school day ended at 13:20 for the two earliest school years (Junior Infants and Senior Infants) while older children (First Class to Sixth Class) finished at 14:20.

The location of Blarney St CBS causes traffic congestion on Blarney St because the street is too narrow in places next to parked vehicles for vehicles to pass in both directions, sometimes leading to near stand-still traffic. In addition to cars idling due to congestion, a small number of drivers were observed to leave their vehicles idling while waiting to pick up children from school, further adding to the exhaust emissions in the vicinity. Blarney St is on a steep hill with the measurement site at an altitude of 40 m. A steep gradient can affect the vertical profile of pollutant distributions and make the street canyon wind field more complex (Limo et al., 2024). The effect of the hill is not explored further in this work; however, it is noted that vehicles driving uphill emit more NO_x than those driving downhill and may lead to variations in the measured ambient mixing ratios (Gidhagen et al., 2004).

The measurement site for this study was a private residence located 115 m west of the Blarney St CBS school and on the same (southern) side of the road. Air was sampled through a ground floor window, 1.5 m from the ground (Figure 5.5), facing the road. Measurements were not taken at night as the ground floor window could not remain open for security purposes.

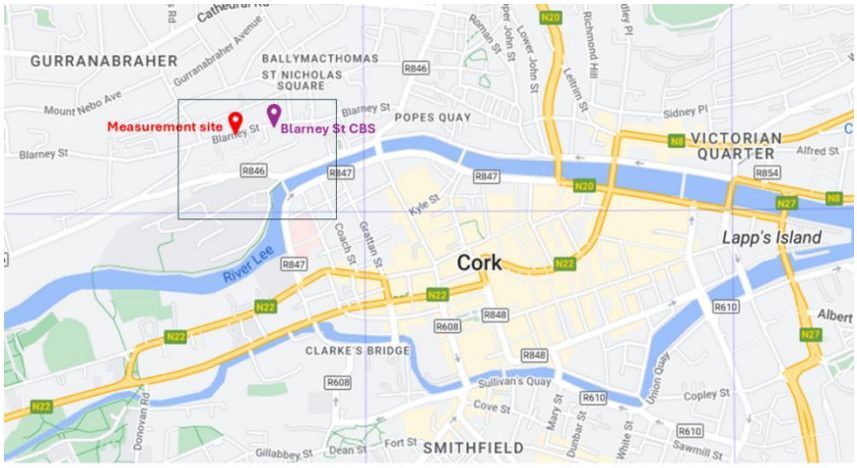


Figure 5.3. Map of Cork City centre and areas to the north, showing the measurement site (red marker) and school (Blarney St CBS, purple marker).

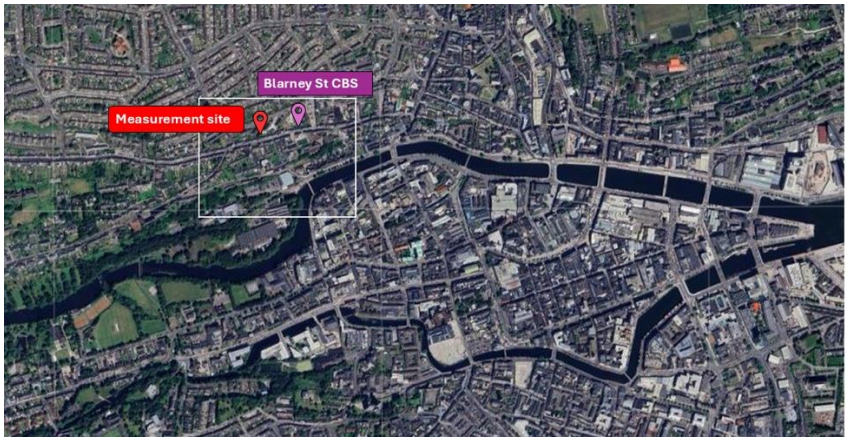


Figure 5.4. Satellite view of Cork City showing the city centre and areas to the north of the centre.



Figure 5.5. Photographs showing Blarney St to the (a) west and (b) east of the measurement site. (c) shows the inlet and exhaust tubing. The inlet is 1.5 m from the ground and covered to protect the system from rain water.

Traffic counts were measured from a first-floor road-facing window at the measurement site using the mobile app RoadCount which uses a camera input coupled with AI to count and categorise passing vehicles with 1 s resolution. Access to the first floor was restricted to the period 11 to 26 September and RoadCount measurements were only recorded during this period. A second traffic counter was sited at City View

Wheels, a business 115 m east of the school and 230 m from the measurement site. The City View Wheels sensor is a Telraam traffic counter and reports hourly, open source traffic data (https://telraam.net/en/location/9000003085/2024-08-15/2024-08-22). The Telraam counter had been in operation since January 2022.

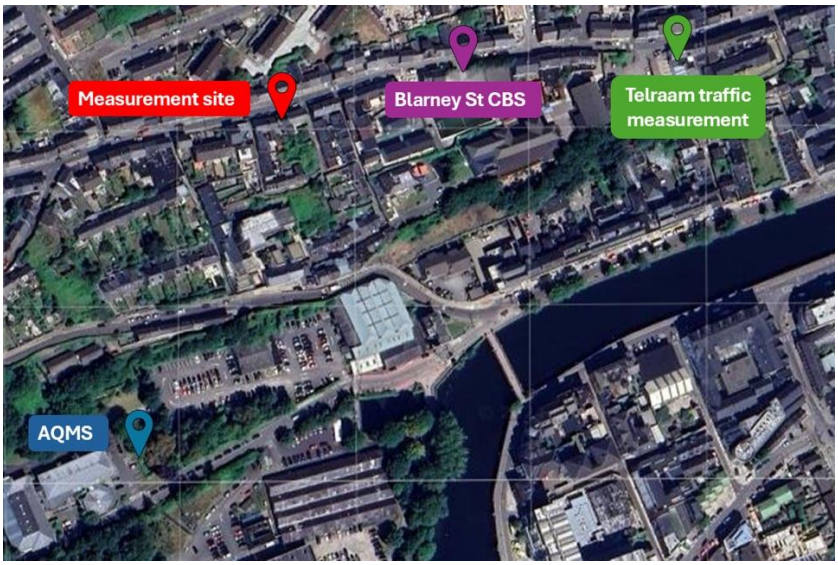


Figure 5.6. A satellite view of the measurement site, Blarney St CBS school located 115 m to the east, the Telraam traffic counting site 230 m east of the measurement site, and the Distillery Fields air quality monitoring station (AQMS), 190 m to the south-west. The AQMS was not near a road but was near a staff car park. The measurement site is on the south side of the street.

The nearest air quality monitoring station (AQMS) is the UCC Distillery Fields station, a background site set in a parkland/riverine setting and run on behalf of the Irish EPA by UCC. This AQMS, which provided background NO_2 concentrations for comparison to Blarney St measurements, was 190 m from the measurement site (Figure 5.6).

Meteorological data such as temperature, wind speed and wind direction were obtained from the Met Éireann Cork Airport weather station, located 6.2 km south of the measurement site. The local wind field at the Blarney St measurement site is expected to be strongly influenced by the narrow east-west street and topography of the city, and could differ appreciably from that at Cork Airport.

The wind rose plot in Figure 5.7 shows the frequency of wind speeds (knots) and directions throughout the entire measurement period. Cork City is noticeably dominated by winds from the west, south-west and south during this period, with frequent high speed winds. Diurnal temperature and wind speed profiles are shown in Figure 5.8, highlighting the fact that both temperature and wind speeds are typically at their maxima in the afternoon due to surface heating (Ephrath et al., 1996). Increased wind speeds at school collection times increases turbulent air conditions and changes NO_2 dispersion compared with lower wind speeds. Under low wind speeds, stagnant conditions would reduce ventilation and concentrations of pollutants typically increase (Vardoulakis et al., 2003).

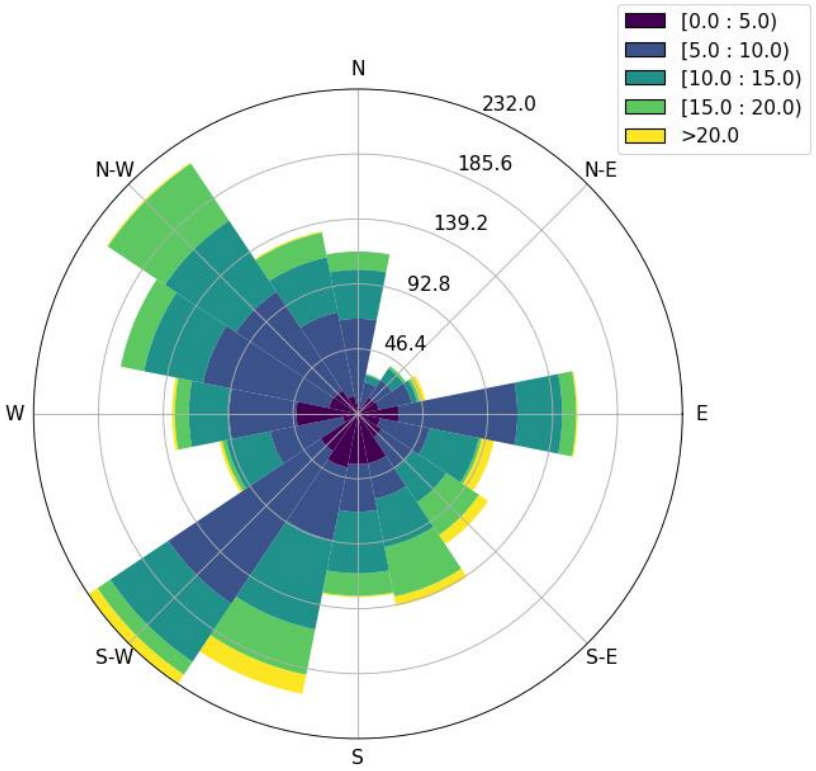


Figure 5.7. Wind rose plot showing the vector-averaged frequency of wind speeds (knots) and direction during the entire measurement period.

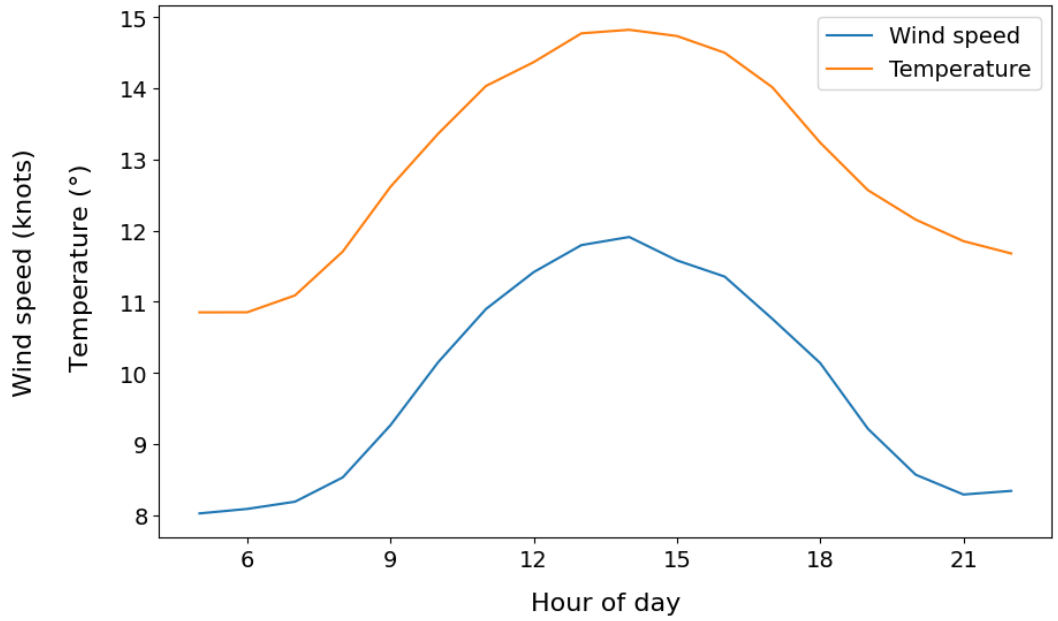


Figure 5.8. Diurnal profiles of wind speed (blue) in knots and temperature (orange) in °C. The highest wind speeds and temperatures are observed between 12:00 and 15:00. These times overlap with school collection times that are of interest in this study.

5.3 Instrument description

The 1 m CEAS instrument described in chapter 4 was set up near a ground floor window in a private residence. Air was sampled at a flow rate of 3.5 L/min via a tube through a partially opened window. The total volume of the optical cavity and inlet tubing was 1.87 L, giving a gas residence time of 32 s. The light source was a blue LED driven with a 46 mA current and housed in a passive heat sink. The system is shown in Figure 5.9. A 20-bit PicoLog data acquisition unit (ADC-20) recorded the PMT output voltage at a 1 s sampling interval. The PMT response was Savitzky-Golay filtered over a 30 s window to smooth the response and match the time response to the sample residence time in the cavity. NO_2 could be measured with a standard deviation of 7.8 ppb in 1 s which improved down to 1.5 ppb when Savitzky-Golay filtered over a 30 s window.

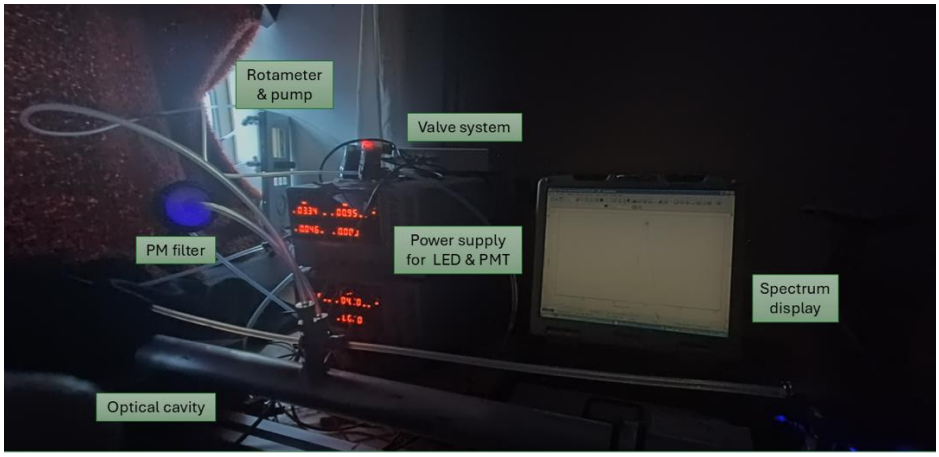


Figure 5.9. Photograph of the 1 m CEAS system at the measurement site on Blarney St. The window covering is partially removed to allow enough light for the photograph.

The instrument cycled between sampling filtered outside air and zero-NO_2 air. The pressures in the ambient air and zero-NO_2 air inlets were equalised by bringing the sample inlet inside to an NO_2-free environment and the pressure was adjusted using a needle valve until the signals in both sample lines were equal. The initial duty cycle was 66% (sampling for 20 minutes and measuring a zero-NO_2 baseline for 10 minutes). The PMT signal was found to drift slightly over time, most likely due to variations in temperature or pressure in the system. To better correct for system drift, the sample air-baseline period was shortened from 5 September to better account for short term drifts. The later measurement cycle time measured outside air for 8 minutes and baseline zero-NO_2 for 2 minutes, shortening the overall time between baseline measurements and increasing the duty cycle to 80%.

Instrument performance

For quantitative measurements, the cavity mirror reflectivity, *R,* must be calibrated. Optical cavity systems have previously calibrated the effective reflectivity by introducing known amounts of absorbing or scattering gases (Flowerday et al., 2023; Washenfelder et al., 2008; Werle et al., 1993; Womack et al., 2022). However, external gas supplies are cumbersome and reduce the practicality and portability of a spectroscopic system. In these measurements, the effective reflectivity was calibrated

using the relationship between the phase shift in an empty cavity and the modulation frequency (Kebabian et al., 2007):

$$tan(\phi_0) = \left(\frac{4\pi df}{c}\right)\left(\frac{R^2}{1-R^2}\right) \quad 5.1$$

where φ_0 is the phase shift in radians in an absorber-free cavity, f is the modulation frequency in Hz, R is the mirror reflectivity, d is the cavity length and c is the speed of light. The LED was modulated between 1500 to 10000 Hz and the phase shift was recorded using a lock-in amplifier (SR830, Stanford Research Systems) with a 1 s time constant. The phase shift was set to 0 radians at 10,000 Hz and increased linearly as the modulation frequency decreased, as seen in Figure 5.10. R was initially calculated to be 0.996 at the beginning of the measurement campaign. After 4 weeks, the effective reflectivity had decreased to 0.988, substantially reducing the effective pathlength and hence the instrument sensitivity. The reflectivity between these first two calibrations was interpolated, assuming a constant rate of loss, to correct concentration values. The cavity mirrors were removed, cleaned and realigned on 17 September, restoring the reflectivity to 0.996 and the effective path length to 250 m. The instrument reflectivity was recalibrated weekly thereafter to give updated R-values and minimise potential variability due to uncertainty in the mirror reflectivities. Figure 5.11 shows the improvement of the mirror reflectivity after cleaning. The mirrors were not cleaned again after this cleaning as the reflectivity remained at a useful level above 0.99.

The instrument sensitivity (1σ) was calculated during the initial baseline period each week and is plotted over the entire measurement period in Figure 5.12. The average deviation of the instrument was 1.84 ± 0.47 ppb. There was a large decrease in standard deviation which coincides with the reflectivity degrading as in Figure 5.11. After the mirrors were cleaned and realigned the deviation increases to > 2 ppb. The sensitivity of the instrument is highly dependent on the mirror reflectivity, which was well-preserved after the first cleaning. The use of a PTFE filter on the inlet helped to conserve the mirror reflectivities and maintain a useful limit of detection for making urban NO_2 measurements. The PTFE and the activated charcoal filters did not need to be changed throughout the measurement period. Although ambient measurements were not taken at night, the instrument could have been left running in an NO_2 free environment to further investigate the instrument performance and longevity.

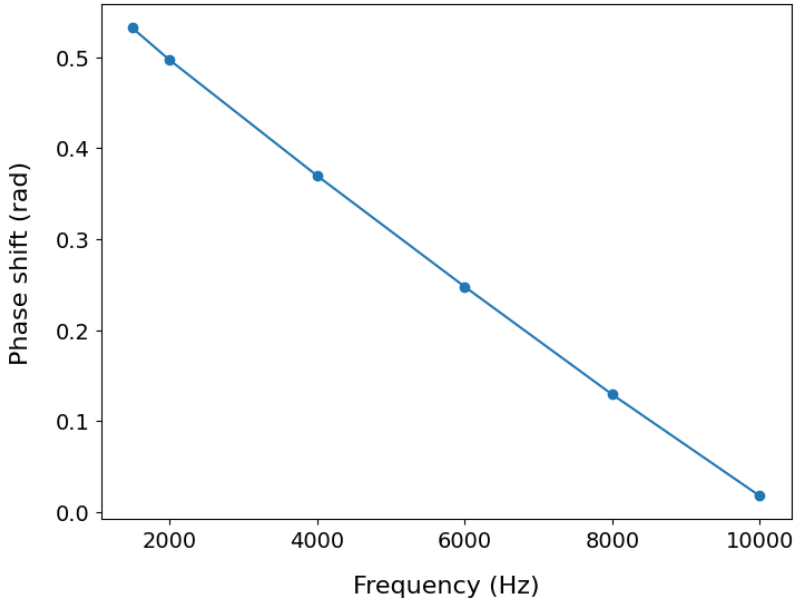


Figure 5.10. The modulation frequency was varied between 1500 and 10,000 Hz, producing an inverted linear response in the phase shift, in radians, to calibrate the CEAS mirror reflectivity.

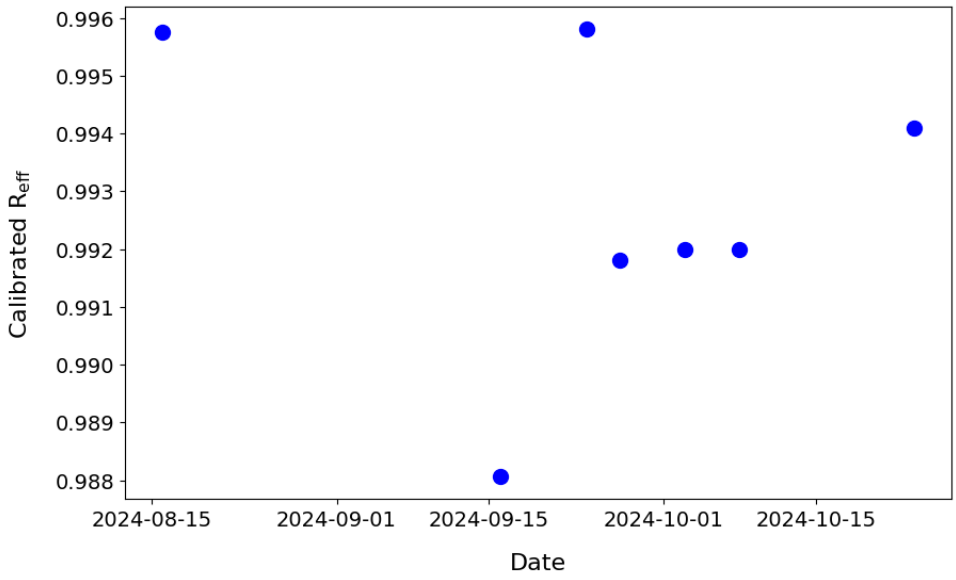


Figure 5.11. Calibrated effective mirror reflectivity (R_{eff}) over time. The mirrors were removed and cleaned on 2024-09-17, improving the reflectivity. R_{eff} was recalibrated more frequently after this cleaning but did not degrade as much.

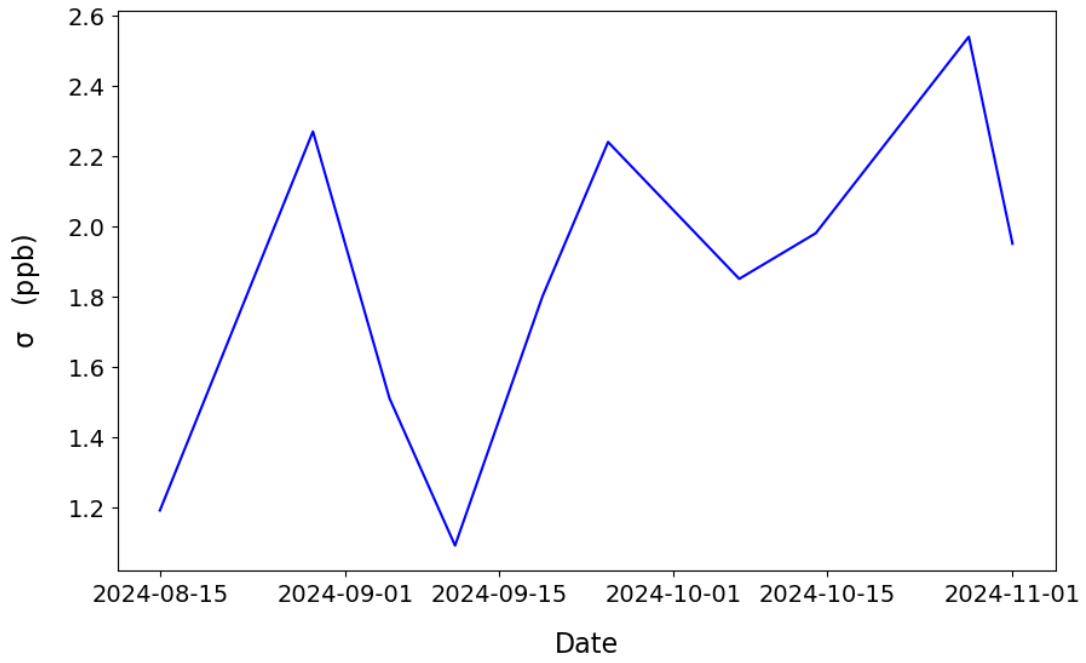


Figure 5.12. Standard deviation of the instrument throughout the measurement period. Standard deviation was calculated from a baseline period with no NO_2 present.

5.4 Results

Validation of NO_2 response

To confirm that the PMT response was from NO_2 absorption within the cavity, the spectra recorded by a spectrometer (Andor, SR163) and CCD camera (Andor, iDUS DV420-A-BV) as described in Chapter 4 were analysed using DOAS Intelligent System (DOASIS) spectral fitting software. A fitted spectrum from 6 September at 09:20 is shown in Figure 5.13. Before fitting, binomial low and high pass filtering was applied to remove broadband effects in the spectrum and to reduce high frequency noise. Three trace gases are included in the DOAS fit: O_3, methylglyoxal (MGLY) and H_2O. Literature absorption cross-sections of all gases were convolved with the instrument resolution obtained from the spectrum of an atomic Hg emission line. The filtered LED structure was also included to improve the overall fit result, following the approach of Su-Wen et al. (2008). Including the LED emission in the fit reduces

the effects of Fabry-Perot étalon structures when the temperature is not highly stable. To account for small deviations in the wavelength scale over time, the reference spectra could be shifted or squeezed throughout the fitting procedure (Hartl et al., 2012). Although glyoxal absorbs in this region, it was not included in the fit as it disimproved the overall fit and increased the residual. It should be noted in Figure 5.13 that the polynomial fit is poor, likely due to crosstalk from the LED structure or O_3 absorption.

The concentration, *c*, of each trace gas in units of molecules/cm^3 is displayed in the plot titles in Figure 5.12 and associated uncertainties were reported in the DOASIS software. These concentrations are equal to mixing ratios of 91 (± 5.0) ppb of NO_2, 88 (± 4.5) ppb of O_3, 0.51 (± 0.29) ppq of MGLY and 48 (± 5.6) ppm of H_2O at ordinary temperatures and pressures. It is noted that water vapour has relatively weak absorption cross sections in this wavelength region ($\pm 10^{-25}$ cm^2 molecule^{-1}). The instrument is therefore not especially sensitive to H_2O and the real water vapour concentration is expected to be much higher than 48 ppm. The MGLY concentration is essentially zero and the instrument is not sensitive to such low concentrations. The NO_2 and O_3 concentrations are high compared with the annual mean NO_2 and O_3 mixing ratios reported by the EPA from the Distillery Fields AQMS background measurement site, 4.0 ppb and 27.1 ppb, respectively. The hourly mean concentrations reported by the EPA from Lower Glanmire Road at this time are 20 ppb of NO_2 and 36 ppb of O_3. Pollutant concentrations are expected to be much higher at the Blarney St measurement site than the Distillery Fields site which is a background AQMS and not surrounded by much traffic. Although the results are also higher than those at the Lower Glanmire Road (LGR) measurement site, which is exposed to relatively heavy traffic, the LGR site is further from the road (which is twice as wide), allowing greater dispersion of locally emitted NO_2. The time-scale for EPA measurements are also averaged over an hour and short periods of high emissions are not captured. Much greater variability in pollutant concentrations is expected when the spectrometer is sampling at 1 min time intervals, as in the Blarney St measurements.

Figure 5.14 shows a time series of measured NO_2 mixing ratios from 8 October in which the CEAS response measured by the PMT is compared to the IBBCEAS response where the measured intensity from 420 to 460 nm is integrated. The

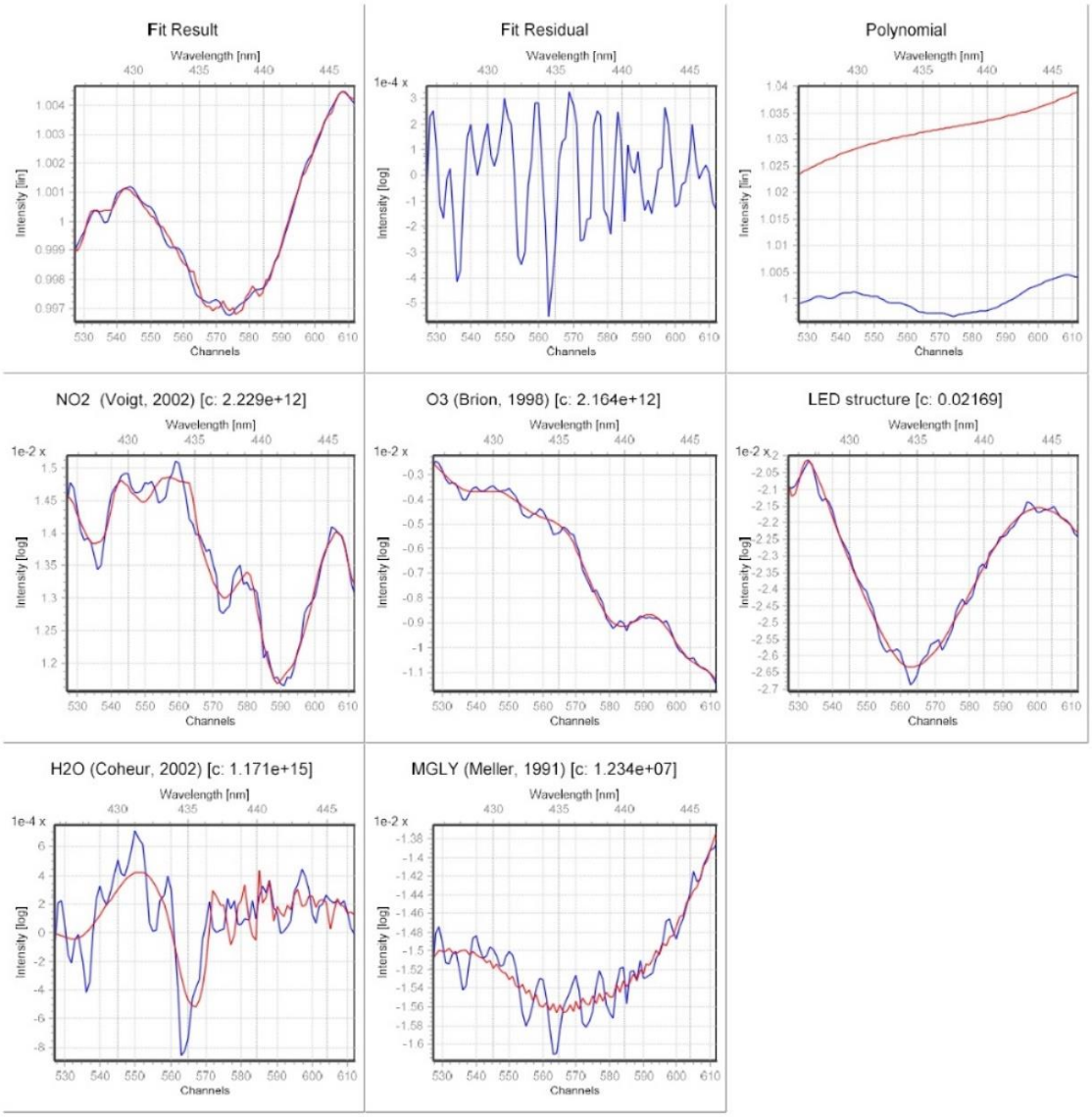


Figure 5.13. DOAS fitting result from 6 September 2024 at 08:45 showing the absorption of NO2 compared with potential interferences from O3, the LED structure, water vapour (H2O) and methylglyoxal (MGLY).

IBBCEAS response accurately represents the signal measured by the PMT which collects all incoming wavelengths and gives an integrated signal convolved with the PMT responsivity curve. Since the pathlength and the NO_2 absorption cross sections are known, the integrated IBBCEAS intensity can be related to concentration and expressed as a mixing ratio. The CEAS response is Savitzky-Golay filtered with a 30 s window and compared to 1 min IBBCEAS measurements. As expected, higher variability in the NO_2 mixing ratio is seen in the PMT measurements. This is evident at 09:50, for example, where the CEAS measured NO_2 quickly rises to 60 ppb and

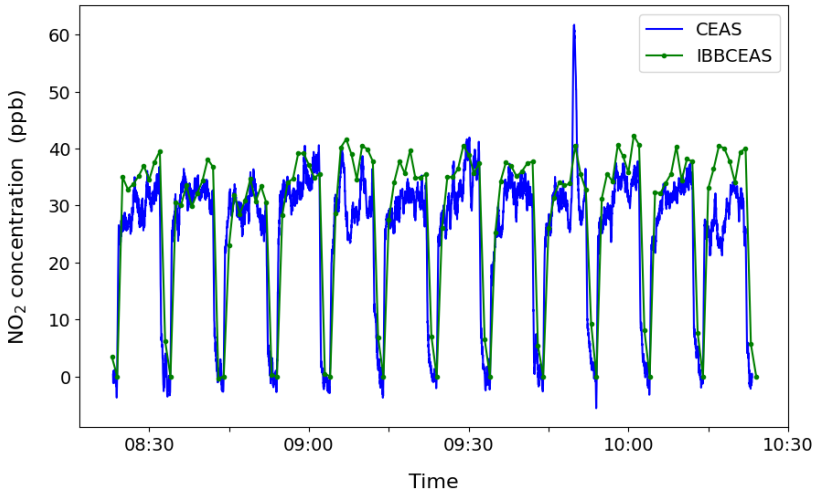


Figure 5.14. Time series showing measured NO_2 mixing ratios on 08/10/2024. PMT measurements are filtered using a 30 s Savitsky-Golay window and IBBCEAS measurements are integrated over 1 min.

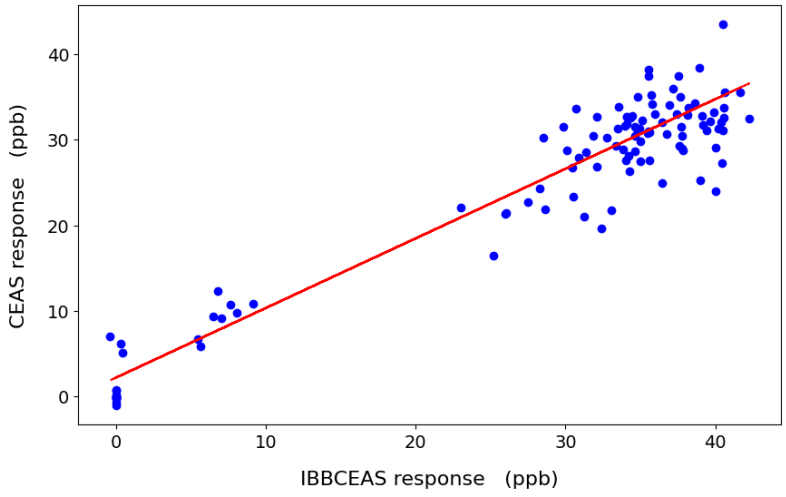


Figure 5.15. Correlation between the integrated IBBCEAS response measured by the CCD spectrograph and the CEAS response measured by the PMT. The CEAS response is averaged to 1 min to match the IBBCEAS acquisition time. Linear fit parameters (red line): $R^2 = 0.92$, slope = 0.81, intercept = 2.16 ppb.

falls rapidly back to 30 ppb. In contrast, the IBBCEAS measurement captures a smaller increase to 40 ppb. These differences highlight the value of higher time resolution to capture fast variations in NO_2, such as emissions of especially polluting vehicles. There is a good correlation between the CEAS and IBBCEAS responses when the

CEAS is averaged over 60 s to match the IBBCEAS measurement time, with an R^2 value of 0.92 and a line of best fit with a slope of 0.81 and an intercept of 2.16 ppb (Figure 5.15). A slope of < 1 shows that the IBBCEAS measurement reports a slightly higher absorption signal than the CEAS instrument, leading to a small offset of approximately 5 ppb.

CEAS systems are temperature and pressure dependent, and instruments often monitor and correct for these parameters. The apparent temperature dependence of the instrument on 20 August is shown in Figure 5.16, where temperature data from the Cork Airport weather station is compared to the raw PMT signal without correcting the baseline. Taking a running baseline with a short cycle time (10 minutes, of which 2 min is with the zero-NO_2 stream) compensates for the slow variation in the system's temperature dependence.

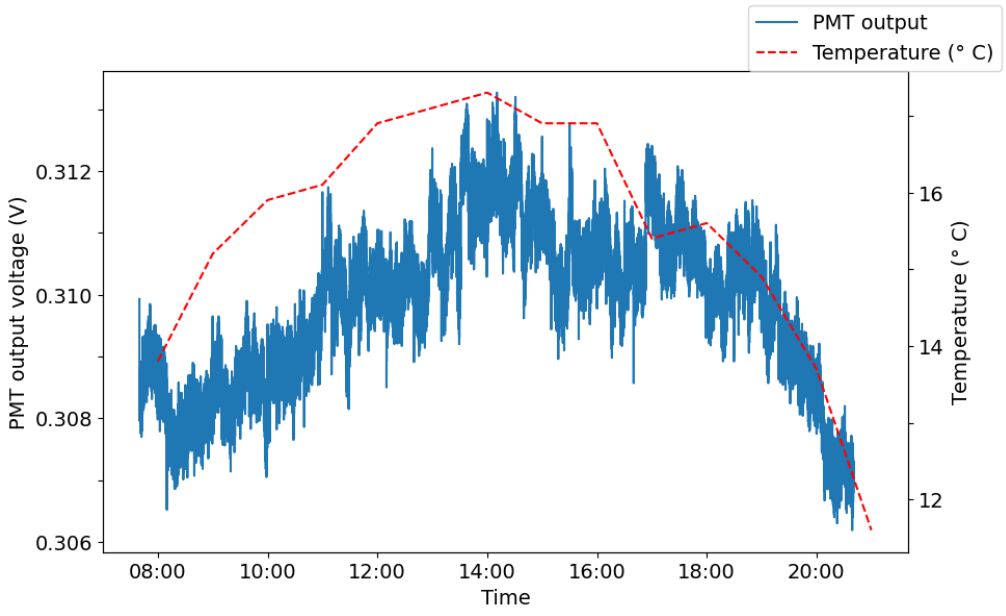


Figure 5.16. Time profile of the 1 m CEAS instrument and measured temperature on 20 August 2024. Temperature data are from the Cork Airport weather station. The displayed output PMT voltage was not corrected by baseline measurements to demonstrate the drift of the system throughout the day which could be related to temperature changes.

Microclimate effects on NO_2 measurement.

Wind speed and direction are key variables for identifying pollution sources near a monitoring site (Yu et al., 2004). Wind plays an important role in dispersing pollutants, with higher wind speeds spreading pollutants further from their emission sources, while low wind speeds can create stagnant air conditions, leading to increased local pollutant concentrations (Chew & Norford, 2018). In cities and large towns, urban design can have a major effect on wind patterns, as tall buildings on either side of narrow streets can create an effective 'street canyon', where natural ventilation is low. Wang et al. (2023) discussed the effect of gaps between buildings on natural urban ventilation, particularly on streets with buildings on both sides, and reported an increased flushing effect on street-level pollutants when there is high speed wind flow between buildings. In the context of this work, NO_2 measurements were taken on Blarney St, a narrow 10 m wide, largely residential street lined with two-storey dwellings.

Blarney St is a long regular street canyon, as defined by Vardoulakis et al. (2003) and Nicholson (1975), with an aspect ratio (H/W) of approximately 1. As previously discussed, the wind field in a street canyon is heavily influenced by the prevailing wind direction and its relative orientation to the street. Winds propagating in the same direction of the street, i.e., parallel, cause a Venturi effect where wind speeds increase through narrow streets (Blocken et al., 2008; Sanjaya et al., 2020) and channel emissions along the street, resulting in increased mixing ratios (Hoydysh, 1994).

The wind field in a street canyon becomes more complex when the wind is coming from a perpendicular direction to the street. Roof-level winds affect the wind flow in the street below. As shown in Figure 5.2, Blarney St experiences mostly skimming flow, which creates a wind vortex on the street, as well as some wake interference which leads to additional minor vortices in the corners of the street canyon (Hunter et al., 1992; Vardoulakis et al., 2003). The measurement site on Blarney St is on the south side of the street, so northernly or southernly winds will disperse emissions through this street canyon vortex. The recirculating velocity of a vortex is 0.33 – 0.5 times the roof-level wind velocity (Berkowicz et al., 1997), so emissions are dispersed quickly around the street and transport time to the NO_2 detector are fast. NO_2 that is emitted from vehicles as a primary source will therefore be detected, as well as some secondary

NO_2 which is formed from the fast reaction of locally emitted NO and O_3 in the air (Berkowicz et al., 1997; Pirjola et al., 2012).

Polar plots combine wind speeds, wind direction and pollutant concentrations to identify the direction of emission sources relative to the monitoring site (Carslaw & Beevers, 2013; Vardoulakis et al., 2003; Westmoreland et al., 2007). A polar plot of emissions measured at Blarney St during the school term is shown in Figure 5.16. Here, the wind direction represents the direction that the wind is coming from. Meteorological data was obtained from the Met Éireann monitoring site at Cork Airport located 6.18 km from the measurement site and the local wind direction on Blarney St is expected to differ. Wind data was filtered to wind speeds less than 10 knots to omit days where wind speeds were unusually high and skewed data, such as on 19 - 20 October, during Storm Ashley when wind speeds of up to 30 knots were recorded.

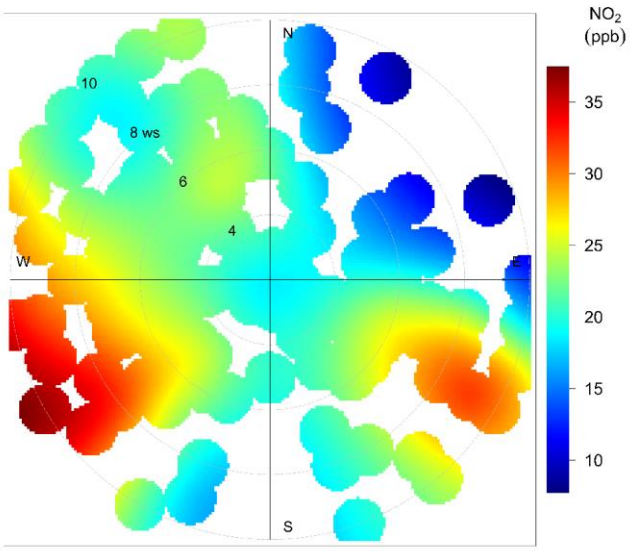


Figure 5.17. Polar plot of NO_2 emissions measured at the Blarney St measurement site during the school term as a function of wind speed and direction. Meteorological data has been filtered to remove high wind speed events > 10 knots.

Blarney St is oriented approximately east to west and winds along these directions dominate in this area, the effect of which can be clearly seen in Figure 5.17. High mixing ratios of NO_2 up to 30 ppb were observed at medium wind speeds (6-8 knots)

to the southeast of the measurement site, indicating that the emission source was not directly at the site, but nearby to the east. The frequency polar plot reveals that the south-east had the highest frequency of increased NO_2 mixing ratios with measurements up to 120 ppb, indicating that major sources of NO_2 are found to the southeast of the measurement site. This is the direction of Cork city centre and the major transport arteries along the northern channel of the River Lee. In addition, the fact that higher concentrations are observed when the wind is coming from the south and that the monitoring site is on the south side of the street, suggests some street canyon recirculation may be occurring, meaning that emissions from the windward side of the street are pulled across to the leeside of the street, as shown in Figure 5.2 (Carslaw & Davison, 2024).

The highest average NO_2 mixing ratios up to 35 ppb were observed coming from the southwest at higher wind speeds of 10 knots, indicating that emissions from the west are coming from further away than those to the east. These emission events can be attributed to nearby roads to the south, such as Sunday's Well, a narrow road which sees moderate traffic volumes, or accumulations of pollution as the air is channelled through the street canyon.

Since the measurement site was on the southside of the street, when the wind blows from the north, NO_2 emissions at the measurement site (windward) may be suppressed by the street canyon effect. Mixing ratios up to 25 ppb were observed from the north-west where there is a large residential area with associated high volumes of traffic, frequent bus routes, and residential heating and cooking.

For comparison of NO_2 dispersion during and after the school term, polar plots of the wind field and NO_2 mixing ratios of the final weeks before the mid-term break (SCH 2) and the mid-term break (MT) are shown in Figure 5.18. The same analysis is not shown for the measurements before the school term and the first weeks of term as they have rather different wind directions. The mixing ratios observed during the end of the school term (Figure 5.18a) are considerably higher on average than the mid-term break (Figure 5.18b), which will be discussed in more detail in the following section. The direction of NO_2 emissions changes, with high mixing ratios coming from predominantly the east and west in SCH 2 compared to high emissions at the measurement site in MT when the wind is coming from the south. Differences in traffic

flow around the school term can explain this stark difference in emission distribution, particularly since the selected weeks have relatively similar wind fields. NO_2 concentrations are particularly low (< 19 ppb) in MT with north-westerly winds, in comparison to SCH 2 which shows higher concentrations up to 30 ppb in the north-west quadrant, suggesting that school traffic not only affects the area directly around the school, but could also affect traffic volumes in the surrounding area, leading to a higher background concentration of NO_2.

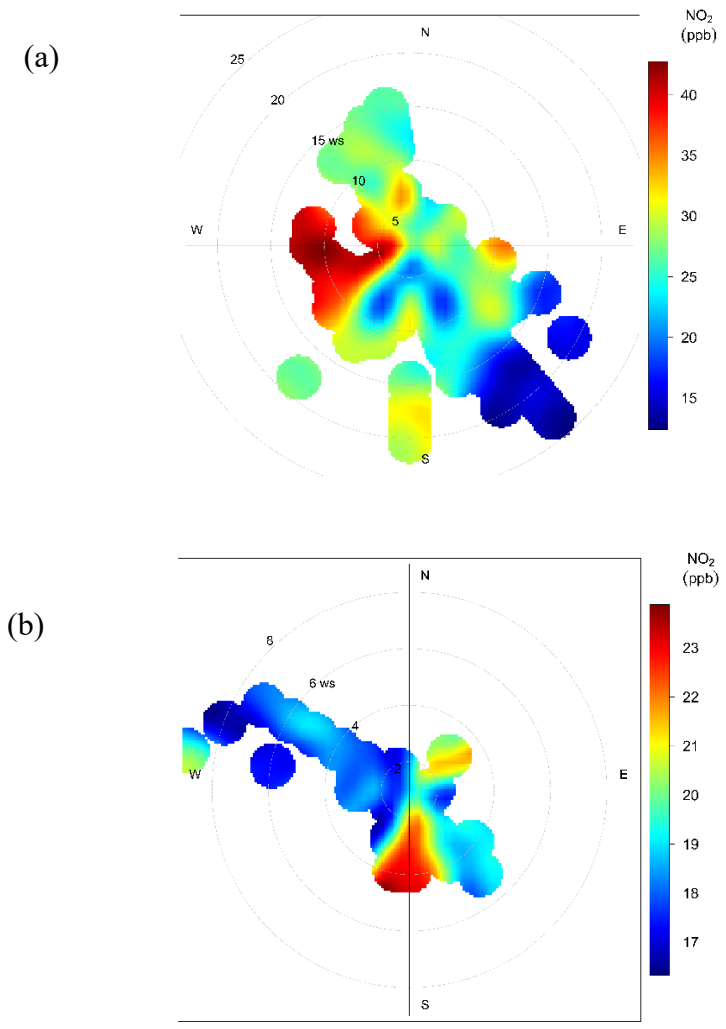


Figure 5.18. Polar plots showing the final weeks of school term before mid-term break (a) and the week of mid-term break (b). Note the difference in colour scales.

Representing pollution data in polar coordinates helps to identify local sources, allowing local authorities to introduce effective mitigation strategies to improve the

local air quality. Wind data used in this analysis was taken from the Cork Airport site as a proxy meteorological measurement. The wind field analysis would be more robust if roof-level wind measurements were made at the measurement site. Simultaneous measurements of NO_2 from either side of the street would also allow a more in-depth analysis on the wind flows caused by street canyoning, as was done by Pirjola et al. (2012) who monitored windward and leeside NO_2 concentrations simultaneously in a mobile measurement campaign. Their measurements showed that upwind concentrations in a street canyon were higher than those downwind. Extensive modelling of the wind fields during the measurement period could provide additional detail on the transport of NO_2 (Vardoulakis et al., 2003) but was beyond the scope of this thesis.

Temporal trends in NO_2

NO_2 mixing ratios vary throughout the day, as is seen in well-documented diurnal profiles, with most trends showing a morning and evening peak that coincide with traffic rush hours (Li et al., 2021; Park et al., 2024; Voiculescu et al., 2020). Solar radiation also plays a role in the diurnal trends since NO_2 is easily photolyzed; as a result, just after solar noon (12:00 UTC, 13:00 DST) photolysis of NO_2 will depress NO_2 concentrations in the afternoon, hence, increased photochemical activity can give higher variation in diurnal profiles, and vice versa (Edwards et al., 2024). At the same time, wind speeds tend to increase in the middle of the day, as shown by the wind speed and temperature diurnal profiles Figure 5.8, and disperse pollutants more effectively. In addition to these meteorological effects, traffic activity can influence the typical daily NO_2 trends. Local NO_2 sources, such as traffic, increase the ambient mixing ratio and can produce unusual NO_2 diurnal profiles (Shen et al., 2023).

A typical NO_2 diurnal profile on St Patrick St, Cork City for 2023 – 2024 is shown in Figure 5.19. These NO_2 concentrations were recorded using an Airnode sensor from data shared by C. Reddy & D.S. Venables. Elevated NO_2 concentrations were observed in the morning, coinciding with rush hour traffic, and again in the evening after 17:00 beginning at rush hour and concentrations continued to increase into the evening, which may be associated with traffic and possibly some emissions from

residential cooking and heating. The microenvironment of St Patrick St is different to the long street canyon on Blarney St, with a low aspect ratio where $W > H$ for the most part. Blarney St is approximately 1 km from St Patrick St, and yet shows substantially different diurnal trends due to its local microenvironment and increased emission sources around school times.

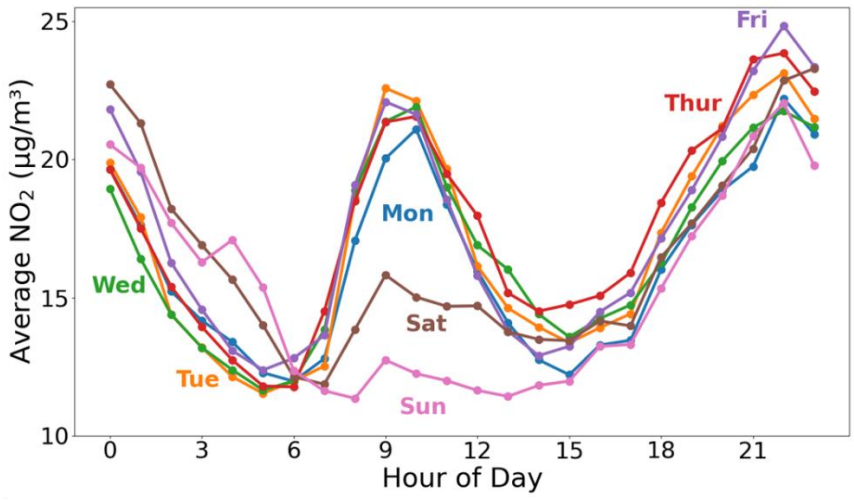


Figure 5.19. Diurnal trends of NO_2 on St Patrick St, Cork City measured by Airnode. This street has a low aspect ratio with good ventilation conditions and does not constitute a street canyon. Data kindly shared by C. Reddy & D.S. Venables.

The diurnal profile of NO_2 on Blarney St across the entire measurement period is shown in Figure 5.20, including the week before school term (out of term) and the mid-term break. Error bars show the deviation from the hourly mean. Notably, the deviation was relatively small for the out of term and mid-term weeks largely because these datasets were smaller, spanning only one week, while the school term data encompassed eight weeks of measurements with high variability in meteorological conditions between week 1 and week 8. Changes in driving patterns may have also contributed to the high variability during the school term, as the traffic volumes varied by day, depending on the weather, for example. The variability at 19:00 is high compared to other times of the day. A large evening peak is however typical in NO_2 diurnal trends.

An afternoon maximum mixing ratio is observed at 12:00 and NO_2 levels remain elevated until 15:00, aligning with the pick-up times at Blarney St CBS (13:20 and 14:20). Typically, there would be a decrease in ambient NO_2 at this time due to ambient temperatures and solar radiation, however, when school is in term, traffic in the surrounding area increases (Liu et al., 2022), leading to more local sources of NO_2 that sustain relatively high NO_2 mixing ratios despite the effects of radiation and meteorology.

Ambient NO_2 concentrations are usually higher in the winter compared to the summer, as discussed by Huang et al. (2022) who observed an approximate increase in mean NO_2 of 10 ppb between autumn and winter from 2005-2020. A similar difference is shown in Figure 5.19 between the out of term week which is at the end of summer and the mid-term week which is in winter where the mean daily mixing ratios are 9.1 ppb and 19.6 ppb, respectively. However, the mean daily mixing ratio during the school term was 29.7 ppb, highlighting that the effect of school traffic can suppress meteorological/seasonal effects on NO_2 emissions.

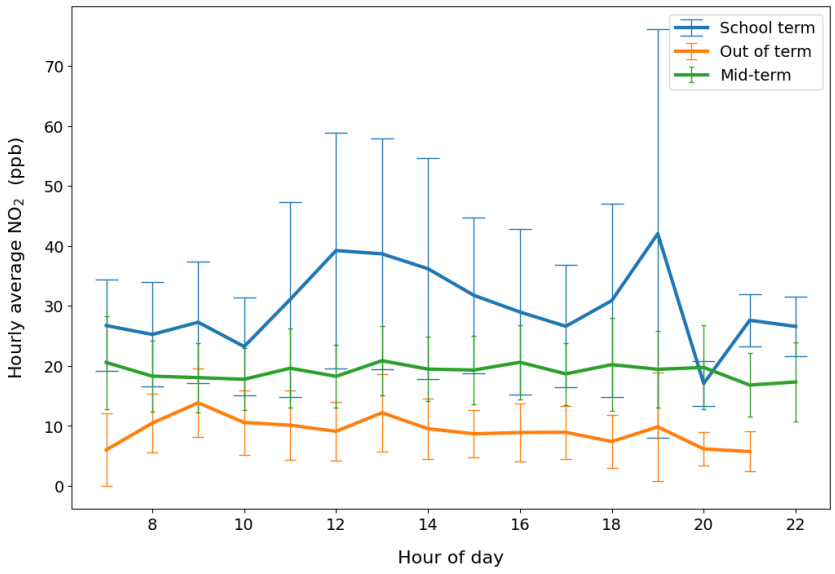


Figure 5.20. Diurnal profiles of all Monday - Friday during each measurement stage: out of term, in term, mid-term. Error bars show the variability of measurements.

Effects of school traffic on NO_2

To better observe the change in NO_2 emissions at the beginning and end of the school term, the difference in hourly NO_2 mixing ratios during the background measurement week before school term began and the first 2 weeks of school term is shown in Figure 5.22. These 3 weeks are initially compared so that there is little variation in meteorological conditions such as ambient temperature and solar radiant intensity, with average temperatures between 16 – 18 °C. However, there were different wind conditions the week before school term when compared to the wind field during the first two weeks of term (Figure 5.21). The prevailing wind direction during the out of term (BG) week is south-westerly, in comparison to a north-westly wind direction in the first two weeks of school term.

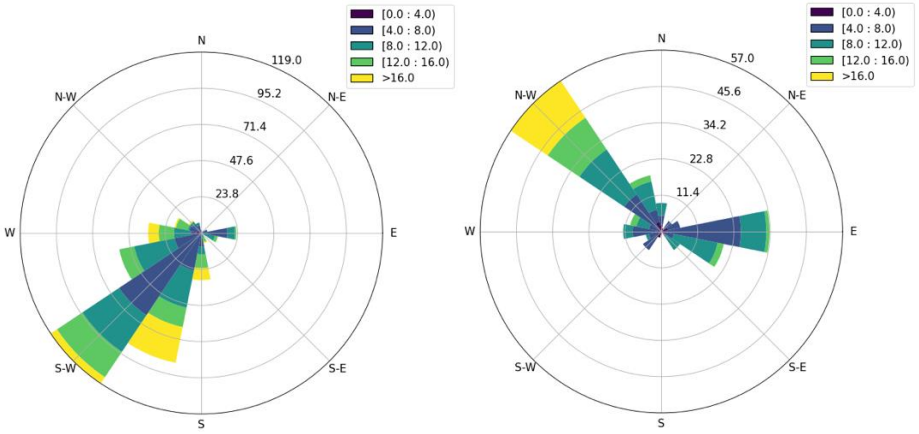


Figure 5.21. Wind rose plots showing the wind field before school term began (left) and during the first two weeks of school term (right). The prevailing wind on the left is south-west and on the right is north-west.

The week out of school term (blue line, Figure 5.21) shows an almost typical NO_2 diurnal profile with a local maximum at 09:00 and 19:00. Typical NO_2 trends would show a decrease in mixing ratio in the afternoon when temperatures are highest and the sun is high in the sky, encouraging photochemical activity (Li et al., 2021). However, Figure 5.22 shows a small peak in NO_2 at 13:00, associated with an increase in heavy vehicles at this time during the pre-term measurements (BG), shown in Figure 5.23. The first 2 weeks of school term (SCH 1) show a large increase in NO_2 across

the day (solid orange line, Figure 5.22), with hourly mean mixing ratios at least twice as large as the BG week. The afternoon peak is intensified between 12:00 – 14:00 where mixing ratios are approximately 6 times higher than the out of term week in the period where the school day ends and parents/guardians arrive to collect children. The number of heavy vehicles at this time was reduced compared to the BG week, and car numbers also increased. It was therefore observed that a major factor affecting traffic volumes and emissions in the local area is the school term and driving behaviours around collection times.

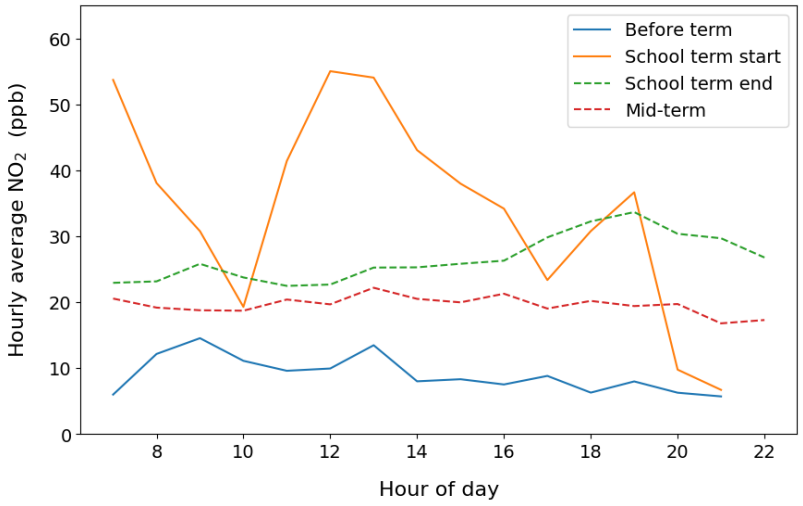


Figure 5.22. Diurnal profile of the background out of term measurements compared with the first 2 weeks of school term (solid lines) and the final two weeks of term compared with the mid-term break (dashed lines).

Traffic patterns on Blarney St are not straightforward. The diurnal trends in traffic flow (Figure 5.23) show that the number of cars were relatively constant across the day. A partial explanation for this may be that drivers that are familiar with the street will avoid it at busy traffic times and may choose a route through Blarney St when traffic is expected to be quieter, suppressing the typical diurnal profile of traffic flow. A similar explanation can be given for heavy vehicle flow on the street, as the number of heavy vehicles reduces when the school term begins (blue and orange lines, Figure 5.23).

Considering the wind field of BG and SCH1 weeks, emissions on the street may have been even higher in SCH1. A prevailing north-westerly wind would be almost perpendicular to Blarney St, which runs south-south-west, causing wind vortices in the street canyon, as described by Hoydysh (1994) and Hunter et al. (1992) and sketched in Figure 5.2. These vortices would circulate fresh air from the north onto the windward side of the street canyon where the measurement site is located. Emissions from surrounding roads and streets to the north may have influenced these measurements.

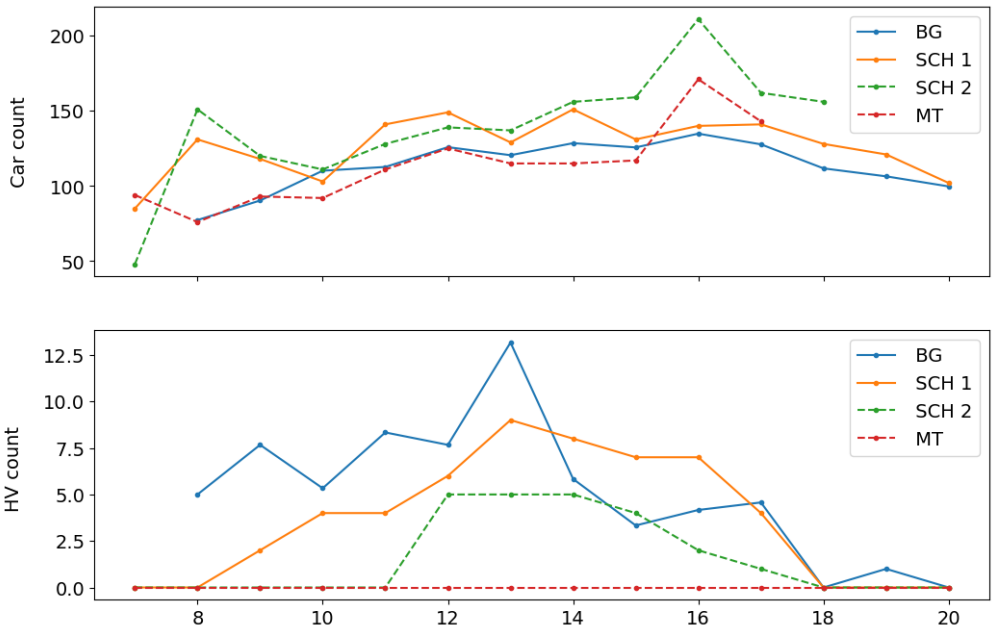


Figure 5.23. Hourly average traffic counts for cars (top) and heavy vehicles (bottom) during the week before school term (BG), the start of the school term (SCH 1), the end of school term (SCH 2) and the mid-term break (MT).

Similarly, the diurnal profile of the last two weeks of school term (SCH 2) was compared to the trends observed during the mid-term break (MT) (dashed lines, Figure 5.22). These weeks compared more closely than SCH 1 and BG weeks, most likely because wind directions were more similar with a south-easterly prevailing wind in both periods (Figure 5.24). It is also noted that there are some westerly winds during the MT week and wind speeds are higher during SCH 2. Higher wind speeds in the final weeks of school term would have increased ventilation on the street and diluted

NO_2 concentrations, accounting for the small difference in SCH 2 and MT diurnal profiles. The diurnal trends for NO_2 appear to flatten during the mid-term break (Figure 5.22), although the peak at 13:00 persists, the only consistent feature across all discussed periods. In this case, the small afternoon peak was not caused by school traffic. The explanation for this feature is unclear. There were no heavy vehicles record passing around this time and the number of cars actually dropped at 13:00 compared with 12:00 (Figure 5.23). Some possible explanations are that this peak in NO_2 was associated with gas cooking or heating emissions from the surrounding area, or a small number of cars with particularly dirty emissions that drive by at lunchtime each day. Results from these traffic counters have not been verified and so may introduce some uncertainty into traffic measurements.

The final weeks of the school term (SCH 2) showed an increase in average NO_2 mixing ratios after noon, with mixing ratios staying raised until 16:00 when a steep increase in NO_2 was observed (Figure 5.22) Similar to the comparison between BG and SCH1, here a midday increase in NO_2 is observed in both SCH2 and MT, however, in both cases, in the school term weeks, NO_2 mixing ratios remained elevated in the hours following this peak. This is most likely due to increased traffic activity and congestion around school collection times at 13:20 and 14:20.

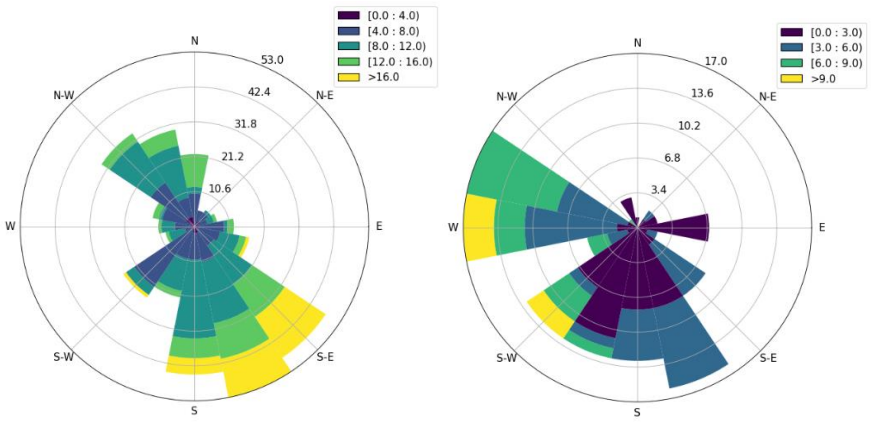


Figure 5.24. Wind rose plots showing the wind field around the measurement site during the last weeks of school term (left) and the mid-term break (MT). Prevailing winds are largely in the south and south-east, although the MT week also shows some westerly winds.

The effect of school times on ambient NO_2 mixing ratios was visualised by plotting kernel density estimate (KDE) plots for 15 minute intervals at times of interest (Figure 5.25.). KDE plots represent a continuous probability density curve based on the sum of the instances of mixing ratios during a given time interval. KDE plots for the school term (SCH), a background out of term week (BG), and mid-term break (MT) are shown in Figure 5.25 for a morning period around school drop-off times (08:00 – 09:00) and an afternoon period around school pick-up times (12:30 – 15:00). The axes on the morning period plots are limited to 150 ppb and the afternoon period was limited to 250 ppb to best visualise the data and compare different periods.

In the morning, bimodal peaks in concentration density were observed for all measurement weeks. During SCH weeks, the bimodal shape of the peak smoothed out between 08:15 – 08:30 (orange line), with an increased density of higher mixing ratios (50 ppb), indicating more instances of high concentrations at this time. Even higher concentrations were seen between 09:00 – 09:15, up to 150 ppb. When compared to BG and MT weeks, it is apparent that there was typically an increase in ambient NO_2 between 08:00 – 08:30, with concentrations falling after this period and density curves become single modal. During SCH weeks, mixing ratios are higher on average and maintain a bimodal distribution throughout the morning.

The afternoon period covered the collection time for the Junior and Senior Infants classes at 13:20, and the 1st to 6th class at 14:20. Once again, all SCH weeks had some instances of mixing ratios higher than shown in Figure 5.25, however for the purpose of comparing between all measured weeks, the x-axes are limited to 250 ppb for afternoon plots. During BG week, mixing ratios skew to the right between 13:00 – 13:30 up to ~ 45 ppb, in-line with a typical increase in traffic around lunch time, and mixing ratios fall after this period. Similarly, during MT week, mixing ratios peak between 13:15 – 13:30 up to ~ 30 ppb. In SCH measurement weeks, the KDE plots are more spread out than BG and MT weeks, indicating that there is much more variability in these mixing ratio measurements. Mixing ratios extend above 100 ppb from 12:45 and remain elevated until 14:30. The highest mixing ratios occurred between the period 13:15 – 14:00, which surrounds school pick-up time for the youngest two classes and immediately precedes the pick-up time for the older classes.

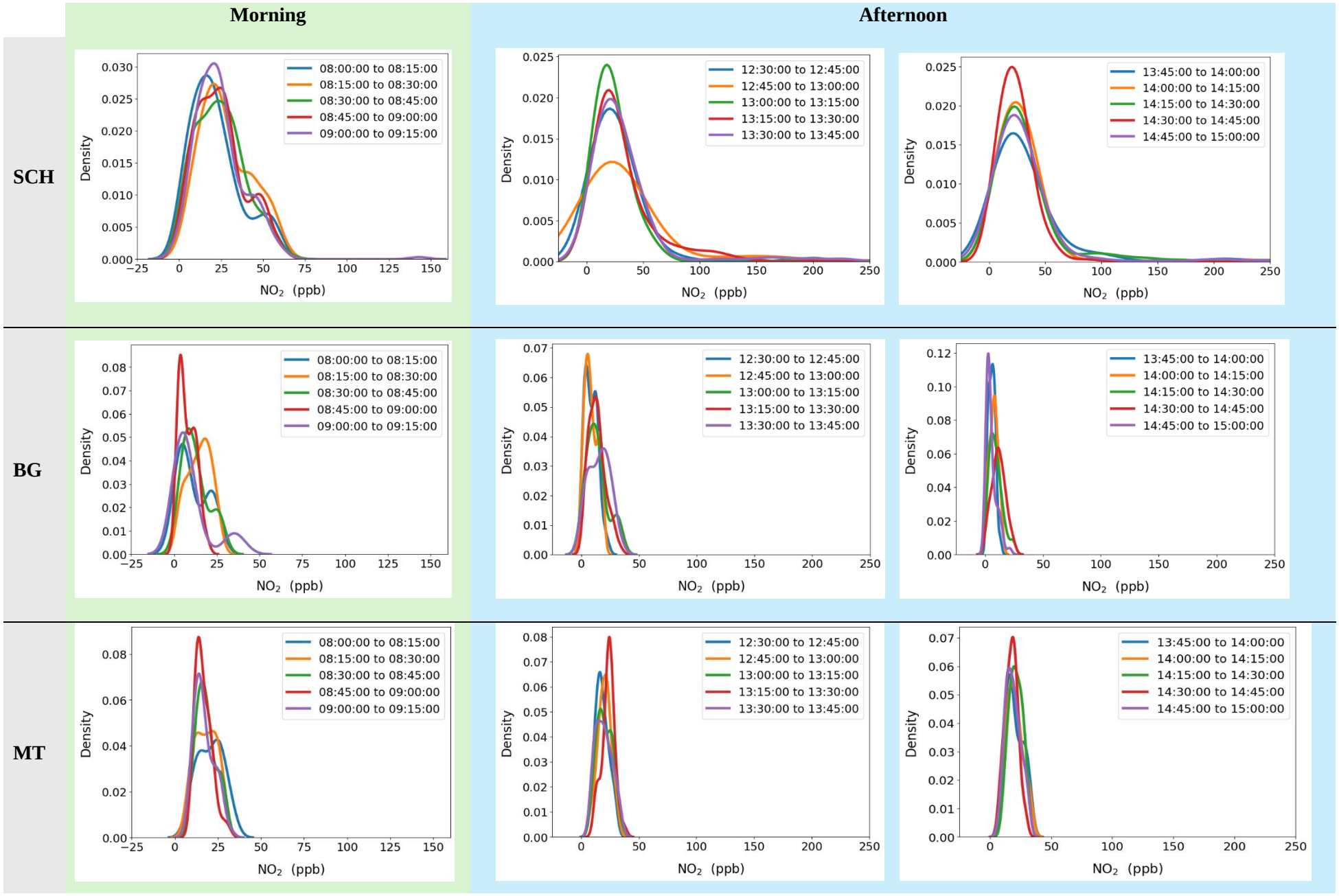


Figure 5.25. Concentration frequencies during specified periods for the school term (SCH), background measurement week (BG) and mid-term break (MT). Note x-axes are matched for all weeks during same time.

NO_2 measurements

Because traffic conditions are heavily influenced by the school term, measurements started one week before the start of the new school year (15/08/2024 – 22/08/2024) to establish a baseline. The NO_2 concentrations collected at the Blarney St monitoring site are compared in Figure 5.26 to the background NO_2 measurements from the UCC Distillery Fields AQMS. The Blarney St measurements were averaged over 30 minutes here for comparison to hourly data from the AQMS and the meteorological variables. Although the Blarney St and AQMS monitoring sites are only 190 m apart, they have strongly diverging exposure to nearby vehicular traffic and other NO_2 sources. There are few vehicle movements near the AQMS, including in the nearby staff car park with approximately 100 spaces, whereas the Blarney St site has higher vehicular traffic volumes and considerable traffic congestion at certain times. Blarney St is also surrounded by other narrow residential streets and could be influenced by vehicular traffic emissions from surrounding busy roads.

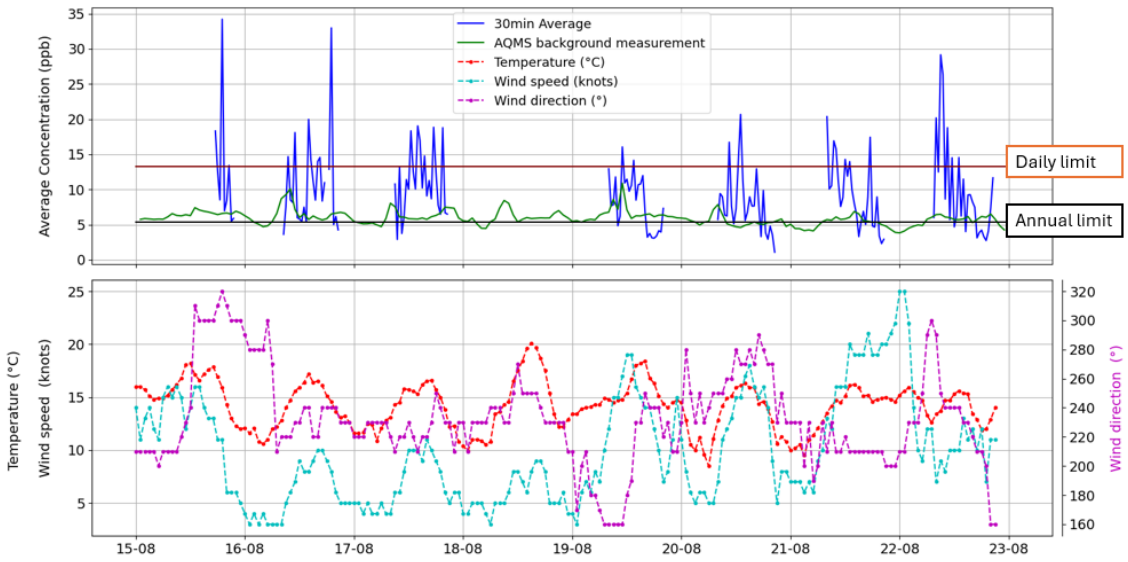


Figure 5.26. Comparing NO_2 concentrations from the measurement site to AQMS background site for August 2024. Meteorological data is shown in the lower panels. The 24-hr mean limit and the annual mean limit air quality guidelines by the WHO are shown as horizontal lines in the top panel.

Meteorological data shows hourly average temperature (°C), wind speed (knots) and wind direction (°). Winds that are generally easterly or westerly would be expected to give rise to air masses travelling along the street canyon, leading to accumulation of traffic pollutants and higher concentrations of NO_2. Vehicles travelling in the same direction as the wind might also give rise to higher NO_2 concentrations as the source of pollution travels with the air mass. In contrast, when the wind blows opposite the direction of travel, observed NO_2 concentrations should be lower as they are emitted into a larger effective volume of air over the same period of time. However, the effects of travelling direction cannot be easily distinguished in this dataset as vehicles were moving in both directions.

Figure 5.26 shows an interesting time period on 22/08/2024 at 09:00 where the wind direction changed suddenly between 300° (northwest) and 240° (southwest). Following this change in wind direction, a sharp change in NO_2 concentration was observed. This change may arise from emissions from residential areas to the northwest, while sources of NO_2 become less significant as the wind shifts to the southwest, a direction characterised by playing fields, parks, and a lower housing and road network density.

Vehicular traffic volumes and NO_2 concentrations

High time resolution traffic data was collected at the measurement site using RoadCount, and 230 m further east along Blarney St using a Telraam sensor (Figure 5.6). The observed traffic flow at the NO_2 measurement site is 1.5 to 2 times lower than the traffic measured at the Telraam site (Figure 5.27). The difference in these measurements indicates that more vehicles are present on the street near Blarney St CBS and may have turned on or off Blarney St before reaching the measurement site. Although Blarney St itself has two-way traffic, many surrounding streets are one way, e.g., Sunday's Well Avenue, Gurranabraher Road and Baker's Road, thus dictating certain vehicular movement patterns on Blarney St that would lead to a decrease in passing vehicles at the measurement site compared to the Telraam site. Cars approaching Blarney St CBS from the east would typically turn up the Old Marketplace or travel back down Blarney St, rather than driving further up a narrow and difficult road unnecessarily. This is an important factor to consider while

interpreting the following traffic data as the number of cars reported by RoadCount may be less than the cars present on the road nearby contributing to NO_2 emissions. Both sensors automatically identify passing vehicles as cars or heavy-duty vehicles, but do not estimate the accuracy of identifying vehicles.

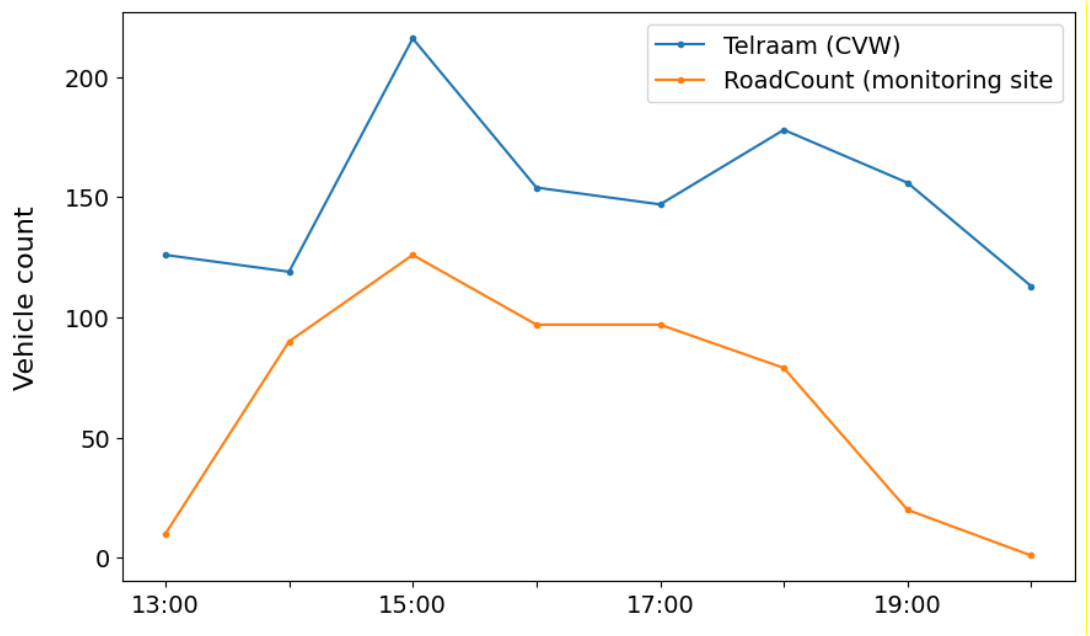


Figure 5.27. Time dependence of Telraam and RoadCount hourly total car counts on 11/09/2024 at sites on Blarney St separated by 230 m. The RoadCount data are factor of 1.5-2.0 lower than the Telraam counts for much of the day.

The association between passing cars and NO_2 measured by the CEAS instrument was investigated by looking at a time series of NO_2 mixing ratio and vehicle counts on Thursday 12/09/2024 between 12:00 and 14:30, capturing traffic conditions during school collection times at 13:20 and 14:20. NO_2 measurements were averaged over 30 seconds to account for the system response time and traffic data has been averaged over 15 minutes for better clarity (Figure 5.28). There was a notable spike in NO_2 mixing ratio up to 70 ppb at 13:00 after 20 cars and 3 heavy vehicles passed in the previous 15 minutes. Vehicle counts and NO_2 mixing ratios then decreased during the following 30 minutes. Increased traffic activity at this time is most likely due to parents/guardians arriving to younger classes (13:20). Measured NO_2 increased again after 14:00, reaching 50 ppb at 14:20. Although traffic passing the measurement site

was not particularly high before the end of school at 14:20, increased traffic flow after 14:30 suggests that there may have been cars present at the school before 14:20 that approached the school without passing the measurement site or cars that had been idling while waiting, and subsequently passed the measurement site while leaving Blarney St. The Telraam traffic sensor reported 127 cars passing between 13:00-14:00 while the high time resolution RoadCount data only reported 79 cars over the same period, highlighting that emissions may be seen at the measurement site for nearby traffic that does not directly pass the measurement site. NO_2 concentrations directly outside the school are therefore expected to be higher than the measurement site. A steep rise in NO_2 was observed at 14:45, corresponding to increased traffic activity and the presence of heavy vehicles.

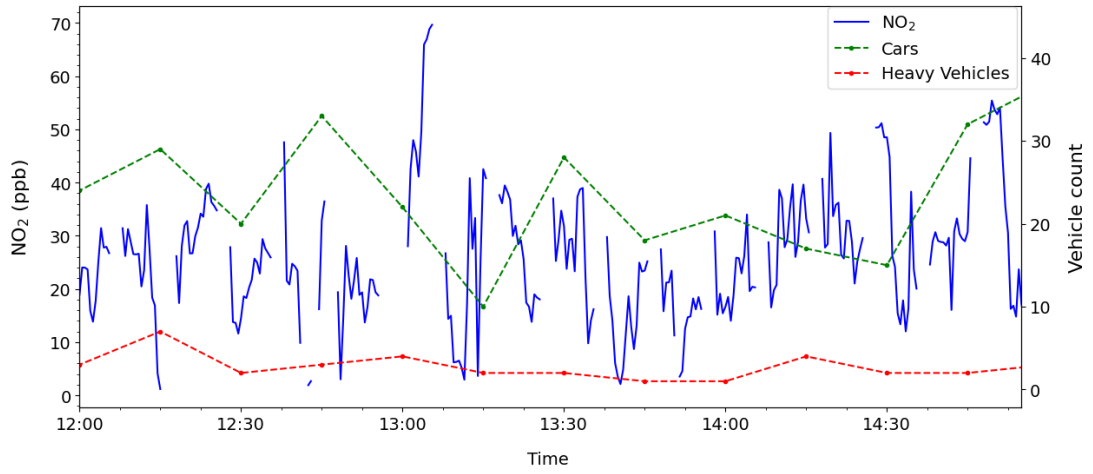


Figure 5.28. Thursday 12/09/2024 traffic and NO_2 time profile around school collection times of 13:20 and 14:20. Heavy vehicle counts include light vans that RoadCount identifies as heavy vehicles.

As a comparison, the same period was isolated from the following Thursday (19/09/2024) and vehicle counts and NO_2 mixing ratio trends were evaluated in Figure 5.29. In contrast to 12/09/2024, the prevailing wind direction was east on 19/09/2024 which would cause a channelling effect and disperse emissions up the street from the school towards the measurement site and beyond. The number of cars on the road was also lower on 19/09/2024 with 88 cars recorded by Telraam between 13:00-14:00 and

95 cars reported by RoadCount. Although the traffic passing the measurement site was higher on the 19th, the overall traffic on the street appears to be reduced according to Telraam data, supported by the fact that average NO_2 concentrations are lower than 12/09/2024.

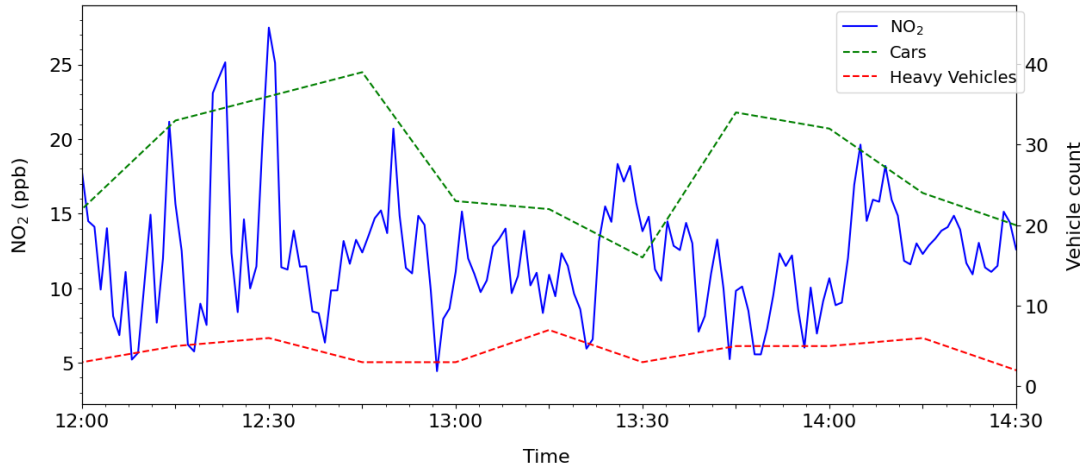


Figure 5.29. Thursday 19/09/2024 time profiles of NO_2 mixing ratio and vehicle volumes around school collection times. Mixing ratios are averaged over 30 s compared to 10-minute averaged traffic data. Heavy vehicle counts include light vans that RoadCount identifies as heavy vehicles.

There were sharp increases to 28 ppb of NO_2 at 12:20 and 12:30 which appear to follow an increase in passing cars in the previous 10 minutes. Another distinct increase in NO_2 was seen at 13:20 with consistent but low numbers of cars reported by RoadCount. Within the context of the school's environment this increase is most likely attributed to the first collection time at 13:20. Another sharp increase in NO_2 was observed at 14:05 following an increase in car flow. When the prevailing wind is parallel to the direction of the street, the wind field is less complex and patterns can be observed between traffic flow and changes in NO_2 mixing ratio.

A morning NO_2 time series is shown in Figure 5.30 from Thursday 19/09/2024. Traffic count data was averaged over 2 minutes in this shorter time period to best visualise the association between traffic volume and NO_2 mixing ratios. There was a

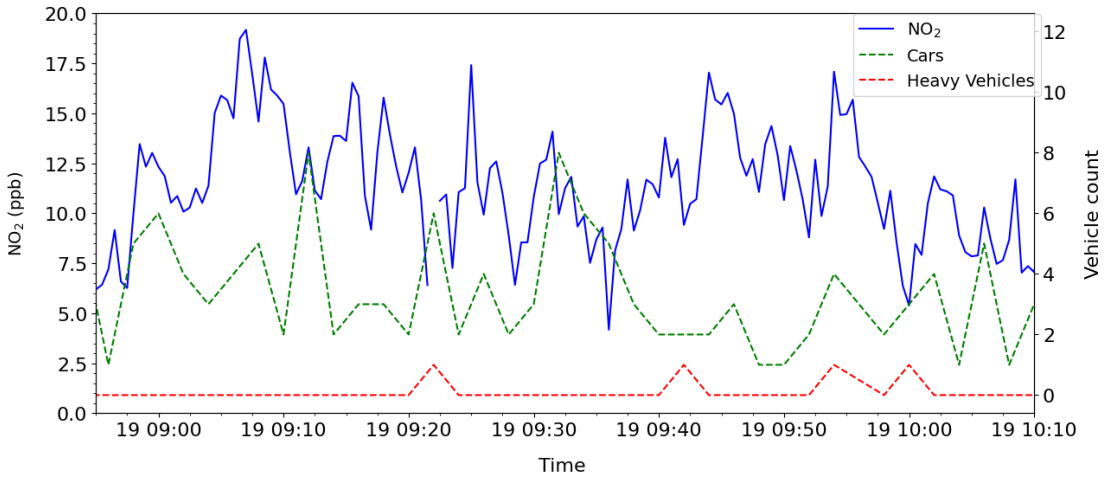


Figure 5.30. Thursday 19/09/2024 traffic correlation in the morning with 30 s averaged mixing ratios and 2 minute averaged traffic counts.

more apparent relationship between vehicle numbers and NO_2 mixing ratios in Figure 5.30 compared to Figure 5.29. An increased number of passing cars at 09:07 and 09:22 is reflected in the NO_2 mixing ratio immediately following these traffic increases. The effect that the direction of wind and travel may have on measured NO_2 concentrations was explored here, provided some assumptions are made. The direction of travel was not measured by RoadCount and so this information is not available. However, the direction of travel can be inferred based on the time delay between increases in NO_2 concentration and a car passing the measurement site. At 09:07 and 09:22 the emissions are seen after the cars pass the measurement site. A possible explanation is that the direction of travel of the majority of passing cars was opposite to the prevailing wind direction, i.e., the traffic was travelling west-east. The opposite case was seen at 09:30, where the emissions were observed just before the traffic passed, suggesting that the cars were travelling in the same direction as the prevailing wind, i.e., east-west, and are effectively driving through their own emission plumes. More robust traffic monitoring would allow these sources to be seen more clearly or may highlight other sources of NO_2.

Variability in meteorological conditions or road turbulence caused by traffic (Hoydysh, 1994) disrupts the usual dispersion of NO_2, and so traffic correlations can only be observed over short time periods if the time resolution of the measurement is sufficiently high. Figure 5.31 shows a correlation plot of 1-minute averaged mixing

ratios and car counts between 09:30 – 09:38 where this traffic event occurs. There is a positive correlation, although there is a lot of variability in the data with an R^2 value of 0.36 and slope of 0.38. Comparably, Kendrick et al. (2015) reported a linear relationship between traffic volume and roadside NO_2 with an R^2 value between 0.14 – 0.27 across a 15 minute interval. Emissions from all traffic surrounding Blarney St affect the mixing ratio at the measurement site. For a complete correlation between vehicle volumes and NO_2 mixing ratios, more traffic measurements are required, ideally from different points in the street, to map all traffic to emissions.

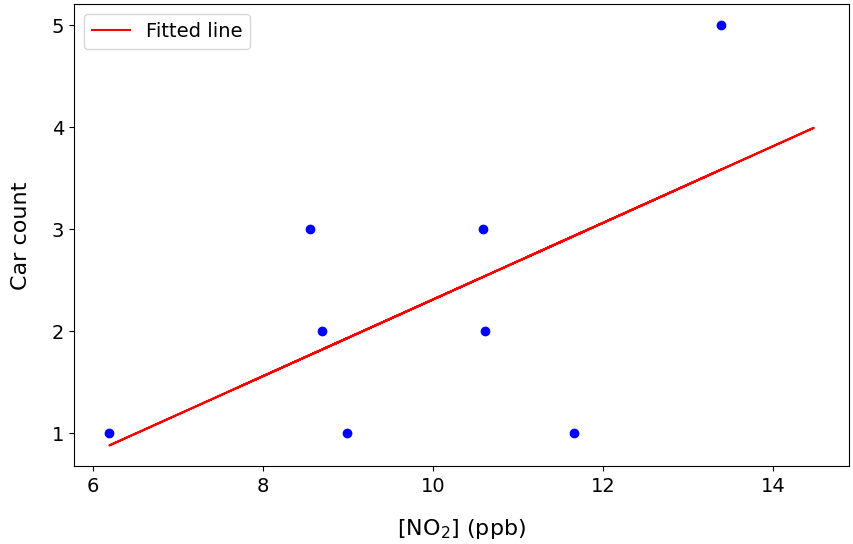


Figure 5.31. Correlation between traffic and NO_2 mixing ratio between 09:30 - 09:38. Mixing ratios and car counts are averaged over 1 minute for best comparison and the traffic data is lagged by 1 minute.

Heavy vehicles (HVs) potentially had a large effect on NO_2 mixing ratios. 3 HVs passed the measurement site between 09:40 and 10:05. All three instances of HVs correspond to a step change of approximately 5 ppb of NO_2. There were also co-incident cars passing at these times, but such a noticeable increase in NO_2 mixing ratio suggests that there is a large effect from HVs which are more likely to be larger diesel vehicles than the cars. More robust traffic monitoring would allow more investigation into these step changes in NO_2.

To further analyse the dependence of NO_2 on vehicle volumes, all traffic count data were concatenated and hourly averages across all weekdays were calculated. The hourly average car count is compared to the hourly mean NO_2 mixing ratios in Figure 5.32 where the colour of each marker represents the hour of the day. Three outlying points in the left of the plot skew what would otherwise be a fairly linear relationship, showing that typically roadside NO_2 concentrations increase with the number of cars, as is expected. However, the outlying points may represent changes in driver behaviour that will be explored further in this section.

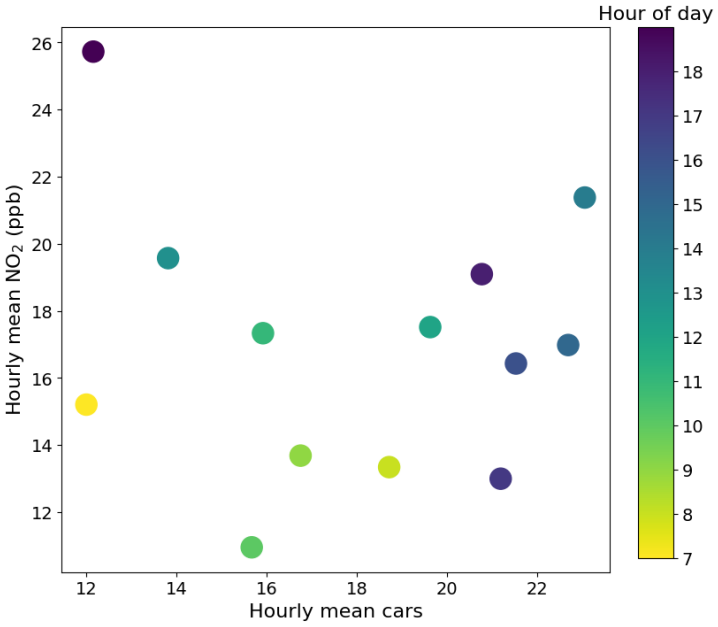


Figure 5.32. The hourly mean number of cars compared with the hourly mean NO_2 mixing ratio with different coloured markers showing the hour of the day. Traffic data was recorded at the measurement site using RoadCount.

The yellow point (07:00 – 08:00) shows an average count of 12 cars but with relatively high NO_2 emissions of 15 ppb. It is possible that these values are associated with emissions from cold vehicle engines ("cold starts"). It is known that cold starts, defined as the cold starting temperature of the vehicle engine and catalytic converter, produce considerably higher NO_2 emissions (Tu et al., 2021). Zare et al. (2021) reported that NO_2 emissions were 1.15 – 2.42 times higher when engines operated

cold, and increasing the share of biofuel in fuel mixtures led to even higher emissions during cold starts.

The highest number of cars (23 cars) and second highest NO_2 mixing ratios (22 ppb) are observed between 13:00 – 14:00, associated with increased traffic on the street for school pick-up time at 13:20 (Junior and Senior infants) and 14:20 (1^{st} to 6^{th} class). The 12:00 – 13:00 (light blue outlying point) shows only 14 cars passing the measurement site, 9 less than at 13:00 - 14:00, however, interestingly, the mean NO_2 mixing ratio is only 2 ppb less at 12:00 – 13:00. A decrease in car count without a corresponding decrease in concentration may indicate that some cars arrive early for school collection and continue to idle while waiting for collection time. Additionally, the street outside Blarney St CBS is particularly narrow for two-way traffic and multiple observations of traffic behaviour at school times indicated that the street becomes very congested around school pick-up times, leading to slower moving or idling traffic. The difference in car count and mixing ratio at 12:00 – 13:00 may also be explained by vehicles simply not passing the measurement site by turning off Blarney St.

The final point for 18:00 – 19:00 (purple) shows the highest mean NO_2 mixing ratio, near 26 ppb, with one of the lowest car counts throughout the day with only 12 cars. This aligns with typical NO_2 diurnal trends which show an evening peak in concentrations linked with residential heating and solid fuel burning. Typical traffic rush-hour in Cork City is from 16:00 – 18:00 (TomTom International, 2024) which means it is reasonable to assume that most commuters arrive home after this time, ie. 18:00 – 19:00. Drivers must parallel park all along the street, fitting into small parking spaces. The high mixing ratios seen at 18:00 – 19:00 could possibly be a result of parking cars, particularly those that may have been nearby the measurement site, leading to an increase in measured NO_2, even without many cars passing through.

5.4 Discussion

Measurements of NO_2 emissions near a primary school on Blarney St in the north of Cork City were carried out to determine the effect of school-related traffic on ambient NO_2 mixing ratios. NO_2 was measured with a standard deviation of 7.8 ppb in 1 s scans, which was improved to 1.5 ppb when Savitzky-Golay filtering was applied over a 30 s window, matching the instrument response time. The effects of traffic, driver behaviour and meteorological conditions were considered and discussed in this chapter.

Polar plots, which consider NO_2 mixing ratios as a function of wind speed and direction, were applied to this measurement campaign to identify the direction of NO_2 sources. Highest concentrations of NO_2 were observed coming from the east and west of the measurement site, which was not surprising given that Blarney St is a narrow street running east to west. Emissions from the east were partly attributed to Blarney St CBS, located 115 m to the east of the measurement site. Higher speed westerly winds most likely blew emissions from a nearby busy road, Sunday's Well, or from the west end of Blarney St where there is another primary school, 1 km away.

NO_2 has a natural diurnal profile with a morning and evening peak, typically lining up with traffic rush hours and low ambient temperatures. Mixing ratios would usually decrease in the late morning to afternoon when the sun is high in the sky and photolysis can occur. However, throughout this measurement campaign, a small increase in NO_2 was observed around 13:00 during BG and MT weeks and was suggestive of a modest lunchtime increase in traffic. During SCH weeks, the afternoon peak reached higher concentrations and extended over a longer time period, lining up with school collection times at 13:20 and 14:20. A seasonal effect on NO_2 could also be observed through these diurnal profiles, where mixing ratios increased by a factor of 2 during the mid-term break at the end of October (MT) compared to the week before school term began (BG) mid-August. An increase in NO_2 is expected in colder, darker months as less photolysis is likely to occur and traffic volumes tend to increase on roads.

KDE plots were presented to visualise how NO_2 mixing ratios change during school drop-off and pick-up times. More instances of high NO_2 mixing ratios were observed during SCH weeks, with more variability in measurements than in BG and MT weeks. Higher NO_2 mixing ratios were seen around school drop-off and pick-up times. Although this is not a surprising result, it is important local evidence that can support

local authorities' efforts to make changes to traffic infrastructure around schools to reduce ambient pollution. Increased variability in NO_2 measurements during the school term can be explained by differences in driver behaviour throughout the school term as well as seasonal NO_2 changeability.

Traffic was counted at the measurement site with high time resolution so that instances of increased NO_2 could be attributed to passing traffic. The number of passing cars and NO_2 mixing ratios were correlated over a short time period of 8 minutes with an R^2 value of 0.36, which compares well with work done by Kendrick et al. (2015) who reported an R^2 value between 0.14 – 0.27 across a 15 minute interval. Meteorological variations, such as temperature, wind speed and direction, affect the dispersion and lifetime of NO_2, adding complexity to the correlation between passing traffic and NO_2 emissions. The direction of travel and the wind direction might also be considered because a lag effect is seen when traffic travels against the wind. Therefore, when counting traffic at a pollutant measurement site, it would also be advantageous to record the direction of travel. It is also important to consider that not all nearby traffic passed the measurement site, as was the case in this measurement campaign, with higher hourly average vehicle counts recorded by a Telraam sensor 230 m from the measurement site. Heavy vehicles were differentiated from light duty vehicles in the traffic measurements in this campaign, and there are some suggestions of step changes in NO_2 mixing ratios of up to 5 ppb on a given day associated with passing heavy vehicles.

Driver behaviour can have a big impact on local NO_2 concentrations during normal rush hour periods and school collection times in the afternoon. To reduce air pollution around schools, drivers should be encouraged to switch off their engines when they arrive at the school to reduce emissions from idling. Although idling likely produces a relatively small portion of emissions, it is an easy change for individual drivers to make to reduce NO_2 emissions. Congestion around the school led to stopped traffic and slow traffic speeds, therefore, it should be recommended that parents/guardians park further away on quieter roads and walk to the school, or ideally cycle or walk to school when possible.

This measurement campaign could have been improved in a number of ways. The instrument could have been calibrated by colocation at the Distillery Fields AQMS to

confirm the instrument sensitivity and selectivity to NO_2. A reference spectral channel was used during the campaign to confirm the response to NO_2, but the uncertainty in this channel was limited by the calibrated cavity mirror reflectivity. Recalibrating the mirror reflectivity more frequently would reduce the uncertainty in these measurements. A signal generator for signal modulation and lock-in amplifier were required for reflectivity calibrations based on the phase shift. The associated systems are relatively high cost; however, this calibration approach is a simpler and safer method of calibration than using external gas supplies to measure known extinction in the cavity. The cavity mirror reflectivity was relatively stable for much of the campaign despite the absence of mirror purge gases. This stability suggests that particulate matter was effectively removed by the filter. The mirrors only required cleaning once, 4 weeks into the 2 month measurement period.

The pressures in the NO_2-free reference inlet and the unfiltered sample inlet needed to be balanced using a needle valve. Monitoring the pressure within the cavity using a pressure probe would allow the user to ensure that the pressure matches in both channels. The charcoal filter was replaced after 4 weeks during instrument maintenance to remove leaks in the tubing system, although the same filter would have feasibly lasted for the entire measurement period.

Traffic flow on Blarney St was only measured for 3 weeks during this campaign due to access restrictions at the measurement site. High time resolution traffic monitoring would have provided more data to find correlations between traffic flow and ambient NO_2 mixing ratios. In addition, recording the direction of travel of passing vehicles would have provided some insight into the effect of vehicle emissions when travelling with or against the prevailing wind direction. To provide a richer analysis of the effect of specifically school traffic, a survey of the students could provide evidence of driver motivations and behaviours.

Modelling of the local wind field in the context of a long street canyon would provide further detail on the sources and transport of NO_2 in this microenvironment (Vardoulakis et al., 2003) and could be supported by monitoring the roof-level wind velocities and directions at the measurement site. Additionally, measurements taken on both the north and south side of the street could have better characterised the wind vortex within the street canyon, as was done by Pirjola et al. (2012) who monitored

NO_2 pavement exposures in a 2.5 week mobile monitoring campaign and found, through simultaneous measurements, that the concentrations on the leeside of a street canyon were consistently higher than the windward side.

The instrument used in this measurement campaign had a fast response time of 30 s which allowed spikes in NO_2 to be observed for passing vehicles, although a higher time resolution would be better suited to this purpose, and could be achieved by reducing the cavity dimensions, i.e., length and diameter. The effective path length within the cavity was relatively small for CEAS systems at 250 m. The sensitivity of the instrument could be increased by improving the effective path length with higher reflectivity mirrors. However, a standard deviation of 1.5 ppb is useful for ambient measurements and the use of shorter path lengths means that this method could potentially be used for remote measurements with similar path lengths, improving the spatial resolution of typical NO_2 open path measurements.

Although the instrument experienced long-term drift in the raw signal, taking reference NO_2-free measurements with a high duty cycle of 80% over a 10 minute cycle allowed this drift to be largely accounted for. The overall system was simple with no external gas supplies needed for cavity mirror calibration or purging. The instrument could be readily reduced in cost and size by replacing standard benchtop power supplies with battery packs and decreasing the length of the cavity.

Chapter 6 Conclusions

This thesis has presented work advancing fast and selective detection of NO_2 for application in urban and transport environments. NO_2 is a toxic trace gas that can severely impact environmental and human health, especially in vulnerable groups such as children, the elderly, pregnant women, or those with pre-existing cardiovascular or respiratory illnesses. The sources, reactions and cycles of NO_2 in the atmosphere have been described, and traffic was identified as a major source of this pollutant, including in Ireland (Environmental Protection Agency, 2023a).

Although NO_2 is one of the most commonly measured gas-phase pollutants, commercial monitoring systems have several disadvantages. These include relatively slow temporal resolution which can be inadequate to study the high spatial and temporal variability in NO_2, low portability, and high system cost. The introduction of commercially available low-cost NO_2 sensors based on electrochemical cells addresses some of these limitations but introduces others. While their lower cost and size is well-suited to the development of sensor networks to improve spatial coverage and resolution, these sensors are strongly influenced by ambient temperature, relative humidity, and are also vulnerable to interference from O_3 (Byrne et al., 2023; Dallo et al., 2021).

The measurement approach developed in this work is based on absorption spectroscopy to achieve good sensitivity and selectivity in a relatively compact system. A key objective has been to achieve these objectives in a lower cost system than commercially available instruments. Many spectroscopic instruments have been developed that use exceptionally long optical pathlengths to selectively detect NO_2 to low ppt-level mixing ratios (Castellanos et al., 2009; Osthoff et al., 2006; Zhou et al., 2022). Such sensitivity is not needed in urban environments in which NO_2 levels can reach mixing ratios of tens to hundreds of ppb. So, this work contributes to this active field by exploring the feasibility of low-cost and two-channel spectroscopic methods for detecting ambient NO_2 across shorter path lengths, and develops a wideband CEAS

instrument with an effective path length of 250 m and a reasonably fast response time of 30 s.

Simulations of four different detection methods were carried out in Chapter 2: three ratiometric two-channel approaches using either optical filters (narrow bandpass and dielectric filters) or a gas filter cell for spectral selection, and a single channel wideband method. The narrow bandpass two-channel approach was explored experimentally as it was determined to have a linear response to NO_2, with good selectivity and sensitivity. A proof-of-principle experiment was carried out using a dispersive spectrograph to monitor the ratiometric response of two narrow channels to NO_2, achieving a standard deviation in measurements of 8 ppb in 1 minute over an effective pathlength of 238 m. The narrow two-channel method was also demonstrated using non-dispersive photodetection with photomultiplier tube modules. This experimental realisation achieved a standard deviation of 71 ppb over an 8 m path in an acquisition time of 1 minute. While this sensitivity is inadequate for ambient monitoring applications, it should be noted that it was achieved with an exceptionally short pathlength and could be theoretically improved to 2.3 ppb over 250 m at the same time resolution (assuming the same signal-to-noise ratio). This approach boasts a simple optical design that could be easily packaged into a compact detection system for *in situ* measurements or used in remote long-path observations.

A drawback of the approach is that light levels were found to be too low to use cheaper photodiode detectors. Lock-in amplifiers were discussed as a suitable amplification method, particularly in remote sensing applications where a modulated active light source inherently distinguishes the signal from background light. Lock-in amplification was shown to be a suitable method for amplifying small, narrowband optical signals using a commercial benchtop lock-in amplifier. However, the commercial lock-in amplifier is not suitable for developing low-cost, portable measurements. An open source digital lock-in amplifier by Harvie & de Mello (2023) was discussed to reduce the system cost by two orders of magnitude and allow the simultaneous measurement of two channels.

In the absence of appropriate signal amplification for two narrow channels, a single wideband CEAS instrument was developed which achieved an effective pathlength of 250 m and a relatively fast response time of 30 s, limited primarily by the large internal

volume of the optical cavity. Reducing the length and diameter of the optical cavity would readily improve the system's time resolution. The standard deviation of measurements was 1.5 ppb and was considered suitable for measuring roadside NO_2 emissions. While the system's wideband approach could not distinguish the unique spectral absorption features of NO_2 and did not have inherently high selectivity, this approach was considered appropriate for application to urban measurements and the traffic microenvironment. In these environments, absorption by NO_2 dominates over the few other gas species that absorb in the same region (primarily glyoxal, methylglyoxal and ozone). Interference from glyoxal and methylglyoxal would be minimal because these species are generally found at sub-ppb mixing ratios in urban settings (Li et al., 2022) and their cross sections are smaller than that of NO_2. Likewise, interference from ozone absorption would normally be small because its absorption cross section ($\pm 10^{-21}$ cm^2 $molecule^{-1}$) is around 2 orders of magnitude smaller than that of NO_2, even as its mixing ratio is often larger. Absorption by water vapour may interfere with measurements between 420 and 460 nm where water vapour has absorption lines with cross-sections around 10^{-25} cm^2 $molecule^{-1}$ (Coheur et al., 2002). Although water vapour is present in much higher concentrations in the atmosphere than NO_2, the absorption at the operating wavelengths of the systems described in this work is 6 orders of magnitude weaker than NO_2. The wideband system was vulnerable to interference from particle scattering and so it was essential that particles were filtered out of the sample stream, making this approach unsuitable for remote sensing applications like DOAS or DIAL (Aminuddin et al., 2019; Lv et al., 2017; Schreier et al., 2019).

Chapter 5 of this thesis focused on the application of the 1 m CEAS instrument in monitoring NO_2 mixing ratios in a traffic environment near a primary school in Cork City. There is a growing interest in measuring NO_2 levels around schools with evidence shown that school drop-off and pick-up times greatly increase local traffic volumes (An et al., 2021). However, there is a need to demonstrate the effect of increased traffic on ambient NO_2 concentrations near schools, particularly since children are identified as an at-risk group in terms of pollutant exposure since their lungs are still developing.

Field measurements were carried out at a site 115 m from a primary school for 2 months, including one week before school term began, eight weeks of school term and

one week of mid-term break. Seasonal variation of NO_2 was observed between the week before school term (mid-August) and the mid-term break (end of October) where average mixing ratios increased by a factor of 2. The effect of in-term school traffic was observed with average mixing ratios increasing by a factor of (at least) 3 compared to the week before school term began and (at least) 1.5 compared with the mid-term break. The temporal distribution of NO_2 around school pick-up and drop-off times was investigated and it was confirmed that these times of interest were associated with an increase in NO_2 mixing ratios outside the school. Traffic around the school was confirmed as a likely source of this increase in NO_2 by analysing meteorological data such as wind speed and direction. The prevailing wind throughout the measurement period came from the south-east which resulted in high concentrations of NO_2 observed from the south-east of the measurement site due to microenvironment effects caused by a street canyon effect.

Traffic flow at the measurement site was monitored for 3 weeks to observe a correlation between NO_2 and the number of passing vehicles. Over a short period of 8 minutes, NO_2 mixing ratios and vehicle numbers were correlated with an R^2 of 0.35, however, care must be taken when interpreting traffic data as not all NO_2-contributing vehicles may have passed the traffic counter. The prevailing wind direction and the direction of travel were also found to influence when traffic emissions would be observed, as was found by Yu et al. (2004). There is evidence that heavy vehicles produced an increase in NO_2 mixing ratios. Monitoring traffic flow highlighted periods around school collection times where roads may be congested from parked vehicles and some drivers may be idling their engines, as inflated NO_2 mixing ratios were observed for only a small number of passing cars. Counting traffic was found to be a valuable addition to NO_2 measurements for identifying sources and behavioural changes that affect pollution levels.

This thesis provides background work for a low-cost and portable NO_2 detector capable of making fast measurements both *in situ* and remotely. The development of appropriate amplification modules is required to advance the development of the narrow two-channel system. A simple CEAS instrument with suitable sensitivity and selectivity was capable of measuring roadside NO_2 mixing ratios near a school and will inform local authorities of the effect that driver behaviours around school collection times have on local air pollution. Such technological advances in low-cost

emission monitoring help inform traffic interventions and infrastructure planning to reduce the negative effects of air pollution (Khreis et al., 2023).

6.1 Future prospects

Development of a narrow two-channel system is ongoing in the same research group and builds on the work presented in this thesis. For example, a shorter optical cavity with mirror separation of 15 cm and effective pathlength of 250 m is currently being developed in the group with the goal of developing a portable field instrument. A schematic of the proposed *in situ* instrument is shown in Figure 6.1 with a 15 cm optical cavity and two narrow channels measured by photodiodes. Supporting electronics such as lock-in amplifiers, power supplies and a pump system are stored on a second level in a cage-type configuration, shown in Figure 6.2. The proposed instrument dimensions are 35 cm × 25 cm × 20 cm, the approximate dimensions of a backpack, forming a relatively compact and lightweight instrument.

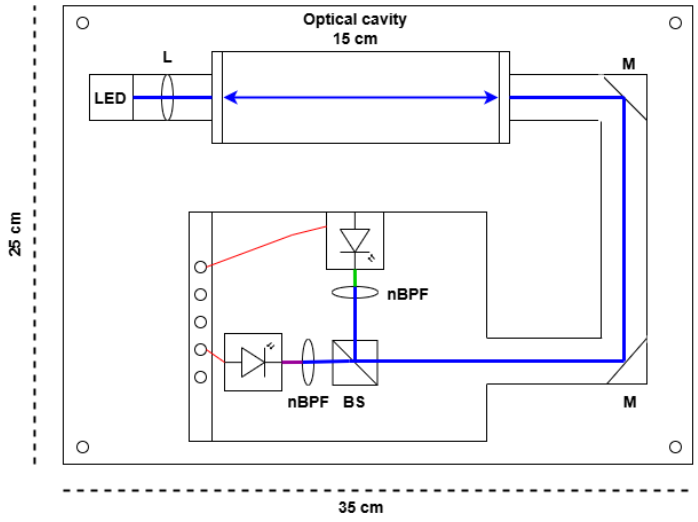


Figure 6.1. Schematic of proposed narrow two-channel instrument with low-cost components. This is the top level of the instrument with dimensions 25 x 35 cm^2.

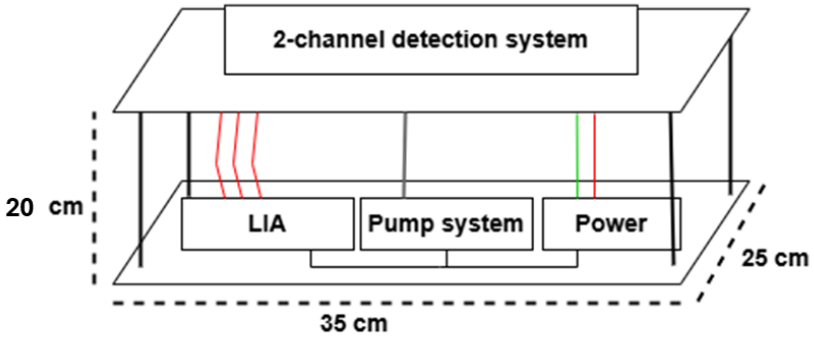


Figure 6.2. Schematic of the full narrow two-channel detector with two levels. The schematic shown in Figure 6.1 is on the top level, with supporting electronics such as lock-in amplifier (LIA), power supplies and pump system stored on the bottom level. The instrument has dimension 35 x 25 x 20 cm^3.

The selective two channel measurements that this work has demonstrated are well-suited to open path measurements where the target gas dominates the absorption in the operating wavelength region, as with NO_2 in an urban roadside environment. Modulating the light signal would be particularly useful in an open path system to discriminate the signal of interest from background ambient light. This approach would differ from the DOAS methodology which uses extensive spectral information and processing to discriminate the absorption of molecular species in the light path. Instrument development work in the group is building on the foundation laid in this thesis and is exploring the feasibility of a relatively straightforward optical configuration and relatively short pathlengths of tens of metres to measure NO_2. Such a system would allow observations of NO_2 emissions across a single road, for example, giving improved spatial resolution compared with other open path systems (Chen et al., 2020; Li et al., 2017). The open-source digital lock-in amplifier (OLIA) discussed in this thesis would provide a cost-effective signal amplification approach for this type of open path system (Harvie et al., 2021).

The field measurements in this thesis were carried out with the instrument located indoors. Further engineering work is required to ruggedise the instrument and adapt it for outdoor measurements. Such changes include replacing the benchtop power supplies with rechargeable battery packs and developing water-tight housing that is tamper-proof. A portable and rugged instrument would be valuable for mobile NO_2

measurements and could be mounted on the back of a bike or in a backpack to better measure exposure to NO_2 for different groups of people (pedestrians, cyclists, motorists) in an urban environment.

The cost analysis laid out in Chapter 4 estimated the cost of the CEAS instrument used in the field campaign to be approximately €3300, comparable to a build cost of €2000 for a NO_2 gas correlation camera developed by L. Kuhn et al. (2022). A low-cost DOAS instrument for simultaneous detection of NO_2 and aerosols by Bacaoco et al. (2020) was estimated to cost between €4900 - €6500. The cost of a lot of optical instruments is limited by the cost of spectrometers and high reflectivity cavity mirrors, as described by Womack et al. (2022) who estimated the cost of their low-cost CEAS instrument for detecting NO_2 to be around €19,000. The cost of the 1 m CEAS instrument developed in this thesis is therefore highly competitive with other low-cost instruments, with considerable scope to reduce the cost to ~€1500 or lower in a two-channel system, discussed in Chapter 4.

The work presented in this thesis shows the potential for selective two-channel instruments to measure urban NO_2 mixing ratios with high selectivity at a relatively low cost, and demonstrates that a single-channel CEAS instrument can make fast measurements of NO_2 in a traffic environment, even with reduced selectivity to the target species and a short optical pathlength. The development of simple, low-cost instruments for detecting NO_2 with relevant sensitivity and selectivity is an active field of research, with the aim of making pollutant monitoring more accessible to local communities that cannot afford expensive commercial monitoring systems. Air pollutants and their chemistry in the atmosphere must be understood and quantified in order for effective mitigation strategies to be implemented.

References

Ab-Rahman, M. S., Al-Hakim Azizan, L., Ramza, H., & Musa, Z. (2012). The Comparison of Experimental and Analytical Study of the Gaussian IntensityDistribution for Light Emitting Diodes Beam. *Journal of Computer Science*, *8*(6), 913–919. https://doi.org/10.3844/jcssp.2012.913.919

Ahmad, N., Lin, C., Lau, A. K. H., Kim, J., Yu, F., Li, C., Li, Y., Fung, J. C. H., & Lao, X. Q. (2024). Improving Ground-Level NO_2 Estimation in China Using GEMS Measurements and a Nested Machine Learning Model. *EGUsphere*. https://doi.org/10.5194/egusphere-2024-558

AIM-TTi Instruments. (2024). EX354RD Data Sheet. In *AIM-TTi Instruments*.

Alam, M. S., Crilley, L. R., Lee, J. D., Kramer, L. J., Pfrang, C., Vázquez-Moreno, M., Ródenas, M., Muñoz, A., & Bloss, W. J. (2020). Interference from alkenes in chemiluminescent NOx measurements. *Atmospheric Measurement Techniques*, *13*(11), 5977–5991. https://doi.org/10.5194/amt-13-5977-2020

Alemany, S., Vilor-Tejedor, N., García-Esteban, R., Bustamante, M., Dadvand, P., Esnaola, M., Mortamais, M., Forns, J., van Drooge, B. L., Álvarez-Pedrerol, M., Grimalt, J. O., Rivas, I., Querol, X., Pujol, J., & Sunyer, J. (2018). Traffic-Related Air Pollution, *APOE* ε4 Status, and Neurodevelopmental Outcomes among School Children Enrolled in the BREATHE Project (Catalonia, Spain). *Environmental Health Perspectives*, *126*(8). https://doi.org/10.1289/EHP2246

Alvarez-Pedrerol, M., Rivas, I., López-Vicente, M., Suades-González, E., Donaire-Gonzalez, D., Cirach, M., de Castro, M., Esnaola, M., Basagaña, X., Dadvand, P., Nieuwenhuijsen, M., & Sunyer, J. (2017). Impact of commuting exposure to traffic-related air pollution on cognitive development in children walking to school. *Environmental Pollution*, *231*, 837–844. https://doi.org/10.1016/j.envpol.2017.08.075

Aminuddin, J., Okude, S., Alimuddin, I., Tursilowati, L., Manago, N., & Kuze, H. (2019). Development of LED-DOAS system for observing aerosol optical properties in the lower troposphere. *Journal of Physics: Conference Series*, *1341*(8). https://doi.org/10.1088/1742-6596/1341/8/082006

An, F., Liu, J., Lu, W., & Jareemit, D. (2021). A review of the effect of traffic-related air pollution around schools on student health and its mitigation. *Journal of Transport & Health*, *23*, 101249. https://doi.org/10.1016/j.jth.2021.101249

Anderson, D. C., Lindsay, A., Decarlo, P. F., & Wood, E. C. (2021). Urban Emissions of Nitrogen Oxides, Carbon Monoxide, and Methane Determined from Ground-Based Measurements in Philadelphia. *Environmental Science and Technology*, *55*(8), 4532–4541. https://doi.org/10.1021/acs.est.1c00294

Ashu-Ayem, E. R., Nitschke, U., Monahan, C., Chen, J., Darby, S. B., Smith, P. D., O'Dowd, C. D., Stengel, D. B., & Venables, D. S. (2012). Coastal Iodine Emissions. 1. Release of I_2 by *Laminaria digitata* in Chamber Experiments. *Environmental Science & Technology*, *46*(19), 10413–10421. https://doi.org/10.1021/es204534v

Averbuch, G., Ronac-Giannone, M., Arrowsmith, S., & Anderson, J. F. (2022). Evidence for Short Temporal Atmospheric Variations Observed by Infrasonic Signals: 1. The Troposphere. *Earth and Space Science*, *9*(3). https://doi.org/10.1029/2021EA002036

Bacaoco, M. Y., Juguilon, V. P., Cafe, A. I., Tugado, C. A., Angela, M., Faustino, B., Bagtasa, G., & Estacio, E. S. (2020). Design of a Low-cost Differential Optical Absorption Spectroscopy Set-up for Simultaneous Monitoring of Atmospheric NO 2 Concentration and Aerosol Optical Thickness. *Science Diliman*, *32*(2).

Badyda, A., & Rogulski, M. (2024). Closing Access Streets to Schools for Vehicular Traffic—Does It Affect the Air Quality? *Sustainability*, *16*(8), 3380. https://doi.org/10.3390/su16083380

Bailey, S. A., Hannun, R. A., Swanson, A. K., & Hanisco, T. F. (2024). A Portable Nitrogen Dioxide Instrument Using Cavity-Enhanced Absorption Spectroscopy. *Atmospheric Measurement Techniques*. https://doi.org/10.5194/amt-2024-61

Balch, J. K., Bradley, B. A., Abatzoglou, J. T., Nagy, R. C., Fusco, E. J., & Mahood, A. L. (2017). Human-started wildfires expand the fire niche across the United States. *Proceedings of the National Academy of Sciences*, *114*(11), 2946–2951. https://doi.org/10.1073/pnas.1617394114

Ball, S. M., & Jones, R. L. (2003). Broad-Band Cavity Ring-Down Spectroscopy. *Chemical Reviews*, *103*(12), 5239–5262. https://doi.org/10.1021/cr020523k

Barrett, S. R. H., Speth, R. L., Eastham, S. D., Dedoussi, I. C., Ashok, A., Malina, R., & Keith, D. W. (2015). Impact of the Volkswagen emissions control defeat device on US public health. *Environmental Research Letters*, *10*(11). https://doi.org/10.1088/1748-9326/10/11/114005

Bauer, S. (2021). Blue-Light Hazard of Light-Emitting Diodes Assessed with Gaussian Functions. *International Journal of Environmental Research and Public Health*, *18*(2), 680. https://doi.org/10.3390/ijerph18020680

Bechle, M. J., Millet, D. B., & Marshall, J. D. (2023). Ambient NO2 Air Pollution and Public Schools in the United States: Relationships with Urbanicity, Race−Ethnicity, and Income. *American Chemical Society*. https://doi.org/10.1021/acs.estlett.3c00507

Bell, M. L., Davis, D. L., & Fletcher, T. (2004). A retrospective assessment of mortality from the London smog episode of 1952: the role of influenza and pollution. *Environmental Health Perspectives*, *112*(1), 6–8. https://doi.org/10.1289/ehp.6539

Berkowicz, R., Hertel, O., Larsen, S. E., Sorensen, N. N., & Nielson, M. (1997). *Modelling traffic pollution in streets*. National Environmental Research Institute.

Bharadwaj, P., Zivin, J. G., Mullins, J. T., & Neidell, M. (2016). Early-Life Exposure to the Great Smog of 1952 and the Development of Asthma. *American Journal of Respiratory and Critical Care Medicine*, *194*(12), 1475–1482. https://doi.org/10.1164/rccm.201603-0451OC

Birks, J. W., Andersen, P. C., Williford, C. J., Turnipseed, A. A., Strunk, S. E., Ennis, C. A., & Mattson, E. (2018). Folded tubular photometer for atmospheric measurements of NO 2 and NO. *Atmos. Meas. Tech*, *11*, 2821–2835. https://doi.org/10.5194/amt-11-2821-2018

Bishop, G. A., Haugen, M. J., Mcdonald, B. C., & Boies, A. M. (2022). Utah Wintertime Measurements of Heavy-Duty Vehicle Nitrogen Oxide Emission Factors. *Environmental Science and Technology*, *56*(3), 1885–1893. https://doi.org/10.1021/acs.est.1c06428

Blocken, B., Moonen, P., Stathopoulos, T., & Carmeliet, J. (2008). Numerical Study on the Existence of the Venturi Effect in Passages between Perpendicular Buildings. *Journal of Engineering Mechanics*, *134*(12), 1021–1028. https://doi.org/10.1061/(ASCE)0733-9399(2008)134:12(1021)

Bonilla-Manrique, O. E., Posada-Roman, J. E., Garcia-Souto, J. A., & Ruiz-Llata, M. (2019a). Sub-ppm-Level Ammonia Detection Using Photoacoustic Spectroscopy with an Optical Microphone Based on a Phase Interferometer. *Sensors*, *19*(13), 2890. https://doi.org/10.3390/s19132890

Bonilla-Manrique, O. E., Posada-Roman, J. E., Garcia-Souto, J. A., & Ruiz-Llata, M. (2019b). Sub-ppm-Level Ammonia Detection Using Photoacoustic Spectroscopy with an Optical Microphone Based on a Phase Interferometer. *Sensors*, *19*(13), 2890. https://doi.org/10.3390/s19132890

Boogaard, H., Patton, A. P., Atkinson, R. W., Brook, J. R., Chang, H. H., Crouse, D. L., Fussell, J. C., Hoek, G., Hoffmann, B., Kappeler, R., Kutlar Joss, M., Ondras, M., Sagiv, S. K., Samoli, E., Shaikh, R., Smargiassi, A., Szpiro, A. A., Van Vliet, E. D. S., Vienneau, D., … Forastiere, F. (2022). Long-term exposure to traffic-related air pollution and selected health outcomes: A systematic review and meta-analysis. *Environment International*, *164*, 107262. https://doi.org/10.1016/j.envint.2022.107262

Bratrakov, P. A. (2016). Nitrogen oxide formation studying at natural gas combustion in non-circular profile furnaces of fire-tube boilers. *International Conference on Oil and Gas Engineering, OGE-2016*, 144–150. https://doi.org/10.1016/j.proeng.2016.07.646

Brown, L., Hayes, E., & Barnes, J. (2024). Mitigating child exposure to traffic-related air pollution on the school commute: Views of parents and teachers in England. *Transportation Research Part D: Transport and Environment*, *136*, 104454. https://doi.org/10.1016/j.trd.2024.104454

Brunner, D., Henne S., Keller, C. A., Reimann, S., Vollmer, M. K., O'Doherty, S., & Maione, M. (2011). An extended Kalman-filter for regional scale inverse emission estimation. *Atmos. Chem. Phys.*, *12*, 29195–29249.

Burkholder, J. B., Sander, S. P., Abbatt, J., Barker, J., Huie, R., Kolb, C. E., Kurylo, M., Orkin, V., Wilmouth, D. M., & Wine, P. (2015). *Chemical Kinetics and Photochemical Data for Use in Atmospheric Studies, Evaluation Number 18*. https://doi.org/10.13140/RG.2.1.2504.2806

Byrne, R., Ryan, K., Venables, D. S., Wenger, J. C., & Hellebust, S. (2023). Highly local sources and large spatial variations in $PM_{2.5}$ across a city: evidence from a city-wide sensor network in Cork, Ireland. *Environmental Science: Atmospheres*, *3*(5), 919–930. https://doi.org/10.1039/D2EA00177B

Byrne, R., Wenger, J. C., & Hellebust, S. (2024). Spatial analysis of $PM_{2.5}$ using a concentration similarity index applied to air quality sensor networks. *Atmospheric Measurement Techniques*, *17*(17), 5129–5146. https://doi.org/10.5194/amt-17-5129-2024

Carey, I. M., Atkinson, R. W., Kent, A. J., van Staa, T., Cook, D. G., & Anderson, H. R. (2013). Mortality Associations with Long-Term Exposure to Outdoor Air Pollution in a National English Cohort. *American Journal of Respiratory and Critical Care Medicine*, *187*(11), 1226–1233. https://doi.org/10.1164/rccm.201210-1758OC

Carslaw, D., & Beevers, S. (2005). Estimations of road vehicle primary NO exhaust emission fractions using monitoring data in London. *Atmospheric Environment*, *39*(1), 167–177. https://doi.org/10.1016/j.atmosenv.2004.08.053

Carslaw, D. C., & Beevers, S. D. (2013). Characterising and understanding emission sources using bivariate polar plots and k-means clustering. *Environmental Modelling & Software*, *40*, 325–329. https://doi.org/10.1016/j.envsoft.2012.09.005

Carslaw, D. C., & Davison, J. (2024). *The openair book: A Guide to the Analysis of Air Pollution Data*.

Castellanos, P., Luke, W. T., Kelley, P., Stehr, J. W., Ehrman, S. H., & Dickerson, R. R. (2009). Modification of a commercial cavity ring-down spectroscopy NO2 detector for enhanced sensitivity. *Review of Scientific Instruments*, *80*(11). https://doi.org/10.1063/1.3244090

Cedeño Laurent, J. G., Parhizkar, H., Calderon, L., Lizonova, D., Tsiodra, I., Mihalopoulos, N., Kavouras, I., Alam, M., Baalousha, M., Bazina, L., Kelesidis, G. A., & Demokritou, P. (2024). Physicochemical Characterization of the Particulate Matter in New Jersey/New York City Area, Resulting from the Canadian Quebec Wildfires in June 2023. *Environmental Science & Technology*. https://doi.org/10.1021/ACS.EST.4C02016

Chen, J., Wang, D. N., Ramachandran, A., Chandran, S., Li, M., & Varma, R. (2020). An open-path dual-beam laser spectrometer for path-integrated urban NO2 sensing. *Sensors and Actuators, A: Physical*, *315*. https://doi.org/10.1016/j.sna.2020.112208

Chen, T., Wang, C., Liang, J., & Li, J. (2021). Application of Derivative Transform Spectroscopy in Gas Detection. *E3S Web of Conferences*, *299*, 02005. https://doi.org/10.1051/e3sconf/202129902005

Chen, X., Ma, W., Zheng, F., Wang, Z., Hua, C., Li, Y., Wu, J., Li, B., Jiang, J., Yan, C., Petäjä, T., Bianchi, F., Kerminen, V.-M., Worsnop, D. R., Liu, Y., Xia, M., & Kulmala, M. (2024). Identifying Driving Factors of Atmospheric N_2O_5 with Machine Learning. *Environmental Science & Technology*. https://doi.org/10.1021/acs.est.4c00651

Cheng, H., Narzo, A. Di, Howell, D., Yevdokimova, K., Zhang, J., Zhang, X., Pan, Q., Zhang, Z., Rogers, L., & Hao, K. (2022). Ambient Air Pollutants and Traffic Factors Were Associated with Blood and Urine Biomarkers and Asthma Risk. *Environmental Science and Technology*, *56*(11), 7298–7307. https://doi.org/10.1021/acs.est.1c06916

Chew, L. W., & Norford, L. K. (2018). Pedestrian-level wind speed enhancement in urban street canyons with void decks. *Building and Environment*, *146*, 64–76. https://doi.org/10.1016/j.buildenv.2018.09.039

Christakis, I., Tsakiridis, O., Kandris, D., & Stavrakas, I. (2023). A Kalman Filter Scheme for the Optimization of Low-Cost Gas Sensor Measurements. *Electronics*, *13*(1), 25. https://doi.org/10.3390/electronics13010025

Clark, C., Crombie, R., Head, J., van Kamp, I., van Kempen, E., & Stansfeld, S. A. (2012). Does Traffic-related Air Pollution Explain Associations of Aircraft and Road Traffic Noise Exposure on Children's Health and Cognition? A Secondary Analysis of the

United Kingdom Sample From the RANCH Project. *American Journal of Epidemiology*, *176*(4), 327–337. https://doi.org/10.1093/aje/kws012

Coheur, P.-F., Fally, S., Carleer, M., Clerbaux, C., Colin, R., Jenouvrier, A., Mérienne, M.-F., Hermans, C., & Vandaele, A. C. (2002). New water vapor line parameters in the 26000–region. *Journal of Quantitative Spectroscopy and Radiative Transfer*, *74*(4), 493–510. https://doi.org/10.1016/S0022-4073(01)00269-2

Coquart, B., Jenouvrier, A., & Merienne, M. E. (1995). The NO2 Absorption Spectrum. II. Absorption Cross-Sections at Low Temperatures in the 400-500 nm Region. In *Journal of Atmospheric Chemistry* (Vol. 21). Kluwer Academic Publishers.

Crooijmans, K. L. H. A., Iñiguez, C., Withworth, K. W., Estarlich, M., Lertxundi, A., Fernández-Somoano, A., Tardón, A., Ibarluzea, J., Sunyer, J., Guxens, M., & Binter, A.-C. (2024). Nitrogen dioxide exposure, attentional function, and working memory in children from 4 to 8 years: Periods of susceptibility from pregnancy to childhood. *Environment International*, *186*, 108604. https://doi.org/10.1016/j.envint.2024.108604

Crosignani, P., Nanni, A., Pepe, N., Pozzi, C., Silibello, C., Poggio, A., & Conte, M. (2021). The Effect of Non-Compliance of Diesel Vehicle Emissions with Euro Limits on Mortality in the City of Milan. *Atmosphere*, *12*(3), 342. https://doi.org/10.3390/atmos12030342

Dakin, J. P., Edwards, H. O., & Weigl, B. H. (1995). Progress with optical gas sensors using correlation spectroscopy. *Sensors and Actuators B: Chemical*, *29*(1–3), 87–93. https://doi.org/10.1016/0925-4005(95)01667-8

Dallo, F., Zannoni, D., Gabrieli, J., Cristofanelli, P., Calzolari, F., De Blasi, F., Spolaor, A., Battistel, D., Lodi, R., Cairns, W. R. L., Fjæraa, A. M., Bonasoni, P., & Barbante, C. (2021). Calibration and assessment of electrochemical low-cost sensors in remote alpine harsh environments. *Atmospheric Measurement Techniques*, *14*(9), 6005–6021. https://doi.org/10.5194/amt-14-6005-2021

Dari-Salisburgo, C., Di Carlo, P., Giammaria, F., Kajii, Y., & D'Altorio, A. (2009). Laser induced fluorescence instrument for NO2 measurements: Observations at a central Italy background site. *Atmospheric Environment*, *43*(4), 970–977. https://doi.org/10.1016/j.atmosenv.2008.10.037

Das, D., & Wilson, A. C. (2011). Very long optical path-length from a compact multi-pass cell. *Applied Physics B*, *103*(3), 749–754. https://doi.org/10.1007/s00340-010-4337-7

Dasgupta, P. K., Bhawal, R. P., Li, Y.-H., & Ibraguimov, A. (2014). Cavity-Enhanced Absorption Measurements Across Broad Absorbance and Reflectivity Ranges. *Analytical Chemistry*, *86*(8), 3727–3734. https://doi.org/10.1021/ac404251w

Dasgupta, P. K., Eom, I.-Y., Morris, K. J., & Li, J. (2003). Light emitting diode-based detectors. *Analytica Chimica Acta*, *500*(1–2), 337–364. https://doi.org/10.1016/S0003-2670(03)00575-0

Davies, J. H. (1970). Correlation spectroscopy. *Analytical Chemistry*, *42*(6), 101A – 112a. https://doi.org/10.1021/ac60288a020

de Jonge, R. W., Xavier, C., Olenius, T., Elm, J., Svenhag, C., Hyttinen, N., Nieradzik, L., Sarnela, N., Kristensson, A., Petäjä, T., Ehn, M., & Roldin, P. (2024). Natural Marine Precursors Boost Continental New Particle Formation and Production of Cloud

Condensation Nuclei. *Environmental Science & Technology*. https://doi.org/10.1021/acs.est.4c01891

De Marcellis, A., Ferri, G., D'Amico, A., Di Natale, C., & Martinelli, E. (2012). A fully-analog lock-in amplifier with automatic phase alignment for accurate measurements of ppb gas concentrations. *IEEE Sensors Journal*, *12*(5), 1377–1383. https://doi.org/10.1109/JSEN.2011.2172602

De Marcellis, A., Palange, E., Liberatore, N., & Mengali, S. (2017). Low-Cost Portable 1 MHz Lock-In Amplifier for Fast Measurements of Pulsed Signals in Sensing Applications. *IEEE Sensors Letters*, *1*(4), 1–4. https://doi.org/10.1109/LSENS.2017.2713449

Denzer, W., Hamilton, M. L., Hancock, G., Islam, M., Langley, C. E., Peverall, R., & Ritchie, G. A. D. (2009). Near-infrared broad-band cavity enhanced absorption spectroscopy using a superluminescent light emitting diode. *The Analyst*, *134*(11), 2220. https://doi.org/10.1039/b916807a

Department for Environment Food & Rural Affairs, N. (2022). *Local Air Quality Management: Technical Guidance (TG22)*.

Diez, S., Lacy, S., Coe, H., Urquiza, J., Priestman, M., Flynn, M., Marsden, N., Martin, N. A., Gillott, S., Bannan, T., Edwards, P. M., & Diez sebastiandiez, S. (2024). Long-term evaluation of commercial air quality sensors: an overview from the QUANT (Quantification of Utility of Atmospheric Network Technologies) study. *Atmos. Meas. Tech*, *17*, 3809–3827. https://doi.org/10.5194/amt-17-3809-2024

Dong, M., Zheng, C., Miao, S., Zhang, Y., Du, Q., Wang, Y., & Tittel, F. (2017). Development and Measurements of a Mid-Infrared Multi-Gas Sensor System for CO, CO2 and CH4 Detection. *Sensors*, *17*(10), 2221. https://doi.org/10.3390/s17102221

Dong, Z., Jiang, Y., Wang, S., Xing, J., Ding, D., Zheng, H., Wang, H., Huang, C., Yin, D., Song, Q., Zhao, B., & Hao, J. (2024). Spatially and Temporally Differentiated NO_x and VOCs Emission Abatement Could Effectively Gain O_3 -Related Health Benefits. *Environmental Science & Technology*. https://doi.org/10.1021/acs.est.4c01345

Dorrington, A. A., & Künnemeyer, R. (2002). A simple microcontroller based digital lock-in amplifier for the detection of low level optical signals. *Proceedings First IEEE International Workshop on Electronic Design, Test and Applications '2002*, 486–488. https://doi.org/10.1109/DELTA.2002.994680.

Dressel, I. M., Demetillo, M. A. G., Judd, L. M., Janz, S. J., Fields, K. P., Sun, K., Fiore, A. M., McDonald, B. C., & Pusede, S. E. (2022). Daily Satellite Observations of Nitrogen Dioxide Air Pollution Inequality in New York City, New York and Newark, New Jersey: Evaluation and Application. *Environmental Science and Technology*, *56*(22), 15298–15311. https://doi.org/10.1021/acs.est.2c02828

Edwards, D. P., Martínez-Alonso, S., Jo, D. S., Ortega, I., Emmons, L. K., Orlando, J. J., Worden, H. M., Kim, J., Lee, H., Park, J., & Hong, H. (2024). Quantifying the diurnal variation in atmospheric NO_2 from Geostationary Environment Monitoring Spectrometer (GEMS) observations. *Atmospheric Chemistry and Physics*, *24*(15), 8943–8961. https://doi.org/10.5194/acp-24-8943-2024

Engel, G. S., Moyer, E. J., Keutsch, F. N., & Anderson, J. G. (2001). Innovations in Cavity Enhanced Laser Absorption Spectroscopy: Using in situ Measurements to Probe the

Mechanisms Driving Climate Change. *NASA Earth Science Technology Conference (ESTC 2003) Proceedings*.

Environmental Protection Agency. (2021). *Air Quality in Ireland 2020*. www.epa.ie

Environmental Protection Agency. (2023a). *Air Quality in Ireland: Report 2022*.

Environmental Protection Agency. (2023b). Hundred of Cork City citizen scientists measure air pollution from traffic. Clean Air Together Cork City - The Results! In *EPA News Releases*. Environmental Protection Agency.

Environmental Protection Agency. (2023c, February). *Hundreds of Cork City citizen scientists measure air pollution from traffic. Clean Air Together Cork City – The Results!* EPA News Releases. https://www.epa.ie/news-releases/news-releases-2023/hundreds-of-cork-city-citizen-scientists-measure-air-pollution-from-traffic-clean-air-together-cork-city--the-results.php#:~:text=The%20Clean%20Air%20Together%20Citizen,linked%20with%20higher%20traffic%20volumes.

Ephrath, J. E., Goudriaan, J., & Marani, A. (1996). Modelling Diurnal Patterns of Air Temperature, Radiation Wind Speed and Relative Humidity by Equations from Daily Characteristics . *Agricultural Systems*, *51*, 377–393.

Ermel, M., Behrendt, T., Oswald, R., Derstroff, B., Wu, D., Hohlmann, S., Stönner, C., Pommerening-Röser, A., Könneke, M., Williams, J., Meixner, F. X., Andreae, M. O., Trebs, I., & Sörgel, M. (2018). Hydroxylamine released by nitrifying microorganisms is a precursor for HONO emission from drying soils. *Scientific Reports*, *8*(1), 1877. https://doi.org/10.1038/s41598-018-20170-1

Eugene Hecht. (2002). *Optics* (A. Black, Ed.; 4th ed.). Pearson Education, Inc.

European Commission. (2017). *Commission warns Germany, France, Spain, Italy and the United Kingdom of continued air pollution breaches*.

European Commission, D.-G. for E. (2021). *COMMUNICATION FROM THE COMMISSION TO THE EUROPEAN PARLIAMENT, THE COUNCIL, THE EUROPEAN ECONOMIC AND SOCIAL COMMITTEE AND THE COMMITTEE OF THE REGIONS Pathway to a Healthy Planet for All EU Action Plan: "Towards Zero Pollution for Air, Water and Soil."*

European Environment Agency. (2023). *European Union emission inventory report 1990-2021*. https://doi.org/10.2800/68478

Evertsen, R., Staicu, A., Dam, N., van Vliet, A., & ter Meulen, J. J. (2002). Pulsed cavity ring-down spectroscopy of NO and NO 2 in the exhaust of a diesel engine. *Applied Physics B: Lasers and Optics*, *74*(4–5), 465–468. https://doi.org/10.1007/s003400200828

Fang, B., Zhao, W., Xu, X., Zhou, J., Ma, X., Wang, S., Zhang, W., Venables, D. S., & Chen, W. (2017). Portable broadband cavity-enhanced spectrometer utilizing Kalman filtering: application to real-time, in situ monitoring of glyoxal and nitrogen dioxide. *Optics Express*, *25*(22), 26910. https://doi.org/10.1364/OE.25.026910

Fiedler, S. E., Hese, A., & Heitmann, U. (2007). Influence of the cavity parameters on the output intensity in incoherent broadband cavity-enhanced absorption spectroscopy. *Review of Scientific Instruments*, *78*(7). https://doi.org/10.1063/1.2752608

Fiedler, S. E., Hese, A., & Ruth, A. A. (2003). Incoherent broad-band cavity-enhanced absorption spectroscopy. *Chemical Physics Letters*, *371*(3–4), 284–294. https://doi.org/10.1016/S0009-2614(03)00263-X

Flowerday, C. E., Thalman, R., Asplund, M. C., & Hansen, J. C. (2023). Broadband Cavity-Enhanced Absorption Spectroscopy (BBCEAS) Coupled with an Interferometer for On-Band and Off-Band Detection of Glyoxal. *Toxics*, *12*(1), 26. https://doi.org/10.3390/toxics12010026

Fong, C., & Brune, W. H. (1997). A laser induced fluorescence instrument for measuring tropospheric NO2. *Review of Scientific Instruments*, *68*(11), 4253–4262. https://doi.org/10.1063/1.1148384

Fonseca, H., Lima, R., & Rativa, D. (2022). A Software-Based Lock-in Amplifier for Optical Spectroscopy Applications. *SBFoton International Optics and Photonics Conference (SBFoton IOPC)*, 1–4. https://doi.org/10.1109/SBFotonIOPC54450.2022.9992701

Fu, L., You, S., Li, G., & Fan, Z. (2023). Enhancing methane sensing with NDIR technology: Current trends and future prospects. *Reviews in Analytical Chemistry*, *42*(1). https://doi.org/10.1515/revac-2023-0062

Fu, M., Ge, Y., Wang, X., Tan, J., Yu, L., & Liang, B. (2013). NOx emissions from Euro IV busses with SCR systems associated with urban, suburban and freeway driving patterns. *Science of The Total Environment*, *452–453*, 222–226. https://doi.org/10.1016/j.scitotenv.2013.02.076

Fuchs, H., Dubé, W. P., Ciciora, S. J., & Brown, S. S. (2008). Determination of inlet transmission and conversion efficiencies for in situ measurements of the nocturnal nitrogen oxides, NO3, N 2O5 and NO2, via pulsed cavity ring-down spectroscopy. *Analytical Chemistry*, *80*(15), 6010–6017. https://doi.org/10.1021/AC8007253

Fujii, T., Fukuchi, T., Goto, N., Nemoto, K., & Takeuchi, N. (2001). Dual differential absorption lidar for the measurement of atmospheric SO_2 of the order of parts in 10^9. *Applied Optics*, *40*(6), 949. https://doi.org/10.1364/AO.40.000949

Gao, J., Chen, H., Liu, Y., Li, Y., Li, T., Tu, R., Liang, B., & Ma, C. (2021). The effect of after-treatment techniques on the correlations between driving behaviours and NO emissions of passenger cars. *Journal of Cleaner Production*, *288*, 125647. https://doi.org/10.1016/j.jclepro.2020.125647

García-Alonso, S., Pérez-Pastor, R., & Sevillano-Castaño, M. L. (2006). Determination of glyoxal and methylglyoxal in atmospheric particulate matter by 2,4-dinitrophenylhydrazine derivatisation. *Toxicological & Environmental Chemistry*, *88*(3), 445–452. https://doi.org/10.1080/02772240600796837

George, L. A., & O'Brien, R. J. (1991). Prototype FAGE determination of NO2. *Journal of Atmospheric Chemistry*, *12*(3), 195–209. https://doi.org/10.1007/BF00048073

Gidhagen, L., Johansson, C., Langner, J., & Olivares, G. (2004). Simulation of NOx and ultrafine particles in a street canyon in Stockholm, Sweden. *Atmospheric Environment*, *38*(14), 2029–2044. https://doi.org/10.1016/j.atmosenv.2004.02.014

Giordano, M. R., Malings, C., Pandis, S. N., Presto, A. A., McNeill, V. F., Westervelt, D. M., Beekmann, M., & Subramanian, R. (2021). From low-cost sensors to high-quality data: A summary of challenges and best practices for effectively calibrating low-cost

particulate matter mass sensors. *Journal of Aerosol Science*, *158*. https://doi.org/10.1016/j.jaerosci.2021.105833

Goin, D. E., Sudat, S., Riddell, C., Morello-Frosch, R., Apte, J. S., Glymour, M. M., Karasek, D., & Casey, J. A. (2021). Hyperlocalized Measures of Air Pollution and Preeclampsia in Oakland, California. *Environmental Science and Technology*, *55*(21), 14710–14719. https://doi.org/10.1021/acs.est.1c02151

Gong, Z., Gao, T., Chen, Y., Zhang, B., Peng, W., Yu, Q., Ma, F., Mei, L., & Chen, K. (2020). Sub-ppb level detection of nitrogen dioxide based on an optimized H-type longitudinal acoustic resonator and a lock-in white-light interferometry demodulation algorithm. *Journal of Quantitative Spectroscopy and Radiative Transfer*, *253*, 107136. https://doi.org/10.1016/j.jqsrt.2020.107136

Grainger, J. F., & Ring, J. (1962). Anomalous Fraunhofer Line Profiles. *Nature*, *193*(4817), 762–762. https://doi.org/10.1038/193762a0

Greater London Authority. (2024). *London-wide ULEZ Six Month Report*. www.london.gov.uk

Griffin, D., Mclinden, C. A., Dammers, E., Adams, C., Stockwell, C. E., Warneke, C., Bourgeois, I., Peischl, J., Ryerson, T. B., Zarzana, K. J., Rowe, J. P., Volkamer, R., Knote, C., Kille, N., Koenig, T. K., Lee, C. F., Rollins, D., Rickly, P. S., Chen, J., … Makar, P. (2021). Biomass burning nitrogen dioxide emissions derived from space with TROPOMI: methodology and validation. *Atmos. Meas. Tech*, *14*, 7929–7957. https://doi.org/10.5194/amt-14-7929-2021

Ha, E. S., Park, R. J., Kwon, H.-A., Lee, G. T., Lee, S. D., Shin, S., Lee, D.-W., Hong, H., Lerot, C., De Smedt, I., Hendrick, F., & Irie, H. (2024). *First evaluation of the GEMS glyoxal products against TROPOMI and ground-based measurements*. https://doi.org/10.5194/egusphere-2024-589

Haller, K. L., & Hobbs, P. C. D. (1991). Double beam laser absorption spectroscopy. *Photonics West - Lasers and Applications in Science and Engineering*. https://doi.org/10.1117/12.44253

Hartl, A., Kuhlmann, G., Wenig, M., Chan, K.-L., Ling, L.-Y., Zheng, N.-N., Qin, M., Sun, Y.-W., Xie, P.-H., & Liu, W.-Q. (2012). Comparing different light-emitting diodes as light sources for long path differential optical absorption spectroscopy NO_2 and SO_2 measurements. *Chinese Physics B*, *21*(11), 119301. https://doi.org/10.1088/1674-1056/21/11/119301

Harvie, A. J. (2021). *OpenLockIn/OLIA*. GitHub. https://github.com/OpenLockIn/OLIA

Harvie, A. J., & De Mello, J. C. (2022). OLIA: an open-source digital lock-in amplifier. *Frontiers in Sensors 4* . https://doi.org/https://doi.org/10.48550/arXiv.2211.08889

Harvie, A. J., & de Mello, J. C. (2023). OLIA: An open-source digital lock-in amplifier. *Frontiers in Sensors*, *4*. https://doi.org/10.3389/fsens.2023.1102176

Harvie, A. J., Yadav, S. K., & de Mello, J. C. (2021). A sensitive and compact optical detector based on digital lock-in amplification. *HardwareX*, *10*, e00228. https://doi.org/10.1016/j.ohx.2021.e00228

Hobbs, P. C. D. (1997). Ultrasensitive laser measurements without tears. *Applied Optics*, *36*.

Holman, C., Harrison, R., & Querol, X. (2015). Review of the efficacy of low emission zones to improve urban air quality in European cities. In *Atmospheric Environment* (Vol. 111, pp. 161–169). Elsevier Ltd. https://doi.org/10.1016/j.atmosenv.2015.04.009

Hopke, P. K., & Querol, X. (2022). Is Improved Vehicular NOx Control Leading to Increased Urban NH3Emissions? In *Environmental Science and Technology* (Vol. 56, Issue 17, pp. 11926–11927). American Chemical Society. https://doi.org/10.1021/acs.est.2c04996

Horowitz, A., Meller, R., & Moortgat, G. K. (2001). The UV–VIS absorption cross sections of the α-dicarbonyl compounds: pyruvic acid, biacetyl and glyoxal. *Journal of Photochemistry and Photobiology A: Chemistry*, *146*(1–2), 19–27. https://doi.org/10.1016/S1010-6030(01)00601-3

Hoydysh, W. (1994). Concentration fields at urban intersections: fluid modeling studies. *Atmospheric Environment*, *28*(11), 1849–1860. https://doi.org/10.1016/1352-2310(94)90324-7

Huang, L., Han, B., Cheng, P., Tian, Z., Yang, W., Ling, J., Ma, W., Yu, Y., Gong, Y., Tian, Y., & Deng, H. (2024). Nitrous Acid and Nitric Oxide Emissions from Agricultural Soils in Guangdong Province: Laboratory Measurement and Emission Estimation. *ACS Earth and Space Chemistry*. https://doi.org/10.1021/acsearthspacechem.4c00048

Huang, X., Ge, Y., Yang, T., Song, Z., Yu, S., Li, Q., Wang, X., Wang, Y., Wang, X., Su, J., Xue, L., Mellouki, A., & Chen, J. (2024). Relaxation of Spring Festival Firework Regulations Leads to a Deterioration in Air Quality. *Environmental Science & Technology*. https://doi.org/10.1021/acs.est.4c00920

Huang, Z., Xu, X., Ma, M., & Shen, J. (2022). Assessment of NO2 population exposure from 2005 to 2020 in China. *Environmental Science and Pollution Research*, *29*(53), 80257–80271. https://doi.org/10.1007/s11356-022-21420-6

Huangfu, P., & Atkinson, R. (2020). Long-term exposure to NO 2 and O 3 and all-cause and respiratory mortality: A systematic review and meta-analysis. *Environment International*, *144*. https://doi.org/10.1016/j.envint.2020.105998

Huber, D. E., Steiner, A. L., & Kort, E. A. (2020). Daily Cropland Soil NOx Emissions Identified by TROPOMI and SMAP. *Geophysical Research Letters*, *47*(22). https://doi.org/10.1029/2020GL089949

Hunter Kerr, G., Goldberg, D. L., & Anenberg, S. C. (2021). COVID-19 pandemic reveals persistent disparities in nitrogen dioxide pollution. *PNAS*, *118*(30). https://doi.org/10.1073/pnas.2022409118/-/DCSupplemental.y

Hunter, L. J., Johnson, G. T., & Watson, I. D. (1992). An investigation of three-dimensional characteristics of flow regimes within the urban canyon. *Atmospheric Environment. Part B. Urban Atmosphere*, *26*(4), 425–432. https://doi.org/10.1016/0957-1272(92)90049-X

Jacquinot, P. (1954). The Luminosity of Spectrometers with Prisms, Gratings, or Fabry-Perot Etalons. *Journal of the Optical Society of America*, *44*(10), 761. https://doi.org/10.1364/JOSA.44.000761

Jacquinot, P. (1960). New developments in interference spectroscopy. *Reports on Progress in Physics*, *23*(1), 305. https://doi.org/10.1088/0034-4885/23/1/305

Jain, S., Presto, A. A., & Zimmerman, N. (2021). Spatial Modeling of Daily PM2.5, NO2, and CO Concentrations Measured by a Low-Cost Sensor Network: Comparison of Linear, Machine Learning, and Hybrid Land Use Models. *Environmental Science and Technology*, *55*(13), 8631–8641. https://doi.org/10.1021/acs.est.1c02653

Jeguirim, M., Belhachemi, M., Limousy, L., & Bennici, S. (2018). Adsorption/reduction of nitrogen dioxide on activated carbons: Textural properties versus surface chemistry – A review. *Chemical Engineering Journal*, *347*, 493–504. https://doi.org/10.1016/j.cej.2018.04.063

Ji, J., Huang, Y., Pi, M., Zhao, H., Peng, Z., Li, C., Wang, Q., Zhang, Y., Wang, Y., & Zheng, C. (2022). Performance improvement of on-chip mid-infrared waveguide methane sensor using wavelet denoising and Savitzky-Golay filtering. *Infrared Physics & Technology*, *127*, 104469. https://doi.org/10.1016/j.infrared.2022.104469

Jiang, X., Han, Y., Qiu, X., Wang, Y., Liu, J., Cheng, Z., Tian, Y., Xu, Y., Chen, X., Fan, Y., Chen, W., Li, W., & Zhu, T. (2024). Ozone Enhances the Inflammation Effects of PM $_{2.5}$ Components Based on an Exposomic Approach in a Panel Study. *Environmental Science & Technology Letters*. https://doi.org/10.1021/acs.estlett.4c00537

Jin, H., Jin, S., Yuan, K., & Cen, S. (2013). Two-Part Gauss Simulation of Phosphor-Coated LED. *IEEE Photonics Journal*, *5*(4), 1600110–1600110. https://doi.org/10.1109/JPHOT.2013.2272783

Jin, X., Fiore, A. M., & Cohen, R. C. (2023). Space-Based Observations of Ozone Precursors within California Wildfire Plumes and the Impacts on Ozone-NO $_{x}$ -VOC Chemistry. *Environmental Science & Technology*, *57*(39), 14648–14660. https://doi.org/10.1021/acs.est.3c04411

Johnson, K. A., & Johnson, D. E. (1995). Methane emissions from cattle. *Journal of Animal Science*, *73*(8), 2483–2492. https://doi.org/10.2527/1995.7382483x

Jung, Y., Pyo, Y. D., Jang, J., Kim, G. C., Cho, C. P., & Yang, C. (2019). NO, NO2 and N2O emissions over a SCR using DOC and DPF systems with Pt reduction. *Chemical Engineering Journal*, *369*, 1059–1067.

Kang, N., Wang, R., Lu, H., Onyai, F., Tang, M., Tong, M., Ni, X., Zhong, M., Deng, J., Dong, Y., Li, P., Zhu, T., & Xue, T. (2024). Burden of Child Anemia Attributable to Fine Particulate Matters Brought by Sand Dusts in Low- and Middle-Income Countries. *Environmental Science and Technology*, *58*, 12954–12965. https://doi.org/10.1021/ACS.EST.4C05305

Katsouyanni, K., Touloumi, G., Samoli, E., Gryparis, A., Le Tertre, A., Monopolis, Y., Rossi, G., Zmirou, D., Ballester, F., Boumghar, A., Anderson, H. R., Wojtyniak, B., Paldy, A., Braunstein, R., Pekkanen, J., Schindler, C., & Schwartz, J. (2001). Confounding and Effect Modification in the Short-Term Effects of Ambient Particles on Total Mortality: Results from 29 European Cities within the APHEA2 Project. *Epidemiology*. https://doi.org/10.1097/00001648-200109000-00011.

Kebabian, P. L., Annen, K. D., Berkoff, T. A., & Freedman, A. (2000). Nitrogen dioxide sensing using a novel gas correlation detector. *Measurement Science and Technology*, *11*(5), 499–503. https://doi.org/10.1088/0957-0233/11/5/308

Kebabian, P. L., Robinson, W. A., & Freedman, A. (2007). Optical extinction monitor using cw cavity enhanced detection. *Review of Scientific Instruments*, *78*(6). https://doi.org/10.1063/1.2744223

Kebabian, P. L., Wood, E. C., Herndon, S. C., & Freedman, A. (2008). A practical alternative to chemiluminescence-based detection of nitrogen dioxide: Cavity attenuated phase shift spectroscopy. *Environmental Science and Technology*, *42*(16), 6040–6045. https://doi.org/10.1021/es703204j

Kendrick, C. M., Koonce, P., & George, L. A. (2015). Diurnal and seasonal variations of NO, NO 2 and PM 2.5 mass as a function of traffic volumes alongside an urban arterial. *Atmospheric Environment*, *122*, 133–141. https://doi.org/10.1016/j.atmosenv.2015.09.019

Kern, C., Trick, S., Rippel, B., & Platt, U. (2006). Applicability of light-emitting diodes as light sources for active differential optical absorption spectroscopy measurements. *Applied Optics*, *45*(9).

Kerschhofer, A., Breitegger, P., & Bergmann, A. (2018). Laser Driver and Analysis Circuitry Development for Quartz-Enhanced Photoacoustic Spectroscopy of NO2 for IoT Purpose. *EUROSENSORS 2018*, 1062. https://doi.org/10.3390/proceedings2131062

Khan, S., Le Calvé, S., & Newport, D. (2020). A review of optical interferometry techniques for VOC detection. *Sensors and Actuators A: Physical*, *302*, 111782. https://doi.org/10.1016/j.sna.2019.111782

Khreis, H., Sanchez, K. A., Foster, M., Burns, J., Nieuwenhuijsen, M. J., Jaikumar, R., Ramani, T., & Zietsman, J. (2023). Urban policy interventions to reduce traffic-related emissions and air pollution: A systematic evidence map. *Environment International*, *172*, 107805. https://doi.org/10.1016/j.envint.2023.107805

Kiendler-Scharr, A., Becker, K.-H., Doussin, J.-F., Fuchs, H., Seakins, P., Wenger, J., & Wiesen, P. (2023). Introduction to Atmospheric Simulation Chambers and Their Applications. In *A Practical Guide to Atmospheric Simulation Chambers* (pp. 1–72). Springer International Publishing. https://doi.org/10.1007/978-3-031-22277-1_1

Kim, T., Kim, Y., Cho, W., Kwak, J.-H., Cho, J., Pyeon, Y., Kim, J. J., & Shin, H. (2024). Ultralow-Power Single-Sensor-Based E-Nose System Powered by Duty Cycling and Deep Learning for Real-Time Gas Identification. *ACS Sensors*. https://doi.org/10.1021/acssensors.4c00471

Kirby, C., Fox, M., & Waterhouse, J. (2000). Reliability of nitrogen dioxide passive diffusion tubes for ambient measurement: in situ properties of the triethanolamine absorbent. *Journal of Environmental Monitoring*, *2*(4), 307–312. https://doi.org/10.1039/b003124k

Kleffmann, J., Lörzer, J. C., Wiesen, P., Kern, C., Trick, S., Volkamer, R., Rodenas, M., & Wirtz, K. (2006). Intercomparison of the DOAS and LOPAP techniques for the detection of nitrous acid (HONO). *Atmospheric Environment*, *40*(20), 3640–3652. https://doi.org/10.1016/j.atmosenv.2006.03.027

Kleffmann, J., & Wiesen, P. (2008). Technical Note: Quantification of interferences of wet chemical HONO LOPAP measurements under simulated polar conditions. *Atmospheric Chemistry and Physics*, *8*(22), 6813–6822. https://doi.org/10.5194/acp-8-6813-2008

Köhring, M., Pohlkötter, A., Willer, U., Angelmahr, M., & Schade, W. (2011a). Tuning fork enhanced interferometric photoacoustic spectroscopy: a new method for trace gas analysis. *Applied Physics B*, *102*(1), 133–139. https://doi.org/10.1007/s00340-010-4222-4

Köhring, M., Pohlkötter, A., Willer, U., Angelmahr, M., & Schade, W. (2011b). Tuning fork enhanced interferometric photoacoustic spectroscopy: a new method for trace gas analysis. *Applied Physics B*, *102*(1), 133–139. https://doi.org/10.1007/s00340-010-4222-4

Kuhn, J., Bobrowski, N., Wagner, T., & Platt, U. (2021). Mobile and high-spectral-resolution Fabry-Pérot interferometer spectrographs for atmospheric remote sensing. *Atmospheric Measurement Techniques*, *14*(12), 7873–7892. https://doi.org/10.5194/amt-14-7873-2021

Kuhn, J., Platt, U., Bobrowski, N., & Wagner, T. (2019). Towards imaging of atmospheric trace gases using Fabry–Pérot interferometer correlation spectroscopy in the UV and visible spectral range. *Atmospheric Measurement Techniques*, *12*(1), 735–747. https://doi.org/10.5194/amt-12-735-2019

Kuhn, L., Kuhn, J., Wagner, T., & Platt, U. (2022). The NO2 camera based on gas correlation spectroscopy. *Atmospheric Measurement Techniques*, *15*(5), 1395–1414. https://doi.org/10.5194/amt-15-1395-2022

Lange, K., Richter, A., Bösch, T., Zilker, B., Latsch, M., Behrens, L. K., Okafor, C. M., Bösch, H., Burrows, J. P., Merlaud, A., Pinardi, G., Fayt, C., Friedrich, M. M., Dimitropoulou, E., Van Roozendael, M., Ziegler, S., Ripperger-Lukosiunaite, S., Kuhn, L., Lauster, B., … Lee, H. (2024). Validation of GEMS tropospheric NO2 columns and their diurnal variation with ground-based DOAS measurements. *Atmospheric Measurement Techniques*, *17*(21), 6315–6344. https://doi.org/10.5194/amt-17-6315-2024

Langridge, J. M., Ball, S. M., Shillings, A. J. L., & Jones, R. L. (2008). A broadband absorption spectrometer using light emitting diodes for ultrasensitive, in situ trace gas detection. *Review of Scientific Instruments*, *79*(12). https://doi.org/10.1063/1.3046282

Laughner, J. L., & Cohen, R. C. (2019). Direct observation of changing NOx lifetime in North American cities. *Science*, *366*(6466), 723–727. https://doi.org/10.1126/science.aax6832

Laurila, T., Cattaneo, H., Pöyhönen, T., Koskinen, V., Kauppinen, J., & Hernberg, R. (2006). Cantilever-based photoacoustic detection of carbon dioxide using a fiber-amplified diode laser. *Applied Physics B*, *83*(2), 285–288. https://doi.org/10.1007/s00340-005-2106-9

Lee, J., Kim, K. H., Kim, Y. J., & Lee, J. (2008). Application of a long-path differential optical absorption spectrometer (LP-DOAS) on the measurements of NO2, SO2, O3, and HNO2 in Gwangju, Korea. *Journal of Environmental Management*, *86*(4), 750–759. https://doi.org/10.1016/j.jenvman.2006.12.044

Leleux, D. P., Claps, R., Chen, W., Tittel, F. K., & Harman, T. L. (2002). Applications of Kalman filtering to real-time trace gas concentration measurements. *Applied Physics B: Lasers and Optics*, *74*(1), 85–93. https://doi.org/10.1007/s003400100751

Li, D., Gao, R., Qin, L., Yue, H., & Sang, N. (2022). New Insights into Prenatal NO2Exposure and Behavioral Abnormalities in Male Offspring: Disturbed Serotonin Metabolism and

Delayed Oligodendrocyte Development. *Environmental Science and Technology*, *56*(16), 11536–11546. https://doi.org/10.1021/acs.est.2c03037

Li, J., Chen, W., & Yu, B. (2011). Recent Progress on Infrared Photoacoustic Spectroscopy Techniques. *Applied Spectroscopy Reviews*, *46*(6), 440–471. https://doi.org/10.1080/05704928.2011.570835

Li, J., Wang, Y., Zhang, R., Smeltzer, C., Weinheimer, A., Herman, J., Boersma, K. F., Celarier, E. A., Long, R. W., Szykman, J. J., Delgado, R., Thompson, A. M., Knepp, T. N., Lamsal, L. N., Janz, S. J., Kowalewski, M. G., Liu, X., & Nowlan, C. R. (2021). Comprehensive evaluations of diurnal NO2 measurements during DISCOVER-AQ 2011: effects of resolution-dependent representation of NO2 emissions. *Atmospheric Chemistry and Physics*, *21*(14), 11133–11160. https://doi.org/10.5194/acp-21-11133-2021

Li, M., Chen, J., Su, M., Yang, H., Ramachandran, A., & Varma, R. (2017). An LP-DOAS Instrument with a Laser Driven Light Source for Open-path Measurement of Atmospheric NO 2 in Shanghai. *Progress in Electromagnetics Research Symposium*.

Li, Q., Gong, D., Wang, H., Wang, Y., Han, S., Wu, G., Deng, S., Yu, P., Wang, W., & Wang, B. (2022a). Rapid increase in atmospheric glyoxal and methylglyoxal concentrations in Lhasa, Tibetan Plateau: Potential sources and implications. *Science of The Total Environment*, *824*, 153782. https://doi.org/10.1016/j.scitotenv.2022.153782

Li, Q., Gong, D., Wang, H., Wang, Y., Han, S., Wu, G., Deng, S., Yu, P., Wang, W., & Wang, B. (2022b). Rapid increase in atmospheric glyoxal and methylglyoxal concentrations in Lhasa, Tibetan Plateau: Potential sources and implications. *Science of The Total Environment*, *824*, 153782. https://doi.org/10.1016/j.scitotenv.2022.153782

Li Su-Wen, Xie Pin-Hua, Liu Wen-Qing, Si Fu-Qi, Li Ang, & Peng Fu-Min. (2008). A study of applicability of light emitting diodes in differential optical absorption spectroscopy measurements. *Acta Physica Sinica*, *57*(3), 1963. https://doi.org/10.7498/aps.57.1963

Li, W. (2011). *Erratum: The Application of Savitzky-Golay Filter on Optical Measurement of Atmospheric Compositions* (pp. E1–E2). https://doi.org/10.1007/978-3-642-21765-4_134

Li, Z., Yan, H., Zhang, X., Shah, S., Yang, G., Chen, Q., Han, S., Zhang, D., Weinberger, D. R., Yue, W., & Tan, H. Y. (2021). Air pollution interacts with genetic risk to influence cortical networks implicated in depression. *Proceedings of the National Academy of Sciences*. https://doi.org/10.1073/pnas.2109310118/-/DCSupplemental

Limo, J., Kauhaniemi, M., Paturi, P., Keskinen, J.-P., Karppinen, A., & Mäkinen, J. (2024). Another one bites the dust – Two street canyons studied with magnetic biomonitoring and OSPM modelling. *Atmospheric Environment*, *319*, 120312. https://doi.org/10.1016/j.atmosenv.2023.120312

Liu, B., Bryson, J. R., Sevinc, D., Cole, M. A., Robert, ·, Elliott, J. R., Bartington, S. E., William, ·, Bloss, J., Shi, Z., & Elliott, R. J. R. (2023). Assessing the Impacts of Birmingham's Clean Air Zone on Air Quality: Estimates from a Machine Learning and Synthetic Control Approach. *Environmental and Resource Economics*, *86*, 203–231. https://doi.org/10.1007/s10640-023-00794-2

Liu, C., Chen, R., Lei, J., Zhu, Y., Zhou, L., Meng, X., Xuan, J., & Kan, H. (2023). Ambient Nitrogen Dioxide and Hospitalizations of Full-Spectrum Respiratory Diseases: A

National Case-Crossover Study. *Environment & Health*. https://doi.org/10.1021/envhealth.3c00039

Liu, F., Bao, H., Ho, H. L., Jin, W., Gao, S., & Wang, Y. (2021). Multicomponent trace gas detection with hollow-core fiber photothermal interferometry and time-division multiplexing. *Optics Express*, *29*(26). https://doi.org/10.1364/OE.446478

Liu, H., Deng, H., Li, Y., Zhao, Y., & Li, X. (2022). School Surrounding Region Traffic Commuting Analysis Based on Simulation. *International Journal of Environmental Research and Public Health*, *19*(11), 6566. https://doi.org/10.3390/ijerph19116566

Liu, K., Guo, X., Yi, H., Chen, W., Zhang, W., & Gao, X. (2009). Off-beam quartz-enhanced photoacoustic spectroscopy. *Optics Letters*, *34*(10), 1594. https://doi.org/10.1364/OL.34.001594

Liu, S., Li, X., Wei, J., Shu, L., Jin, J., Fu, T.-M., Yang, X., & Zhu, L. (2024). Short-Term Exposure to Fine Particulate Matter and Ozone: Source Impacts and Attributable Mortalities. *Environmental Science & Technology* . https://doi.org/10.1021/acs.est.4c00339

Liu, S., Luo, Z., Tan, Z., & Long, X. (2016). Gas trace detection with cavity enhanced absorption spectroscopy: a review of its process in the field. In C. Zhang, X.-C. Zhang, & M. Tani (Eds.), *Society of Photo-Optical Instrumentation Engineers (SPIE) Conference Series* (p. 100301C). https://doi.org/10.1117/12.2245984

Liu, X., Qiao, S., & Ma, Y. (2022). Highly sensitive methane detection based on light-induced thermoelastic spectroscopy with a 2.33 μm diode laser and adaptive Savitzky-Golay filtering. *Optics Express*, *30*(2), 1304. https://doi.org/10.1364/OE.446294

Liu, Y., Geng, G., Cheng, J., Liu, Y., Xiao, Q., Liu, L., Shi, Q., Tong, D., He, K., & Zhang, Q. (2023). Drivers of Increasing Ozone during the Two Phases of Clean Air Actions in China 2013−2020. *Cite This: Environ. Sci. Technol*, *57*, 8964. https://doi.org/10.1021/acs.est.3c00054

Liu, Y., Pan, J., Zhang, H., Shi, C., Li, G., Peng, Z., Ma, J., Zhou, Y., & Zhang, L. (2019). Short-Term Exposure to Ambient Air Pollution and Asthma Mortality. *American Journal of Respiratory and Critical Care Medicine*, *200*(1), 24–32. https://doi.org/10.1164/rccm.201810-1823OC

Liu, Z., Lin, B., Campbell, J. F., Yu, J., Geng, J., & Jiang, S. (2024). Martian column CO_2 and pressure measurement with spaceborne differential absorption lidar at 1.96 μm. *Atmospheric Measurement Techniques*, *17*(9), 2977–2990. https://doi.org/10.5194/amt-17-2977-2024

Liu, Z., Liu, C., & Mostafavi, A. (2023). Beyond Residence: A Mobility-based Approach for Improved Evaluation of Human Exposure to Environmental Hazards. *Environmental Science & Technology*. https://doi.org/10.1021/ACS.EST.3C04691

Lobell, D. B., Di Tommaso, S., & Burney, J. A. (2022). Globally ubiquitous negative effects of nitrogen dioxide on crop growth. *Science Advances*, *8*(22). https://doi.org/10.1126/sciadv.abm9909

Luo, H., Zhang, Q., Meng, X., Kan, H., & Chen, R. (2024). Air Pollution and Cardiac Arrest: A More Significant Intermediate Role of COPD than Cardiac Events. *Environmental Science & Technology*. https://doi.org/10.1021/ACS.EST.4C00083

Luo, P., Ying, J., Li, J., Yang, Z., Sun, X., Ye, D., Liu, C., Wang, J., & Mao, Y. (2023). Air Pollution and Allergic Rhinitis: Findings from a Prospective Cohort Study. *Environmental Science & Technology*. https://doi.org/10.1021/ACS.EST.3C04527

Lv, L., Liu, W., Zhang, T., Chen, Z., Dong, Y., Fan, G., Xiang, Y., Yao, Y., Yang, N., Chu, B., Teng, M., & Shu, X. (2017). Observations of particle extinction, PM2.5 mass concentration profile and flux in north China based on mobile lidar technique. *Atmospheric Environment*, *164*, 360–369. https://doi.org/10.1016/j.atmosenv.2017.06.022

Maji, K. J., Li, Z., Vaidyanathan, A., Hu, Y., Stowell, J. D., Milando, C., Wellenius, G., Kinney, P. L., Russell, A. G., & Talat Odman, M. (2024). Estimated Impacts of Prescribed Fires on Air Quality and Premature Deaths in Georgia and Surrounding Areas in the. *Cite This: Environ. Sci. Technol*, *58*, 12343–12355. https://doi.org/10.1021/acs.est.4c00890

Manchanda, C., Harley, R. A., Marshall, J. D., Turner, A. J., & Apte, J. S. (2024). Integrating Mobile and Fixed-Site Black Carbon Measurements to Bridge Spatiotemporal Gaps in Urban Air Quality. *Environmental Science & Technology*. https://doi.org/10.1021/acs.est.3c10829

Marinov, M. B., Ganev, B., Djermanova, N., & Tashev, T. D. (2019). Analysis of Sensors Noise Performance Using Allan Deviation. *2019 IEEE XXVIII International Scientific Conference Electronics (ET)*, 1–4. https://doi.org/10.1109/ET.2019.8878552

Maya-Hernández, P. M., Álvarez-Simón, L. C., Teresa Sanz-Pascual, M., & Calvo-López, B. (2014). An Integrated Low-Power Lock-In Amplifier and Its Application to Gas Detection. *Sensors*, *14*, 15880–15899. https://doi.org/10.3390/s140915880

Maze, M., Taqi, M. O., Tolba, R., Abdel-Wareth, A. A. A., & Lohakare, J. (2024). Estimation of methane greenhouse gas emissions from livestock in Egypt during 1989 to 2021. *Scientific Reports*, *14*(1), 14992. https://doi.org/10.1038/s41598-024-63011-0

Mazurenka, M., Wada, R., Shillings, A. J. L., Butler, T. J. A., Beames, J. M., & Orr-Ewing✉, A. J. (2005). Lasers and Optics Fast Fourier transform analysis in cavity ring-down spectroscopy: application to an optical detector for atmospheric NO 2. *Appl. Phys. B*, *81*, 135–141. https://doi.org/10.1007/s00340-005-1834-1

Meller, R., Raber, W., Crowley, J. N., Jenkin, M. E., & Moortgat, G. K. (1991). The UV-visible absorption spectrum of methylglyoxal. *Journal of Photochemistry and Photobiology A: Chemistry*, *62*(2), 163–171. https://doi.org/10.1016/1010-6030(91)87017-P

Meng, X., Liu, C., Chen, R., Sera, F., Vicedo-Cabrera, A. M., Milojevic, A., Guo, Y., Tong, S., De Sousa Zanotti Stagliorio Coelho, M., Saldiva, P. H. N., Lavigne, E., Correa, P. M., Ortega, N. V., Osorio, S., Garcia, Kyselý, J., Urban, A., Orru, H., Maasikmets, M., … Kan, H. (2021). Short term associations of ambient nitrogen dioxide with daily total, cardiovascular, and respiratory mortality: Multilocation analysis in 398 cities. *The BMJ*, *372*. https://doi.org/10.1136/bmj.n534

Mielke, L. H., Stutz, J., Tsai, C., Hurlock, S. C., Roberts, J. M., Veres, P. R., Froyd, K. D., Hayes, P. L., Cubison, M. J., Jimenez, J. L., Washenfelder, R. A., Young, C. J., Gilman, J. B., De Gouw, J. A., Flynn, J. H., Grossberg, N., Lefer, B. L., Liu, J., Weber, R. J., & Osthoff, H. D. (2013). Heterogeneous formation of nitryl chloride and its role as a

nocturnal NOx reservoir species during CalNex-LA 2010. *Journal of Geophysical Research Atmospheres*, *118*(18), 10,638-10,652. https://doi.org/10.1002/JGRD.50783

Mijling, B., Jiang, Q., De Jonge, D., & Bocconi, S. (2018). Field calibration of electrochemical NO2 sensors in a citizen science context. *Atmospheric Measurement Techniques*, *11*(3), 1297–1312. https://doi.org/10.5194/amt-11-1297-2018

Miller, S. J., & Vela, M. A. (2013). The Effects of Air Pollution on Educational Outcomes: Evidence from Chile. *IDB Working Paper Series, No. IDB-WP-468, InterAmerican Development Bank (IDB)*.

Mills, I., Williamson, T., Moorcroft, S., Pearce, H., & Marner, B. (2022). *70 years since the great London smog: 1952 air quality in a modern context*.

Mitsuishi, K., Iwasaki, M., Takeuchi, M., Okochi, H., Kato, S., Ohira, S.-I., & Toda, K. (2018). Diurnal Variations in Partitioning of Atmospheric Glyoxal and Methylglyoxal between Gas and Particles at the Ground Level and in the Free Troposphere. *ACS Earth and Space Chemistry*, *2*(9), 915–924. https://doi.org/10.1021/acsearthspacechem.8b00037

Moe, A. E., Marx, S., Banani, N., Liu, M., Marquardt, B., & Wilson, D. M. (2005). Improvements in LED-based fluorescence analysis systems. *Sensors and Actuators B: Chemical*, *111–112*, 230–241. https://doi.org/10.1016/j.snb.2005.01.057

Mount, G. H., Sanders, R. W., Schmeltekopf, A. L., & Solomon, S. (1987). Visible spectroscopy at McMurdo Station, Antarctica: 1. Overview and daily variations of NO_2 and O_3, Austral Spring, 1986. *Journal of Geophysical Research: Atmospheres*, *92*(D7), 8320–8328. https://doi.org/10.1029/JD092iD07p08320

Murphy, P. C., Callanan, P., McCauley, J., McKenna, D. J., Fionnagáin, D. Ó., Louis, C. K., Redman, M. P., Cañizares, L. A., Carley, E. P., Maloney, S. A., Coghlan, B., Daly, M., Scully, J., Dooley, J., Gajjar, V., Giese, C., Brennan, A., Keane, E. F., Maguire, C. A., … Gallagher, P. T. (2021). First results from the REAL-time Transient Acquisition backend (REALTA) at the Irish LOFAR station. *Astronomy & Astrophysics*, *655*, A16. https://doi.org/10.1051/0004-6361/202140415

Myhre, G., Myhre, C. E. L., Samset, B. H., & Storelvmo, T. (2013). Atmospheric aerosols from human activity influence climate. Uncertainties in the understanding of their effects limit our knowledge about climate change. *Nature Education Knowledge* , *4*.

M□rienne, M. F., Jenouvrier, A., & Coquart, B. (1995). The NO2 absorption spectrum. I: Absorption cross-sections at ambient temperature in the 300?500 nm region. *Journal of Atmospheric Chemistry*, *20*(3), 281–297. https://doi.org/10.1007/BF00694498

Nadgir, A., Thurston, R., Larsen, K. A., Shivaram, N., Brister, M. M., & Slaughter, D. S. (2021). SILIA: software implementation of a multi-channel, multi-frequency lock-in amplifier for spectroscopy and imaging applications. *Measurement Science and Technology*, *32*(12), 125501. https://doi.org/10.1088/1361-6501/ac2436

Nam, W., Cho, C., Perdigones, B., Siek Rhee, T., & Min, K.-E. (2022). Development of a broadband cavity-enhanced absorption spectrometer for simultaneous measurements of ambient NO3, NO2, and H2O. *EGUsphere*. https://doi.org/10.5194/egusphere-2022-145

Nasse, J. M., Eger, P., Pöhler, D., Schmitt, S., Frieß, U., & Platt, U. (2019). Recent improvements of long-path DOAS measurements: impact on accuracy and stability of

short-term and automated long-term observations. *Atmospheric Measurement Techniques*, *12*(8), 4149–4169. https://doi.org/10.5194/amt-12-4149-2019

Nicholson, S. E. (1975). A pollution model for street-level air. *Atmospheric Environment (1967)*, *9*(1), 19–31. https://doi.org/10.1016/0004-6981(75)90051-7

Noda, I. (2014). Frontiers of two-dimensional correlation spectroscopy. Part 2. Perturbation methods, fields of applications, and types of analytical probes. *Journal of Molecular Structure*, *1069*, 23–49. https://doi.org/10.1016/j.molstruc.2014.01.016

O'Keefe, A., & Deacon, D. A. G. (1988). Cavity ring-down optical spectrometer for absorption measurements using pulsed laser sources. *Review of Scientific Instruments*, *59*(12), 2544–2551. https://doi.org/10.1063/1.1139895

Okorn, K., & Iraci, L. T. (2024). *An overview of outdoor low-cost gas-phase air quality sensor deployments: current efforts, trends, and limitations*. https://doi.org/10.5194/egusphere-2024-1004

Okure, D., Ssematimba, J., Sserunjogi, R., Gracia, N. L., Soppelsa, M. E., & Bainomugisha, E. (2022). Characterization of Ambient Air Quality in Selected Urban Areas in Uganda Using Low-Cost Sensing and Measurement Technologies. *Environmental Science and Technology*, *56*(6), 3324–3339. https://doi.org/10.1021/acs.est.1c01443

Osthoff, H. D., Brown, S. S., Ryerson, T. B., Fortin, T. J., Lerner, B. M., Williams, E. J., Pettersson, A., Baynard, T., Dubé, W. P., Ciciora, S. J., & Ravishankara, A. R. (2006). Measurement of atmospheric NO2 by pulsed cavity ring-down spectroscopy. *Journal of Geophysical Research Atmospheres*, *111*(12). https://doi.org/10.1029/2005JD006942

Papaconstantinou, R., Demosthenous, M., Bezantakos, S., Hadjigeorgiou, N., Costi, M., Stylianou, M., Symeou, E., Savvides, C., & Biskos, G. (2023). Field Evaluation of Low-cost Electrochemical Air Quality Gas Sensors at Extreme Temperature and Relative Humidity Conditions. *Atmospheric Measurement Techniques*, *16*, 3313–3329. https://doi.org/10.5194/amt-16-3313-2023

Park, J., Choi, Y., Jung, J., Lee, K., & Yeganeh, A. K. (2024). First top-down diurnal adjustment to NOx emissions inventory in Asia informed by the Geostationary Environment Monitoring Spectrometer (GEMS) tropospheric NO2 columns. *Scientific Reports*, *14*(1), 24338. https://doi.org/10.1038/s41598-024-76223-1

Peng, Q., Palm, B. B., Fredrickson, C. D., Lee, B. H., Hall, S. R., Ullmann, K., Campos, T., Weinheimer, A. J., Apel, E. C., Flocke, F., Permar, W., Hu, L., Garofalo, L. A., Pothier, M. A., Farmer, D. K., Ku, I. T., Sullivan, A. P., Collett, J. L., Fischer, E., & Thornton, J. A. (2021). Observations and Modeling of NO xPhotochemistry and Fate in Fresh Wildfire Plumes. *ACS Earth and Space Chemistry*, *5*(10), 2652–2667. https://doi.org/10.1021/acsearthspacechem.1c00086

Peng, W. X., Ledingham, K. W. D., Marshall, A., & Singhal, R. P. (1995). Urban air pollution monitoring: laser-based procedure for the detection of NO x gases. *The Analyst*, *120*(10), 2537. https://doi.org/10.1039/an9952002537

Phantawesak, N., Coyle, F., & Stettler, M. E. J. (2022). Long-Term In-Use NOxEmissions from London Buses with Retrofitted NOxAftertreatment. *Environmental Science and Technology*, *56*(11), 6968–6977. https://doi.org/10.1021/acs.est.1c05083

Pirjola, L., Lähde, T., Niemi, J. V., Kousa, A., Rönkkö, T., Karjalainen, P., Keskinen, J., Frey, A., & Hillamo, R. (2012). Spatial and temporal characterization of traffic emissions in urban microenvironments with a mobile laboratory. *Atmospheric Environment*, *63*, 156–167. https://doi.org/10.1016/j.atmosenv.2012.09.022

Platt, U., & Stutz, J. (2008). Evaluation of DOAS Spectra, Sensitivity and Detection Limits. In *Differential Optical Absorption Spectroscopy* (pp. 287–328). Springer Berlin Heidelberg. https://doi.org/10.1007/978-3-540-75776-4_8

Platt, U., Wagner, T., Kuhn, J., & Leisner, T. (2021). The "ideal" spectrograph for atmospheric observations. *Atmospheric Measurement Techniques*, *14*(10), 6867–6883. https://doi.org/10.5194/amt-14-6867-2021

Pommier, M. (2022). Estimations of NOx emissions, NO2 lifetime and their temporal variation over three British urbanised regions in 2019 using TROPOMI NO2 observations. *Environmental Science: Atmospheres*, *3*(2), 408–421. https://doi.org/10.1039/d2ea00086e

Ponczek, M., Franco, M. A., Carbone, S., Rizzo, L. V., Monteiro dos Santos, D., Morais, F. G., Duarte, A., Barbosa, H. M. J., & Artaxo, P. (2022). Linking the chemical composition and optical properties of biomass burning aerosols in Amazonia. *Environmental Science: Atmospheres*, *2*(2), 252–269. https://doi.org/10.1039/D1EA00055A

Popa, D., & Udrea, F. (2019). Towards Integrated Mid-Infrared Gas Sensors. *Sensors*, *19*(9), 2076. https://doi.org/10.3390/s19092076

Qi, M., Dixit, K., Marshall, J. D., Zhang, W., & Hankey, S. (2022). National Land Use Regression Model for NO $_2$ Using Street View Imagery and Satellite Observations. *Environmental Science & Technology*, *56*(18), 13499–13509. https://doi.org/10.1021/acs.est.2c03581

Qian, Y., Henneman, L. R. F., Mulholland, J. A., & Russell, A. G. (2019). Empirical Development of Ozone Isopleths: Applications to Los Angeles. *Environmental Science & Technology Letters*, *6*(5), 294–299. https://doi.org/10.1021/acs.estlett.9b00160

RADICAL. (2024, February). *The Irish Air Simulation Chamber (IASC)*. https://radical-air.eu/2024/02/19/the-irish-air-simulation-chamber-iasc/

Ravindran, V., Sakar, S., Rönnberg, S., & Bollen, M. H. J. (2020). Characterization of the impact of PV and EV induced voltage variations on LED lamps in a low voltage installation. *Electric Power Systems Research*, *185*, 106352. https://doi.org/10.1016/j.epsr.2020.106352

Rawat, P., Crawford, J. H., Travis, K. R., Judd, L. M., Demetillo, M. A. G., Valin, L. C., Szykman, J. J., Whitehill, A., Baumann, E., & Hanisco, T. F. (2024). *Maximizing the Use of Pandora Data for Scientific Applications*. https://doi.org/10.5194/amt-2024-114

Rendón, A., Wirth, V., Salazar, J. F., Palacio, C. A., & Brötz, B. (2014). Mechanisms of Air Pollution Transport in Urban Valleys as a Result of the Interplay Between the Temperature Inversion and the Urban Heat Island Effect. *AGU Fall Meeting Abstracts*. https://ui.adsabs.harvard.edu/abs/2014AGUFM.B13I0327R

Road Safety Authority. (2021, August 26). *RSA launches new guidelines for improving road safety around schools*. News. https://www.rsa.ie/news-

events/news/details/2021/08/26/rsa-launches-new-guidelines-for-improving-road-safety-around-schools

Rowell, A., Terry, M. E., & Deary, M. E. (2021). Comparison of diffusion tube–measured nitrogen dioxide concentrations at child and adult breathing heights: who are we monitoring for? *Air Quality, Atmosphere & Health*, *14*(1), 27–36. https://doi.org/10.1007/s11869-020-00909-4

Rozenberg, G. . V. (2012). *Twilight: A Study in Atmospheric Optics*. Springer.

Rück, T., Bierl, R., & Matysik, F.-M. (2018). NO2 trace gas monitoring in air using off-beam quartz enhanced photoacoustic spectroscopy (QEPAS) and interference studies towards CO2, H2O and acoustic noise. *Sensors and Actuators B: Chemical*, *255*, 2462–2471. https://doi.org/10.1016/j.snb.2017.09.039

Ryffel, B., Hamacher, J., Manoussa Ethel Fanny, S., Erard, F., Zhang, J., Wei, Y., & Fang, Z. (2019). Ozone Pollution: A Major Health Hazard Worldwide. *Front. Immunol*, *10*, 2518. https://doi.org/10.3389/fimmu.2019.02518

Saltzman, B. E. (1954). Colorimetric Microdetermination of Nitrogen Dioxide in Atmosphere. *Analytical Chemistry*, *26*(12), 1949–1955. https://doi.org/10.1021/ac60096a025

Sanjaya, Y., Priambodo, D., Sarli, P. W., & Setio, H. D. (2020). The effect of Street canyon width towards wind flow in between high-rise buildings. *IOP Conference Series: Materials Science and Engineering*, *930*(1), 012044. https://doi.org/10.1088/1757-899X/930/1/012044

Savitzky, Abraham., & Golay, M. J. E. (1964). Smoothing and Differentiation of Data by Simplified Least Squares Procedures. *Analytical Chemistry*, *36*(8), 1627–1639. https://doi.org/10.1021/ac60214a047

Schneider, S. R., Lee, K., Santos, G., & Abbatt, J. P. D. (2021). Air Quality Data Approach for Defining Wildfire Influence: Impacts on $PM_{2.5}$, NO_2, CO, and O_3 in Western Canadian Cities. *Environmental Science & Technology*, *55*(20), 13709–13717. https://doi.org/10.1021/acs.est.1c04042

Schreier, S. F., Richter, A., & Burrows, J. P. (2019). Near-surface and path-averaged mixing ratios of NO2 derived from car DOAS zenith-sky and tower DOAS off-axis measurements in Vienna: A case study. *Atmospheric Chemistry and Physics*, *19*(9), 5853–5879. https://doi.org/10.5194/acp-19-5853-2019

Shaik, K. S. (1988). *Atmospheric Propagation Effects Relevant to Optical Communications*.

Shen, Y., Jiang, F., Feng, S., Xia, Z., Zheng, Y., Lyu, X., Zhang, L., & Lou, C. (2023). Increased diurnal difference of NO2 concentrations and its impact on recent ozone pollution in eastern China in summer. *Science of The Total Environment*, *858*, 159767. https://doi.org/10.1016/j.scitotenv.2022.159767

Shi, L., Rosenberg, A., Wang, Y., Liu, P., Danesh Yazdi, M., Réquia, W., Steenland, K., Chang, H., Sarnat, J. A., Wang, W., Zhang, K., Zhao, J., & Schwartz, J. (2022). Low-Concentration Air Pollution and Mortality in American Older Adults: A National Cohort Analysis (2001-2017). *Environmental Science & Technology*, *56*(11), 7194–7202. https://doi.org/10.1021/acs.est.1c03653

Shiina, T. (2019). LED mini lidar for atmospheric application. *Sensors (Switzerland)*, *19*(3). https://doi.org/10.3390/s19030569

Sigrist, M. W., Winefordner, J. D., & Kolthoff, I. M. (1994). *Air Monitoring by Spectroscopic Techniques*. Wiley.

Sihler, H., Kern, C., Pöhler, D., & Platt, U. (2009). Applying light-emitting diodes with narrowband emission features in differential spectroscopy. *Optics Letters*, *34*(23), 3716–3719.

Skřínský, J., Janečková, R., Grigorová, E., Střižík, M., Kubát, P., Herecová, L., Nevrlý, V., Zelinger, Z., & Civiš, S. (2009). Allan variance for optimal signal averaging—monitoring by diode–laser and CO2 laser photo-acoustic spectroscopy. *Journal of Molecular Spectroscopy*, *256*(1), 99–101. https://doi.org/10.1016/j.jms.2009.02.006

Soldevila, F., Clemente, P., Tajahuerce, E., Uribe-Patarroyo, N., Andrés, P., & Lancis, J. (2016). Computational imaging with a balanced detector. *Scientific Reports*, *6*. https://doi.org/10.1038/srep29181

Solomon, S., Schmeltekopf, A. L., & Sanders, R. W. (1987). On the interpretation of zenith sky absorption measurements. *Journal of Geophysical Research: Atmospheres*, *92*(D7), 8311–8319. https://doi.org/10.1029/JD092iD07p08311

Spinelle, L., Gerboles, M., Villani, M. G., Aleixandre, M., & Bonavitacola, F. (2015). Field calibration of a cluster of low-cost available sensors for air quality monitoring. Part A: Ozone and nitrogen dioxide. *Sensors and Actuators, B: Chemical*, *215*, 249–257. https://doi.org/10.1016/j.snb.2015.03.031

Spuler, S., & Linne, M. (2002). Numerical analysis of beam propagation in pulsed cavity ring-down spectroscopy. *Applied Optics*. https://doi.org/https://doi.org/10.1364/AO.41.002858

Stanford Research Systems. (1993). *MODEL SR830 DSP Lock-In Amplifier*. www.thinkSRS.com

Stutz, J., & Platt, U. (1996). Numerical analysis and estimation of the statistical error of differential optical absorption spectroscopy measurements with least-squares methods. *Applied Optics*, *35*(30), 6041. https://doi.org/10.1364/AO.35.006041

Su, J., McCormick, M. P., Johnson, M. S., Sullivan, J. T., Newchurch, M. J., Berkoff, T. A., Kuang, S., & Gronoff, G. P. (2021). Tropospheric NO2measurements using a three-wavelength optical parametric oscillator differential absorption lidar. *Atmospheric Measurement Techniques*, *14*(6), 4069–4082. https://doi.org/10.5194/amt-14-4069-2021

Suzuki, H., Miyao, Y., Nakayama, T., Pearce, J. K., Matsumi, Y., Takahashi, K., Kita, K., & Tonokura, K. (2011). Comparison of laser-induced fluorescence and chemiluminescence measurements of NO2 at an urban site. *Atmospheric Environment*, *45*(34), 6233–6240. https://doi.org/10.1016/j.atmosenv.2011.07.065

Tang, G., Xu, C., Shao, L., Wang, S., & Li Tao. (2009). Study on measurement lower limit of DOAS system based on kalman filter. *Journal of Physics: Conference Series 147*.

Teledyne. (2010). *Operation Manual Model T200 NO/NO 2 /NO X Analyzer*. http://www.teledyne-api.com/

Thalman, R., Baeza-Romero, M. T., Ball, S. M., Borrás, E., Daniels, M. J. S., Goodall, I. C. A., Henry, S. B., Karl, T., Keutsch, F. N., Kim, S., Mak, J., Monks, P. S., Muñoz, A., Orlando, J., Peppe, S., Rickard, A. R., Ródenas, M., Sánchez, P., Seco, R., … Volkamer, R. (2015). Instrument intercomparison of glyoxal, methyl glyoxal and NO2 under simulated atmospheric conditions. *Atmospheric Measurement Techniques*, *8*(4), 1835–1862. https://doi.org/10.5194/amt-8-1835-2015

Thalman, R., & Volkamer, R. (2010). Inherent calibration of a blue LED-CE-DOAS instrument to measure iodine oxide, glyoxal, methyl glyoxal, nitrogen dioxide, water vapour and aerosol extinction in open cavity mode. *Atmospheric Measurement Techniques*, *3*(6), 1797–1814. https://doi.org/10.5194/amt-3-1797-2010

The Ella Roberta Foundation. (2024). Https://Www.Ellaroberta.Org/about-Ella Accessed on 11/06/2024. https://www.ellaroberta.org/about-ella

The European Parliament. (2024). *DIRECTIVE OF THE EUROPEAN PARLIAMENT AND OF THE COUNCIL on ambient air quality and cleaner air for Europe (recast)*.

Thomas, B., Miffre, A., David, G., Cariou, J.-P., & Rairoux, P. (2012). Remote sensing of trace gases with optical correlation spectroscopy and lidar: theoretical and numerical approach. *Applied Physics B*, *108*(3), 689–702. https://doi.org/10.1007/s00340-012-5040-7

Thornton, J. A., Wooldridge, P. J., & Cohen, R. C. (2000). Atmospheric NO_2: In Situ Laser-Induced Fluorescence Detection at Parts per Trillion Mixing Ratios. *Analytical Chemistry*, *72*(3), 528–539. https://doi.org/10.1021/ac9908905

TomTom International. (2024, November). *Cork traffic report*. https://www.tomtom.com/traffic-index/cork-traffic/

Tonne, C., & Wilkinson, P. (2013). Long-term exposure to air pollution is associated with survival following acute coronary syndrome. *European Heart Journal*, *34*, 1306–1311. https://doi.org/10.1093/eurheartj/eht045

Torzo, G., & Delfitto, G. (2022). The lock-in amplifier: what is it for? how to build one? *Revista Brasileira de Ensino de Fisica*, *44*. https://doi.org/10.1590/1806-9126-RBEF-2022-0072

Tryner, J., Quinn, C., Molina Rueda, E., Andales, M. J., L'Orange, C., Mehaffy, J., Carter, E., & Volckens, J. (2023). AirPen: A Wearable Monitor for Characterizing Exposures to Particulate Matter and Volatile Organic Compounds. *Environmental Science & Technology*, *57*(29), 10604–10614. https://doi.org/10.1021/acs.est.3c02238

Tu, R., Xu, J., Wang, A., Zhai, Z., & Hatzopoulou, M. (2021). Effects of ambient temperature and cold starts on excess NOx emissions in a gasoline direct injection vehicle. *Science of The Total Environment*, *760*, 143402. https://doi.org/10.1016/j.scitotenv.2020.143402

Turner, M. C., Jerrett, M., Pope, C. A., Krewski, D., Gapstur, S. M., Diver, W. R., Beckerman, B. S., Marshall, J. D., Su, J., Crouse, D. L., & Burnett, R. T. (2016). Long-Term Ozone Exposure and Mortality in a Large Prospective Study. *American Journal of Respiratory and Critical Care Medicine*, *193*(10), 1134–1142. https://doi.org/10.1164/rccm.201508-1633OC

Tuzson, B., Mangold, M., Looser, H., Manninen, A., & Emmenegger, L. (2013). Compact multipass optical cell for laser spectroscopy. *Optics Letters*, *38*(3), 257. https://doi.org/10.1364/OL.38.000257

Uhl, D., Bruder, L., & Stienkemeier, F. (2021). A flexible and scalable, fully software-based lock-in amplifier for nonlinear spectroscopy. *Review of Scientific Instruments*, *92*(8). https://doi.org/10.1063/5.0059740

U.S. Environmental Protection Agency, O. of A. Q. P. and S. (2008). *Final Ozone NAAQS Regulatory Impact Analysis*. https://www.epa.gov/sites/default/files/2020-07/documents/naaqs-o3_ria_final_2008-03.pdf

Van Veen, E. H., & De Loos-Vollebregt, M. T. C. (1990). Kalman filtering of data from overlapping lines in inductively coupled plasma-atomic emission spectrometry. *Spectrochimica Acta Part B: Atomic Spectroscopy*, *45*(3), 313–328. https://doi.org/10.1016/0584-8547(90)80106-S

Vardoulakis, S., Fisher, B. E. A., Pericleous, K., & Gonzalez-Flesca, N. (2003). Modelling air quality in street canyons: a review. *Atmospheric Environment*, *37*(2), 155–182. https://doi.org/10.1016/S1352-2310(02)00857-9

Venables, D. S., Gherman, T., Orphal, J., Wenger, J. C., & Ruth, A. A. (2006). High Sensitivity *in Situ* Monitoring of NO_3 in an Atmospheric Simulation Chamber Using Incoherent Broadband Cavity-Enhanced Absorption Spectroscopy. *Environmental Science & Technology*, *40*(21), 6758–6763. https://doi.org/10.1021/es061076j

Vilcins, D., Christofferson, R. C., Yoon, J.-H., Nazli, S. N., Sly, P. D., Cormier, S. A., & Shen, G. (2024). Updates in Air Pollution: Current Research and Future Challenges. *Annals of Global Health*, *90*(1). https://doi.org/10.5334/aogh.4363

Villena, G., Bejan, I., Kurtenbach, R., Wiesen, P., & Kleffmann, J. (2011). Interferences of commercial NO 2 instruments in the urban atmosphere Interferences of commercial NO 2 instruments in the urban atmosphere and in a smog chamber Interferences of commercial NO 2 instruments in the urban atmosphere. *Atmos. Meas. Tech. Discuss*, *4*, 4269–4293. https://doi.org/10.5194/amtd-4-4269-2011

Voiculescu, M., Constantin, D.-E., Condurache-Bota, S., Călmuc, V., Roșu, A., & Dragomir Bălănică, C. M. (2020). Role of Meteorological Parameters in the Diurnal and Seasonal Variation of NO2 in a Romanian Urban Environment. *International Journal of Environmental Research and Public Health*, *17*(17), 6228. https://doi.org/10.3390/ijerph17176228

Volten, H., Brinksma, E. J., Berkhout, A. J. C., Hains, J., Bergwerff, J. B., Van Der Hoff, G. R., Apituley, A., Dirksen, R. J., Calabretta-Jongen, S., & Swart, D. P. J. (2009). NO2 lidar profile measurements for satellite interpretation and validation. *Journal of Geophysical Research Atmospheres*, *114*(24). https://doi.org/10.1029/2009JD012441

von Stülpnagel, R., Riach, N., Hologa, R., Kees, J., & Gössling, S. (2024). School route safety perceptions of primary school children and their parents: Effects of transportation mode and infrastructure. *International Journal of Sustainable Transportation*, *18*(6), 465–477. https://doi.org/10.1080/15568318.2024.2350992

Wada, R., & Orr-Ewing, A. J. (2005). Continuous wave cavity ring-down spectroscopy measurement of NO2 mixing ratios in ambient air. *The Analyst*, *130*(12), 1595. https://doi.org/10.1039/b511115c

Wang, G., Meng, L., Gou, Q., Hanoune, B., Crumeyrolle, S., Fagniez, T., Coeur, C., Akiki, R., & Chen, W. (2023). Novel Broadband Cavity-Enhanced Absorption Spectrometer for Simultaneous Measurements of NO2 and Particulate Matter. *Analytical Chemistry*, *95*(6), 3460–3467. https://doi.org/10.1021/acs.analchem.2c05237

Wang, H., Chen, J., & Lu, K. (2017). Development of a portable cavity-enhanced absorption spectrometer for the measurement of ambient NO₃ and N₂O<sub>5</sub >: experimental setup, lab characterizations, and field applications in a polluted urban environment. *Atmospheric Measurement Techniques*, *10*(4), 1465–1479. https://doi.org/10.5194/amt-10-1465-2017

Wang, H., Zhang, S., Wu, X., Wen, Y., Li, Z., & Wu, Y. (2023). Emission Measurements on a Large Sample of Heavy-Duty Diesel Trucks in China by Using Mobile Plume Chasing. *Environmental Science & Technology*. https://doi.org/10.1021/ACS.EST.3C03028

Wang, J., Wang, Z., Ji, X., Liu, J., & Liu, G. (2017). A simplified digital lock-in amplifier for the scanning grating spectrometer. *Review of Scientific Instruments*, *88*(2). https://doi.org/10.1063/1.4974755

Wang, Q., Wang, J., Li, L., & Yu, Q. (2011a). An all-optical photoacoustic spectrometer for trace gas detection. *Sensors and Actuators B: Chemical*, *153*(1), 214–218. https://doi.org/10.1016/j.snb.2010.10.035

Wang, Q., Wang, J., Li, L., & Yu, Q. (2011b). An all-optical photoacoustic spectrometer for trace gas detection. *Sensors and Actuators B: Chemical*, *153*(1), 214–218. https://doi.org/10.1016/j.snb.2010.10.035

Wang, Q., & Yu, Q. (2010). Polymer diaphragm based sensitive fiber optic Fabry-Perot acoustic sensor. *Chinese Optics Letters*, *8*(3), 266–269.

Wang, X., Younan, D., Millstein, J., Petkus, A. J., Garcia, E., Beavers, D. P., Espeland, M. A., Chui, H. C., Resnick, S. M., Gatz, M., Kaufman, J. D., Wellenius, G. A., Whitsel, E. A., Manson, J. E., Rapp, S. R., Chen, J.-C., Member, E. B., Wachter, K. W., Designed, J.-C. C., & Performed, J.-C. C. (2021). Association of improved air quality with lower dementia risk in older women. *Proceedings of the National Academy of Sciences*. https://doi.org/10.1073/pnas.2107833119/-/DCSupplemental

Wang, Y., Zhong, K., He, J., Xu, J., & Kang, Y. (2023). Impacts of wind flow across street-side building gaps on traffic pollutant dispersion at pedestrian level with different block heights. *Building and Environment*, *246*, 110972. https://doi.org/10.1016/j.buildenv.2023.110972

Washenfelder, R. A., Langford, A. O., Fuchs, H., & Brown, S. S. (2008). Atmospheric Chemistry and Physics Measurement of glyoxal using an incoherent broadband cavity enhanced absorption spectrometer. In *Atmos. Chem. Phys* (Vol. 8). www.atmos-chem-phys.net/8/7779/2008/

Wayne, R. P. (2000). *Chemistry of Atmospheres* (3rd ed.). Oxford.

Wei, L., Donaire-Gonzalez, D., Helbich, M., van Nunen, E., Hoek, G., & Vermeulen, R. C. H. (2024). Validity of Mobility-Based Exposure Assessment of Air Pollution: A Comparative Analysis with Home-Based Exposure Assessment. *Environmental Science & Technology*, *58*(24), 10685–10695. https://doi.org/10.1021/acs.est.3c10867

Wei, S., Xu, T., Jiang, T., & Yin, D. (2021). Chemosensory Dysfunction Induced by Environmental Pollutants and Its Potential As a Novel Neurotoxicological Indicator: A Review. In *Environmental Science and Technology* (Vol. 55, Issue 16, pp. 10911–10922). American Chemical Society. https://doi.org/10.1021/acs.est.1c02048

Werle, P., Mücke, R., & Slemr, F. (1993). The limits of signal averaging in atmospheric trace-gas monitoring by tunable diode-laser absorption spectroscopy (TDLAS). *Applied Physics B Photophysics and Laser Chemistry*, *57*(2), 131–139. https://doi.org/10.1007/BF00425997

Westmoreland, E. J., Carslaw, N., Carslaw, D. C., Gillah, A., & Bates, E. (2007). Analysis of air quality within a street canyon using statistical and dispersion modelling techniques. *Atmospheric Environment*, *41*(39), 9195–9205. https://doi.org/10.1016/j.atmosenv.2007.07.057

Wheeler, M. D., Newman, S. M., Orr-Ewing, A. J., & Ashfold, M. N. R. (1998). Cavity ring-down spectroscopy. *Journal of the Chemical Society, Faraday Transactions*, *94*(3), 337–351. https://doi.org/10.1039/a707686j

Wilkins, E. T. (1954). Air pollution aspects of the London fog of December 1952. *Quarterly Journal of the Royal Meteorological Society*, *80*(344), 267–271. https://doi.org/10.1002/qj.49708034420

Wilkinson, I., Garcia, I. A., Whitaker, B. J., Hamard, J.-B., & Blanchet, V. (2010). The photodissociation of NO2 by visible and ultraviolet light. *Physical Chemistry Chemical Physics*, *12*(48), 15766. https://doi.org/10.1039/c0cp01551b

Wolf, M. J., Esty, D. C., Kim, H., Bell, M. L., Brigham, S., Nortonsmith, Q., Zaharieva, S., Wendling, Z. A., De Sherbinin, A., & Emerson, J. W. (2022). New Insights for Tracking Global and Local Trends in Exposure to Air Pollutants. *Environmental Science and Technology*, *56*(7), 3984–3996. https://doi.org/10.1021/acs.est.1c08080

Womack, C. C., Brown, S. S., Ciciora, S. J., Gao, R. S., Mclaughlin, R. J., Robinson, M. A., Rudich, Y., & Washenfelder, R. A. (2022). A lightweight broadband cavity-enhanced spectrometer for NO2 measurement on uncrewed aerial vehicles. *Atmospheric Measurement Techniques*, *15*(22), 6643–6652. https://doi.org/10.5194/amt-15-6643-2022

Wong, Y. K., Chan, W. W., Gu, D., Yu, J. Z., & Lau, A. K. H. (2024). Tracking Source Variations of Inhalation Cancer Risks and Ozone Formation Potential in Hong Kong over Two Decades (2000–2020) Using Toxic Air Pollutant Monitoring Data. *Environment & Health*. https://doi.org/10.1021/envhealth.3c00209

World Health Organisation. (2016). *Ambient air pollution: A global assessment of exposure and burden of disease*.

World Health Organization. (2021). WHO Global Air Quality Guidelines: Particulate matter (PM2.5 and PM10), ozone, nitrogen dioxide, sulfur dioxide and carbon monoxide. *World Health Organization*.

World Health Organization Regional Office for Europe. (2006). Air Quality Guidelines: Global Update 2005. *World Health Organisation*. www.euro.who.int

Wu, T., Zha, Q., Chen, W., Xu, Z., Wang, T., & He, X. (2014). Development and deployment of a cavity enhanced UV-LED spectrometer for measurements of atmospheric HONO and NO2 in Hong Kong. *Atmospheric Environment*, *95*, 544–551. https://doi.org/10.1016/j.atmosenv.2014.07.016

Xia, J., Feng, C., Zhu, F., Zhang, S., Kolomenskii, A. A., Dong, J., & Schuessler, H. A. (2021). Real-time measurement of methane in a turbulent atmosphere over kilometer long paths with denoising methods. *Measurement*, *168*, 108467. https://doi.org/10.1016/j.measurement.2020.108467

Xing, Y., Urasinska-Wojcik, B., & Gardner, J. W. (2018). Plasmonic enhanced CMOS non-dispersive infrared gas sensor for acetone and ammonia detection. *2018 IEEE International Instrumentation and Measurement Technology Conference (I2MTC)*, 1–5. https://doi.org/10.1109/I2MTC.2018.8409745

Xu, C., & You, C. (2023). Agricultural expansion dominates rapid increases in cropland fires in Asia. *Environment International*, *179*, 108189. https://doi.org/10.1016/j.envint.2023.108189

Xu, J., Zhao, H., Zhang, Y., Yang, W., Wang, X., Geng, C., Li, Y., Guo, Y., Han, B., Bai, Z., Vedal, S., & Marshall, J. D. (2023). Reducing Indoor Particulate Air Pollution Improves Student Test Scores: A Randomized Double-Blind Crossover Study. *Environmental Science and Technology*. https://doi.org/10.1021/ACS.EST.3C10372/SUPPL_FILE/ES3C10372_SI_001.PDF

Xue, R., Ai, B., Lin, Y., Pang, B., & Shang, H. (2019). Spatial and Temporal Distribution of Aerosol Optical Depth and Its Relationship with Urbanization in Shandong Province. *Atmosphere*, *10*(3), 110. https://doi.org/10.3390/atmos10030110

Yang, G. G., Kim, D.-H., Samal, S., Choi, J., Roh, H., Cunin, C. E., Lee, H. M., Kim, S. O., Dincă, M., & Gumyusenge, A. (2023). Polymer-Based Thermally Stable Chemiresistive Sensor for Real-Time Monitoring of NO_2 Gas Emission. *ACS Sensors*. https://doi.org/10.1021/acssensors.3c01530

Yang, L. H., Hagan, D. H., Rivera-Rios, J. C., Kelp, M. M., Cross, E. S., Peng, Y., Kaiser, J., Williams, L. R., Croteau, P. L., Jayne, J. T., & Ng, N. L. (2022). Investigating the Sources of Urban Air Pollution Using Low-Cost Air Quality Sensors at an Urban Atlanta Site. *Environmental Science and Technology*, *56*(11), 7063–7073. https://doi.org/10.1021/acs.est.1c07005

Yang, X., Wu, X., Hao, H., & He, Z. (2008). Mechanisms and assessment of water eutrophication. *Journal of Zhejiang University SCIENCE B*, *9*(3), 197–209. https://doi.org/10.1631/jzus.B0710626

Yi, H., Cazaunau, M., Gratien, A., Michoud, V., Pangui, E., Doussin, J. F., & Chen, W. (2021). Intercomparison of IBBCEAS, NitroMAC and FTIR analyses for HONO, NO2 and CH2O measurements during the reaction of NO2 with H2O vapour in the simulation chamber CESAM. *Atmospheric Measurement Techniques*, *14*(8), 5701–5715. https://doi.org/10.5194/amt-14-5701-2021

Yi, H., Liu, K., Chen, W., Tan, T., Wang, L., & Gao, X. (2011). Application of a broadband blue laser diode to trace NO_2 detection using off-beam quartz-enhanced photoacoustic spectroscopy. *Optics Letters*, *36*(4), 481. https://doi.org/10.1364/OL.36.000481

Yombo Phaka, R., Merlaud, A., Pinardi, G., Friedrich, M. M., Van Roozendael, M., Müller, J.-F., Stavrakou, T., De Smedt, I., Hendrick, F., Dimitropoulou, E., Bopili Mbotia Lepiba, R., Phuku Phuati, E., Lomami Djibi, B., Jacobs, L., Fayt, C., Mbungu Tsumbu, J.-P., & Mahieu, E. (2023). Ground-based Multi-AXis Differential Optical Absorption Spectroscopy (MAX-DOAS) observations of NO 2 and H 2 CO at Kinshasa and comparisons with TROPOMI observations. *Atmos. Meas. Tech*, *16*, 5029–5050. https://doi.org/10.5194/amt-16-5029-2023

Yoo, J. Y., Park, C. J., Kim, K. Y., Son, Y.-S., Kang, C.-M., Wolfson, J. M., Jung, I.-H., Lee, S.-J., & Koutrakis, P. (2015). Development of an activated carbon filter to remove NO 2 and HONO in indoor air. *Journal of Hazardous Materials*, *289*, 184–189. https://doi.org/10.1016/j.jhazmat.2015.02.038

Yu, K. N., Cheung, Y. P., Cheung, T., & Henry, R. C. (2004). Identifying the impact of large urban airports on local air quality by nonparametric regression. *Atmospheric Environment*, *38*(27), 4501–4507. https://doi.org/10.1016/j.atmosenv.2004.05.034

Yuan, X., Liu, H., & Gao, Y. (2015). Diesel Engine SCR Control: Current Development and Future Challenges. *Emiss. Control Sci. Technol*, *1*, 121–133. https://doi.org/10.1007/s40825-015-0013-z

Zalicki, P., & Zare, R. N. (1995). Cavity ring-down spectroscopy for quantitative absorption measurements. *The Journal of Chemical Physics*, *102*(7), 2708–2717. https://doi.org/10.1063/1.468647

Zare, A., Stevanovic, S., Jafari, M., Verma, P., Babaie, M., Yang, L., Rahman, M. M., Ristovski, Z. D., Brown, R. J., & Bodisco, T. A. (2021). Analysis of cold-start NO2 and NOx emissions, and the NO2/NOx ratio in a diesel engine powered with different diesel-biodiesel blends. *Environmental Pollution*, *290*, 118052. https://doi.org/10.1016/j.envpol.2021.118052

Zare, R. N., & Dagdigian, P. J. (1974). Tunable Laser Fluorescence Method for Product State Analysis. *Science*, *185*(4153), 739–747. https://doi.org/10.1126/science.185.4153.739

Zel'dovich, Y. B. (1946). The Oxidation of Nitrogen in Combustion Explosions. *Acta Physicochimia U.S.S.R.* , *21*, 577–628.

Zhang, G., Hao, H., Wang, Y., Jiang, Y., Shi, J., Yu, J., Cui, X., Li, J., Zhou, S., & Yu, B. (2021). Optimized adaptive Savitzky-Golay filtering algorithm based on deep learning network for absorption spectroscopy. *Spectrochimica Acta Part A: Molecular and Biomolecular Spectroscopy*, *263*, 120187. https://doi.org/10.1016/j.saa.2021.120187

Zhang, T., Kang, J., Meng, D., Wang, H., Mu, Z., Zhou, M., Zhang, X., & Chen, C. (2018). Mathematical Methods and Algorithms for Improving Near-Infrared Tunable Diode-Laser Absorption Spectroscopy. *Sensors*, *18*(12), 4295. https://doi.org/10.3390/s18124295

Zhang, W.-J., Bagreev, A., & Rasouli, F. (2008). Reaction of NO $_2$ with Activated Carbon at Ambient Temperature. *Industrial & Engineering Chemistry Research*, *47*(13), 4358–4362. https://doi.org/10.1021/ie800249s

Zhang, X., van der A, R., Ding, J., Eskes, H., van Geffen, J., Yin, Y., Anema, J., Vagasky, C., L. Lapierre, J., & Kuang, X. (2023). Spaceborne Observations of Lightning NO2 in the Arctic. *Environmental Science and Technology*, *57*(6), 2322–2332. https://doi.org/10.1021/acs.est.2c07988

Zhang, Y., Jiang, P., Cao, W., Li, X., & Lai, J. (2020). High-sensitivity ethylene gas sensor based on NDIR and dual-channel lock-in amplifier. *Optik*, *223*, 165630. https://doi.org/10.1016/j.ijleo.2020.165630

Zhao, B., Johnston, F. H., Salimi, F., Kurabayashi, M., & Negishi, K. (2020). Short-term exposure to ambient fine particulate matter and out-of-hospital cardiac arrest: a nationwide case-crossover study in Japan. *The Lancet Planetary Health*, *4*(1), e15–e23. https://doi.org/10.1016/S2542-5196(19)30262-1

Zheng, K., Zheng, C., Zhang, Y., Wang, Y., & Tittel, F. K. (2018). Review of incoherent broadband cavity-enhanced absorption spectroscopy (Ibbceas) for gas sensing. In *Sensors* (Vol. 18, Issue 11). MDPI AG. https://doi.org/10.3390/S18113646

Zheng, Z., Wang, H., Chen, X., Wang, J., Li, X., Lu, K., Yu, G.-H., Huang, X., & Fan, S. (2024a). A mini broadband cavity enhanced absorption spectrometer for nitrogen dioxide measurement on the unmanned aerial vehicle platform. *Atmospheric Environment*, *321*, 120361. https://doi.org/10.1016/j.atmosenv.2024.120361

Zheng, Z., Wang, H., Chen, X., Wang, J., Li, X., Lu, K., Yu, G.-H., Huang, X., & Fan, S. (2024b). A mini broadband cavity enhanced absorption spectrometer for nitrogen dioxide measurement on the unmanned aerial vehicle platform. *Atmospheric Environment*, *321*, 120361. https://doi.org/10.1016/j.atmosenv.2024.120361

Zhong, W., Liu, Y., Yin, Q., Zhao, R., Ding, Y., Wang, C., Chen, T., Dou, X., & Xue, X. (2024). *A photon-level dual-comb interferometer for turbulent open-air trace gases detection applications*.

Zhou, J., Zhao, W., Zhang, Y., Fang, B., Cheng, F., Xu, X., Ni, S., Zhang, W., Ye, C., Chen, W., & Venables, D. S. (2022). Amplitude-Modulated Cavity-Enhanced Absorption Spectroscopy with Phase-Sensitive Detection: A New Approach Applied to the Fast and Sensitive Detection of NO $_2$. *Analytical Chemistry*, *94*(7), 3368–3375. https://doi.org/10.1021/acs.analchem.1c05484

Zhou, S., Shen, C.-Y., Zhang, L., Liu, N.-W., He, T.-B., Yu, B.-L., & Li, J.-S. (2019). Dual-optimized adaptive Kalman filtering algorithm based on BP neural network and variance compensation for laser absorption spectroscopy. *Optics Express*, *27*(22), 31874. https://doi.org/10.1364/OE.27.031874